Technical Report Documentation Page

1. Report No. SSRP-2001/25	2. Government Accession No.	3. Recipient's Catalog No.
4. Title and Subtitle SEISMIC DESIGN AND PERFORMANCE OF PRECAST CONCRETE SEGMENTAL BRIDGE COLUMNS		5. Report Date May 2002
		6. Performing Organization Code
7. Author(s) Joshua T. Hewes and M. J. Nigel Priestley		8. Performing Organization Report No. UCSD / SSRP-2001/25
9. Performing Organization Name and Address Department of Structural Engineering School of Engineering University of California, San Diego La Jolla, California 92093-0085		10. Work Unit No. (TRAIS)
		11. Contract or Grant No. 59A0051
12. Sponsoring Agency Name and Address California Department of Transportation Division of Engineering Services 1801 30th St., West Building MS-9 Sacramento, California 95807		13. Type of Report and Period Covered Final Report (1 of 1)
		14. Sponsoring Agency Code

15. Supplementary Notes
Prepared in cooperation with the State of California Department of Transportation.

16. Abstract

This research involved the investigation of the performance of unbonded post-tensioned precast concrete segmental bridge columns under lateral earthquake loading. Two columns with a high aspect ratio and two columns with a low aspect ratio were tested under simulated lateral seismic loading. Steel jackets of different thickness were used to confine the plastic end region at the base of each column. The test units all contained the same amount of prestressing steel and each was tested twice: the first time with a relatively low initial tendon stress, and the second with a higher initial prestress level. An analytical model describing the column force-displacement behavior was used to predict column response prior to testing.

All test units performed well for the first test with the low initial tendon stress. The columns underwent large nonlinear displacements up to drifts on the order of 4.0% without experiencing significant or sudden loss of strength. For the second tests, the units with thicker steel jackets performed better than those with thinner jackets. Use of the thicker jackets enabled the columns to achieve a drift of 6.0% with only minimal capacity degradation. Because of the unbonded tendon design, the residual drift after the tests was minimal. Observed column damage was low in general, and consisted primarily of minor concrete crushing at the column base. The analytical model reasonably predicted the column force-displacement response.

17. Key Words Seismic Design, Seismic Performance, Precast, Concrete, Post-tensioned, Bridge Columns	18. Distribution Statement Unlimited	
19. Security Classification (of this report)	20. Security Classification (of this page)	21. No. of Pages ~230

22. Price

Form DOT F 1700.7 (8-72)   Reproduction of completed page authorized

DISCLAIMER

The contents of this report reflect the views of the authors who are responsible for the facts and accuracy of the data presented herein. The contents do not necessarily reflect the official views or policies of the State of California or the Federal Highway Administration. This report does not constitute a standard, specification or regulation.

ABSTRACT

This research involved the investigation of the performance of unbonded post-tensioned precast concrete segmental bridge columns under lateral earthquake loading. Two columns with a high aspect ratio and two columns with a low aspect ratio were tested under simulated lateral seismic loading. Steel jackets of different thickness were used to confine the plastic end region at the base of each column. The specimens all contained the same amount of prestressing steel and each was tested twice: the first time with a relatively low initial tendon stress, and the second with a higher initial prestress level. An analytical model describing the column force-displacement behavior was used to predict column response prior to testing.

All specimens performed well for the first test with the low initial tendon stress. The columns underwent large nonlinear displacements up to drifts on the order of 4.0% without experiencing significant or sudden loss of strength. For the second tests, the specimens with thicker steel jackets performed better than those with thinner jackets. Use of the thicker jackets enabled the columns to achieve a drift of 6.0% with only minimal capacity degradation. Because of the unbonded tendon design, the residual drift after the tests was minimal. Observed column damage was low in general, and consisted primarily of minor concrete crushing at the column base. The analytical model reasonably predicted the column force-displacement response.

ACKNOWLEDGEMENTS

LIST OF SYMBOLS

A	Cross sectional area
A_c	Concrete cross sectional area
A_g	Gross concrete cross sectional area
A_s	Prestressing steel cross sectional area
A_h	Cross sectional area of hoop or spiral reinforcement
C	Column concrete compression force
c	Neutral axis depth
cov	Concrete cover distance to the longitudinal reinforcement
D	Diameter of column
D_j	Diameter of steel jacket
E_c	Young's Modulus of concrete
E_s	Young's Modulus of prestressing steel
F_s	Prestressing steel force
F_{si}	Initial prestressing steel force
f_c	Concrete stress
f_c'	Unconfined concrete compression strength
f'_{cc}	Confined concrete compression strength
f_l	Lateral confining stress
f_s	Prestressing steel stress
f_{si}	Initial prestressing steel stress
$f_{s,inelastic}$	Prestressing steel stress after yielding of prestressing steel
f_{yh}	Hoop or spiral reinforcement yield stress
f_{yj}	Steel jacket yield stress
H	Column height
K_{eff}	Column secant stiffness at maximum displacement response
K_i	Column stiffness at theoretical decompression force
L	Distance between the point of maximum moment and point of contra-flexure
L_p	Analytical plastic hinge length
L_t	Unbonded tendon length

l_g	Linear potentiometer gage length
l_w	Distance between linear potentiometers on opposite column faces
M	Moment
M_1	Decompression moment
M_2	Yield moment
M_3	Moment in non-linear region of response
P	Axial dead load
P_a	Axial force from dead load and prestress force
P_1	Lateral force at stage one response level
P_2	Lateral force at stage-two response level
P_3	Lateral force at stage-three response level
s	Spacing of transverse reinforcement
t_j	Steel jacket wall thickness
V	Column shear force
V_d	Design shear strength
V_c	Concrete shear strength
V_p	Shear strength due to axial compression force
V_s	Shear strength of transverse reinforcement
V_{sj}	Shear strength of steel jacket
x	Distance to concrete fiber from centroid of section
x	Distance from linear potentiometer to extreme concrete compression fiber
α	Angle between diagonal compression strut and column axis
α	Column aspect ratio shear strength factor
β	Longitudinal reinforcement ratio shear strength factor
γ	Allowable shear stress factor
Δ_t	Total displacement
Δ_p	Plastic displacement
Δ_e	Elastic displacement
Δ_p	Plastic displacement
Δ_u	Ultimate displacement

Δ_1	Displacement at stage one response
Δ_1	Displacement measured by a linear potentiometer in a curvature cell
Δ_2	Yield displacement
Δ_2	Displacement measured by a linear potentiometer in a curvature cell
Δ_{2e}	Elastic component of displacement at stage two response
Δ_{2p}	Plastic component of displacement at stage two response
Δ_{3e}	Elastic component of displacement at stage three response
Δ_{3p}	Plastic component of displacement at stage three response
ΔF_s	Incremental prestress force increase
Δf_s	Incremental prestress stress increase
ΔL_t	Increase in tendon length
ε_s	Prestressing steel strain
$\Delta \varepsilon_s$	Prestressing steel strain increase
ε_c	Concrete strain
ε_{cc}	Concrete strain at peak concrete stress
ε_{cu}	Ultimate concrete strain
ε_{sm}	Steel strain at maximum stress
ρ_j	Volumetric ratio of steel jacket
ρ_l	Longitudinal reinforcement ratio
ϕ	Curvature
ϕ_p	Plastic curvature
ϕ_u	Ultimate curvature
ϕ_1	Critical section curvature at stage one response
ϕ_2	Critical section curvature at stage two response
ϕ_3	Critical section curvature at stage three response
θ	Angle between an inclined flexure-shear crack and the column axis
θ	Column drift ratio
θ_p	Plastic rotation

TABLE OF CONTENTS

CHAPTER 1 INTRODUCTION

1.1 General

The use of precast segmental construction for concrete bridges in the United States has increased in recent years due to the demand for shortened construction periods and the desire for innovative designs that yield safe, economical and efficient structures. However, knowledge of the behavior and performance of precast segmental bridges during earthquakes is lacking, and consequently their widespread use in seismic regions such as California is yet to be realized. As part of a cooperative research effort funded by Caltrans and conducted at the University of California, San Diego, testing of large-scale precast concrete segmental bridge components was conducted at the Charles Lee Powell Structural Research Laboratories located at UCSD. This report documents the testing of precast concrete segmental bridge columns under simulated lateral seismic loading and presents conclusions and design recommendations based on the experimental findings.

Unbonded post-tensioned precast concrete segmental bridge columns are constructed by stacking precast segments one on top of the other and then connecting the assembly structurally with vertical post-tensioned prestressing tendons passing through ducts located in the precast segments. The tendons are anchored in the foundation below the column and in the bent cap at the column top. Constructing bridge columns in this manner offers several advantages over conventional R.C. designs. Construction schedules can be shortened significantly since bridge components can be rapidly produced at the precasting facility, where assembly lines and steam curing increase the efficiency of concrete construction. Additionally, the erection of a segmented bridge in the field can proceed rapidly, thus reducing the disruption to existing traffic infrastructure.

Another key advantage of the precast system is its expected seismic performance. Residual column drift will be negligible, and damage in the form of concrete spalling minimal and limited to the region near the compression toe of the column. Residual cracks in the column will not exist, and footing damage resulting from strain penetration

1

of longitudinal bars into the footing that is typical of R.C. columns will not be present. Hence, a precast concrete segmental bridge column will remain functional immediately after a moderate seismic event and will require minimal repair. Given their exceptional seismic performance, these columns would be particularly attractive in bridges designated as lifeline structures.

The seismic performance characteristics described above are a direct consequence of the unbonded tendon design. A schematic of column response in the transverse direction is shown in Figure 1.1. As the precast column displaces laterally under earthquake excitation, a wide flexural crack is formed at the interface between the column base and the foundation as the column rotates rigidly about its compression toe. The prestressing steel is stretched once the base crack opening extends to the location of the tendon. Since the tendon is unbonded over the height of the column, incremental strains are not concentrated at the crack and if the initial prestress level is carefully selected, inelastic straining of the prestressing steel does not occur. This is important for several reasons. First, the ability to transfer shear across the component interfaces by shear friction is dependent on the clamping force provided by the prestressing tendon. The column stiffness is also reliant on the prestressing force and hence is not reduced drastically if the prestress is maintained. Finally, the restoring force provided to the column by the prestress is maintained during and after the earthquake ensuring that the column returns to the undeformed position.

Special detailing is required to confine the concrete in the plastic end region of a precast segmental column since high longitudinal concrete compression strains associated with rigid rotation of the column about its base are expected near the critical section. Closely spaced transverse spiral reinforcement could be used to provide the necessary confinement. This detail would result in significant cosmetic damage in the form of spalled cover concrete near the base. If however, the bottom precast column unit is encased in a steel jacket, major spalling of cover concrete in the plastic end region can be avoided. Only minor concrete crushing at the gap between the bottom of the jacket and top of the footing will occur, and little post-earthquake repair will be needed.

precast segments

base crack and
prestressing
tendon

steel jacket
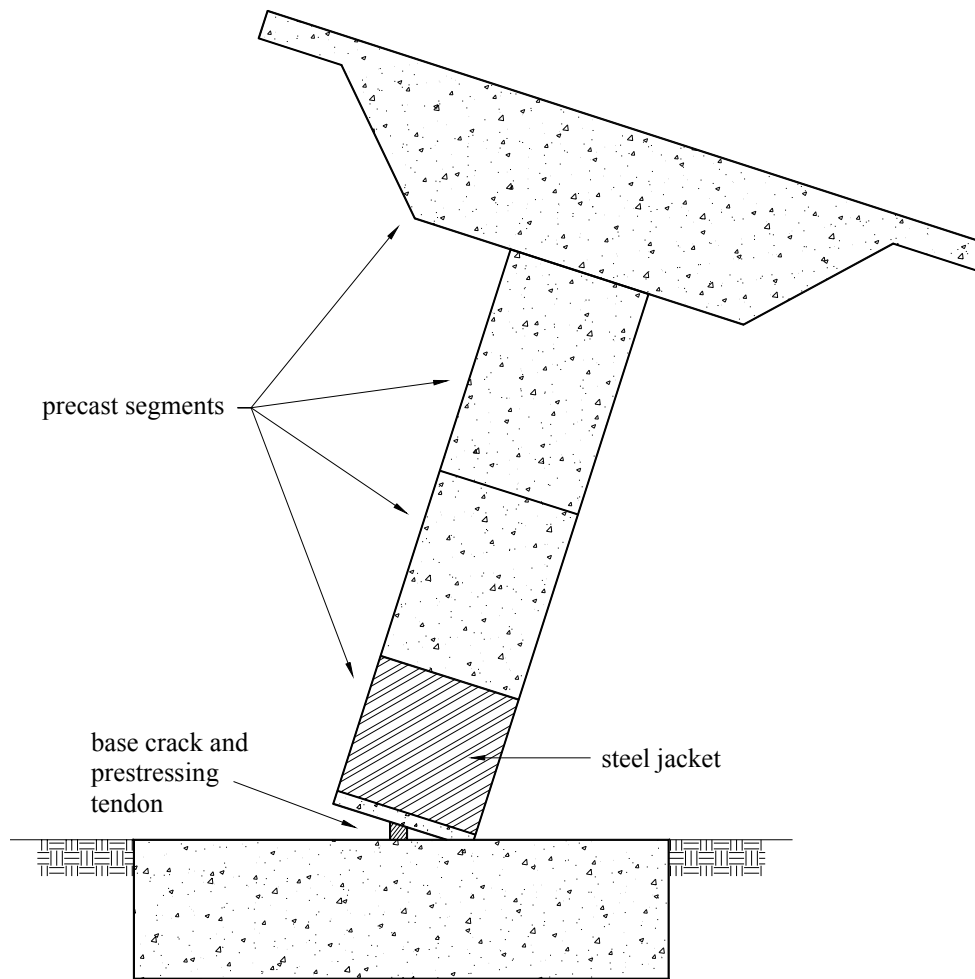
Figure 1.1 Idealized Transverse Column Response

1.2 Research Objective

This research effort involved both the analytical and experimental investigation of the behavior of post-tensioned precast concrete segmental bridge columns under lateral seismic loading. The main goal of the research was to determine the appropriate design details that ensure good seismic performance of the precast column system. The prestressing steel area and initial stress, the transverse reinforcement level for confinement of the base and for shear, the jacket height, the connection details at segment interfaces, and column aspect ratio were of prime interest in the program. In order to aid

the effort of understanding the influences of the above parameters on system performance, an analytical model was developed to describe the behavior of the columns under horizontal seismic input.

Four large-scale test model units were designed and tested. Two test units had an aspect ratio (column height divided by column diameter) of six, and two an aspect ratio of three. The prestressing steel tendons were unbonded to the surrounding concrete, and steel jackets were used to confine the base region of each column. It was desired to investigate the performance of the columns under both low and high levels of initial prestress. Since column damage was expected to be low, it was decided that each column could be effectively used twice. The columns were tested a first time under a relatively low initial prestress level. The columns were subsequently repaired, post-tensioned again to a higher initial prestress level, and tested a second time.

CHAPTER 2 ANALYTICAL PROCEDURES

2.1 Introduction

The theoretical background necessary for predicting the response of precast segmental columns under horizontal seismic loading is presented in this chapter. First, a description of the mechanical behavior of precast segmental columns under lateral seismic loading is given. The procedure used to calculate the force-displacement response of the column is developed next. Considerations regarding the modeling of concrete and prestressing steel constitutive behavior are then discussed. The shear strength of a precast segmental column is presented last.

2.2 Overview of Column Response

The behavior of a precast column under seismic loading differs fundamentally from that of a conventional reinforced concrete column. In the design of most reinforced concrete bridges, the designer selects and carefully details locations where inelastic response is to occur. These locations of concentrated inelastic behavior are usually in the bridge columns in the form of plastic hinges, where yielding of reinforcement and plastic straining of concrete act together to dissipate energy input by the earthquake. It is the deformation of the materials in the plastic hinges which allows rotation and hence displacement of the column top. In the precast column, large structural deformations are not due to plastic deformation within a hinge region, but rather, are due to rigid rotation of the entire column about its base. The response of a precast column is similar to a rocking foundation, where the foundation lifts off the ground once the moment resistance provided by gravity is overcome. In the case of the precast column, it is both the column vertical dead load (tributary deck weight and column self-weight) and the prestressing force which provide moment resistance against overturning. Hysteretic energy dissipation of the precast system is small relative to that of a conventional reinforced concrete column.

Figure 2.1 gives a depiction of a precast column under lateral seismic loading at three key stages of response. Included in the diagrams are the earthquake force, **E**, the vertical dead load, **P**, the initial prestressing force, $\mathbf{F_{si}}$, and the concrete longitudinal compressive strain profile and neutral axis depth at the critical section. In the figure, and throughout this report, the prestressing tendon is assumed located at mid-depth of the cross-section. A representative stress-strain curve for the prestressing steel is shown in Figure 2.2, where the initial prestressing steel stress after losses and before seismic excitation is $\mathbf{f_{si}}$. At a certain level of excitation, the precompression at the column base will be lost at the extreme tension fiber. This condition defines the first significant point of column response, and is represented by elastic behavior. At this stage of response, the prestressing steel stress will not have changed appreciably from the original value, $\mathbf{f_{si}}$.
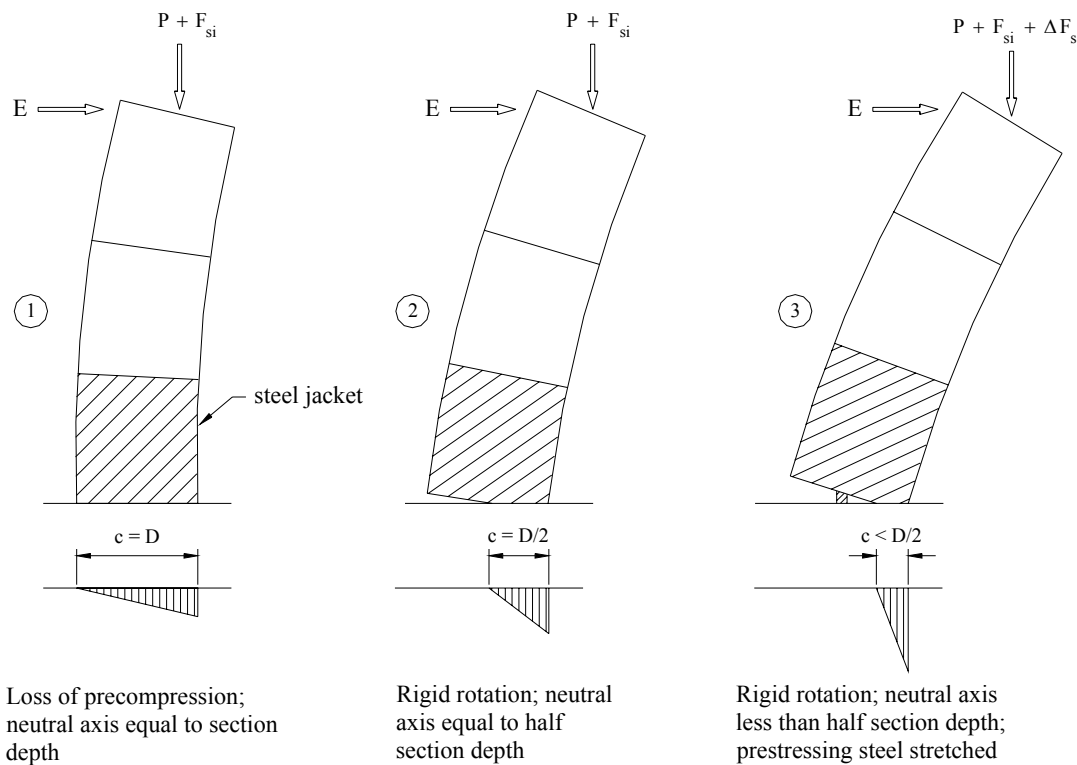

Figure 2.1 Precast column at key stages of response

6

As seismic forces increase, a crack will form at the column base and begin to propagate into the section depth. Eventually the base crack will reach mid-depth of the section. This condition defines the second stage of column response as it represents the beginning of significant nonlinearity in response. With a further decrease of neutral axis depth, the prestressing tendon is stretched and the steel stress will increase by $\Delta \mathbf{f_s}$. Fluctuations in steel stress during the seismic event will remain in the elastic regime if the initial stress, $\mathbf{f_{si}}$, is carefully selected (point 3 in Fig. 2.2). If however the initial stress is too high, or if the maximum column displacement is larger than expected, the steel stress may enter the inelastic portion of the stress-strain curve (point 3' in Fig. 2.2). Upon unloading to the undeformed position, the effective stress will be reduced to $\mathbf{f_{s,inelastic}}$. The consequence of this is partial, or in the extreme case complete loss of the tendon prestress force. Since the ability to transfer shear between precast segments is dependent on the clamping force provided by the prestressing tendon, it is vital that the designer can accurately predict the prestressing steel stress increase under seismic input.
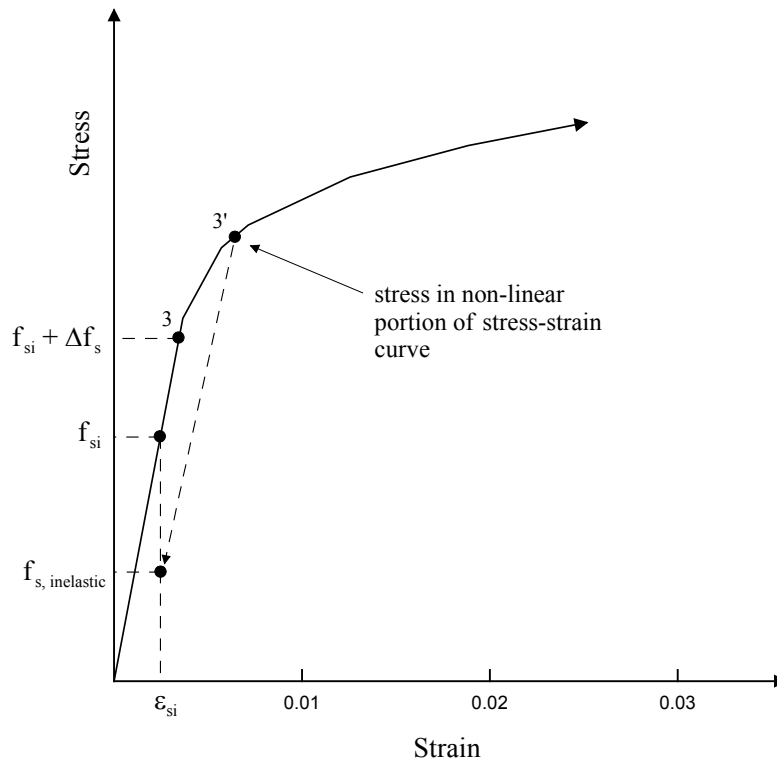

Figure 2.2.2 Prestressing steel stress-strain behavior

2.3 Force – Displacement Response

The theoretical lateral force-displacement response of a precast column is depicted in Figure 2.3. The key stages of response described previously are indicated by points 1-3 in the figure. The overall response is similar to a nonlinear-elastic relationship. Residual displacement of the column does not exist because the tendon prestressing force acts to recenter the column after the earthquake. No hysteresis is shown in the response since the energy dissipation associated cyclic yielding of longitudinal reinforcement in a conventional reinforced concrete column is not present in the precast system. However, energy will be dissipated in the system through plastic straining of concrete near the critical section and yielding of the steel jacket, and consequently some hysteresis will be present.
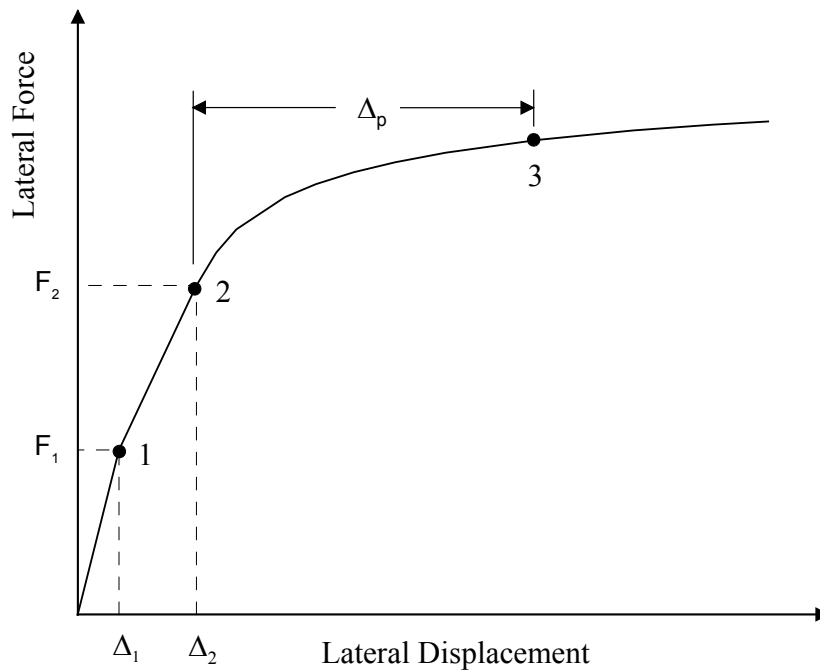

Figure 2.2.3 Idealized force-displacement response of precast column

2.3.1 Moment – Curvature Analysis

A conventional analysis to determine the moment-curvature behavior at the critical section is not adequate since the total vertical force due to prestress and axial dead load is not constant, but rather increases as the tendon is stretched. For a conventional reinforced concrete column, the total vertical force acting on the column is known and must be balanced by the resultant concrete compression force, **C**. To calculate the moment-curvature response, one needs only to select values of the concrete extreme fiber compressive strain, ε_c, and iterate for the neutral axis depth, **c**, using equilibrium considerations and the concrete and steel reinforcement stress-strain relationships. Since the steel reinforcement is assumed perfectly bonded to the concrete, strain compatibility at the section can be used to calculate the resultant steel and concrete forces. However, in the precast column, the tendon is not bonded to the surrounding concrete and strain compatibility between the prestressing steel and concrete does not exist. Thus, for a given concrete strain and neutral axis depth, the prestressing steel strain is not uniquely determined.

In the method presented herein, an analogy is made between a precast column and conventional reinforced concrete column. This is done despite the fundamental difference in behavior of the two systems described previously. In addition, an iterative process involving not only the extreme fiber concrete strain and neutral axis depth, but also the prestress force, is used.

During the early stages of column response, the prestressing steel force is essentially unchanged from its initial value, **F$_{si}$**. The moment-curvature response is calculated by picking values for the extreme fiber concrete compression strain, ε_c, and iterating for the neutral axis depth, **c**, which satisfies equilibrium of vertical forces acting on the section:

$$C = P + F_{si} \qquad (2.1)$$

The concrete compression resultant is obtained by integration of the concrete stress-strain relationship over the neutral axis depth:

$$C = \int_{D/2-c}^{D/2} f_c \, dA \qquad (2.2)$$

where f_c is the confined concrete stress-strain relationship (as discussed subsequently) and D is the column diameter. The section moment capacity is given by:

$$M = \int_{D/2-c}^{D/2} f_c \, x \, dA \qquad (2.3)$$

This method is the same as that given by conventional reinforced concrete theory, and is used up to and including the point when the neutral axis depth equals half the diameter of the column (i.e., the 'stage two' response level).

For the third stage of response, the following procedure is adopted. Although large nonlinear displacements of a precast column are due to rigid rotation of the column about the compression toe, it is assumed that the precast column behaves like a conventional reinforced concrete column, and that a plastic hinge is located at the interface between the column base and foundation. Consider Figure 2.4, which depicts the deformed shape of a precast column during the third stage response, and shows a close-up view of the interface between the column base and the foundation. As shown, the angle formed between the base of the column and top of the foundation is assumed equal to the column plastic rotation, θ_p, which is:

$$\theta_p = \phi_p L_p \qquad (2.4)$$

where ϕ_p is the plastic curvature and L_p is the plastic hinge length equal to half the section diameter (Eq. 2.5). It is noted that the analytical plastic hinge length given for a

10

precast column differs from the value typically used for reinforced concrete (Eq. 2.6), and was determined by calibration of the analytical model with the experimental test results.

Precast column:
$$L_p = \frac{D}{2}$$
(2.5)

R.C. column:
$$L_p = 0.08L + 0.022 f_{ye} d_{bl} \quad (mm, MPa)$$
(2.6)

In the above, f_{ye} and d_{bl} are the expected yield stress and diameter of the longitudinal reinforcement, respectively [5]. The plastic curvature is defined as the total section curvature minus the elastic curvature (Eq. 2.7). The total curvature is calculated from the concrete compression strain at the extreme fiber and the neutral axis depth (Eq. 2.8), while the elastic curvature is the taken as the curvature at stage two response (Eq. 2.9).

$$\phi_p = \phi_t - \phi_e$$
(2.7)

$$\phi_t = \frac{\varepsilon_c}{c}$$
(2.8)

$$\phi_e = \phi_2$$
(2.9)

Referring again to Figure 2.4, the prestressing steel is stretched once the base crack propagates past mid-depth of the section. Associated with the tendon elongation is an increase of prestressing steel stress, Δf_s, and hence force, ΔF_s. Knowing the unbonded length of the tendon, L_t, the column diameter, D, and the neutral axis depth, c (calculated as described subsequently), the increase in tendon strain, $\Delta \varepsilon_s$, is given by:

$$\Delta \varepsilon_s = \frac{\Delta L}{L_t} = \frac{\theta_p (D/2 - c)}{L_t}$$
(2.10)

11

The corresponding prestress stress increase is calculated as:

$$\Delta f_s = \Delta \varepsilon_s E_s \tag{2.11}$$

where E_s is the prestressing steel modulus of elasticity. Using the prestressing steel cross-sectional area, A_s, the total force increase in the tendon due to the base crack opening is given by:

$$\Delta F_s = \Delta f_s A_s \tag{2.12}$$

Calculation of the moment-curvature response for the third stage of the response is performed as follows.

I. Select the extreme fiber concrete compression strain, ε_c, and guess the neutral axis depth, c:

$$\phi_t = \frac{\varepsilon_c}{c} \tag{2.8}$$

$$\phi_p = \phi_t - \phi_e \tag{2.7}$$

$$\theta_p = \phi_p L_p \tag{2.4}$$

II. Update the total prestressing force, F_s:

$$F_s = F_{si} + \Delta F_s \tag{2.13}$$

$$F_s = (f_{si} + \Delta f_s) A_s \tag{2.14}$$

$$F_s = (f_{si} + \Delta\varepsilon_s \, E_s \,) \, A_s \qquad\qquad (2.15)$$

$$F_s = \left[f_{si} + \frac{\theta_p \, (D/2 - c) \, E_s}{L_t} \right] A_s \qquad\qquad (2.16)$$

III. Check equilibrium of vertical forces:

$$C = \int_{D/2-c}^{D/2} f_c \, dA \qquad\qquad (2.2)$$

$$C \overset{?}{=} P + F_s \qquad\qquad (2.17)$$

If equilibrium is not satisfied, a new value for the neutral depth axis is chosen and steps two and three are repeated until equilibrium is achieved. When the correct neutral axis is found, the column moment capacity is calculated by:

$$M = \int_{D/2-c}^{D/2} f_c \, x \, dA \qquad\qquad (2.3)$$

IV. The complete moment-curvature response is obtained by incrementing the value of extreme fiber concrete strain, ε_c, and repeating the above steps until the ultimate concrete compression strain, ε_{cu}, is reached.
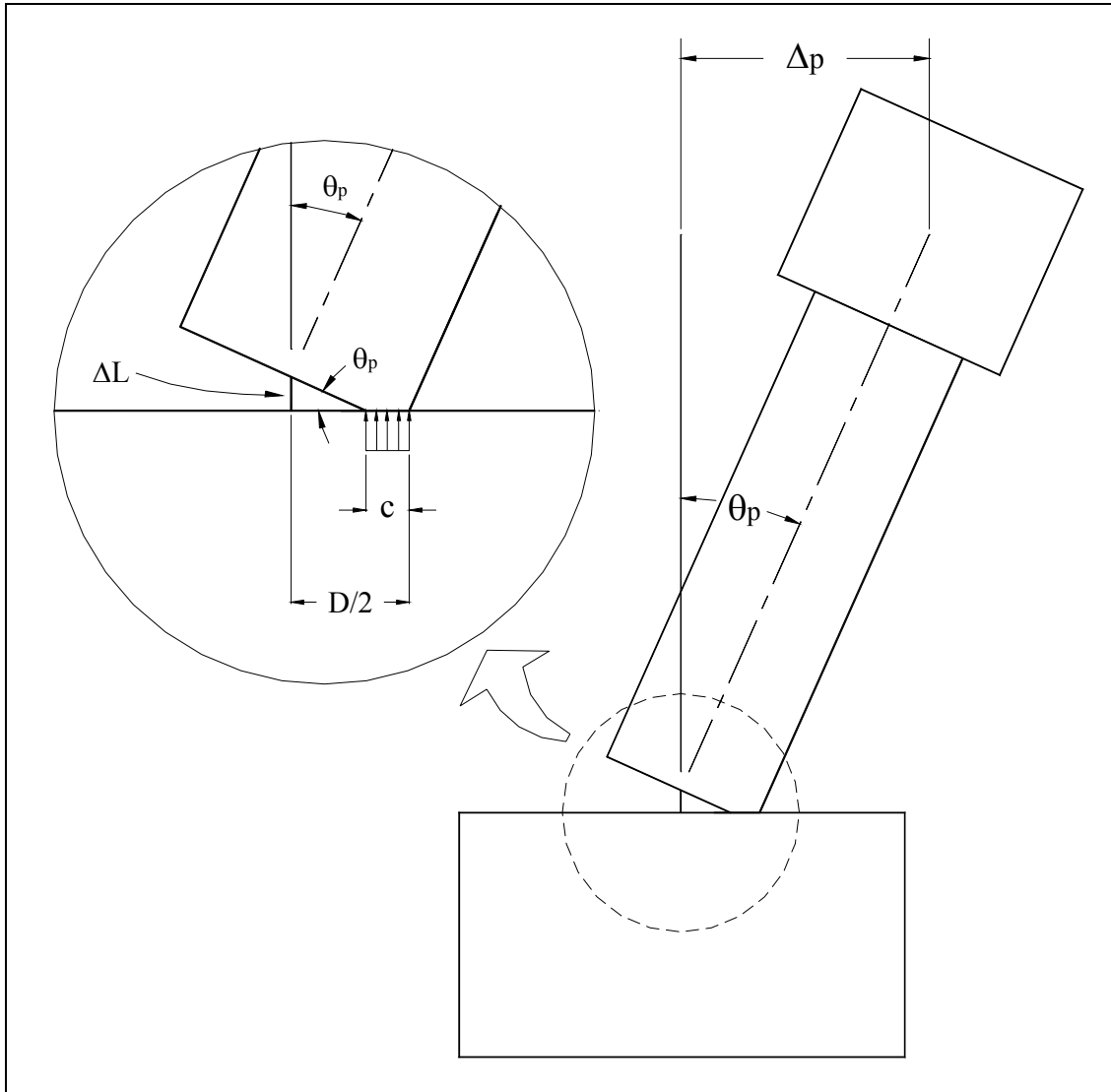
13

Figure 2.2.4 Rigid rotation of the column about the compression toe

2.3.2 Elastic Displacement

Based on moment-curvature analysis of the section and considering a cantilever column fixed at the base, the displacement at the first stage of response is calculated from the section curvature using simple beam theory as given below:

$$\Delta_1 = \frac{1}{3}\phi_1 H^2 \tag{2.18}$$

where **H** is the column height measured from the point of maximum moment to the point of contra-flexure. The corresponding lateral force is:

$$F_1 = \frac{M_1}{H} \tag{2.19}$$

The displacement at the second stage of response is determined by linearly extrapolating from the displacement at stage one to obtain the elastic component of displacement, and adding to this an additional component associated with the rigid rotation of the column about the compression toe. Referring to Figure 2.5, the displacement at the second stage of response is calculated as:

$$\Delta_2 = \Delta_{2e} + \Delta_{2p} \tag{2.20}$$

$$\Delta_{2e} = \frac{F_2}{F_1}\Delta_1 \tag{2.21}$$

$$\Delta_{2p} = \left\{ \phi_2 - \frac{F_2}{F_1}\phi_1 \right\} L_p H \tag{2.22}$$

where **L$_p$** was defined previously in Eq. 2.5 and:

$$F_2 = \frac{M_2}{H} \tag{2.23}$$

Point 2 corresponds to the stage when the crack at the column base has propagated to mid-depth of the section, and is taken as the yield point of the force-displacement response. It should be noted however, that the word "yield" is not meant to reflect any yielding of the prestressing steel reinforcement, but rather is used to describe the point where significant nonlinearity in column response begins.
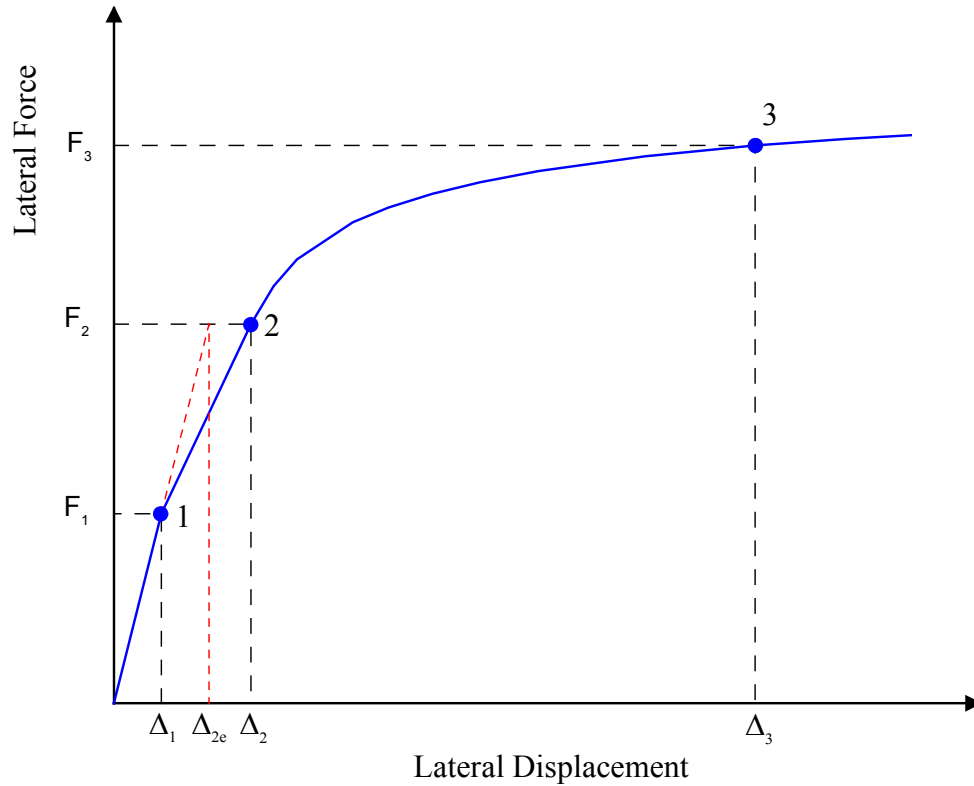

Figure 2.2.5 Force – displacement response envelope

2.3.3 Plastic Displacement

Displacements during the third stage of response are largely due to rigid rotation of the column about its compression toe, with significant opening of the base crack. Column displacements for stage three are:

$$\Delta_3 = \Delta_{3e} + \Delta_{3p} \tag{2.24}$$

$$\Delta_{3e} = \frac{F_3}{F_2} \Delta_2 \qquad\qquad (2.25)$$

$$\Delta_{3p} = \left\{ \phi_3 - \frac{F_3}{F_2} \phi_2 \right\} L_p H \qquad\qquad (2.26)$$

where:

$$F_3 = \frac{M_3}{H} \qquad\qquad (2.27)$$

2.4 Material Constitutive Behavior

The assumed material behavior of the concrete and prestressing steel used in the test units is presented in this section.

2.4.1 Concrete Stress-Strain Model

Because high compression strains are expected to develop in the plastic end region, and since damage in the form of spalled concrete is to be minimized, a steel jacket is used to provide confinement to the concrete near the column base. The jacket enhances the compression strength of the core concrete and enables a high concrete compression strain to be developed.

Calculation of the lateral confining stress provided by the jacket is analogous to that done for conventional transverse spiral or hoop reinforcement. Considering a jacket with diameter, D_j, wall thickness, t_j, and yield strength f_{yj}, the lateral confining stress is given by:

$$f_l = \frac{2f_{yj}t_j}{D_j - 2t_j} \approx \frac{2f_{yj}t_j}{D_j} \tag{2.28}$$

The ultimate concrete compression strain is calculated by [4]:

$$\varepsilon_{cu} = 0.004 + \frac{1.4\rho_j f_{yj}\varepsilon_{sm}}{f'_{cc}} \tag{2.29}$$

where ρ_j is the effective volumetric ratio of confining steel, ε_{sm} is the strain at maximum steel stress, and f'_{cc} is the confined concrete compressive strength. The volumetric ratio of confinement is given by:

$$\rho_j = \frac{4t}{D} \tag{2.30}$$

The model for the stress-strain behavior of confined concrete proposed by Mander *et al.* [4] has been used widely and has been incorporated into moment-curvature software programs designed for conventionally reinforced concrete columns. This model was used in the moment-curvature analysis described previously. Figure 2.6 shows a representative stress-strain curve for a volumetric confinement ratio of ρ_j = 2.0%, unconfined concrete compressive strength of f'_c = 41.4MPa, and steel yield strength of f_{yj}=276 MPa.
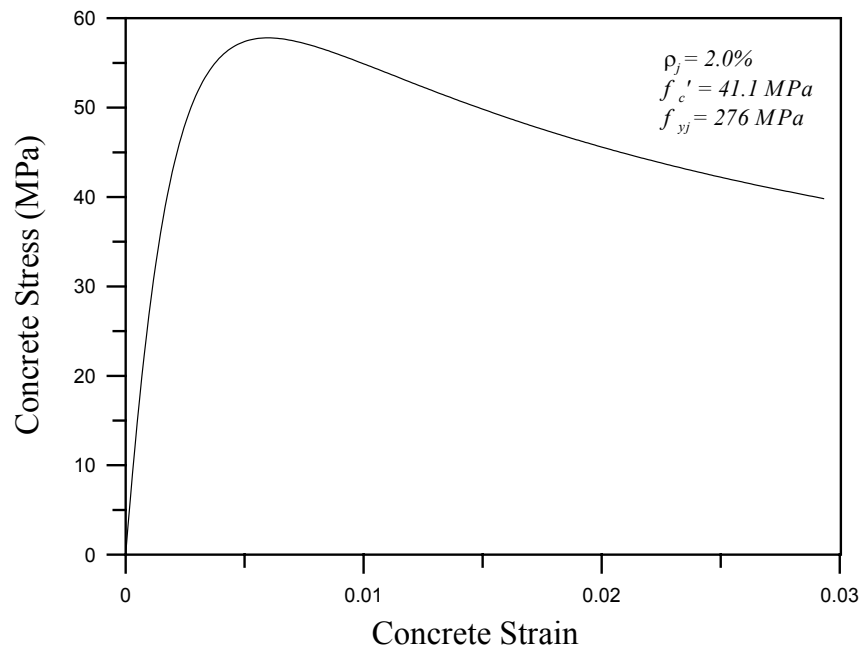

Figure 2.6 Mander model for confined concrete stress-strain relationship

Comment is due regarding the use of the Mander model for the moment-curvature analysis of precast columns. A precast column will have a relatively high level of axial stress at the column base since the prestressing force provides axial load that is in addition to vertical dead load. Therefore, a high strength concrete is used in the precast column to avoid early degradation and strength loss under seismic loading. Since the Mander model was not developed specifically for high strength concrete, its use in the analysis could introduce error. Research has indicated that the strength gain due to passive confinement for high strength concrete is less than that for concrete of lower

19

strength. This is because less microcracking and dilation occurs in high strength concrete prior to failure. Therefore, less hoop strain is induced in the transverse reinforcement (steel jacket or spiral) and consequently the lateral confining stress is reduced. An over-prediction of the strength of the concrete would cause a smaller neutral axis depth to be predicted. Associated with the smaller neutral axis depth would be a larger lever arm between the resultant internal forces, and thus larger moment capacity. Also, the smaller neutral axis depth would result in a higher predicted tendon force since for the analytical model presented, the prestress force increase due to gap opening at the column base increases as the neutral axis depth decreases (see Eq. 2.16). Thus, the moment capacity would also be larger because of the increased total prestress force.

High strength concrete is typically more brittle than concrete of lower strength, and exhibits less overall ductility. The descending branch of the Mander stress-strain model may thus be too gradual for high strength concrete, and consequently column strengths may be over-predicted at high concrete compressive strains.

The degree to which the above issues affect the analytical response is not certain. However, it is believed that acceptable results should be obtained using the Mander model.

2.4.2 Prestressing Steel Stress-Strain Model

A nonlinear stress-strain model was used for the 7-wire low-relaxation prestressing strand [6]. The stress-strain curve given by the equations below is shown in Figure 2.7.

Prestress steel limit of proportionality: $\varepsilon_{lp} = 0.0086$ (2.31)

Reduced ultimate prestress steel strain: $\varepsilon_{lp} = 0.030$ (2.32)

$$\varepsilon_s \leq 0.0086 : \quad f_s = 28,500\, \varepsilon_s \tag{2.33}$$

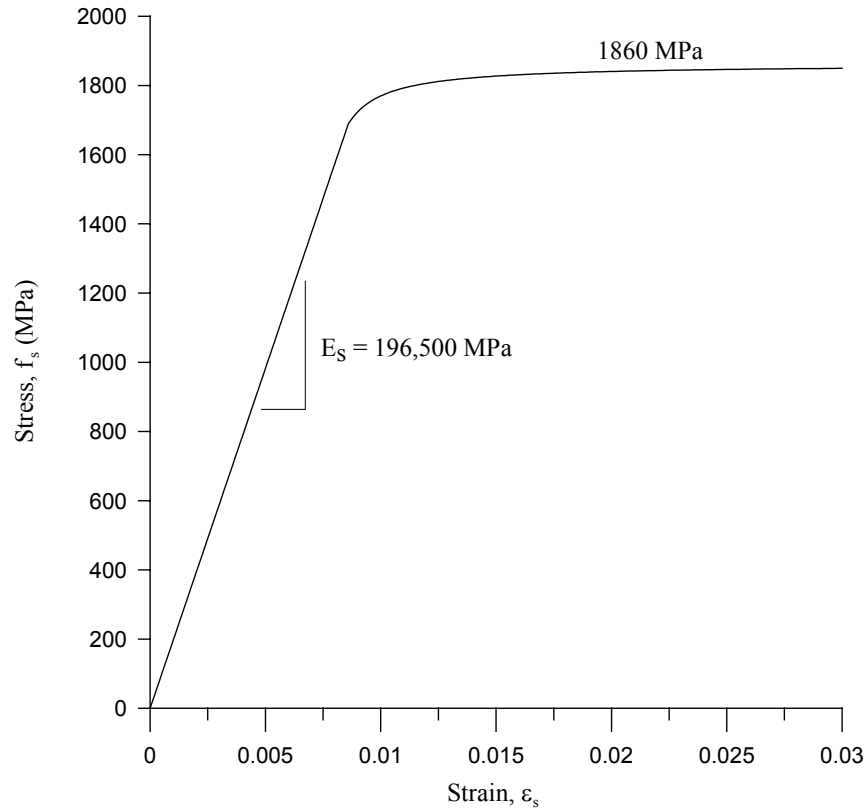$$\varepsilon_s \geq 0.0086 : \quad f_s = 270 - \frac{0.04}{\varepsilon_s - 0.007} \tag{2.34}$$

Figure 2.2.7 Prestressing steel stress-strain model

21

2.5 Column Shear Strength Model

The design shear strength of a precast segmental column with unbonded prestressing steel is based on the approach of Kowalsky and Priestley [3]. In the approach, the column shear strength is composed of contributions from a concrete shear resisting mechanism, a truss mechanism, and an axial compression component.

$$V_d = V_c + V_s + V_p \qquad (2.35)$$

The concrete mechanism strength is given by:

$$V_c = \alpha \beta \gamma \sqrt{f_c'} \, (\, 0.8 A_g) \qquad (2.36)$$

The factor α is a function of column aspect ratio and the factor β accounts for the longitudinal steel ratio. Values for α and β are given by Eq. 2.30 and Eq. 2.31. The factor γ is related to the allowable shear stress, and reduces with increasing ductility. Figures 2.8 (a) and 2.8 (b) give the relationship of γ to member curvature ductility demand and displacement ductility demand, respectively.

$$1 \le \alpha = 3 - \frac{M}{VD} \le 1.5 \qquad (2.37)$$
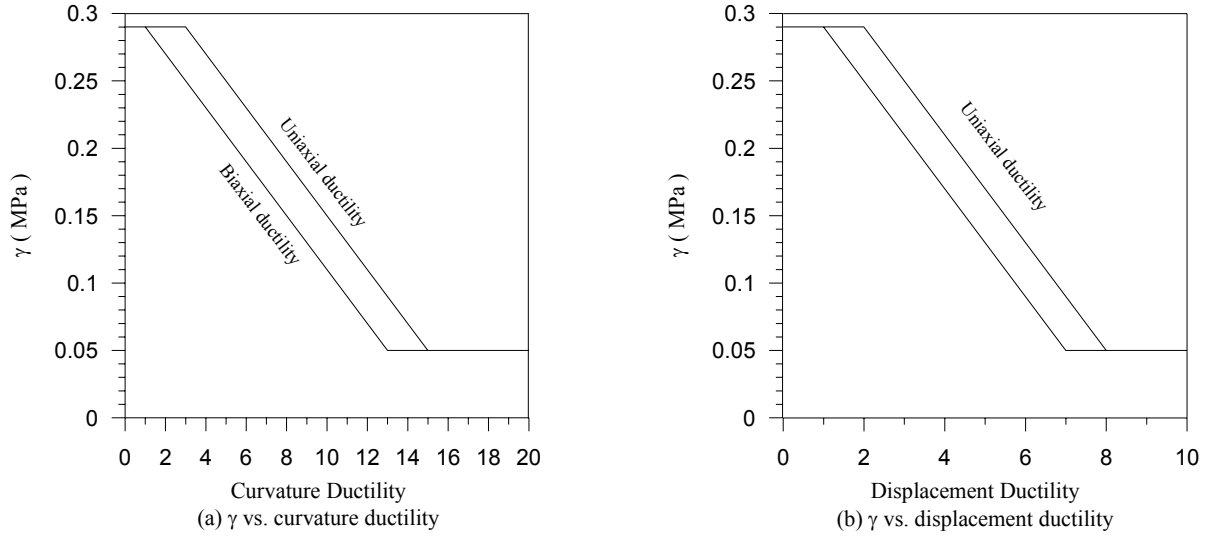
$$\beta = 0.5 + 20 \rho_l \le 1 \qquad (2.38)$$

(a) γ vs. curvature ductility

(b) γ vs. displacement ductility

Figure 2.2.8 γ factor for concrete shear strength component

The contribution from transverse spiral reinforcement, **V_s**, is given for circular columns by:

$$V_s = \frac{\pi}{2} A_{sp} f_y \frac{D - c - cov}{s} cot(\theta)$$

(2.39)

where **A_{sp}** and **f_y** are the cross-sectional area and yield stress of the hoop reinforcement, respectively. The variable **c** is neutral axis depth and **cov** is the concrete cover distance measured to the longitudinal reinforcement. The variable **θ** is the angle between an inclined flexure shear crack and the column axis, and is taken as **θ = 35°** for design purposes. For the steel jacket encased column segment, the following gives a conservative estimate of jacket shear strength [5]:

$$V_s = \frac{\pi}{2} t_j f_{yj} D_j cot(\theta)$$

(2.40)

The shear strength resulting from the axial compression acting on the column, provided by the horizontal component of the diagonal compression strut is calculated by:

$$V_p = P_a \frac{(D-c)}{2L} \quad for \ P_a > 0 \tag{2.41}$$

$$V_p = 0 \quad for \ P_a \leq 0 \tag{2.42}$$

$$P_a = F_{si} + \Delta F_s + P \tag{2.43}$$

where $\mathbf{P_a}$ is the total axial compressive force which includes the initial prestress force, $\mathbf{F_{si}}$, the incremental prestress force, $\mathbf{\Delta F_s}$, and the applied vertical dead load, $\mathbf{P}$. The variable $\mathbf{L}$ is the length of the column between the point of maximum moment and the point of contra-flexure.

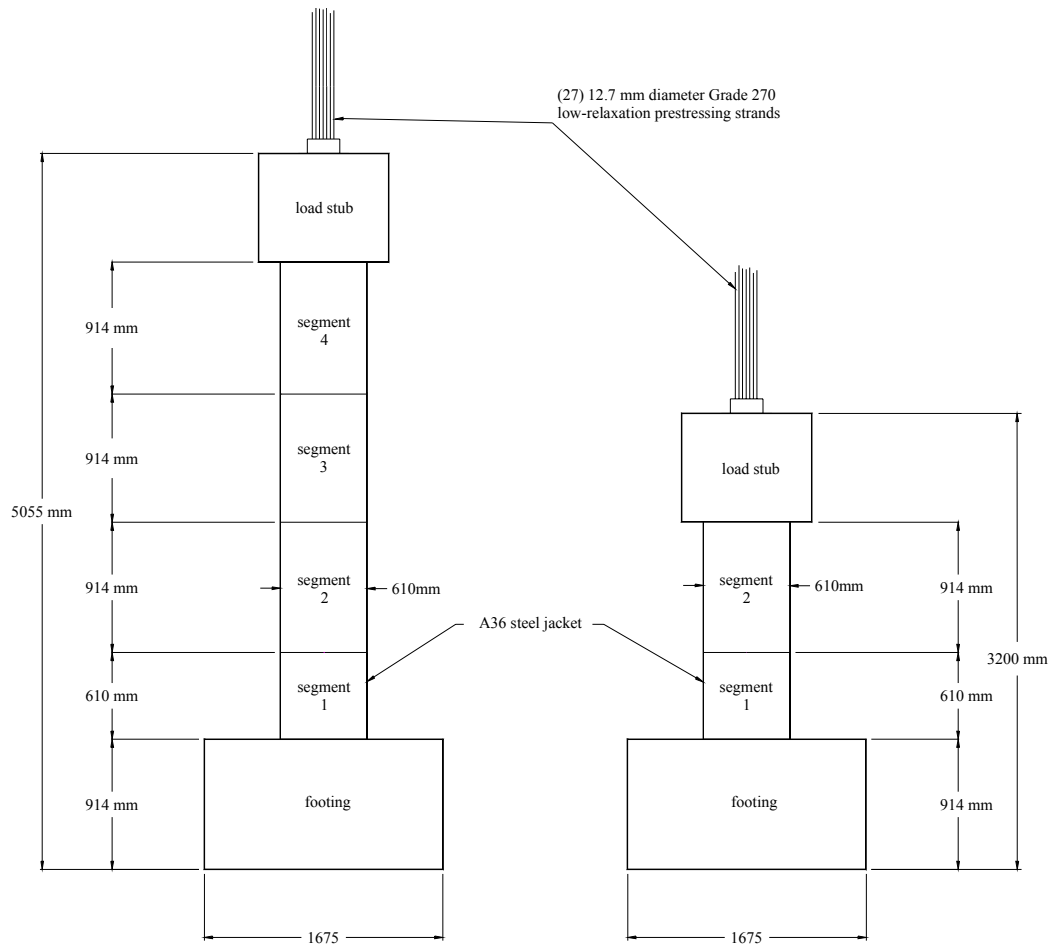# CHAPTER 3 MODELING, TEST SET-UP AND INSTRUMENTATION

3.1 Introduction

Modeling procedure, test set-up, and instrumentation used for the low and high aspect ratio test units are presented in this chapter. Test units JH1 and JH2 were columns with an aspect ratio of six, while units JH3 and JH4 had an aspect ratio of three. All units were tested in single bending, and hence the aspect ratio typically defined as M/VD – where M is the maximum moment at the critical section, V is the column shear, and D is the column diameter – is equal to the column height H divided by the diameter: H/D.

3.2 Prototype Structure

The test model units were not based on a specific prototype structure. However, in order to compare the performance of the precast system with conventional reinforced concrete design, the geometry of the test units was chosen similar to that of a conventionally reinforced circular concrete column tested previously at UCSD [2]. This reinforced concrete reference column was a 40% scale model of a circular prototype bridge column.
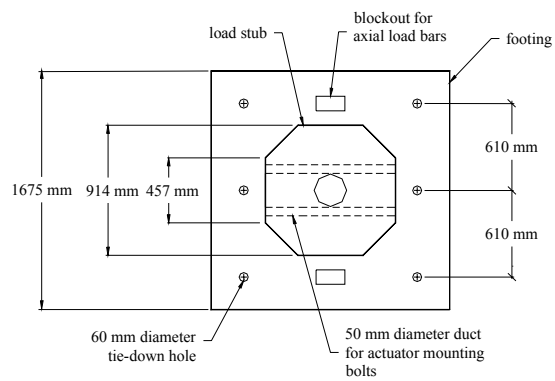
3.3 Laboratory Test Model

The overall dimensions of the test units are shown in Figure 3.1. All test units were built using precast concrete units and constructed in a segmental fashion. The anchorages for each end of the tendon were cast within the footing and column cap segments, which were heavily reinforced because of the high concrete compressive stresses induced by the prestressing tendon. In addition to the footing and cap segments, test units JH1 and JH2 consisted of four precast cylindrical concrete segments while test units JH3 and JH4 consisted of two precast cylindrical segments. The cylindrical segments had a hollow core to allow for passage of the prestressing tendon.

(27) 12.7 mm diameter Grade 270
low-relaxation prestressing strands

load stub

914 mm   segment 4

914 mm   segment 3

5055 mm

914 mm   segment 2   610mm

A36 steel jacket

610 mm   segment 1

914 mm   footing

1675

Test units JH1 and JH2

load stub

segment 2   610mm   914 mm

3200 mm

segment 1   610 mm

footing   914 mm

1675

Test units JH3 and JH4

blockout for
axial load bars

load stub   footing

1675 mm   914 mm   457 mm

610 mm

610 mm

60 mm diameter
tie-down hole

50 mm diameter duct
for actuator mounting
bolts

Top view of test units

Figure 3.1 Overall dimensions of precast column test units

3.4   Test Set-Up

A schematic representation of the test set-up for units JH3 and JH4 is shown in Figure 3.3. The set-up for units JH1 and JH2 was similar to that for JH3 and JH4. For each test, the column footing was connected to the laboratory strong floor by six 44.5 mm diameter high strength post-tensioning bars stressed to 890 kN each. The cyclic lateral point load was applied at the column top by a servo-controlled 980 kN capacity hydraulic actuator with a ±610 mm stroke reacting off the laboratory strong wall. Horizontal load levels in the actuator were monitored during the test through a load cell and the horizontal displacement at the actuator level measured using a string displacement transducer and an independent reference column. A constant axial compressive load of 890 kN was applied to the column by a transfer beam and a pair of 35 mm diameter high-strength steel post-tensioning bars loaded by two 150 ton hollow core jacks reacting off the laboratory strong floor. This externally applied axial load was used to model the dead load of the tributary deck weight and column self-weight. The applied axial load level was the same for all of the tests.

Curvature along the column height was measured by a system of aluminum brackets attached to threaded rods. For the non-jacketed column segments, the rods were embedded in the core concrete. To prevent any possible shear strength enhancement from the embedded rods, each curvature fixture was composed of two separate rod sections spaced 25 mm apart with PVC sleeves around each rod assembly within the core of the column. For test units JH1 and JH2, the curvature rods for the jacketed column segment were tack welded to the steel jacket and did not penetrate into the segment core concrete. Since slip of the steel jacket with respect to the concrete core was observed during tests on units JH1 and JH2, and in order to accurately measure curvature in the concrete core, 25 mm diameter holes through the jacket were provided at locations of the threaded rods for units JH3 and JH4. The holes allowed longitudinal movement of the jacket relative to the core concrete without it bearing against the embedded rods. Uplift and slip of the footing were monitored during the test by linear potentiometers. Strains in the steel jacket, transverse reinforcement and tendon strands were monitored during

testing by electrical resistance strain gages. The layout of the strain gages and the potentiometers for units JH3 and JH4 is illustrated in Figure 3.4. A similar array of instrumentation was used for units JH1 and JH2. Data from the instrumentation was logged using a NEFF 470 data acquisition system with a 12-bit analog-to-digital converter in conjunction with in-house developed software. Column curvature was obtained from the displacement measured in one potentiometer with respect to the other as described below (see Figure 3.2):

$$\phi = \frac{\text{rotation}}{\text{gauge length}} = \frac{(\Delta_2 - \Delta_1)/l_w}{l_g} \qquad (3.1)$$

where $(\Delta_2 - \Delta_1)$ represents the relative displacement between the two potentiometers, l_w is the distance between the two potentiometers and l_g is the gauge length. Note that the average concrete surface compression strain may be obtained by Eq. 3.2:

$$\varepsilon_c = \frac{\Delta_2}{l_g} - x\phi \qquad (3.2)$$
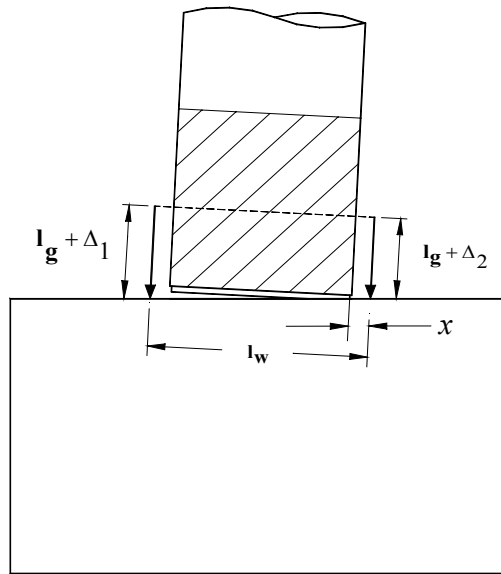
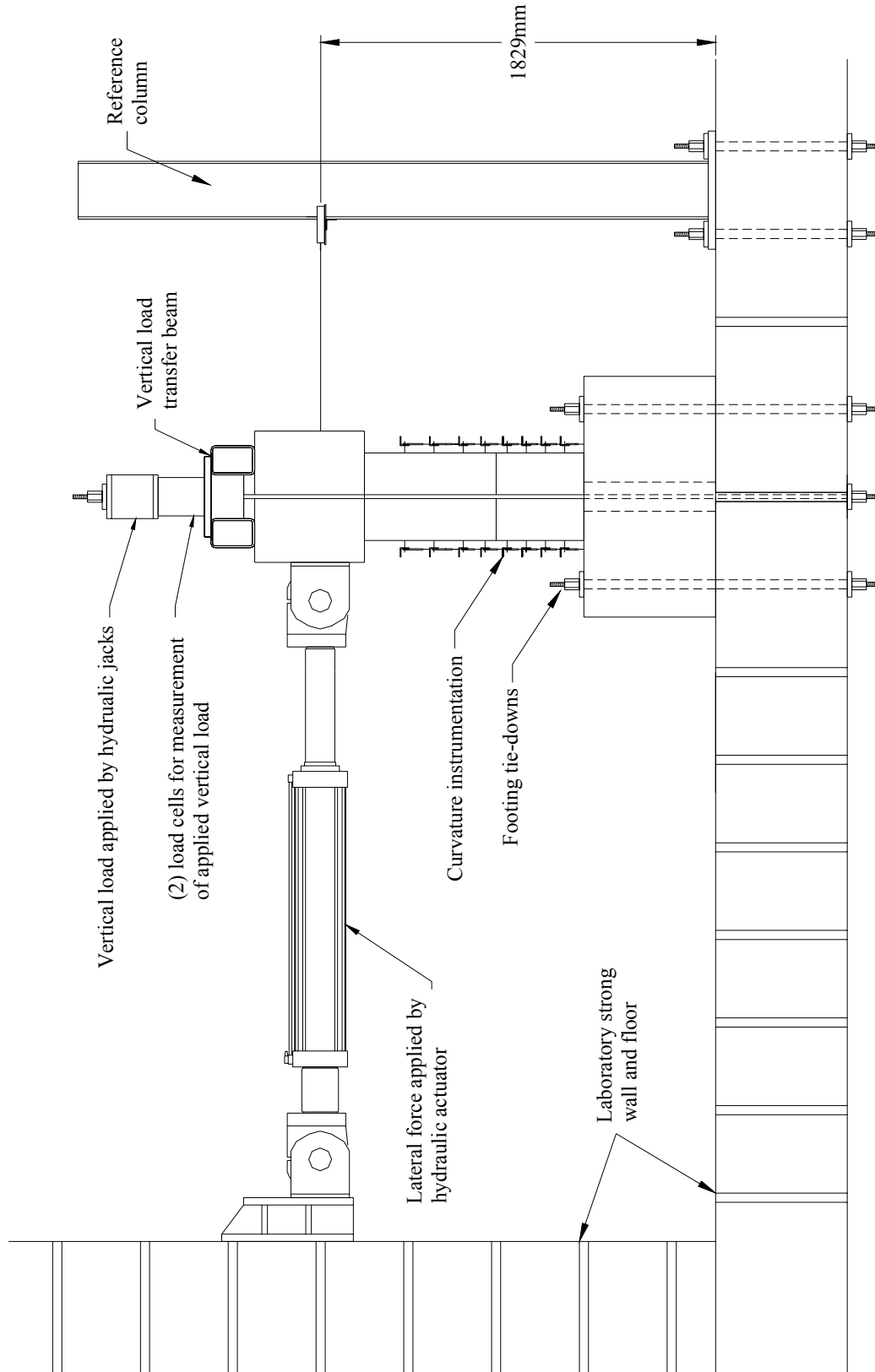Figure 3.2 Column curvature calculation from linear potentiometer readings

Figure 3.3 Schematic of test set-up for specimens JH3 and JH4

1829mm

Reference column

Vertical load transfer beam

Vertical load applied by hydraulic jacks

(2) load cells for measurement of applied vertical load

Curvature instrumentation

Footing tie-downs

Lateral force applied by hydraulic actuator

Laboratory strong wall and floor

29

Figure 3.4 Schematic of test instrumentation for units JH3 and JH4

Tendon strain gage locations

Loading Direction

DHOR

DN1
DN2
DN3
DN4
DN5
DN6
DN7
DN8

DN9

DS1,2 @ 200 mm
DS3,4@ 150 mm
DS5-8@ 130 mm

DS9, DS10

Strain Gages:
(18) transverse spiral
(30) steel jacket
(10) prestressing steel

Linear Potentiometers:
(16) curvature
(6) shear
(3) uplift/slip
(1) horizontal

+ = 90° rosette, 5 mm gage length
● = single gage, 5 mm gage length
▲ = single gage, 1 mm gage length

HN1-6
HE1-3
HW1-3
HS1-6

HW1-3, HE1-3 @ 300 mm

25 mm

JN, JS, JE, JW @ 135 mm

25 mm

HS1-6, HN1-6 @ 150 mm

75 mm

3.5   Loading Sequence

The loading sequence utilized for the tests is shown graphically in Figure 3.5. The first few cycles of each test were conducted in the elastic range under load control, with one cycle each performed at one-half, one, and one and a half times the theoretical load to cause decompression of the extreme tension fiber of the section at the column base, P_1. Subsequent cycles during the test were conducted in displacement control. Since each column was to be tested twice, it was desired to limit the damage in the first test of each column to an amount that could be repaired relatively easily (i.e., epoxy injection of residual cracks and patching of spalled cover concrete). Thus, the maximum drift imposed during the first test of each specimen was dictated by the observed damage at a particular drift. The column drift is defined as the displacement at the level of the applied load divided by the column height to the applied load:

$$\theta = \frac{\Delta}{H} \tag{3.3}$$

During testing, inspection of the specimen for damage was done primarily during the first and third loading cycles. In order to monitor the development of cracks through the various stages of testing, black and red felt tipped pens were used to mark cracks observed for the push and pull loading directions, respectively. The cracks were labeled by marking a transverse bar at the end along with a number designating the force/drift level. For cracks observed during the third cycle, a superscript of '3' was added to the label.
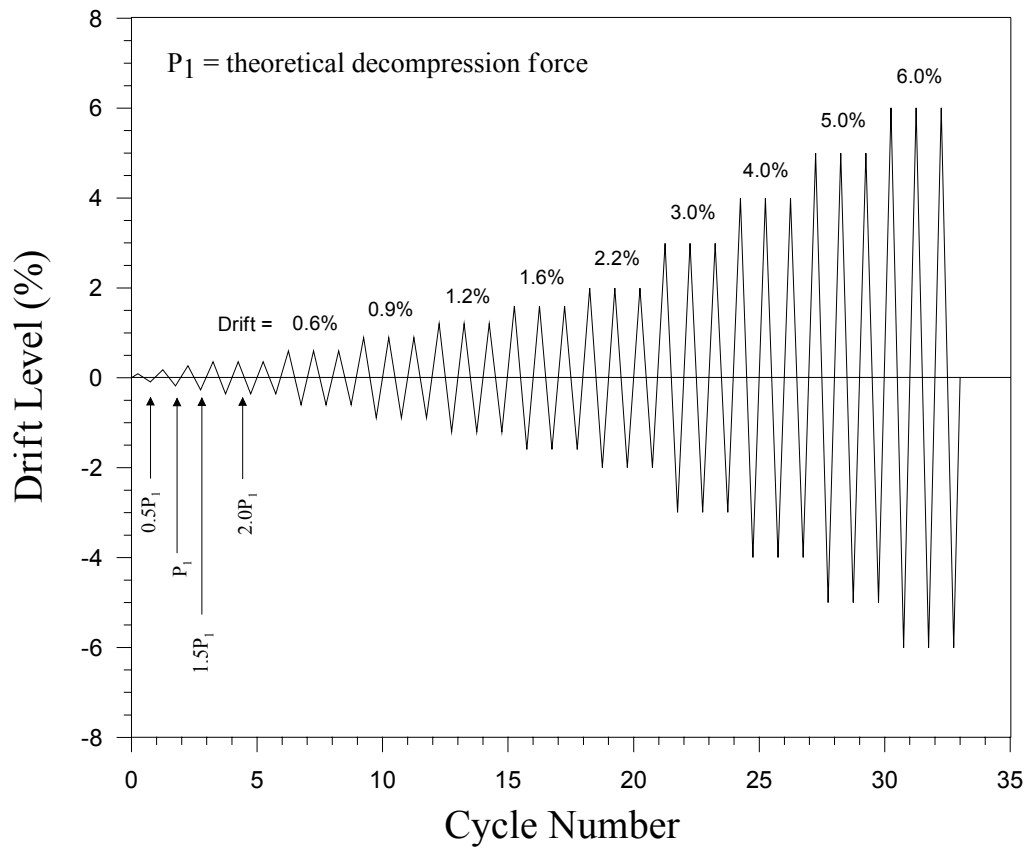
Figure 3.5 Lateral loading sequence for the first and second test of each unit

CHAPTER 4 HIGH ASPECT RATIO COLUMNS

4.1 Design of Columns

The design of the test units was guided by principles of capacity based design. It was desired to achieve ductile behavior under simulated seismic loading while limiting damage to low levels that could be repaired with little effort. Crushing of the concrete at the base of the column below the jacket was expected, while spalling of concrete in the non-jacketed column segments was to be avoided. To ensure ductile response, brittle failure modes such as shear failure and fracture of prestressing steel had to be guarded against through careful detailing of the transverse reinforcement and selection of initial prestress level. Key elements in the design included the amount of confinement to provide at the column base, the height of the steel jacket, the prestressing steel area and initial stress level, the size and spacing of transverse reinforcement in the non-jacketed column segments, and the concrete compressive strength.

A column diameter of 610mm was selected for both test units JH1 and JH2. Parametric studies were conducted in order to investigate the effects of prestressing steel area and initial stress and the level of confinement at the column base, on the force-displacement response of the columns. The concrete compressive strength, f_c', was taken as 41.4 MPa. Based on the parameter studies, a prestressing steel area, A_s, of 2665 mm^2 (ρ_l = 1%) was selected for both units. A steel jacket thickness, t_j, of 6 mm (ρ_j = 3.9%) was chosen for JH1, while that for JH2 was 2.8 mm (ρ_j = 1.9%). It was decided to test each unit twice, with an initial tendon stress of 45% of the ultimate tensile stress (0.4 x f_u = 837 MPa) for both units for the first test, and 60% of ultimate (0.6 x f_u = 1116 MPa) for the second test.

In order to avoid spalling of concrete in segments above the steel jacket, concrete longitudinal compression strains above the jacket needed to be lower than the crushing strain of the concrete. Moment curvature analyses were conducted for the non-jacketed segment using the program SEQMC. The axial load used in the analyses was equal to the

applied axial dead load of **P** = 890 kN plus the total prestress force in the tendon at the maximum column displacement. The concrete strength was taken as 41.4 MPa for the non-jacketed segments. Based on the analysis, a jacket height of 610mm was selected.

The final design details of the specimens are shown in Figures 4.1 and 4.2. The test model units both had an aspect ratio **H/D** of six. Each consisted of a precast footing and load stub and four precast 609.6 mm diameter cylindrical column segments. The main longitudinal reinforcement in each column consisted of a single unbonded tendon comprised of (27) 12.7 mm diameter ASTM A779 Grade 270 (1860 MPa) low-relaxation steel prestressing strands with a total cross-sectional area of 2665 mm^2. The unbonded tendon length, **L$_t$**, was 4953 mm. Segments two thru four (i.e., the three non-jacketed segments) also contained eight Grade 60 #4 longitudinal bars spaced evenly around the perimeter of the section, with a cover of 25.4 mm. The bottom column segment (segment one) was encased in an ASTM A569, A36 steel shell with a wall thickness, **t$_j$**, of 6.0 mm and 2.8 mm for specimens JH1 and JH2 respectively. The steel jacket did not extend the full height of the bottom segment, but rather terminated approximately 25 mm above the interface between the column and footing. The upper segments were reinforced transversely with Grade 60 #3 bar spiral spaced at 75 mm with a cover of approximately 12 mm. As stated above, a target initial stress in the tendon of 45% and 60% of ultimate was chosen for the first and second test of each specimen, respectively.
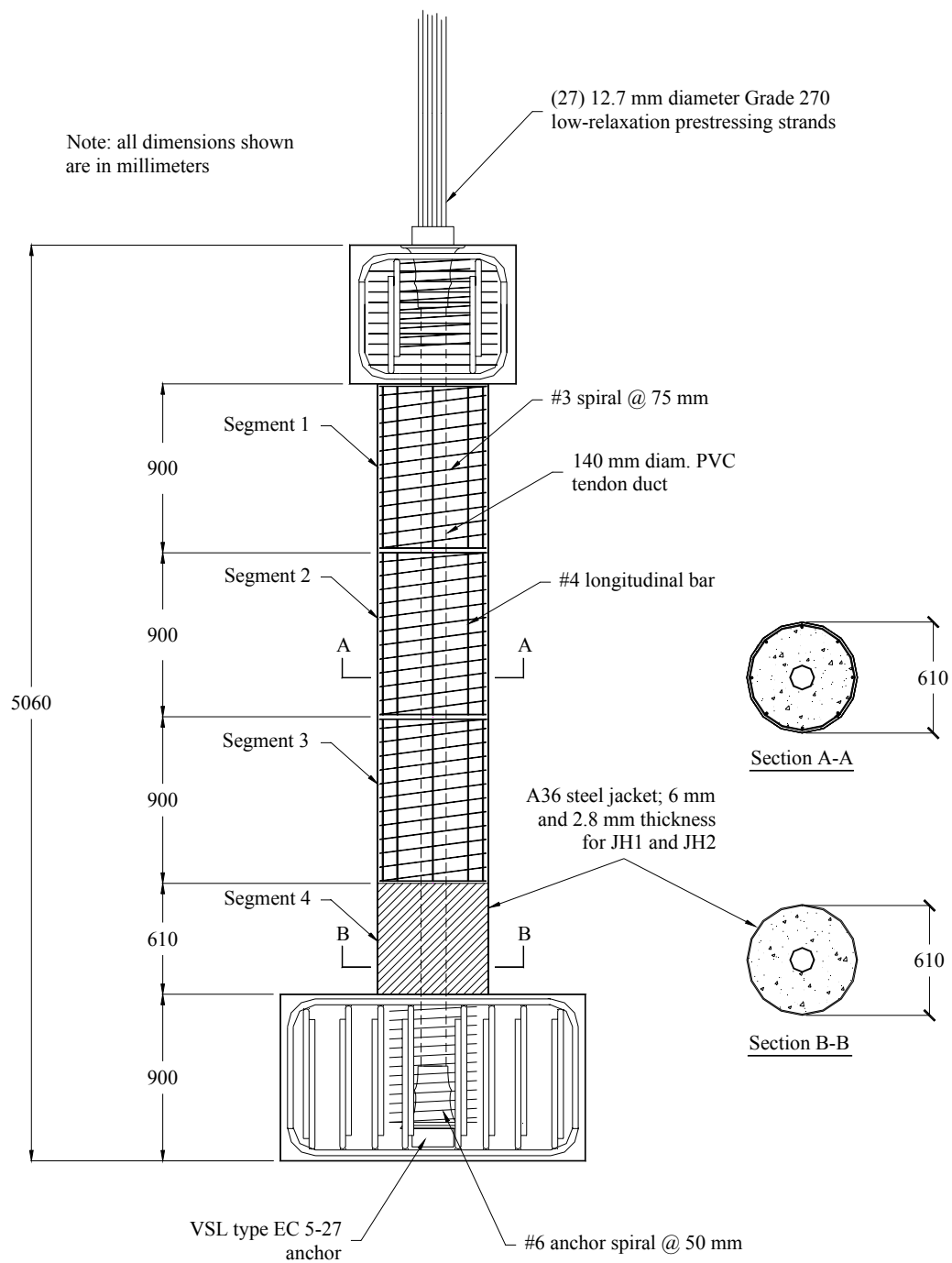
Figure 4.1 Test unit JH1 and JH2 column reinforcement details

9 U-bar (8 total)

6 anchor spiral @ 50 mm
(220 mm radius)

footing

column load stub

#4 A706 welded hoops @ 50 mm
(750 mm radius)

#9 U-bars

250 mm

200 mm

100 mm

200 mm

100 mm

200 mm

250 mm

tendon duct

#4 j-hook

225 mm

150 mm

300 mm

150 mm

225 mm
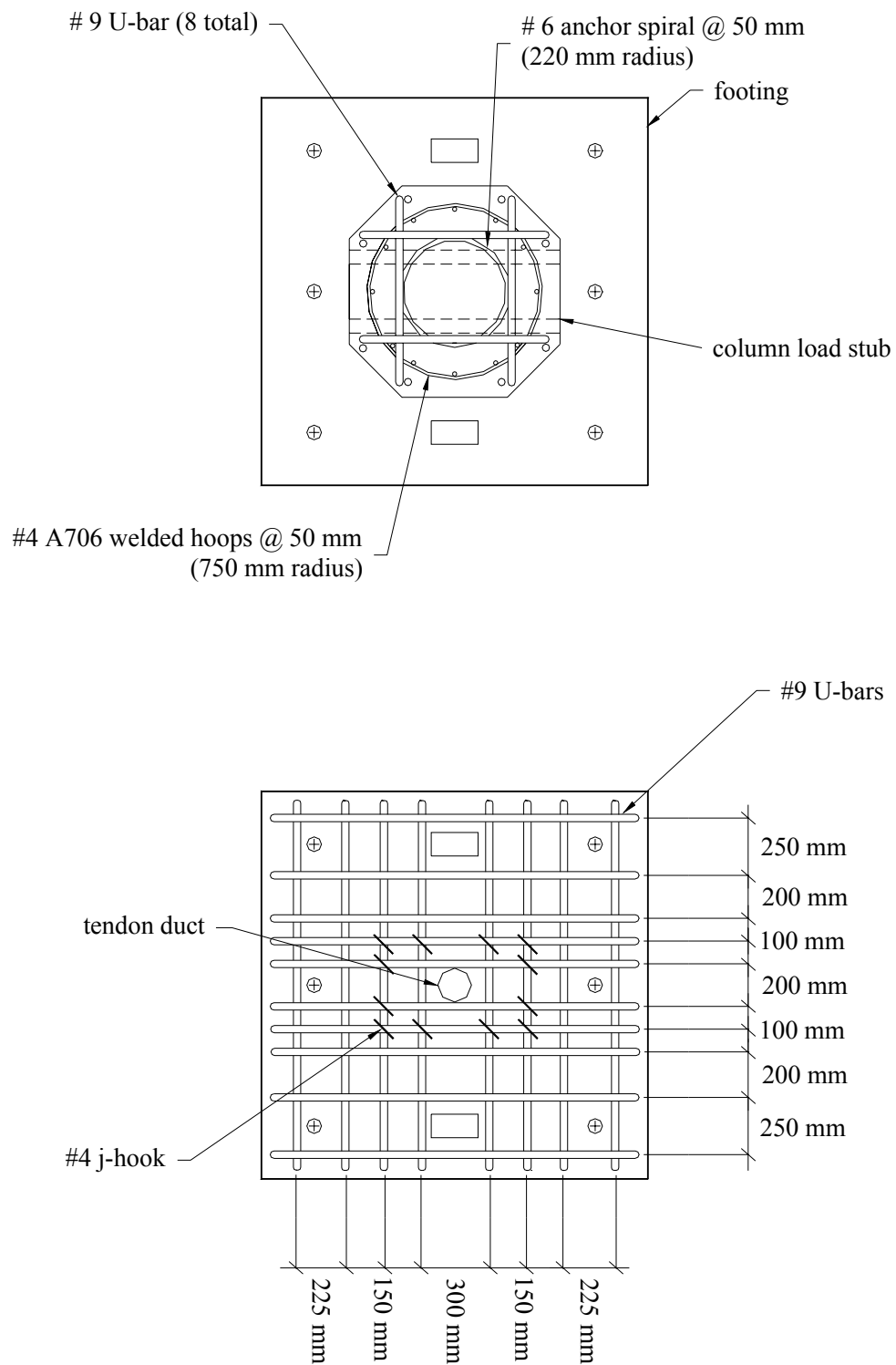
Figure 4.2 Specimen JH1 and JH2 footing and load stub reinforcement details

4.2   Construction Procedure

The test units were constructed at the Powell Structural Research Laboratories on the University of California, San Diego campus (UCSD). The footing reinforcement cages were assembled on the laboratory casting bed. The interior four # 9 bars of the footing top mat reinforcement in both the transverse and loading directions were not placed until the tendon and tendon anchorage were lowered into the footing reinforcement cage. The tendon was shipped from the supplier to the laboratory with one end assembled: the tendon strands had been placed through the anchor and bearing plate and the strand wedges "seated" in the anchor head. A scaffolding system was constructed around the footing to allow for the lowering of the tendon into the footing cage, and for the support of the tendon during casting of the footing. The tendon and anchor were lowered into the footing cage until the anchor head rested on the bottom mat reinforcement, approximately 100 mm above the bottom of the footing. To locate the anchor spiral reinforcement at the proper height, two # 5 straight bars were placed on each side of the anchor spiral in a direction parallel to that of the loading, at heights of approximately $\pm$ 200 mm from the footing mid-height. The anchor spiral reinforcement was tied to these bars while the anchor itself was secured to the footing bottom mat reinforcement using "tie wire". To keep concrete from entering the anchor and tendon duct during casting, care was taken to seal around the strand wedges at the anchor head, the bearing plate/anchor head interface and the anchor/tendon duct connection using a silicon sealant. Once the tendon and its anchorage were centered in the footing and secured in place, the #9 top mat bars and "J-hook" bars were placed. Figure 4.4 shows a photograph of the footing reinforcement cage prior to placing of the formwork. The footings of each unit test were cast on the same day using the same concrete batch.

The column segments were each precast separately. Each reinforcement cage for segments 2-4 was tied and placed on the casting bed, and 'sonotube' used as the formwork. The PVC pipe to be used as the tendon duct was lowered through the center of the reinforcement cage and into a 16 mm deep circular recess in the casting bed. This recess provided for a 16mm protrusion of the PVC from the bottom of the segment after

casting, which was used to align or "index" the segments during the stacking phase of the construction process. For segment one of the columns, sonotube was not used since the concrete was poured directly into the steel jacket.

The reinforcement cage for each load stub was tied and placed on the casting bed. After the formwork was placed, the stressing end anchor was lowered into the interior portion of the cage. The anchor was held at the correct height and kept centered using supports connected to the formwork. The anchor spiral was held at the correct height in the same manner as that in the footing. A silicon sealant was again used to prevent leakage of concrete into the tendon duct and anchor during the casting process. A photograph of the load stub reinforcement prior to casting is shown in Figure 4.5. The reinforcement cage of one of the non-jacketed column segments is shown in Figure 4.6, while Figure 4.7 shows the jacketed segments prior to casting. The column segments and load stubs were cast on the same day using the same concrete batch.

Once the concrete had cured sufficiently, the assembly of each test specimen occurred in the following manner. The footing was positioned in the laboratory, leveled and "hydrostone", a gypsum based cement, poured underneath it to provide a uniform bearing surface. Figure 4.8 shows the footing of specimen JH1 after being placed in the laboratory. Also visible in the photo is the scaffolding system erected around the footing to hold the tendon in a vertical position. The bottom segment of the column (segment 1 – the steel encased portion of the column) was hoisted over the top of the scaffolding system and centered over the tendon. The segment was lowered over the tendon down to approximately 50 mm above the top of the footing, and aluminum shims were placed in between the top of the footing and the bottom of the segment. The segment was then lowered slowly until the PVC protrusion indexed with the female PVC connection at the top of the footing and until the segment rested on the shims. The segment was made "plumb" by adjusting the number and/or thickness of shims. Once the segment was sufficiently level, the position of the shims was marked and the segment was raised several feet above the footing to allow for the application of epoxy to the bottom of the

segment. The epoxy layer was applied in an even thickness of approximately 10mm. Since the average total thickness of the shims used was approximately 5mm, excess epoxy was squeezed out as the segment was lowered back down onto the shims. This approach of applying an epoxy layer greater than the shim thickness ensured that no voids would exist between the footing and segment once the segment was resting on the shims. Figure 4.9 shows test unit JH1 after the jacketed segment was lowered into position. The epoxy was allowed to cure for 24 hours before the next segment was lowered down over the tendon and onto the top the first segment (Figure 4.10). This process of shimming, leveling and epoxy application was repeated for the remaining segments and load stub. Figures 4.11 – 4.14 depict assembly of the test units.

The damaged regions at the column base and above the jacket were repaired after the first test of each specimen. Loose concrete was removed and the regions scrubbed with a wire brush. The areas were rinsed with water to remove any remaining concrete particles and then allowed to dry. The spalled concrete above the steel jacket at the base of the second column segment was reinstated by patching the area with SikaTop 123 – a polymer-modified, Portland cement, 2-component, fast-setting, non-sag patching mortar. The residual crack at the column base was grouted using Sikadur 35 – a high-modulus, low-viscosity, high-strength epoxy resin adhesive. Figures 4.15 and 4.16 show the base crack during the grouting process and the patched region above the steel jacket, respectively.

After the spalled region above the jacket was repaired, the lower half of the second column segment was wrapped with fiberglass in an effort to prevent spalling of cover concrete during the second test. Five layers of the Tyfo® Fibrwrap® SEH-51 Composite System were applied in segments in order to work around the existing curvature rods and instrumentation. Each continuous band was installed with a six-inch minimum overlap back onto itself. Figure 4.3 illustrates the layout of the fiberglass wrap, while Figure 4.17 shows the column during installation of the jacket.
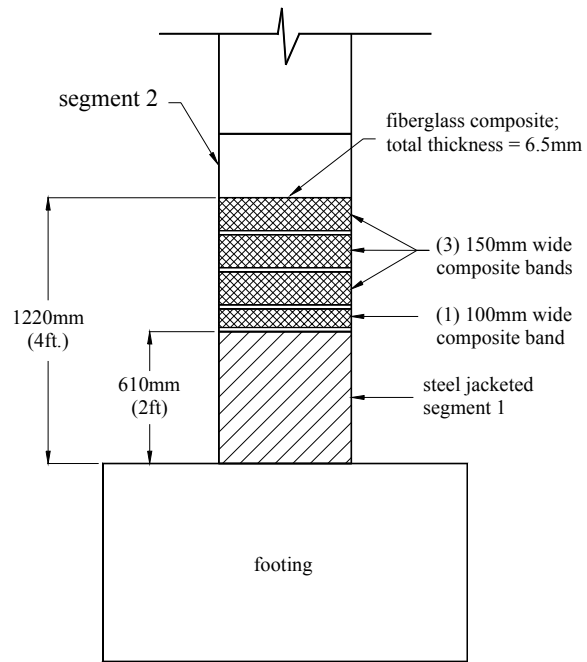
Figure 4.3 Composite wrap details

Figure 4.4 Footing reinforcement cage with tendon installed

Figure 4.5 Load stub reinforcement cage

Figure 4.6 Column segment reinforcing cage

Figure 4.7 Jacketed column segment prior to casting

Figure 4.8 Test unit footing positioned in laboratory

Figure 4.9 Footing with column segment 1 positioned

Figure 4.10 Application of epoxy at interface between segments 1 and 2

Figure 4.11 Positioning of segment 3

Figure 4.12 Lowering segment 4 down over prestressing tendon

Figure 4.13 Test units during construction

Figure 4.14 Post-tensioning the assembled test units

Figure 4.15 Close-up of grouting of the base residual crack

Figure 4.16 Patching of spalled region at bottom of segment 2

Figure 4.17 Wrapping segment two with a composite jacket

This Page Left Blank

4.3   Materials Testing

Material properties of concrete and steel used in the construction of specimens JH1 and JH2 were determined through testing at UCSD's Charles Lee Powell Structural Research Laboratories. The compression strength of concrete was measured at 7 days, 21 days, and 28 days and on the day of each test. The results are listed in Table 4.1. Values in the table are an average strength based on three tests on unconfined concrete cylinders (152.4 mm diameter x 304.8 mm height), which were cast during the pour.

Table 4.1 Concrete compressive strength for specimens JH3 and JH4 ($f_c^{'}$, MPa)

Specimen	7-Day	21-Day	28-Day	Day of Test 1	Day of Test 2
JH1				48.7 ± 0.6	57.0 ± 1
	32.3 ± 1	42.1 ± 0.2	44.0 ± 0.3		
JH2				50.8 ± 1.1	55.5 ± 1
Footing	38.7 ± 0.7	--	49.5 ± 1	61.4 ± 1	--

Tensile tests were conducted on the steel reinforcing bars used in the load stubs and non-jacketed column segments and on the plate material used for steel jackets. Three coupons 305mm in length were tested in a SATEC 490 kN capacity uniaxial testing machine for each of the reinforcing bar sizes. A complete stress-strain relationship up to the ultimate stress was obtained for each coupon. For tests on the #3 and #6 bar spiral, a well-defined yield plateau was not observed since the material had already been deformed. Thus, the yield strength was taken as the stress at 0.2% offset strain, consistent with ASTM standards. Values for the yield strength and ultimate strength are listed in Table 4.2. No pull-test data was obtained for the #9 bars used in the footings and load stubs. 'Dog-bone' shaped coupons were manufactured for tensile tests on the steel jacket material. The dimensions, tolerances and manufacturing procedure of the coupons conformed to ASTM standards. Three coupons each were tested for the two material thickness', with a

complete stress-strain relationship up to the ultimate stress obtained for each coupon. Since a well-defined yield point was not observed in tests on either material thickness, the yield strength was also taken as the stress at 0.2% offset strain. The yield and ultimate strengths are listed in Table 4.2.

Table 4.2 JH3 and JH4 Yield and ultimate strengths of reinforcing steel

Description	Size	Yield Strength (MPa)	Ultimate Strength (MPa)
Longitudinal bars	#4 (12.7mm)	443 ± 2	728 ± 2
Anchor Spiral	#6 (19.1mm)	421 ± 2	685 ± 2
Segment Spiral	#3 (9.5mm)	465 ± 12	691 ± 8
Load Stub Hoops	#4 (12.7mm)	414 ± 3	614 ± 2
Thin coupons	2.9 mm thick	283 ± 7	390 ± 7
Thick coupons	6.2 mm thick	303 ± 3	464 ± 3

The adhesive used to bond the precast components together was Sikadur 31 – High Mod Gel. It is a two component solvent-free, moisture insensitive, high modulus, high strength epoxy adhesive. The expected properties of this material at the age of 14 days were compressive strength of 82.7 MPa, tensile strength of 24.8 MPa, and shear strength of 23.4 MPa.

4.4 Column Prestressing

4.4.1 First Stressing

The specimens were post-tensioned using a hydraulic stressing ram at a concrete age of 66 days. Strain gages mounted on the tendon strands, transverse spiral and steel jacket were connected to the data acquisition system and an initial set of readings was taken prior to the post-tensioning operation. Strain on the concrete surface was measured at four points around the circumference of the column using a demountable mechanical strain-measuring device (demec device). An initial set of readings was taken for the demec points prior to stressing.

During stressing, load levels in the tendon were calculated using an analog pressure transducer connected to the ram hydraulics and a calibration chart. In addition, four electrical resistance strain gages mounted on the tendon strands and connected to a data acquisition system with real-time digital display were used to monitor strains in the prestressing steel.

Because of the relatively unbonded free tendon length, a significant strain loss due to wedge seating was expected. The estimated mechanical seating of the wedges was 10 mm. The corresponding expected prestress force loss was 1007 kN. Thus, to achieve the design total prestress force of 2230 kN after losses, an applied total force of 3237 kN was required. Specimen JH1 was post-tensioned first. After stressing, it was found that a tendon force 22% higher than expected existed in the tendon based on readings from the prestressing steel strain gages readings. The cause of this was believed to be due to a lower mechanical wedge seating than assumed. Because of this, the level of prestress force applied to specimen JH2 prior to wedge seating was lower than that applied to JH1 and was approximately 2850 kN.

Figure 4.18 shows the tensile strains in the prestressing steel during stressing of JH1 and JH2. For specimen JH1, all four gages mounted on the tendon functioned, while for

specimen JH2, only two of the four gages worked. The average of the four strain gage readings for JH1 prior to seating the strand wedges was 6225 $\mu\varepsilon$, corresponding to a total tendon force of 3260 kN. This is slightly higher than the force of 3237 kN indicated by the pressure transducer connected to the ram hydraulics. After seating the wedges, the average strain reading for the tendon gages was 5213 $\mu\varepsilon$, and the corresponding tendon force equal to 2730 kN. As mentioned above, this is 22% higher than the calculated prestress force after losses. Using the observed strain loss indicated by the strain gages, the actual wedge seating was found to be approximately 6.1 mm. The average readings of the two strain gages for specimen JH2 prior to seating the wedges was 5438 $\mu\varepsilon$, and the associated tendon force equal to 2848 kN. The average strain after losses was 4156 $\mu\varepsilon$, and the corresponding prestress force was 2177 kN.

For both specimens, the average concrete surface strain after losses measured using the demec gage was significantly higher than predicted. Average concrete strains of 397$\mu\varepsilon$ and 374$\mu\varepsilon$ were observed for specimens JH1 and JH2, respectively. Using an elastic modulus based on the experimentally determined concrete compressive cylinder strength, the predicted concrete strains are 329 $\mu\varepsilon$ and 267 $\mu\varepsilon$ for specimens JH1 and JH2, respectively. These are somewhat lower than the observed values given above. It should be noted however that the initial readings taken at each set of demec points prior to the post-tensioning operation showed a wide scatter. Thus, little confidence is given to the accuracy of the strain readings from the demec gage for the first stressing.

Continuous readings were taken for the demec points in the time between the stressing operation and the first test of each specimen. Using these readings and the initial strain readings in the tendon strands on the day of testing, prestress losses of 40 kN and 42 kN were calculated for specimens JH1 and JH2, respectively. The day of test total prestress force for each specimen was calculated using the tendon gage readings and the above losses. For specimen JH1, the final prestress was taken as 2730 kN – 40 kN = 2690 kN, while that for JH2 was 2177 kN – 42 kN = 2135 kN.

4.4.2   Second Stressing

After repairing the damage incurred during the first test, each specimen was post-tensioned to a higher tendon force level. A prestress level of 60% of the ultimate strength of the tendon was desired for the second test of each specimen. Readings from the tendon strain gages after the first test of each specimen indicated that a decrease in the tendon force of 163 kN and 170 kN occurred for specimens JH1 and JH2, respectively. Thus, the prestress force prior to the second stressing for JH1 was 2690 kN – 163 kN = 2527 kN, and that for specimen was 2135 kN – 170kN = 1965 kN. A total force of 3850 kN was applied to specimen JH1 prior to wedge seating, while a prestress of 3710 kN was applied to JH2. Using an assumed wedge seating of approximately 6.4 mm, the predicted force in each tendon after losses was 3180 kN and 3039 kN for specimens JH1 and JH2, respectively. Only two of the four the strain gages mounted on the tendons of each specimen functioned properly during stressing. An average of the gage readings for JH1 indicated a force increase of 710 kN in the tendon, corresponding to a total prestress force of 2527 kN + 710 kN = 3237 kN. The average strain readings for gages on JH2 indicated a force increase of 440 kN, and the corresponding total prestress after losses was 1965 kN + 440 kN = 2405 kN.

Several sets of readings were recorded for each demec point location on each specimen prior to the second stressing. The independent readings were all very close and thus it is felt that a good "zero" was established for each set of points. The prestress force increase was calculated using the average surface strain increase measured by the demec gage and an elastic modulus based on the compressive cylinder strength of the concrete. The calculated force increase for specimen JH1 was 770 kN, while that for JH2 was 672 kN. Good agreement between the force increase calculated using the demec points and tendon strain gages was achieved for JH1. The increase in prestress force given by the demec readings is significantly higher than that indicated by the tendon strain gages for specimen JH2.

It is believed that the demec gage readings should give a reasonable estimate of the force increase in the tendon of each specimen. The reason for the low strain readings recorded for the prestressing steel of JH2 is not understood. The final prestress force after losses was calculated as an average of the force increase indicated by the demec gage and tendon strain gages. For specimen JH1, the total tendon force taken as 2527 kN + 740 kN = 3267 kN while that for JH2 was 1965kN + 556 kN = 2521 kN. The prestress loss measured for the period between the end of the second post-tensioning and the second test was negligible for both specimens.

It must be noted that there exists some uncertainty in the actual total prestress force for each specimen. The above gives only a "best-estimate" of the true prestress force. An error on the order of 10% - 20% is not unreasonable. However, since additional axial load was applied to the specimens (as described in the Section 3.4), the error in total vertical load acting on the column should not be extreme.
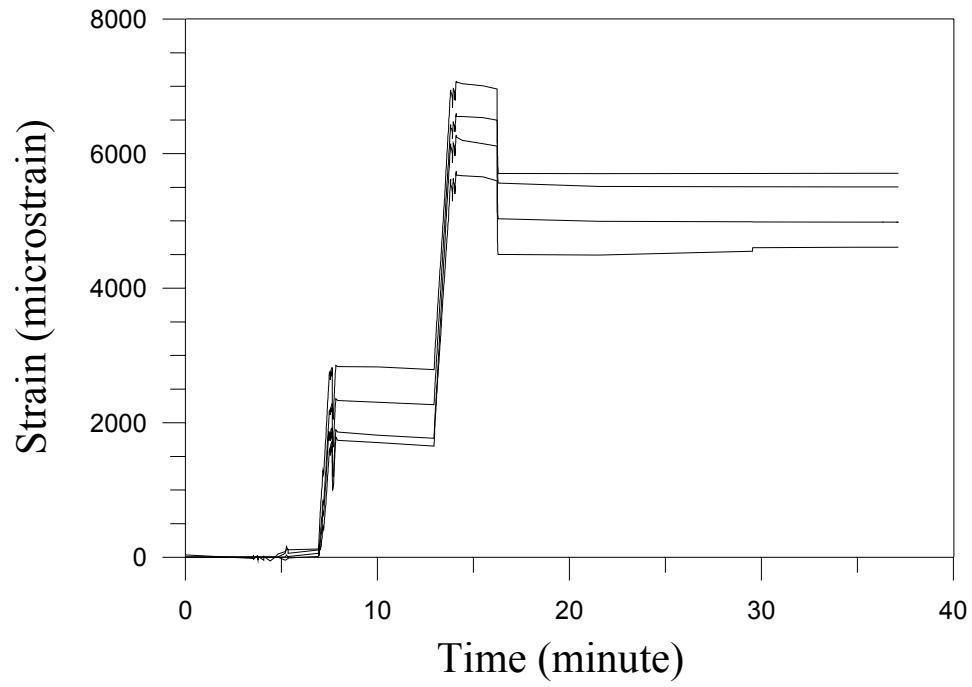
(a) Specimen JH1
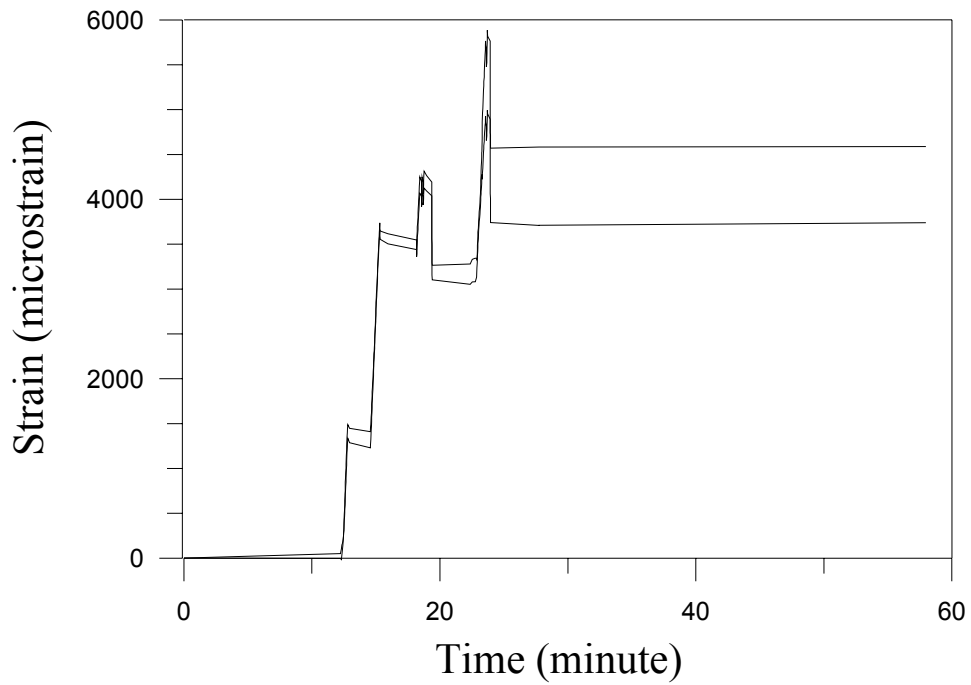
(b) Specimen JH2

Figure 4.4.18 Tendon strains during first prestressing of specimens JH1 and JH2

55

4.5   Experimental Results – Specimen JH1-T1

4.5.1   Observations under Repeated Cyclic Loading

A description of the behavior of specimen JH1 is given along with some supporting photographic illustrations. The push direction is indicated by plus sign (+) and the pull direction by a minus sign (-).

±0.5 P1 (Pmax=37.3 kN and Pmin=-37.4 kN)

There was no cracking observed in either the push or pull direction.

±P$_1$ (P$_{max}$= 74.9 kN and P$_{min}$= -75.0 kN)

There was no cracking observed in either the push or pull direction.

±1.5P$_1$ (P$_{max}$= 112.2 kN and P$_{min}$= -112.5 kN)

Flexural cracking was observed at the interface between column segments one and two directly adjacent to the top of the steel jacket during the pull loading.

3 cycles at 0.36% drift (P$_{max}$ = 125.6 kN and P$_{min}$ = -118.6 kN)

During the push direction of loading, flexural cracking was observed at the interface between segments one and two. A small flexural crack at the interface between the footing and segment one was observed during the first pull loading.

3 cycles at 0.6% drift (P$_{max}$= 164.7 kN and P$_{min}$= -156.2 kN)

Flexural cracking at the footing/column interface as well as extension of the crack at the top of the steel jacket was observed during the first push loading cycle. Flexural cracks in segment two were observed at heights of approximately 275mm, 425mm and 575 mm above the steel jacket for the first cycle of loading. Cracks at the interfaces between the footing and segment one, and between segment one and segment two, were observed to have opened to approximately 0.5-1.0 mm during the first cycle of loading.

3 cycles at 0.9% drift (P_{max}= 186.7 kN and P_{min}= -175.6 kN)

The formation of flexural cracks continued to progress up the height of the column. The crack width at the base of the column was observed to be 1-1.5 mm and the neutral axis depth from the compression edge was approximately 350 mm. Minor crack extensions were observed after the third loading cycle.

3 cycles at 1.2% drift (Pmax= 196.9 kN and Pmin= -185.3 kN)

Flexural cracks were observed in the third column segment at this drift level. After three complete loading cycles, segment two was observed to have cracks somewhat evenly spaced along its full height. Minor spalling of concrete at the gap between the jacket toe and the footing was observed. The crack opening at the footing level was 2 mm and the neutral axis depth was observed to be around 300 mm. Figure 4.19 shows the crack pattern on the south face of the column.

3 cycles at 1.6% drift (P_{max}= 206.1 kN and P_{min}= -194.9 kN)

Continued minor concrete spalling at the column compression toe was observed for both the push and pull loading directions (see Figure 4.20). Two new flexural cracks, approximately 200mm above the joint between segment two and segment three, were observed in segment three on both the south and north faces after the first push and pull loading cycle. The crack at the column base opened to 3 – 4 mm during cycles at this drift level.

3 cycles at 2.0% drift (P_{max}= 210.4 kN and P_{min}= -199.4 kN)

Increased spalling of concrete below the jacket toe was observed. Vertical cracking and the beginning of concrete crushing were observed in the compression face of segment two just above the steel jacket during the first pull loading direction. The crack widths at the column base and at the interface between segment one and segment two were approximately 5 mm and 2 mm respectively.

3 cycles at 3.0% drift (P_{max}= 217.0 kN and P_{min}= -206.3 kN)

During the first push loading, significant crushing of concrete and vertical splitting was observed in segment two at the compression face directly above the steel-jacketed segment. This is shown in Figure 4.21. The cover concrete in an area of approximately 175 mm by 175 mm just above the steel jacket had separated from the concrete core. An increased amount of concrete crushing at the column compression toe over previous drift levels was also observed. Upon unloading from the first half-cycle, the test was paused at zero horizontal load before deciding to continue with the first pull loading. Spalling of cover concrete and vertical cracking in segment two just above the jacketed segment at the south generator were also observed during the first pull loading. Crack openings of 10 mm and 5 mm were observed at the column base and at the jacketed segment/segment two joint, respectively. The opening at the interface between the column base and footing is shown in Figure 4.22. The damaged region at the base of the second column segment is also visible in the photo. During the second cycle push loading, the crack opening at the interface between segments one and two was larger than during the first cycle. It appeared as though the column was beginning to hinge about the top of the steel-jacketed segment, rather than about the column base. Continued vertical cracking in segment two on the compression face as well as crushing just below the jacketed segment was observed for both the push and pull directions during the second loading cycle. No further damage to the column was observed during the third cycle of loading.

Test End

The damaged region at the column base at the north side is shown in Figure 4.23. Figure 4.24 shows the region directly above the steel jacket after the loose concrete had been removed and prior to repair. A residual crack at the column base existed due to the crushed concrete in that region. The damage below the jacket was however, essentially cosmetic and could be repaired relatively easily. No inclination of the flexural cracks was observed. All cracks observed in the non-jacketed column segments closed completely once the lateral force was removed at test end. The prestressing steel did not

fracture during the test. As expected, the residual drift of the column was very low and was equal to 0.14%.
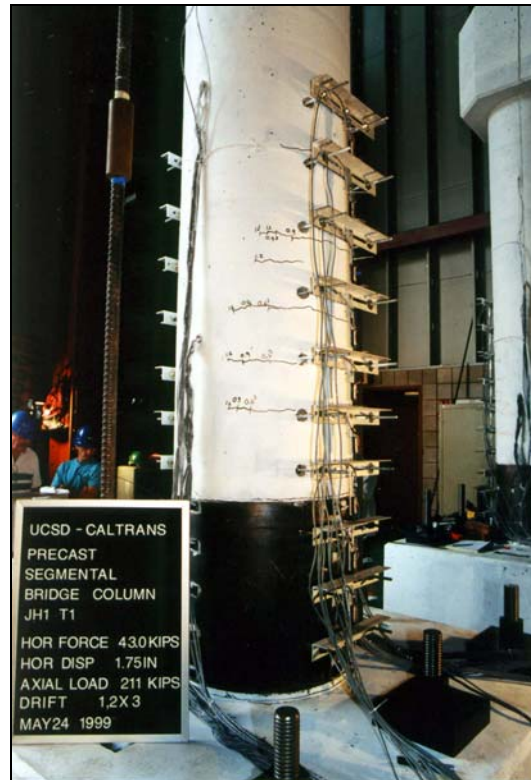
Figure 4.19 JH1 – Test 1 Crack pattern at 1.2% drift
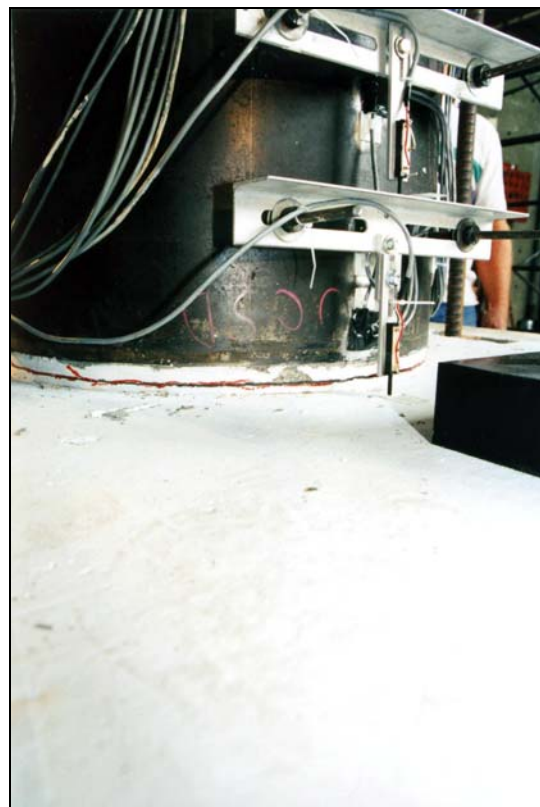
Figure 4.20 JH1 – Test 1 Spalling below jacket at 1.6% drift

60
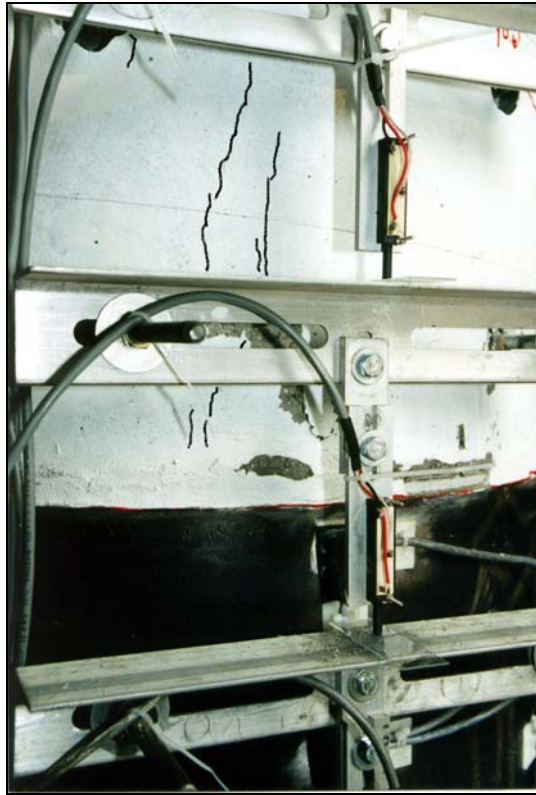
Figure 4.21 JH1 – Test 1 Damaged region above jacket at segment 3 base at 3.0% drift
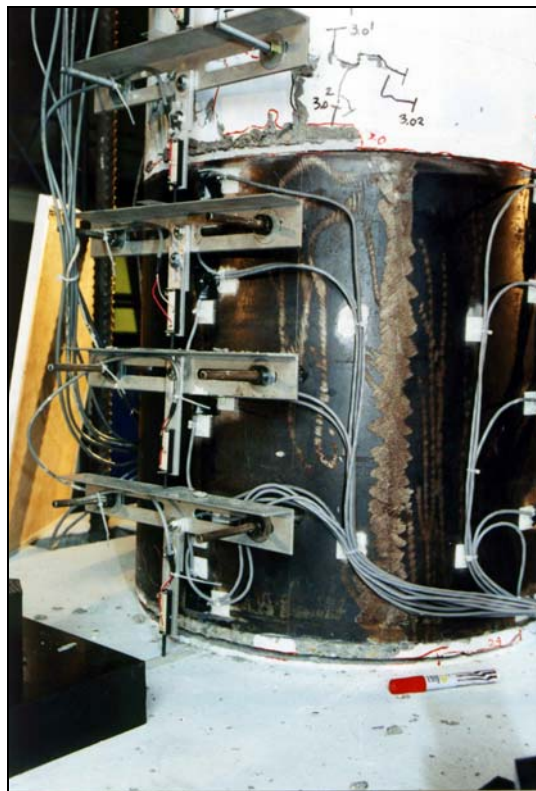
Figure 4.22 JH1 – Test 1 Crack at column base at 3.0% drift
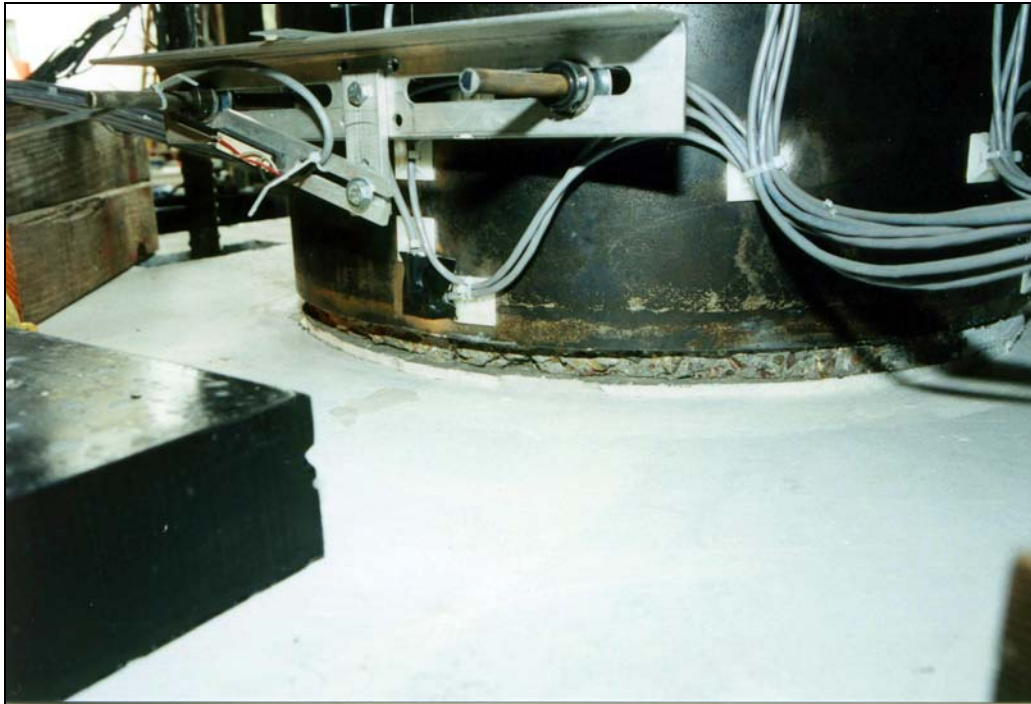
Figure 4.23 JH1 I Test 1 Damage below jacket at test end
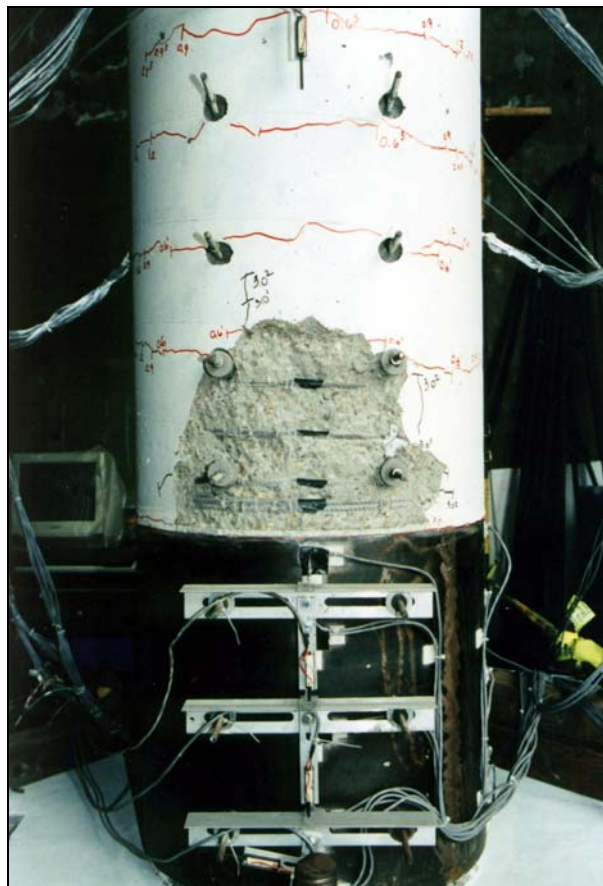
Figure 4.24 JH1 – Test 1 Spalled region above jacket at test end

4.5.2 Force-Displacement Response

The force-displacement response for the first test of specimen JH1 is displayed in Figure 4.25. Stable, hysteretic response was observed for both directions of loading up to the maximum imposed drift of 3.0%. Significant non-linear behavior initiated at a force level of approximately 160 kN, or 2.25 times the theoretical load to cause decompression at the column base (i.e., 2.25 x P_1). Maximum column strengths were achieved at the maximum imposed drift of 3.0% and were 217.0 kN and -206.3 kN for the push and pull loading directions, respectively. Though the response was stable throughout the test, there can be seen two spikes of the force for the negative direction of loading at 3.0% drift. These spikes occurred during unloading from the third pull cycle at test end and were a result of actuator instability.
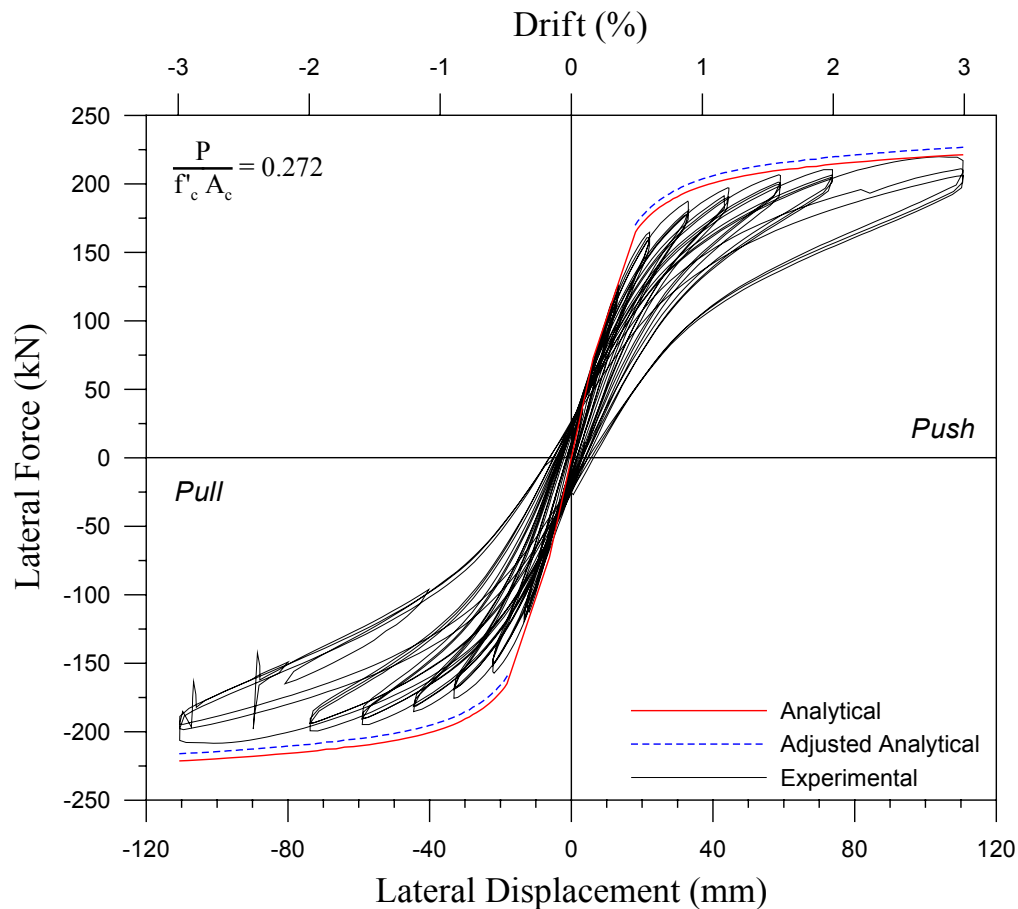
Figure 4.25 JH1–Test 1 Force-displacement response

The analytical force-displacement response envelope calculated by the procedure detailed in Chapter 2 is shown in Figure 4.25 along with the experimental hysteresis. The predicted initial stiffness of the specimen agrees well the experimental stiffness. Column strength is overestimated for the pull direction of loading after the initial elastic stages of testing, while the analytical curve essentially follows the experimental response for the push direction. The reason for the difference of column strength for the two directions of loading is given as the following. If the transfer beam used to apply the axial compressive load **P** was mistakenly positioned eccentric to the column axis instead of directly over the axis, the applied lateral force **E** would be reduced for one direction of loading and increased for the other, compared to the case of no eccentricity. Consider Figure 4.26, which shows the axial load **P** acting on the column with an eccentricity **ecc**. If the transfer beam were positioned to the left of the column axis, then the lateral force in the push direction for a given drift would be increased and be given by Eq. 4.1, while that for the pull direction would be reduced and be given by Eq. 4.2. The eccentricity of the axial load can be found by considering the difference in lateral force for the two directions of loading at a given drift level (Eq. 4.3 and 4.4). The eccentricity was calculated for several drift levels and found to be approximately **ecc** = 22mm.

To adjust the analytical response envelope for the above, the amount given by Eq. 4.5 is added to push direction forces and subtracted from pull direction forces. The curve indicated by the dashed line in Figure 4.25 shows the adjusted analytical response. The adjusted curve indicates that column strength was slightly over predicted by the analytical model. The second-slope stiffness is however, well predicted.

The difference between the adjusted analytical and experimental column strength may be because the Mander model, not developed specifically for high strength concrete, may predict higher than actual confined compressive strengths for the concrete. The difference might also be due to error in the initial prestress force, F_{si}, assumed in the analysis.

In light of the this, and that the error in predicted strength is 10% or less for drifts up to 1.0% and approximately 5% or less for higher drift levels, it can be said that the analytical curve agrees reasonably well with the experimental response.
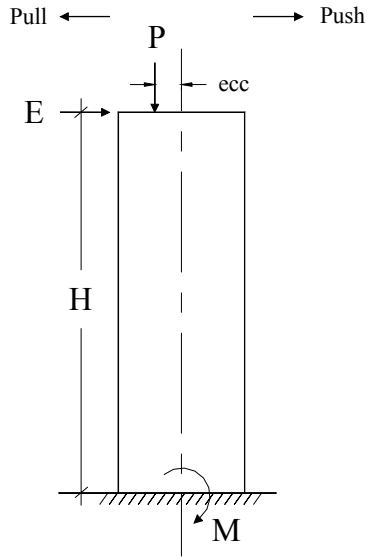
$$E_{push} = \frac{M}{H} + \frac{P}{H}ecc \qquad (4.1)$$

$$E_{pull} = \frac{M}{H} - \frac{P}{H}ecc \qquad (4.2)$$

$$E_{push} - E_{pull} = \frac{M + P\,ecc \; - \; M + P\,ecc}{H} \qquad (4.3)$$

$$ecc = \frac{E_{push} \; - \; E_{pull}}{2P}H \qquad (4.4)$$

Figure 4.26

$$E_{ecc} = \frac{P}{H}ecc \qquad (4.5)$$

The initial stiffness of the specimen did not deteriorate drastically until high drift levels. In order to quantify any decrease in the initial elastic stiffness, $\mathbf{K_i}$, defined as the stiffness at a force level equal to the theoretical decompression force, is introduced and given is by Eq. 4.6:

$$\mathbf{K}_i = \frac{\mathbf{P}_1}{\Delta_1} \qquad (4.6)$$

where $\mathbf{P_1}$ is the theoretical decompression force and Δ_1 is the displacement observed at that force level during loading to a given drift. The loading stiffness, $\mathbf{K_i}$, is calculated during reloading to the second positive peak after one complete cycle at the particular drift. The decrease in initial column stiffness is depicted in Figure 4.27. For low to moderate drifts, the stiffness decreased by about one third while at the maximum imposed drift of 3.0%, the initial loading stiffness had dropped to 40% of its original value.
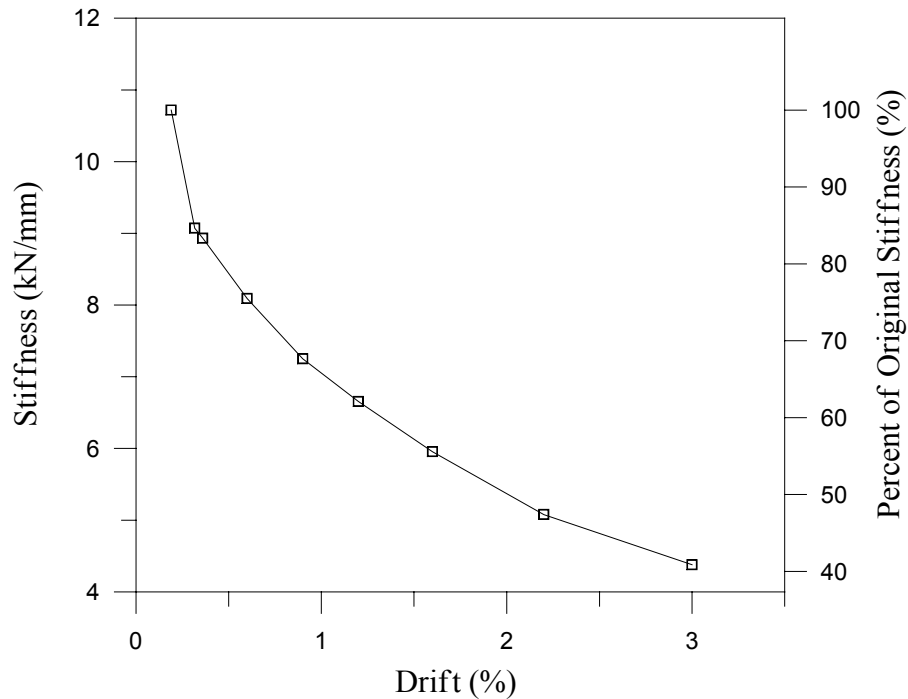
Figure 4.27 JH1–Test 1 Initial loading stiffness versus drift

The hysteretic energy dissipation of the specimen, indicated by the area within the force-displacement loops, was low for all drift levels. Using the calculated area within the loops and the procedure given in Ref. 5, an equivalent viscous damping ratio was calculated for the various drift levels. The damping coefficient is shown as a function of drift in Figure 4.28. It can be seen that the damping increased from around 4% for early stages of testing to 7% at the maximum drift. The increase in the damping coefficient at high drifts may be due to the energy dissipated by crushing of concrete at both the column base and above the jacket in column segment two. It was found that for the higher drift levels, the hysteretic energy dissipated during the second cycle was less than the first – the damping coefficients were lower by several percent.
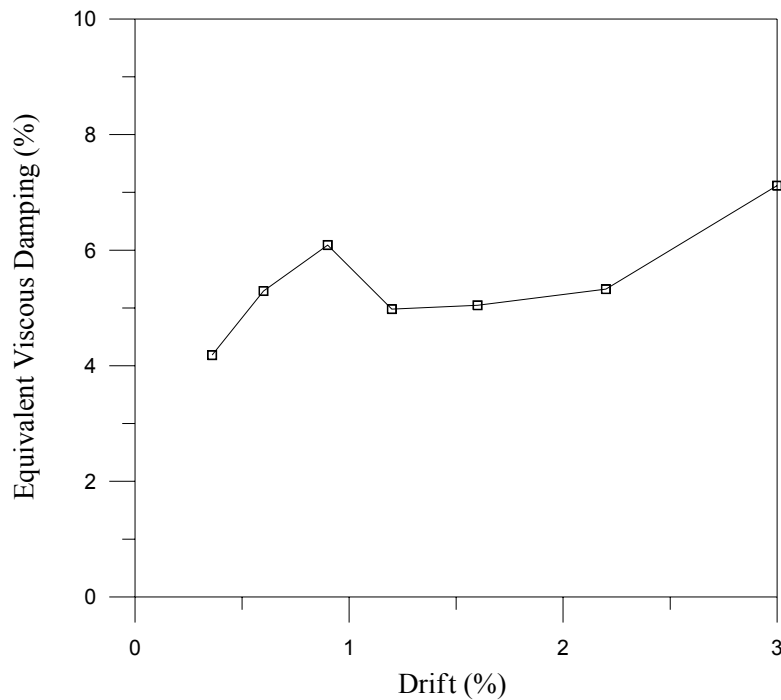
Figure 4.28 JH1 – Test 1 Equivalent viscous damping

4.5.3   Test Data

A large array of instrumentation was used to monitor various quantities of interest during testing. This included linear potentiometers to measure displacements and curvature and

strain gages mounted on reinforcing steel. The data recorded during testing is presented in a reduced form as strain and curvature profile plots using values recorded at peak displacements during the first cycle of loading for each force or drift level.

Column Curvature

Curvature along the column height is shown in Figure 4.29. The curvature values were calculated as described previously in Section 3.4. The large curvatures for high drifts at the base of the column and at a height of approximately 600 mm are due to the crack opening between the bottom of the column and the footing, and between the first and second column segments, respectively. Thus, the displacement measured at the top of the column at high drifts was due not only to the rotation of the column about its compression toe, but also to rotation about the top of the steel jacketed segment. This is contrary to the analytical model presented, which assumes the majority of crack opening occurs at the column base. It is believed that the curvatures at the base as calculated are higher than actual, since the assumption that plane sections remain plane might not be valid. This idea is evidenced by the discontinuity of the critical section at the neutral axis observed during testing.

Because much of the column rotation is concentrated at the base of the column, high curvatures and thus high compression strains develop at the compression toe. An estimate of the extreme fiber concrete strain at the critical section for 3.0% drift is given as (see En. 3.2):

$$\varepsilon_c = \frac{4.5\text{mm}}{167\text{mm}} - (60\text{mm})(1.06\text{x}10^{-4}\text{ mm}^{-1}) = 0.021$$

The predicted strain from the moment-curvature analysis for 3.0% drift is $\varepsilon_c = 0.014$.
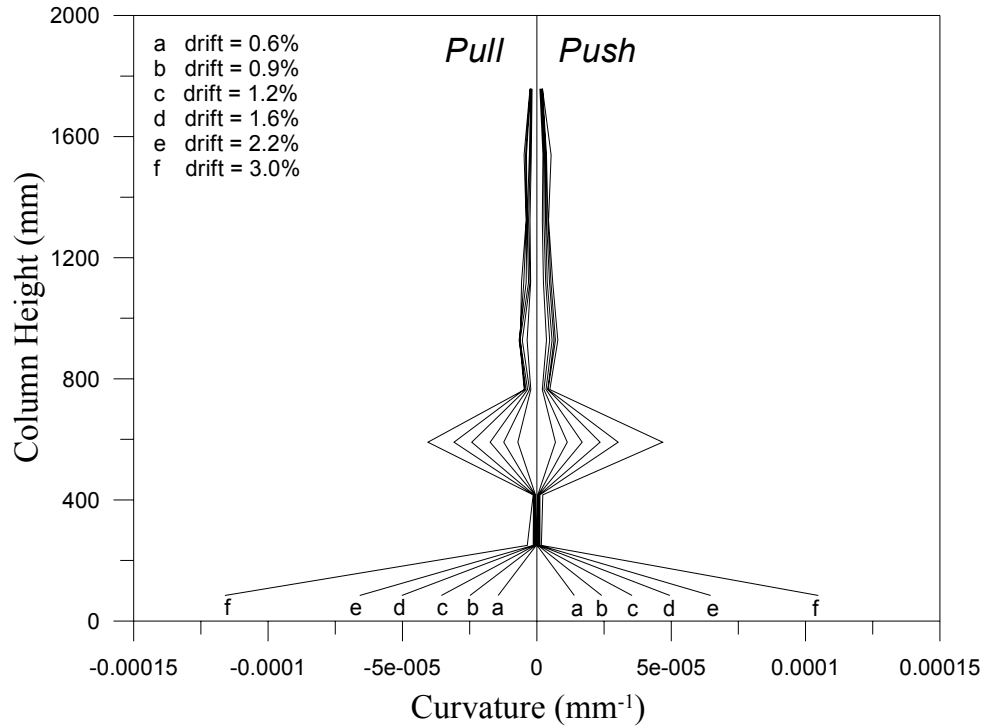
Figure 4.29 JH1–Test 1 Curvature along column height

Prestressing Steel Strain

A comparison between the analytical and experimental increase in tendon strain due to opening of the crack at the column base is shown Figure 4.30. Readings from the strain gages mounted on the tendon strands were used to construct the experimental curve. For each strain gage, the readings at peak displacement and at zero horizontal displacement prior to the peak were subtracted to give a value of incremental strain. The strain gages were mounted on opposite sides of the tendon arrangement. Since the analytical model assumes all the prestressing steel to be located exactly at mid-depth of the section, and since the gauged strands were actually located a finite distance away from the center, the experimental values from opposite sides of the tendon arrangement were averaged. It should be noted that only two of the four strain gages functioned properly during testing.

It can be seen that the tendon strain increase is over-predicted except at low drift levels. Following the analytical model presented in Chapter 2, this implies that the actual neutral axis depth was larger than predicted. As mentioned previously, the Mander model may

over-estimate the confined strength of high strength concrete, and consequently predict a smaller neutral axis depth. In light of the uncertainty regarding the strain gage readings and the fact that the maximum error is on the order of 30% or less, it can be argued that the predicted and observed curves agree within reason. Note also that the an error of 30% in the predicted tendon strain increase leads to only 2% error for the total vertical force (prestress plus applied axial load) acting on the column.
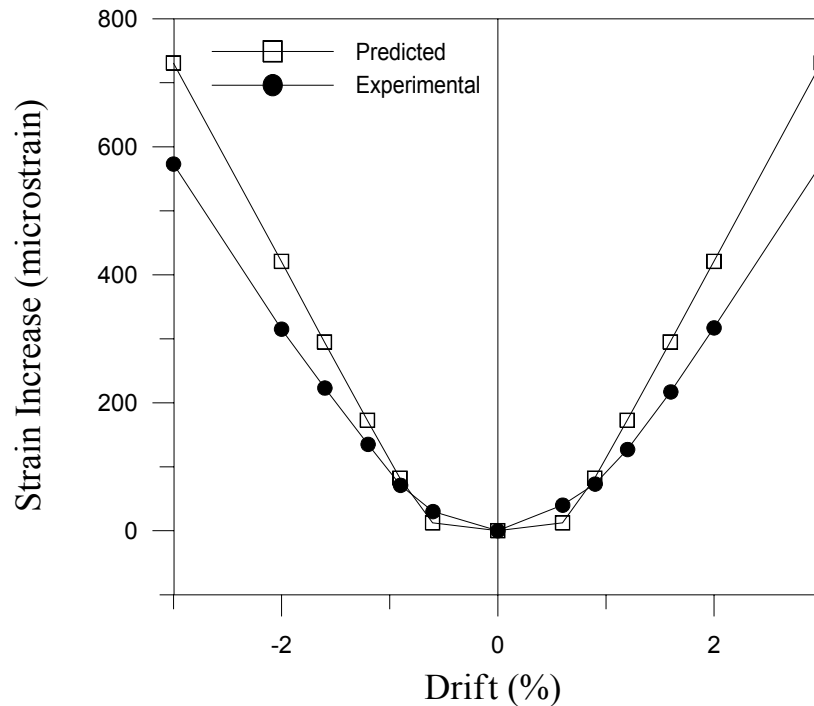
Figure 4.30 JH1−Test 1 Predicted and experimental tendon strain increase

Steel Jacket Strains

Five pairs of orthogonal strain gages were mounted on the north and south generators of the steel jacket oriented in the vertical and horizontal directions. Five horizontal gages were mounted at the east and west generators. Figures 4.31 and 4.32 show the hoop strain profiles at the north and south generators, respectively. Large hoop strains near the base of the jacket developed because of confining action of the jacket on the compressed concrete at the column compression toe. Maximum hoop strains at the jacket toe occurred at 3.0% drift and were 1800 $\mu\varepsilon$ and 4900 $\mu\varepsilon$ for the north and south generators,

respectively. Relatively large hoop strains also occurred at the top of the jacket due to the high concrete compressive strain at the interface between column segments one and two.

Hoop strains at the east and west generators are shown in Figures 4.33 and 4.34. The strains are caused by both the shear acting on the column and by the influence of confining action of the jacket at the column compression toe. The strains are higher near the bottom of the jacket since the higher concrete compressive strain near the base causes higher levels of dilation of the core concrete. The maximum observed strains of 650 $\mu\epsilon$ and 750 $\mu\epsilon$ for the push and pull directions are well below the material yield strain of approximately 1550 $\mu\epsilon$.

The vertical strain profiles for the north and south generators are displayed in Figures 4.35 and 4.36. The vertical strains at the compression generators (north for push/south for pull) are induced by the bending action of the column and are significant for both directions of loading. Maximum strains of approximately 600 $\mu\epsilon$ and 1850 $\mu\epsilon$ were observed for the push and pull directions at a drift of 3.0%.

Transverse Spiral Strains

Strains in the spiral reinforcement of the non-jacketed column segments are shown in Figures 4.37 and 4.38 for the north and south generators. The negative or compression strains observed at the north generator are not expected since dilation of the compressed concrete induces circumferential tension in the spiral. It is believed that a change in polarity of the strain gage signals somehow occurred. The hoop strains increase down the height of the column since the moment, and thus the concrete compressive strains, increase down the column height. For the 3.0% drift level, a marked increase in strain occurred for the gage at 750 mm above the footing. This location corresponds to just above the top of the jacket where significant spalling of the cover concrete was observed. The maximum strain for the push direction was just below the yield strain of 2200 $\mu\epsilon$, while that for the pull direction was 700 $\mu\epsilon$.

Hoop strains at the east and west sides of the column are shown in Figures 4.39 and 4.40. The strains are relatively small except at the bottom of the second column segment on the east side where the strain jumps from positive to negative. The changes in sign of the strains there and along the full height at the west generator are not understood, but may be due to gage instability and/or swapped strain gage leads.
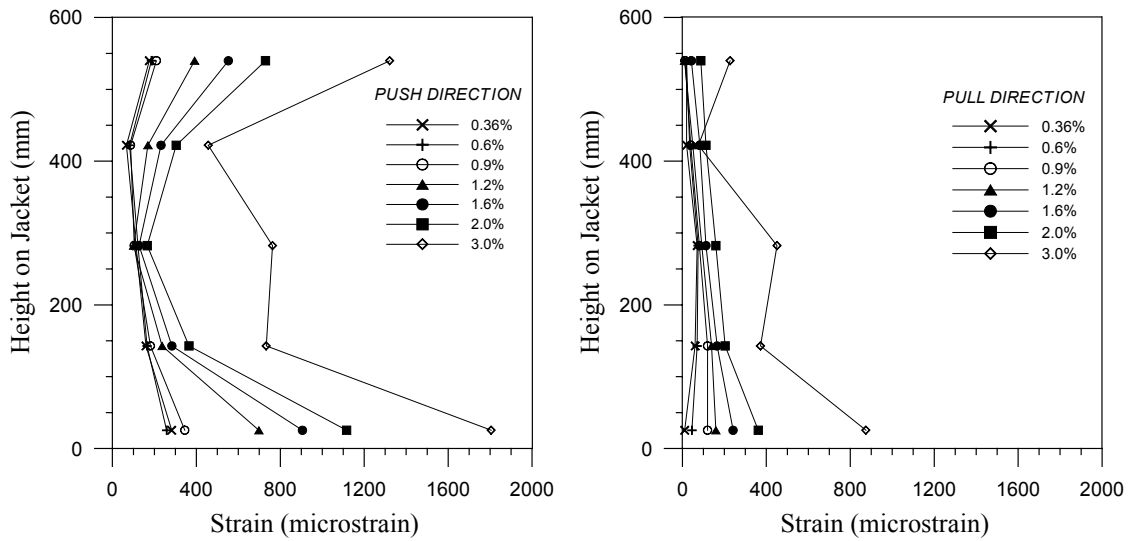
Figure 4.31 JH1 – Test 1 Jacket hoop strain at north generator
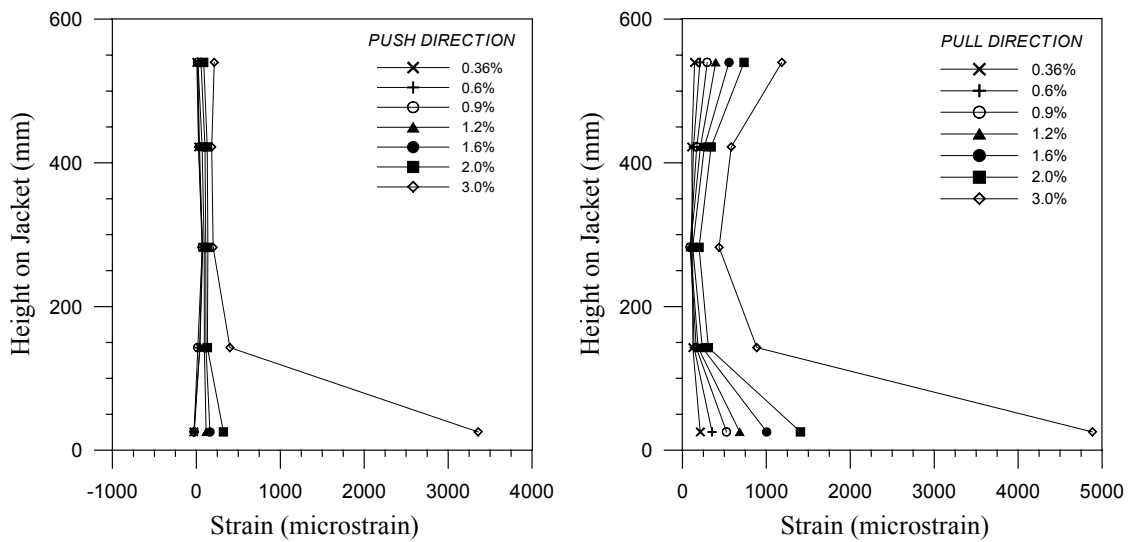
Figure 4.32 JH1 – Test 1 Jacket hoop strain at south generator
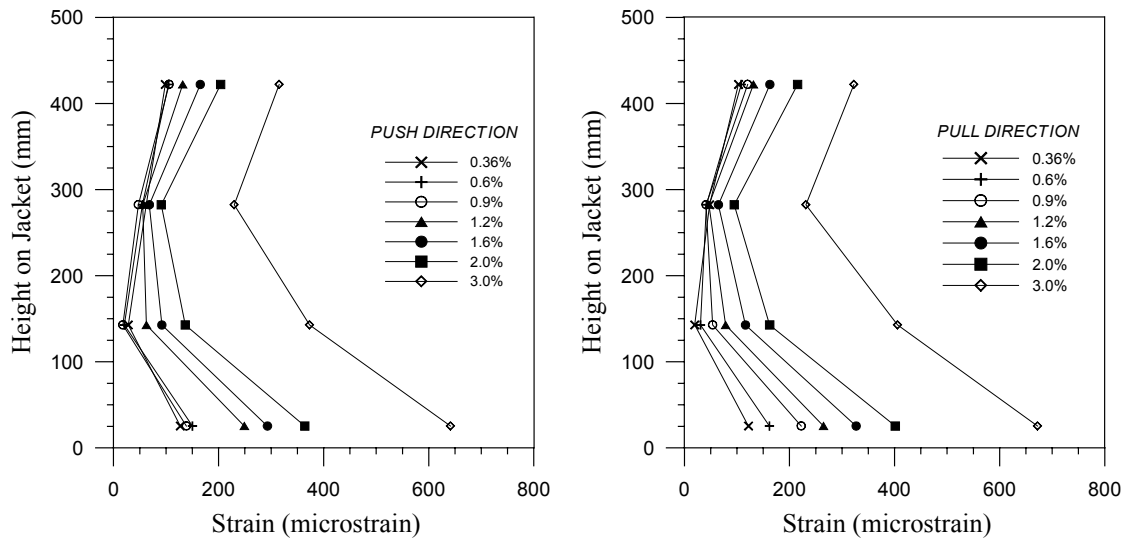
Figure 4.33 JH1 – Test 1 Jacket hoop strain at east generator
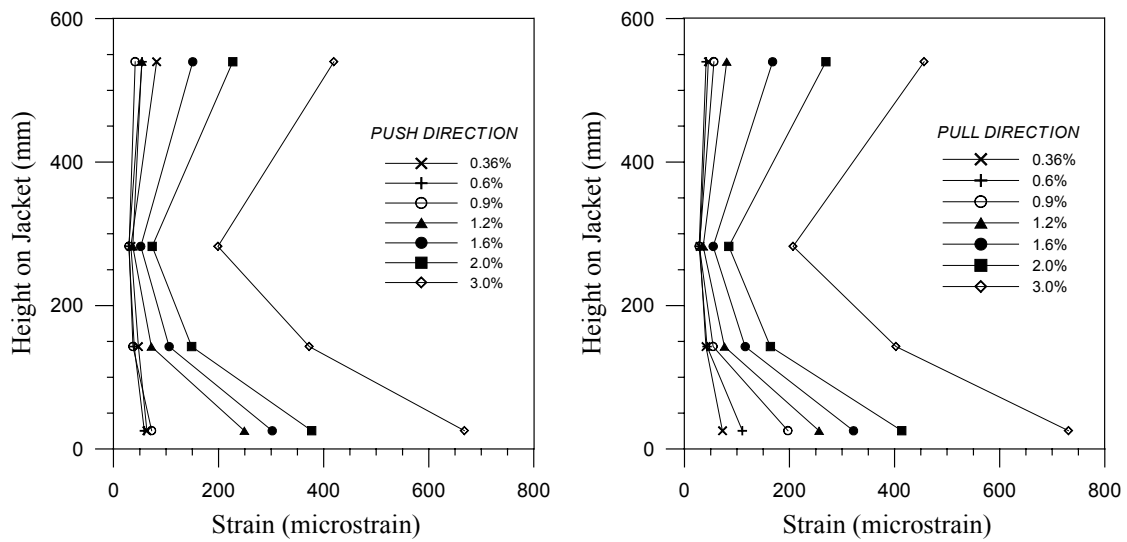
Figure 4.34 JH1 – Test 1 Jacket hoop strain at west generator
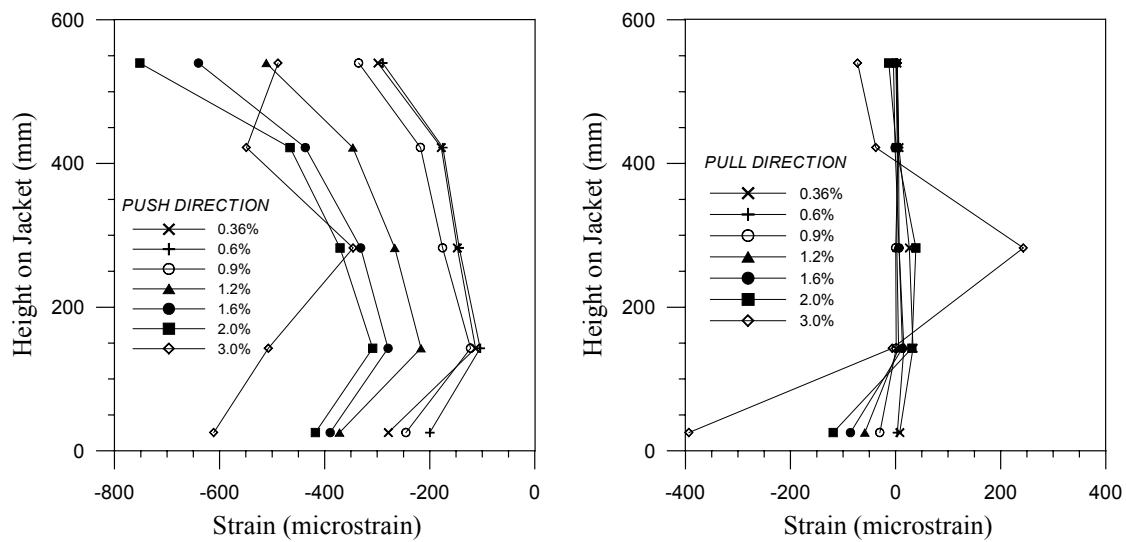
Figure 4.35 JH1 – Test 1 Jacket vertical strain at north generator
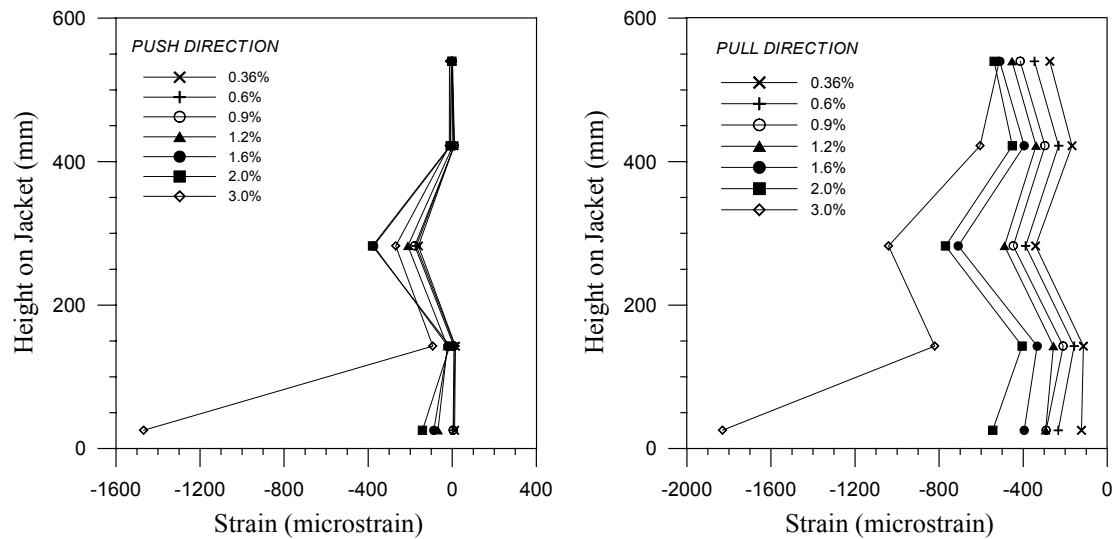
Figure 4.36 JH1 – Test 1 Jacket vertical strain at south generator
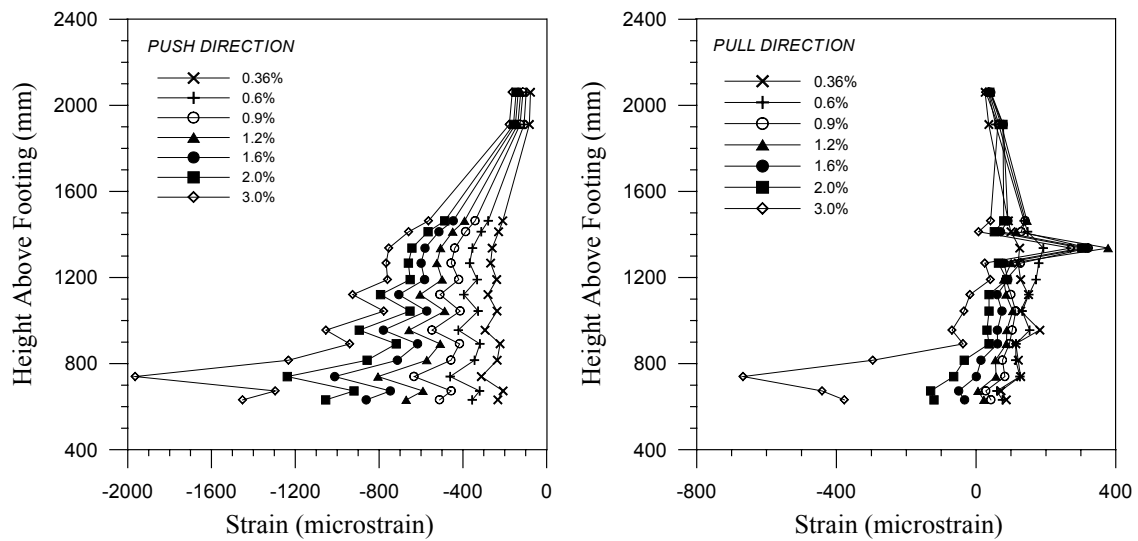
Figure 4.37 JH1 – Test 1 Spiral strains at north generator
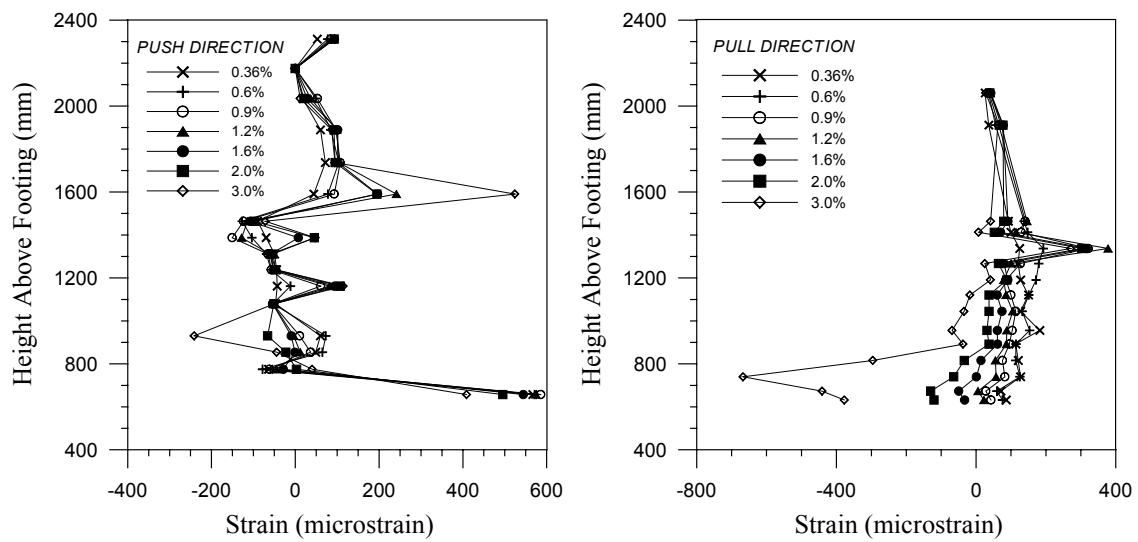
Figure 4.38 JH1 – Test 1 Spiral strain at south generator
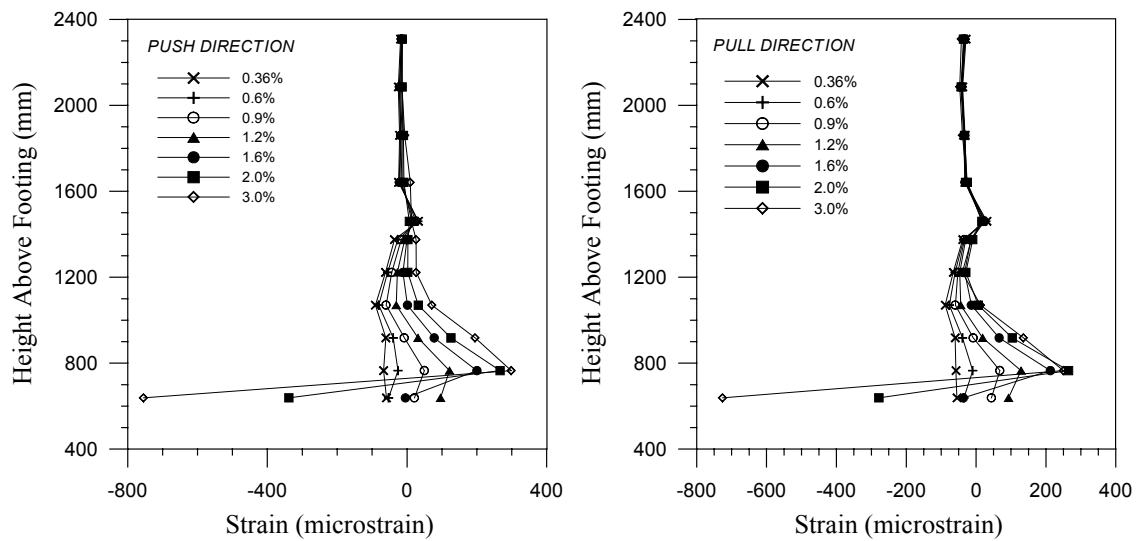
Figure 4.39 JH1 – Test 1 Spiral strain at east generator
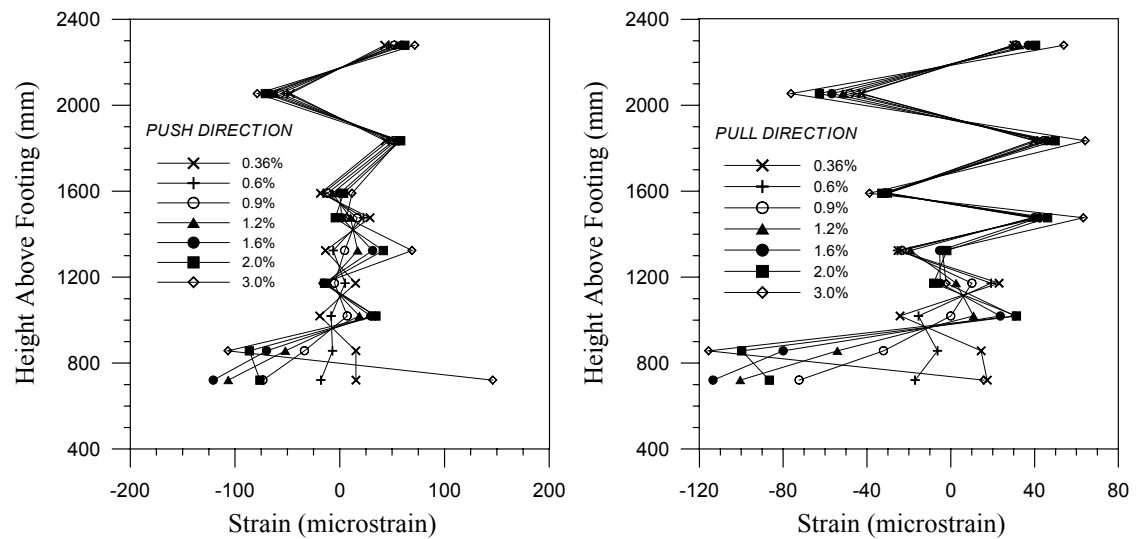
Figure 4.40 JH1 – Test 1 Spiral strain at west generator

4.6   Experimental Results – Specimen JH1-T2

4.6.1   Observations under Repeated Cyclic Loading

The planned loading sequence after repairing the damage from the first test and re-stressing to the higher force level, called for one cycle each to be performed in force control at one-half, one, and one-and-a-half times the theoretical force to cause decompression at the critical section (P_1). After switching to displacement control, three cycles were to then be performed at twice the decompression force. The displacements observed during the first cycle at **1.5 x P_1** however, were larger than those predicted for the next target level of **2 x P_1**. It was thus decided to switch to displacement control after the first cycle at **1.5 x P_1** and then perform two more cycles at that level. A summary of the observed behavior is given below. The push direction of loading is represented by a plus sign (+), while the pull direction is signified by a minus sign (-).

± 0.5 P_1 (P_{max}= 43.2 kN and P_{min}= -44.2 kN)

There was no cracking observed in either the push or pull direction.

$\pm P_1$ (P_{max}= 86.8 kN and P_{min}= -87.8 kN)

A hairline crack was observed below the steel jacket at the footing/column interface for the pull loading direction.

3cycles at 0.36% drift (P_{max}= 111.2 kN and P_{min}= -108.3 kN)

Flexural cracking at the base of the column, below the steel jacket, was observed for the push direction of loading.

3 cycles at 0.6% drift (P_{max}= 145.9kN and P_{min}= -142.5 kN)

The neutral axis depth was approximately 450 mm from the extreme compression edge at this drift. Several cracks in column segment two were noted to have formed at locations of previous cracks from the first test. The crack width at the base of the column was about 1 mm.

3 cycles at 0.9% drift (P_{max}= 179.9 kN and P_{min}= -176.6 kN)

The depth to the neutral axis from the compression edge decreased to 340 mm. Several cracks in the segment above the steel jacket were noticed at the gaps between the fiberglass bands.

3 cycles at 1.2% drift (P_{max}= 200.0 kN and P_{min}= -197.5 kN)

Opening of the crack at the footing/column interface was more noticeable, increasing to approximately 3 mm. A crack at the interface between the top of the steel jacket and column segment two was observed and had a width of around 0.5-1 mm.

3 cycles at 1.6% drift (P_{max}= 218.5 kN and P_{min}= -214.8 kN)

At the footing level, the neutral axis depth was around 280 mm from the extreme compression fiber and the crack width at the tension side was approximately 6 mm. The epoxy below the toe of the jacket was intact and showed no signs of deterioration. Minor crack extensions were observed in the segment above the jacket during the third cycle.

3 cycles at 2.2% drift (P_{max}= 228.5 kN and P_{min}= -225.1 kN)

Some damage to the epoxy repair below the jacket was noticed at the extreme compression fiber. The neutral axis depth at the critical section was on the order of 200 mm from the compression edge.

3 cycles at 3.0% drift (P_{max}= 242.1 kN and P_{min}= -239.2 kN)

The neutral axis depth decreased to about 175 mm. The opening of the crack at the column base was around 8 mm at the tension edge. At the top of the jacket, the crack width between the jacketed segment and segment two was around 3-4 mm.

3 cycles at 4.0% drift (P_{max}= 243.5 kN and P_{min}= -239.5 kN)

The epoxy at the column compression toe continued to "crush" at this level of drift. The neutral axis depth at the base decreased to 150 mm from the compression edge. The crack opening at the base was on the order of 12-14 mm at the extreme tension fiber.

3 cycles at 5.0% drift (P$_{max}$= 243.4 kN and P$_{min}$= -235.9 kN)

The crack at the column base continued to widen and was approximately 18-19 mm. No further opening of the crack adjacent to the top of the jacket was observed.

3 cycles at 6.0% drift (P$_{max}$= 243.4 kN and P$_{min}$= -235.9 kN)

The estimated width of the crack at the footing level was 22-23 mm. Significant damage to the epoxy below the jacket toe was observed for cycles at this drift. In addition, concrete within the section near the compression toe was crushed to some degree. This was noticed at the crack opening at the extreme tension fiber, where one could actually see into the central portion of the cross section due to the large lift-off of the column from the footing. A photograph of the base crack is shown in Figure 4.41. Some spalling of concrete below the steel jacket at the east and west generators was observed. The gap between the bottom of the jacket and the top of the footing at the extreme compression edge was reduced slightly due to slippage of the jacket with respect to the concrete core and due to the rotation of the segment. An overall view of the column at the 6% drift level is displayed in Figure 4.42.

Test End

Observed damage to the column during testing consisted of the damage below the jacket at the critical section and the small flexural cracks in the upper column segments. A residual crack at the level of the footing at the north and south generators existed due to the damaged epoxy. Crushing of concrete at the shear generators was relatively minor. No concrete crushing was observed in the upper, non-jacketed column segments, and the flexural cracks there closed completely after the lateral force was removed. Fracture of strands did not occur during the test. The residual drift of specimen was on the order of 0.15-0.2 % after testing.

Figure 4.41 JH1 –Test 2 Crack at column base at 6.0% drift

Figure 4.42 JH1 – Test 2 Overall view of specimen at 6.0% drift

4.6.2 Force-Displacement Response

The lateral force-displacement response for the second test of specimen JH1 is shown in Figure 4.43. The response of the column was stable and symmetric up to the maximum imposed drift of 6.0%. Equal strengths were achieved for the push and pull directions of loading. The beginning of significant non-linear response initiated at a force of around 200 kN - a force level which corresponds to approximately 2.2 times P_1. The maximum column strengths occurred at a drift of 4.0% and were 243.5 kN and -239.5 kN for the push and pull directions, respectively. Degradation of the column strength was minimal at higher drifts, with a decrease in capacity of 3% and 5% observed at the maximum imposed drift for the push and pull directions.
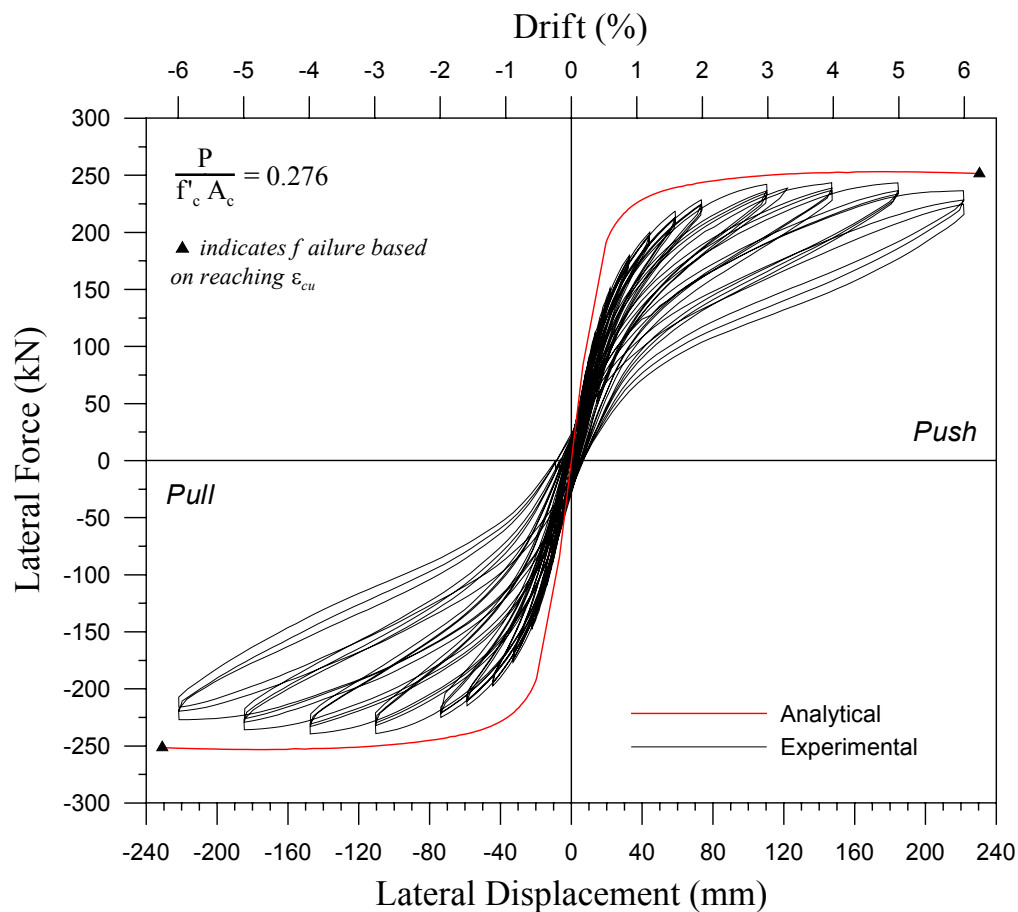
Figure 4.43 JH1–Test 2 Force-displacement response

The analytical force-displacement response envelope is shown in Figure 4.43 along with the experimental hysteretic response. The initial stiffness of the specimen is not well predicted. This is because the column had been tested previously. Despite reinstating the spalled cover concrete above the jacket and epoxy grouting the base crack below the jacket, the original column stiffness was not restored. Although column strength was over-predicted for all drift levels, the shape of the analytical curve for moderate to high drifts follows the experimental reasonably well. At high drifts, the observed decrease in strength is slightly larger than predicted by the analytical curve. Two reasons are given for this. First, as explained previously in Section 1.5.2, the Mander model may over-predict the confined compressive strength, f'_{cc}, of high strength concrete. Predicted column strengths would thus be higher than actual. In addition, the larger drop in strength than predicted may be caused by the descending branch of the Mander stress-strain curve being too gradual since high strength concrete tends to be less ductile than concrete of lower strength. The difference between the analytical and experimental force-displacement response at moderate to high drift levels is less than 10%. In light of this, the uncertainty in initial prestress force, and the fact that the column had been tested previously, it can be said that the analytical prediction agrees with the experimental behavior well.

The predicted failure point of the test unit is also shown in Figure 4.43. The predicted failure was based on reaching the ultimate concrete compression strain, ε_{cu}, and hence rupture of the steel jacket (as given by the energy-balance approach detailed in Ref. 4). However, the value for ε_{cu} given by Eq. 2.29 is typically conservative by 50%, and thus it is believed that a significant reserve in displacement capacity existed.

The initial loading stiffness of the column for both first and second tests is displayed in Figure 4.44. The vertical axis on the right side of the graph represents the stiffness at a particular drift for the second test as a percentage of the original stiffness measured at the theoretical decompression point (P_1) during the first test. It can be seen that the column stiffness was restored to approximately 70% of that observed for the first test after epoxy

grouting the base crack and patching the spalled concrete in column segment two. In general, the decrease in stiffness as a function of imposed drift was less dramatic for the second test than the first. After 1.6% drift, the second test stiffness is actually slightly higher than the first. The epoxy used at the column base to repair the damaged region after the first test was more ductile than concrete, and thus did not deteriorate as significantly as the concrete did for the first test.

The equivalent viscous damping for the first and second test is shown in Figure 4.45. It can be seen that the hysteretic energy dissipation increased slightly with increasing drift. The equivalent viscous damping for the second test was lower than that for the first test for all drift levels. This may be caused by the significant crushing of concrete at the column base and by the spalling of cover concrete above the jacket observed for the first test. The difference between the first and second test equivalent viscous damping is not great, however: the maximum damping for the first test was about 7% while that for the second test was 6%. Considering both curves, an average equivalent viscous damping of 5% could be assumed.
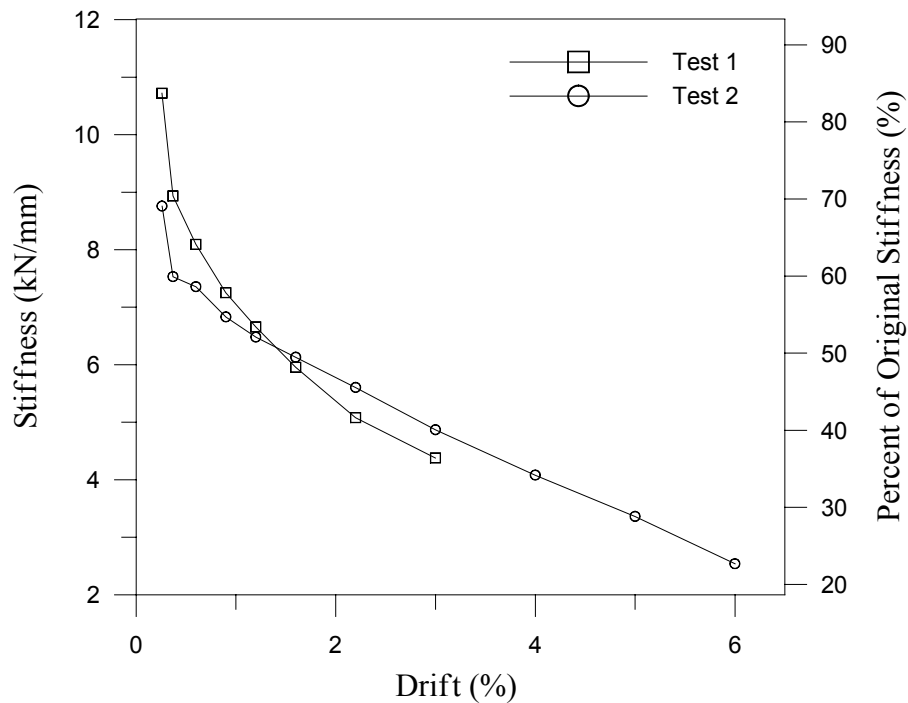
Figure 4.44 JH1 – Test 2 Initial loading stiffness versus drift
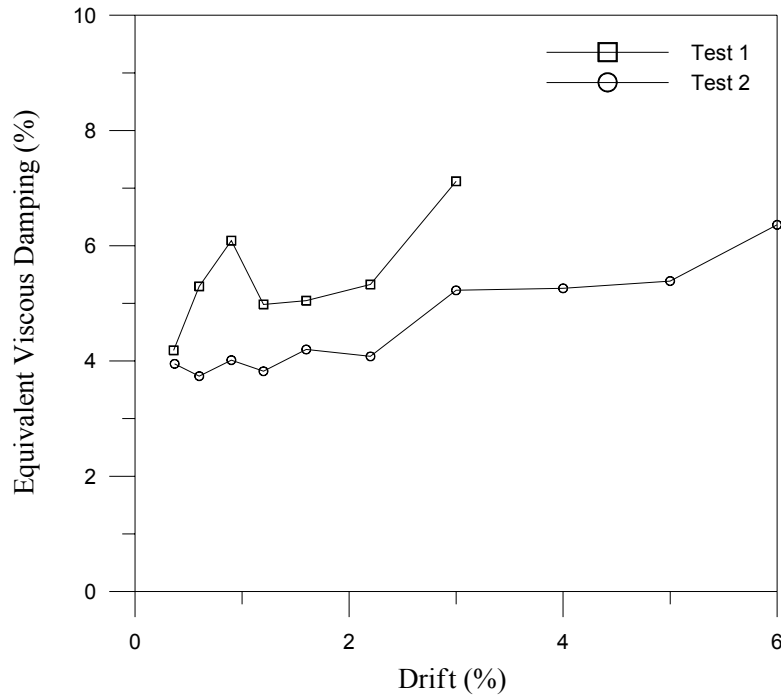
Figure 4.45 JH1 – Test 2 Equivalent viscous damping versus drift

4.6.3   Test Data

Curvature and strain profiles constructed using data recorded at peak displacement during the first cycle of loading are presented in this section. Profiles for drifts between 0.6% and 6.0% are shown. In addition to the prestressing steel, jacket and spiral strain profiles, hoop strains in the fiberglass bands measured at the north and south generators are shown.

Column Curvature

Figure 4.46 shows the distribution of curvature along the column height for the second test of JH1.   The profiles look similar to those for the first test, with curvature concentrated at the base and at the interface between column segments three and four. Curvatures at the column base for drifts equal to and less than 3.0% are almost identical

85

to those observed for the first test. An estimate of the concrete longitudinal compression strain at the extreme fiber of the critical section for the 6.0% drift level is given below.

$$\varepsilon_c = \frac{10 \text{ mm}}{166 \text{ mm}} - (57.2 \text{ mm})(2.7x10^{-4} \text{ mm}^{-1}) = 0.045$$

The predicted strain from the moment-curvature analysis for 6.0% drift is 0.031.

Prestressing Steel Strain

The predicted and experimental tendon strain increase curves are given in Figure 4.47. The analytical model over-predicts the strain increase by approximately 30% on average. Reasons given in Section 4.5.3 for the discrepancy between observed and predicted strain increase for the first test of JH1 also apply for the second test.
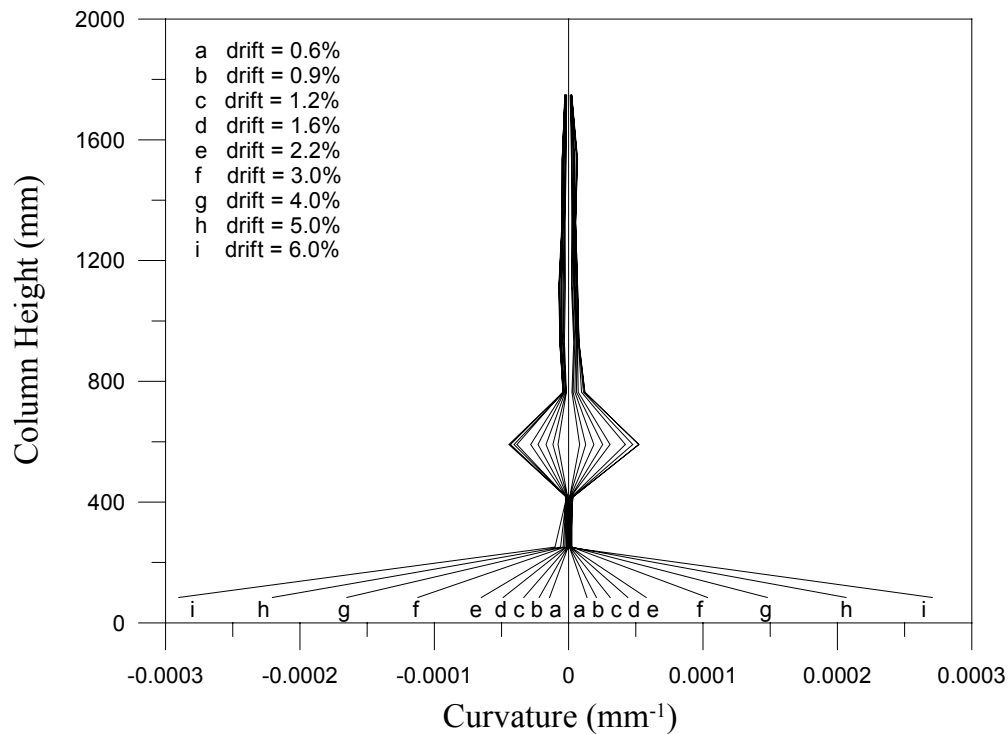
Figure 4.46 JH1–Test 2 Curvature along column height

Steel Jacket Strains

Hoop strain profiles for the north and south generators are shown in Figures 4.48 and 4.49, respectively. Note that the strain gage mounted near the bottom of the jacket at the south side did not function properly and thus was not used in the strain profile. Hoop strains are largest at the bottom of the jacket for the same reasons given for the first test. At the base of the jacket, hoop strains slightly higher than the yield strain occurred at a drift of 1.6%. At the maximum drift of 6.0%, the hoop strain at the jacket toe was several times the yield strain of the material. Yielding of the jacket occurred as high as mid-height of the segment for 6.0% drift. Figure 4.50 shows the hoop strains in the jacket at west generator. The strains are substantially higher near the base of the jacket. The maximum strain occurred at a drift of 6.0% and was approximately 1250 $\mu\varepsilon$. Data for the east generator strain gages was not obtained due to a problem with the data acquisition system.

Vertical strains in the jacket at the north and south generators are shown in Figures 4.51 and 4.52. Significant strains were induced at both the north and south sides of the jacket due to bending of the segment. Strains above the yield strain of the material occurred at the bottom of the jacket at high drifts. Strains at the north generator are higher for the push direction of loading since at the compression side, dilation of concrete enhances the bond between the inner core concrete and the steel jacket. Strains at the south generator are higher for the pull direction for the same reason.

Transverse Spiral Strains

Strains in the transverse spiral reinforcement along the column height are shown in Figures 4.53 - 4.56. The maximum strains in the spiral are similar in magnitude to those observed for the first test. The erratic strain readings along the height observed for some of the profiles are believed to be due to gage instability. Interpretation of the data in a meaningful way is thus difficult. It can be said however that hoop strains at a height of around 800 mm above the footing at the north generator (the region just above the steel jacket where spalling had occurred during the first test) are high since dilation of the

compressed concrete is greater than higher up on the column. The strains at the east and west generators are low in general, but the trend of increasing strain down the column is visible.

Fiberglass Jacket Strains

Two electrical resistance strain gages with a gage length of 60 mm were mounted on the lower two fiberglass rings at both the north and south generators. The gages were oriented in the horizontal position in order to measure hoop strains associated with the confining action of the wrap on the compressed concrete. Strain profiles are shown in Figures 4.57 and 4.58 for the north and south generators, respectively. The maximum observed strains occurred just above the top of the steel jacket were approximately 1750 $\mu\varepsilon$ and 1500 $\mu\varepsilon$ for the north and south sides, respectively
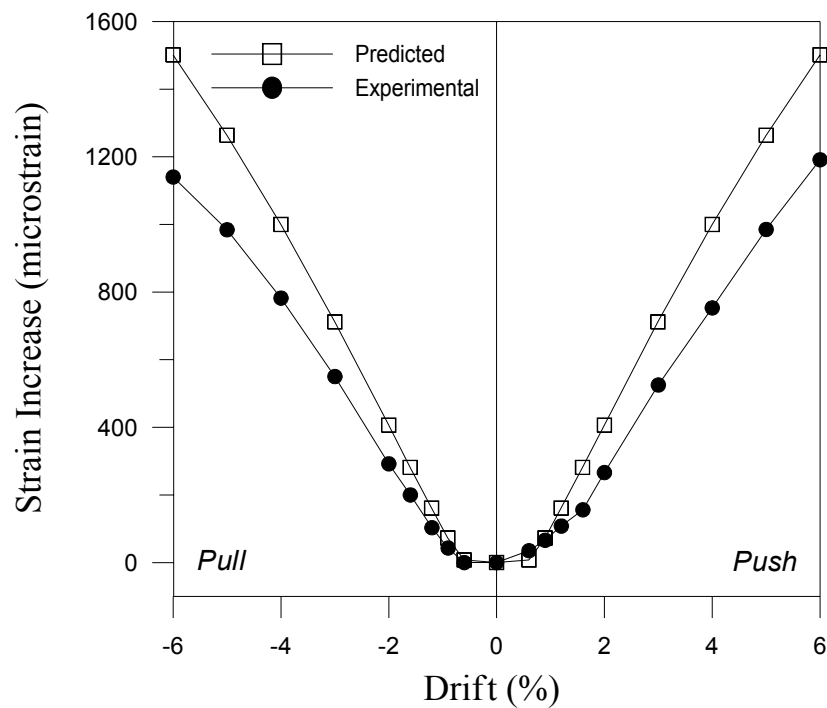
Figure 4.47 JH1 – Test 2 Predicted and experimental tendon strain increase
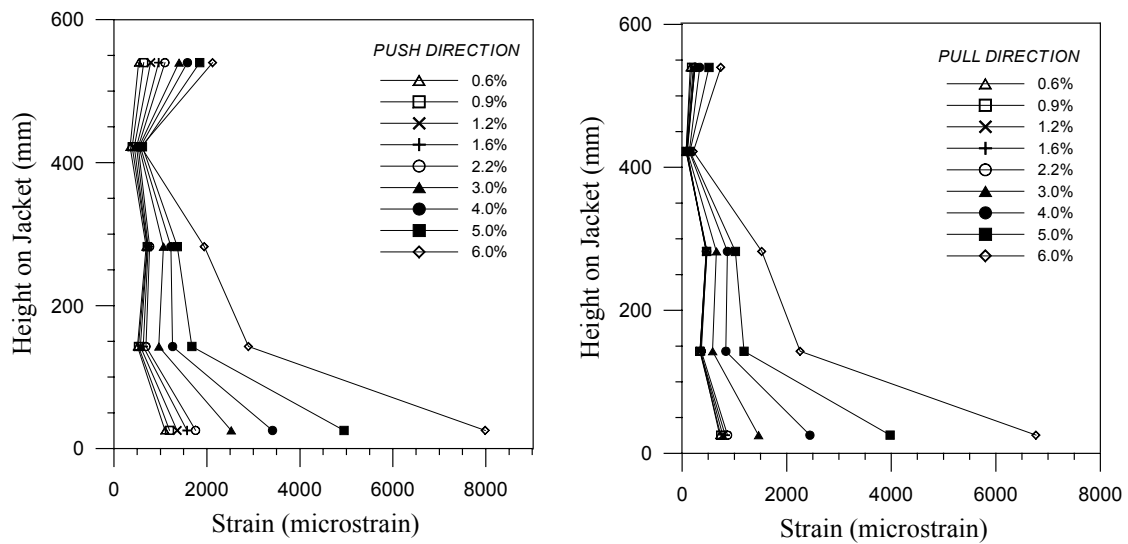
Figure 4.48 JH1 – Test 2 Jacket hoop strain at north generator
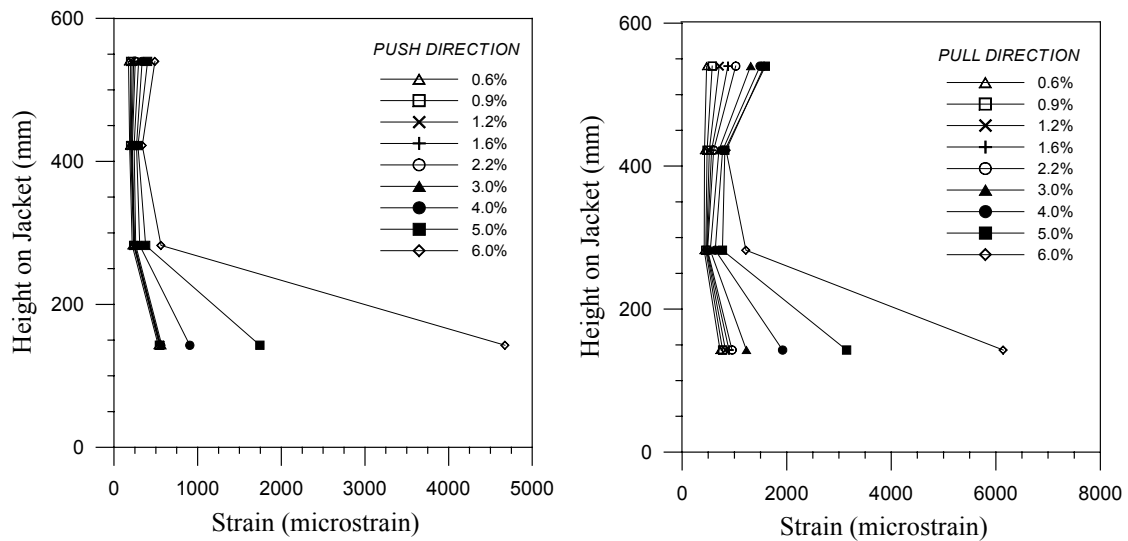
Figure 4.49 JH1 – Test 2 Jacket hoop strain at south generator
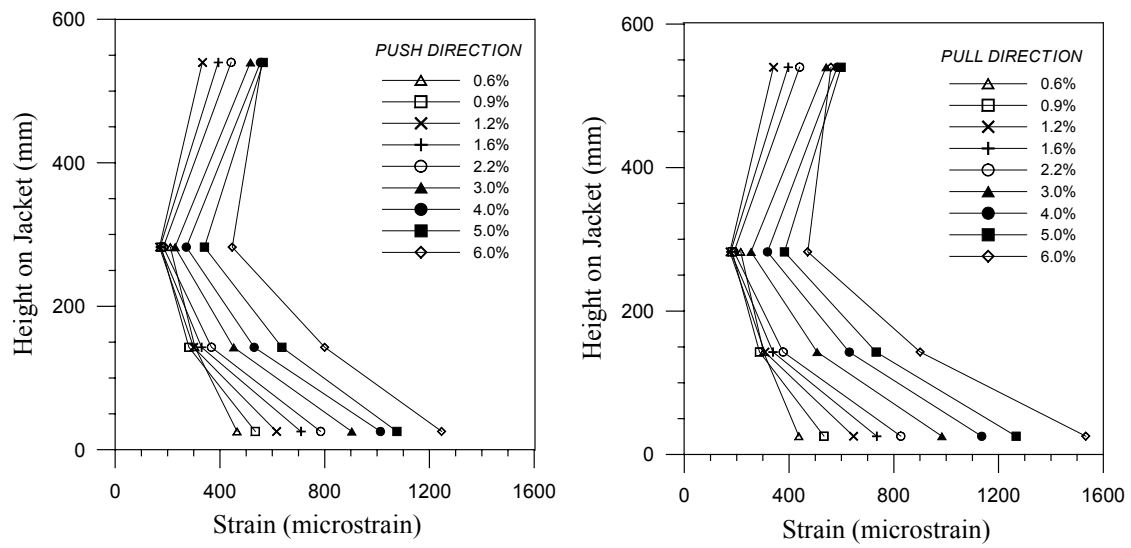
Figure 4.50 JH1 – Test 2 Jacket hoop strain at west generator
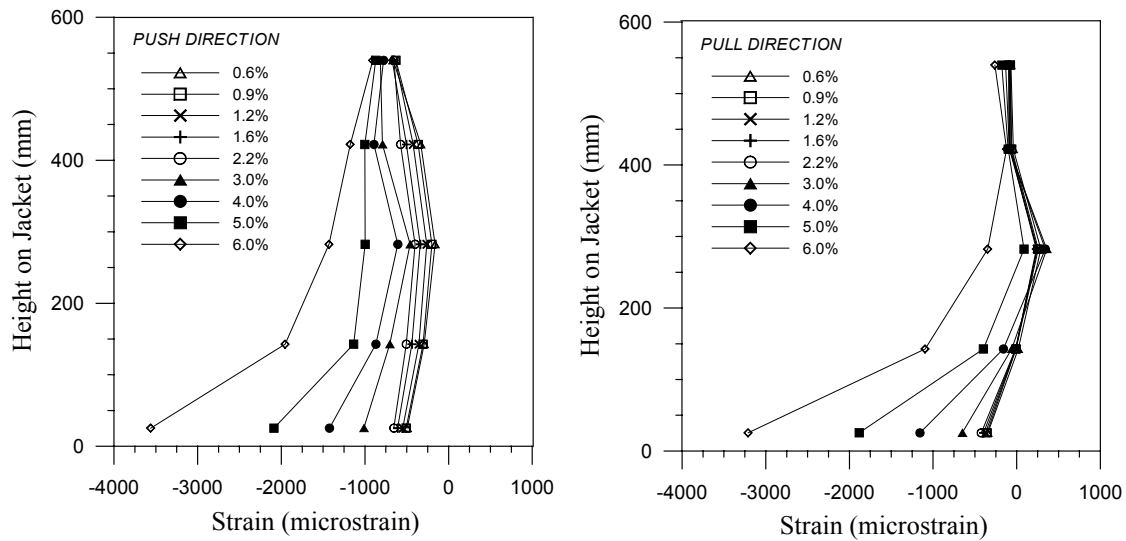
Figure 4.51 JH1 – Test 2 Jacket vertical strain at north generator
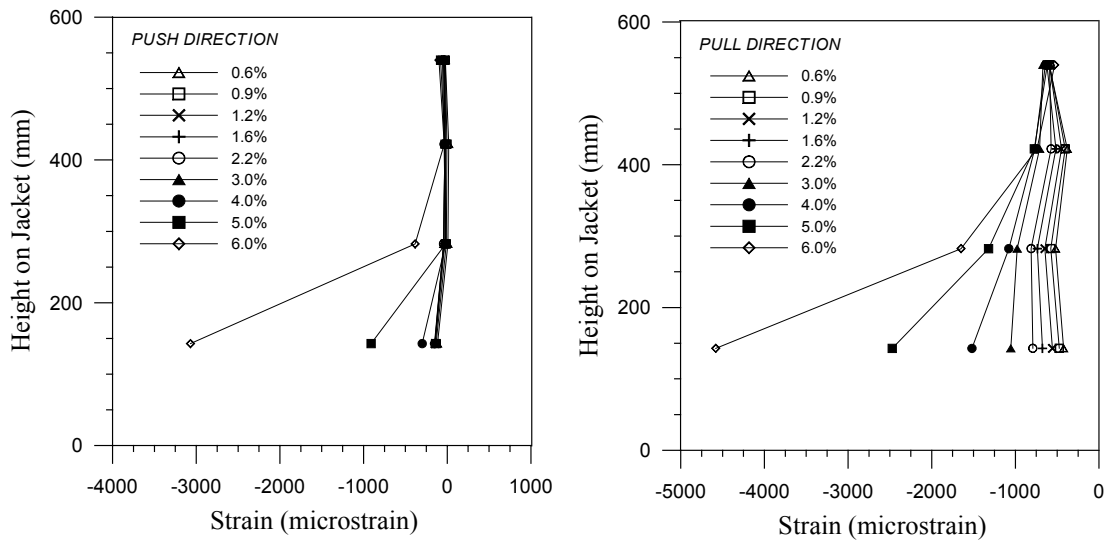
Figure 4.52 JH1 – Test 2 Jacket vertical strain at south generator
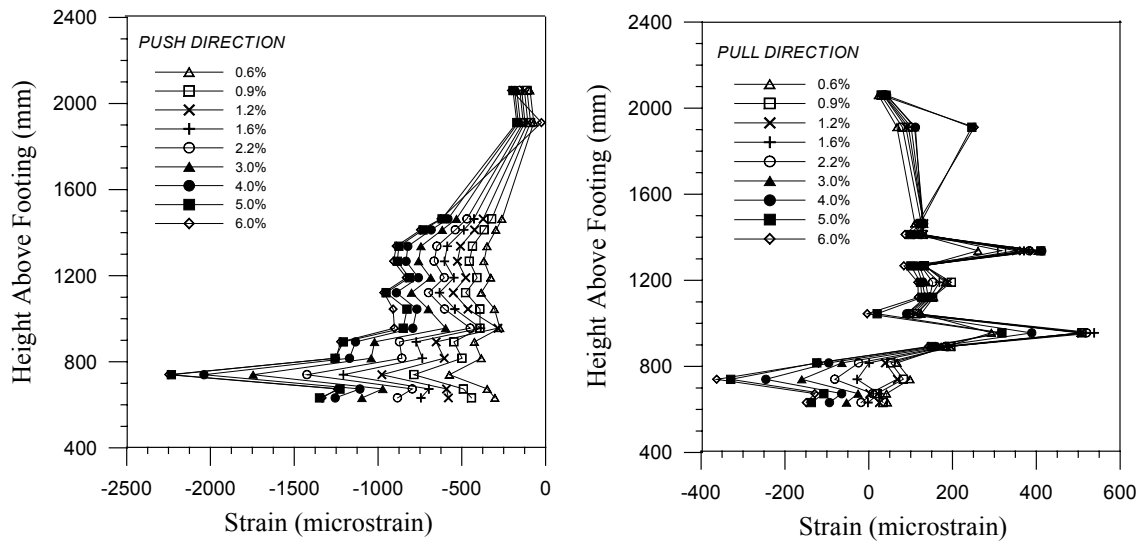
Figure 4.53 JH1 – Test 2 Spiral strain at north generator
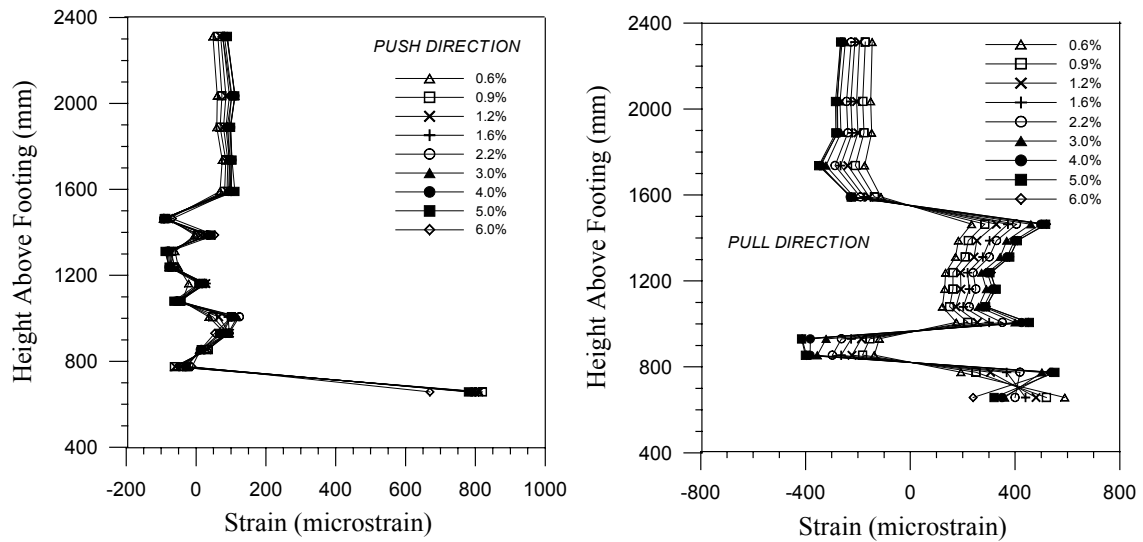
Figure 4.54 JH1 – Test 2 Spiral strain at south generator
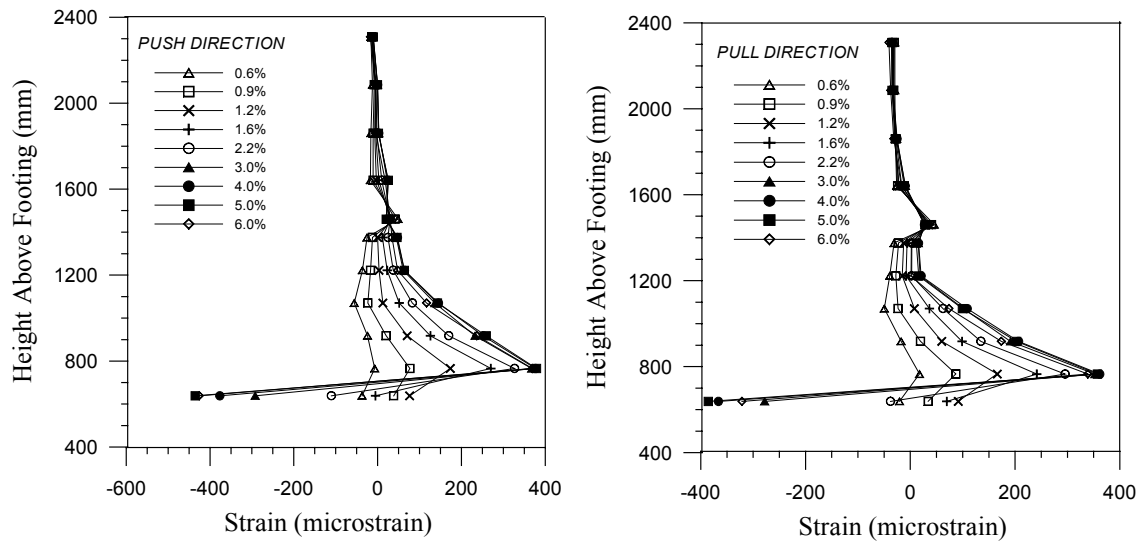
Figure 4.55 JH1 – Test 2 Spiral strain at east generator
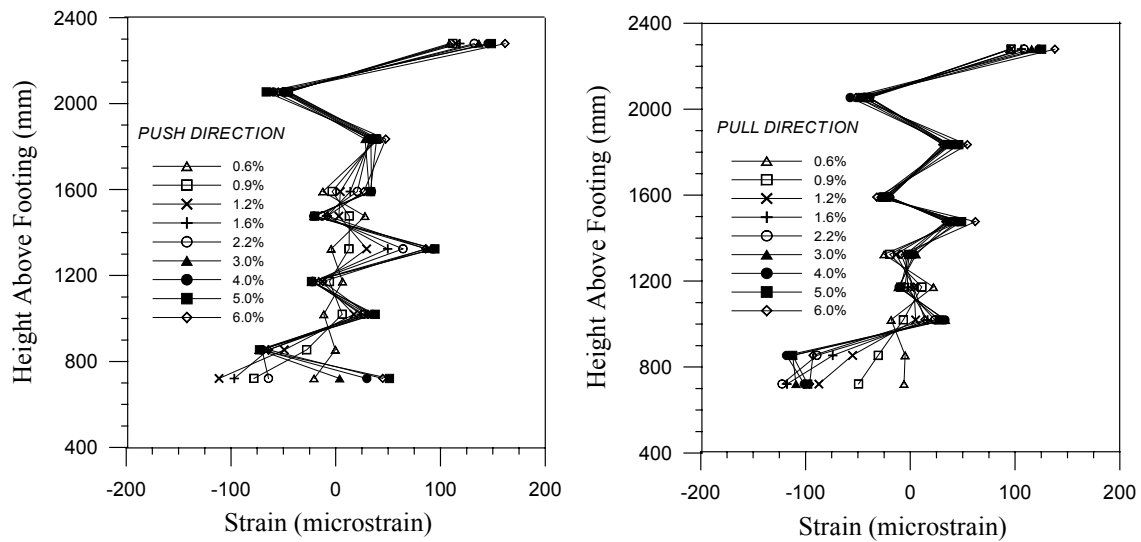
Figure 4.56 JH1 – Test 1 Spiral strain at west generator
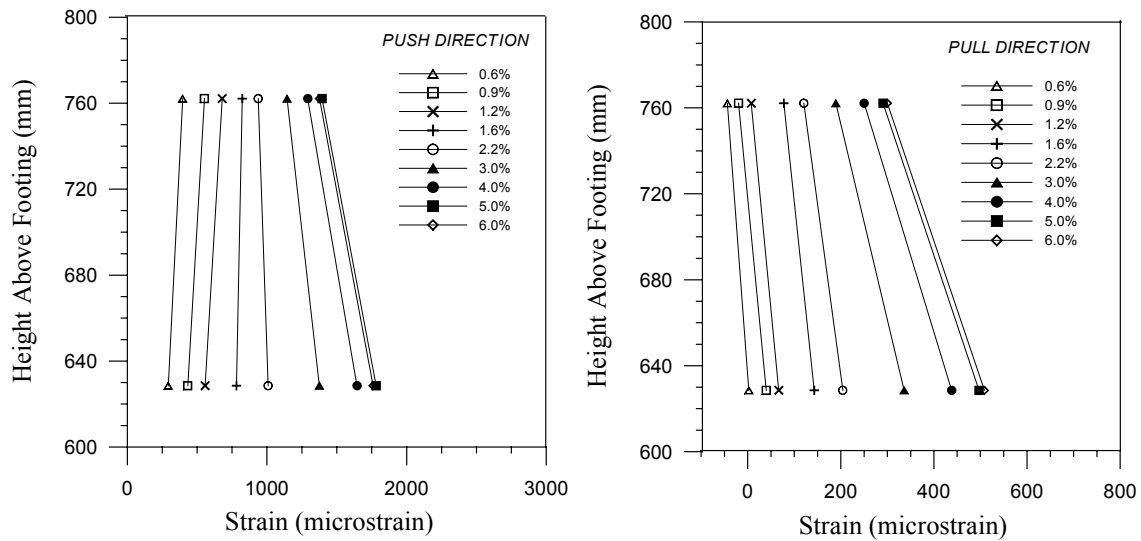
Figure 4.57 JH1 – Test 2 Fiberglass jacket hoop strain at north generator
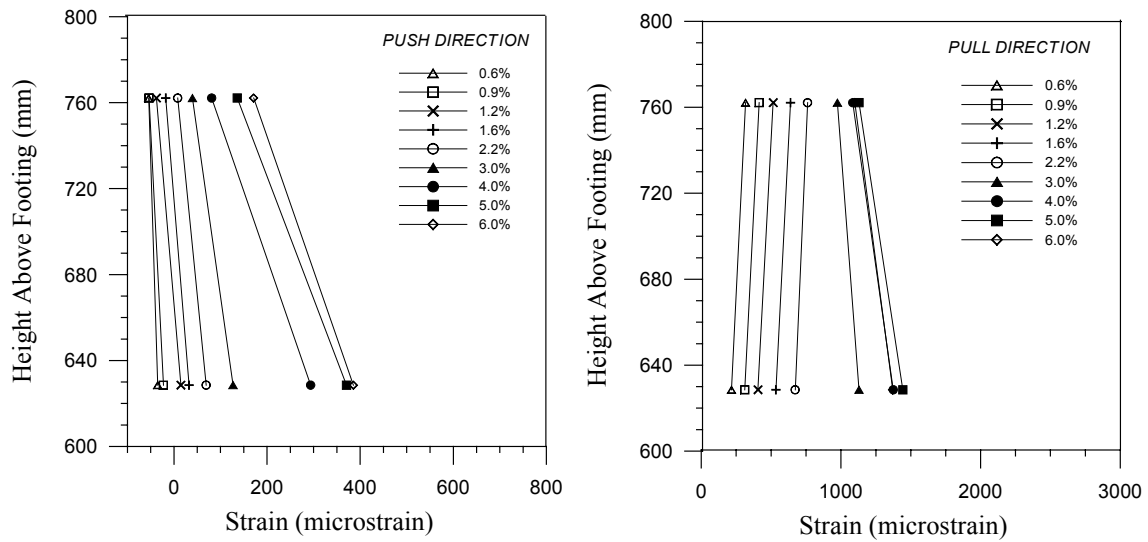
Figure 4.58 JH1 – Test 2 Fiberglass jacket hoop strain at south generator

4.7 Experimental Results – Specimen JH2-T1

4.7.1 Observations under Repeated Cyclic Loading

A description of the behavior of specimen JH2 during the first test is given along with some supporting photographic illustrations. The planned loading sequence given in Section 3.5 called for one cycle each to be performed in force control at one-half, one, and one-and-a-half times the theoretical force to cause decompression at the critical section (P_1). After switching to displacement control, three cycles were to then be performed at twice the decompression force. The displacements observed during the first cycle at **1.5 x P_1** however, were larger than those predicted for the next force target level of **2 x P_1**. It was thus decided to switch to displacement control after the first cycle at **1.5 x P_1** and then perform two more cycles at that level.

±0.5 P_1 (P_{max}=39.1 kN and P_{min}= -39.4 kN)

No cracking was observed for either direction of loading.

±P_1 (P_{max}= 78.5 kN and P_{min}= -78.7 kN)

A horizontal flexural crack was observed below the steel jacket at the footing level for both the push and pull direction of loading.

3 cycles at ±1.5P_d (P_{max}= 117.6 kN and P_{min}= -117.9 kN)

Flexural cracks at the interface between segments one and two were observed for both the push and pull directions of loading. Cracking at the column base was noted for the pull direction of loading.

3 cycles at 0.6% drift (P_{max}= 162.0 kN and P_{min}= -154.1 kN)

More pronounced flexural cracks at the column base were observed during the first cycle of loading. The flexural crack between the steel jacketed segment and segment above was approximately 1mm for both directions of loading. Flexural cracks were observed in

the second column segment at heights of 300 mm and 450 mm above the top of the jacket.

3 cycles at 0.9% drift (P_{max}= 182.0 kN and P_{min}= -173.0 kN)

New flexural cracks at a 250mm spacing were observed in segment two during the first half-cycle at this drift level. Existing cracks in the segment extended towards the column sides in the first pull half-cycle of loading. Crack openings of approximately 1mm and 2mm were observed at the interface between segments one and two, and at the column base, respectively.

3 cycles at 1.2% drift (P_{max}= 196.1 kN and P_{min}= -185.3 kN)

Significant extension of existing cracks towards the column sides was observed in segment two for both the first push and pull loading. At this drift level, flexural cracks were spaced evenly along the full height of the second column segment up to the bottom of the third segment. Figure 4.59 shows the crack pattern at the south generator for the third push loading. The crack at the column base opened to approximately 2mm. Incipient spalling of concrete at the gap between the jacket toe and footing was observed for the push loading direction.

3 cycles at 1.6% drift (P_{max}= 203.5 kN and P_{min}= -192.5 kN)

Minor crushing of concrete below the steel jacket at the column compression toe was noted for cycles at this drift level. Extension of existing flexural cracks in column segment number two was noted for both directions of loading in the first cycle. New flexural cracks were observed approximately 125 mm below the interface between segments two and three, at the interface between those segments, and at a distance off 100 mm above the interface. At the footing level, the crack opening was approximately 3 mm.

3 cycles at 2.0% drift (P_{max}= 205.8 kN and P_{min}= -194.2 kN)

Continued minor spalling of concrete below the steel jacket at the critical section was observed. Continued spalling was observed for both loading directions for the third cycle. The depth of the neutral axis was noted to be 125-150 mm at the column base and the column had lifted off the footing approximately 5mm on the tension side.

3 cycles at 3.0% drift (P_{max}= 206.9 kN and P_{min}= -191.5 kN)

Crushing of the concrete at the column compression toe was increased significantly for this drift level. The damaged region is shown in Figure 4.60. Vertical cracks and incipient spalling were observed at the extreme compression edge just above the steel jacket in column segment two for both directions of loading.

3 cycles at 4.0% drift (P_{max}= 192.4 kN and P_{min}= -179.3 kN)

The width of the base crack was approximately 12-13 mm at this drift. Concrete spalling below the jacket increased and minor crushing was observed at the bottom of the second column segment, just above the top of the jacket. Spalling at the base extended from the extreme compression fiber around the circumference to the east and west generators.

Test End

Damage to the column was concentrated primarily at the column base below the jacket toe, where significant crushing of concrete occurred. Because of the crushed concrete in that region, a residual crack of approximately 3 mm (as measured at the extreme fiber of the section) existed at the footing/column interface. The crack and spalled region are shown in Figure 4.61. Little work would be required however, to repair the damage. The damage above the jacket could also be repaired relatively easily by removing any loose cover concrete, and by patching the area with mortar. No inclined cracks were observed during the test, and the flexural cracks observed along the height of the column closed completely once the lateral force was removed at test end. It should be noted that the crack openings remained small except at the base of the column where the column lifted

off the footing at the tension side, and at the top of the jacket where a crack formed between column segment two and three. The prestressing steel did not fracture during the test and the residual drift of the column after the test measured just over 0.3%.

Figure 4.59 JH2 – Test 1 Crack pattern at 1.2% drift

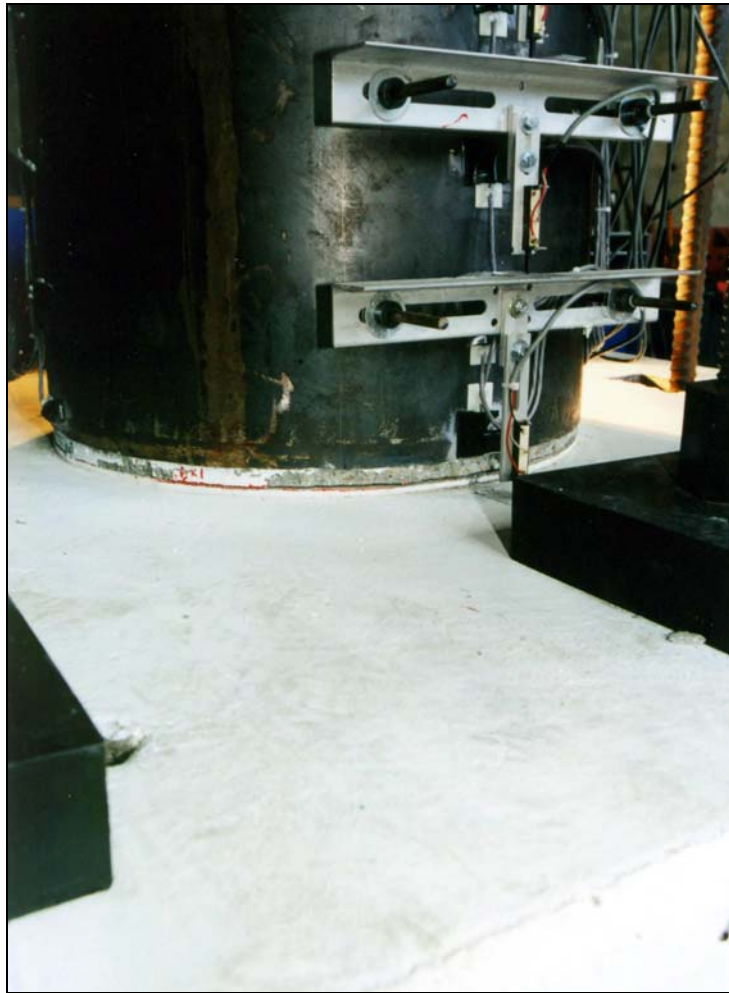
Figure 4.60 JH2 –Test 1 Damage below jacket at 3.0% drift

Figure 4.61 JH2 – Test 1 Residual crack at column base at end of test

4.7.2 Force – Displacement Response

The lateral force-displacement response of the column for the first test is shown in Figure 4.62. The specimen exhibited stable and symmetric hysteretic behavior up to the maximum imposed drift of 4.0%. Significant non-linear response initiated at a force of 160 kN, or approximately 2.5 x P_1. The maximum column strengths for the push and pull loading directions were 206.9 kN and –194.2 kN, and occurred at drifts of 3.0% and 2.0%, respectively. Degradation of the column strength was not dramatic, with capacities at the 4.0% drift approximately 7% lower than the maximum observed values.
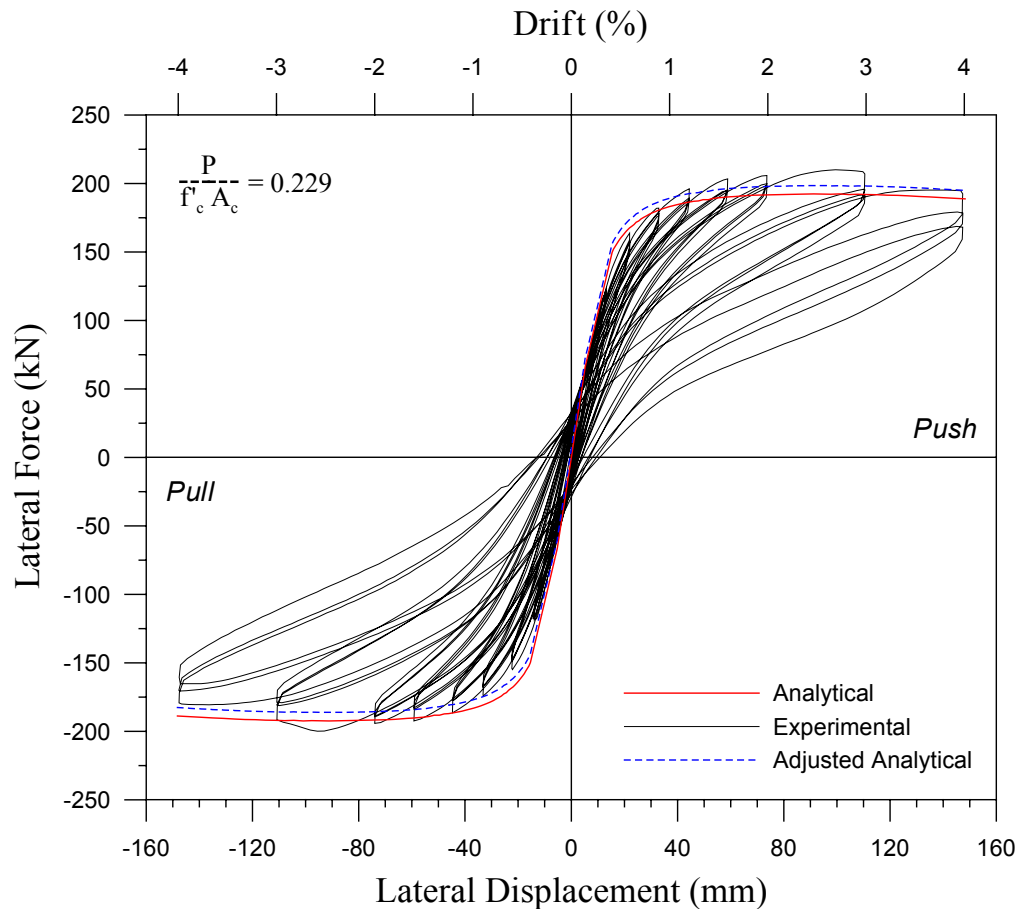
Figure 4.62 JH2 – Test 1 Force-displacement response

The analytical force-displacement response envelope is also shown in Figure 4.62. Similar to the first test of unit JH1, it is believed that the axial load transfer beam was positioned slightly off the column axis, and consequently the observed strength in the pull direction of loading was lower than that for the push loading direction. The analytical curve was adjusted for this as detailed for specimen JH1 in Section 4.5.2. The predicted initial stiffness follows the experimentally observed stiffness well. Column strength after the initial stages is under-predicted for both loading directions. Deviation of the predicted strength from observed is not great however, with a maximum error for the push and pull directions of 5%.

The initial stiffness of the column is shown in Figure 4.63. After the initial elastic cycles, the stiffness decreased almost linearly with increasing drift. At moderate drifts, the stiffness had dropped to approximately 50% of its original value while at the maximum imposed drift of 4.0%, the stiffness was approximately one quarter of the original. At the maximum drift, the initial stiffness was only slightly higher the effective column stiffness, K_{eff}, equal to the force at maximum displacement divided by the maximum displacement.

Similar to specimen JH1, the hysteretic energy dissipation of specimen JH2 was low. The damping coefficient is shown as a function of drift in Figure 3.64. The damping increased from around 4% for early stages of testing to just less than 9% at the maximum drift. The increase in the calculated equivalent viscous damping is associated with the increased level of crushing of concrete below the jacket and the minor spalling observed at the bottom of the second column segment. At the maximum imposed drift, the second cycle damping was lower than the first, and was around 7%.
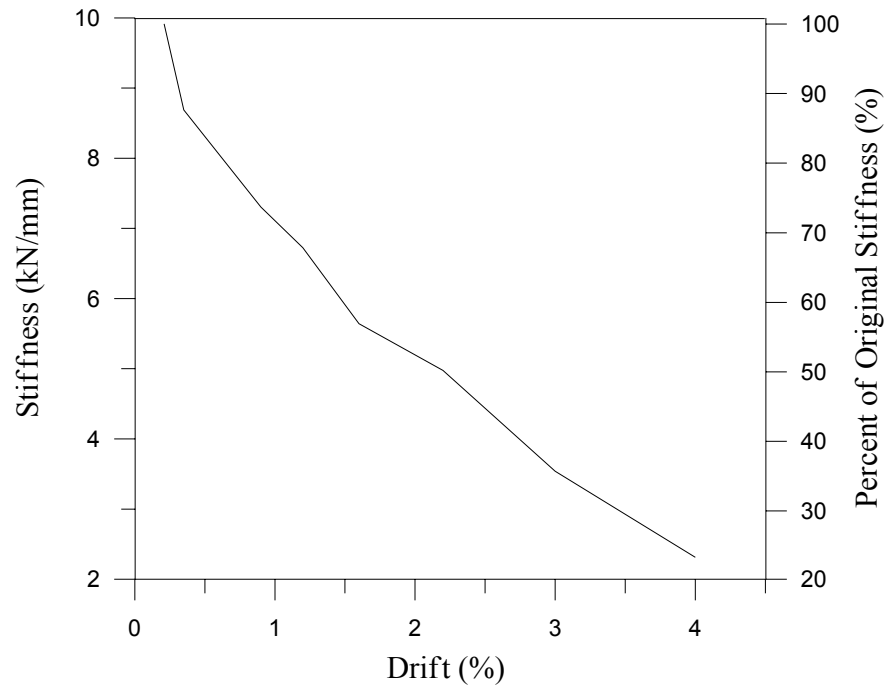
Figure 4.63 JH2 – Test 1 Initial loading stiffness versus drift
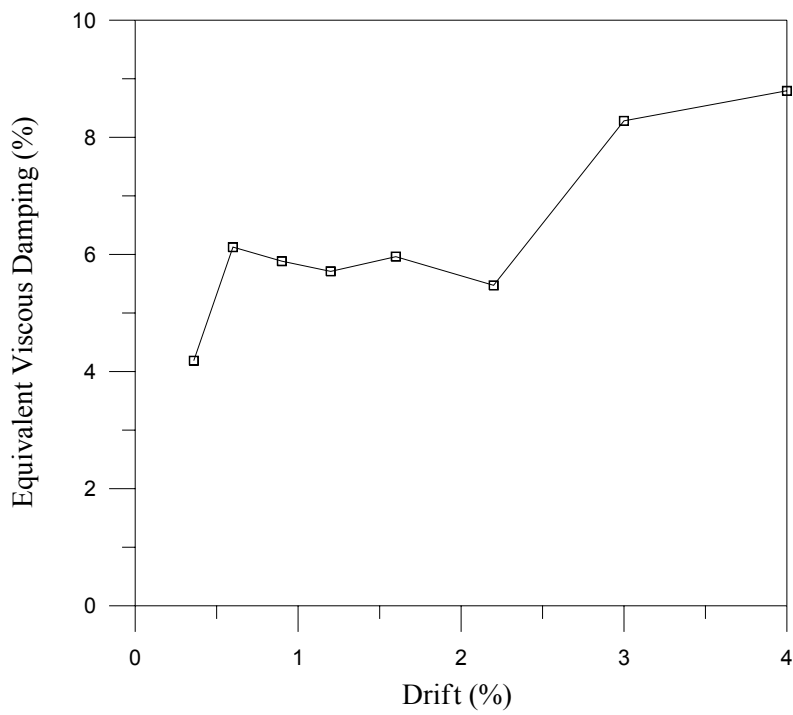
Figure 4.64 JH2 – Test 2 Equivalent viscous damping versus drift

4.7.3   Test Data

Data recorded during testing for the strain gages and linear potentiometers is presented in this section. Profiles of strains in the prestressing steel, steel jacket and the transverse spiral reinforcement, and of curvature along the column height are shown for drifts between 0.6% and 4.0%.

Column Curvature

Curvature along the column height is depicted in Figure 4.65. The curvatures are highest near the column base and at 600 mm above the base for the same reasons detailed in Section 4.5.3 for specimen JH1. The measured curvatures at each drift for specimen JH2 are lower than those observed for the first test of specimen JH1 since the axial load ratio was higher for JH1. The maximum curvature measured at the base occurred at a drift 4.0% and was $1.75x10^{-4}$ mm^{-1}. The corresponding concrete compressive strain is:

$$\varepsilon_c = \frac{6.8 \text{ mm}}{174 \text{ mm}} - (57 \text{ mm})(1.75x10^{-4} \text{ mm}^{-1}) = 0.029$$

The predicted extreme fiber concrete strain is 0.021.

Prestressing Steel Strain

The increase in tendon strain as a function of drift predicted by the analytical model is shown in Figure 4.66. The predicted strain increase is higher than the observed. At low drifts, the error is on the order of 100%, while at high drifts the strain increase is over-predicted by approximately 50%. The lower than predicted observed strain increase implies larger neutral axis depths for the given drift levels. As was stated for the first test of specimen JH1, the neutral axis depth may be under-predicted by the Mander model since it predicts higher confined concrete compressive strengths than what may be appropriate for high strength concrete. This would result in over-prediction of the tendon strain increase (see Eq. 2.16).
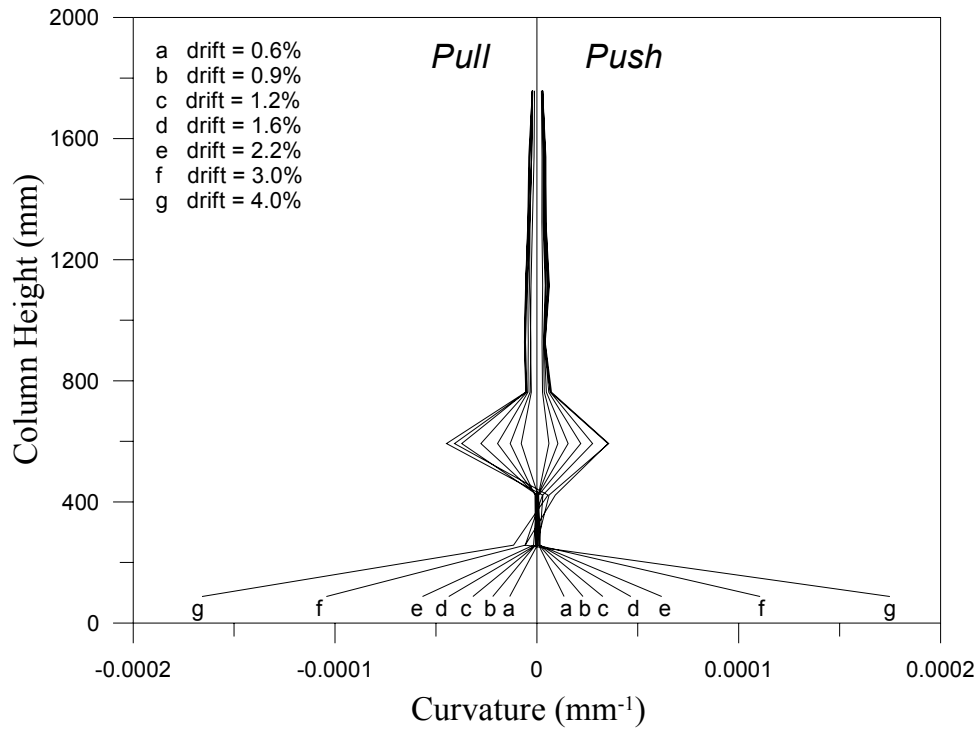
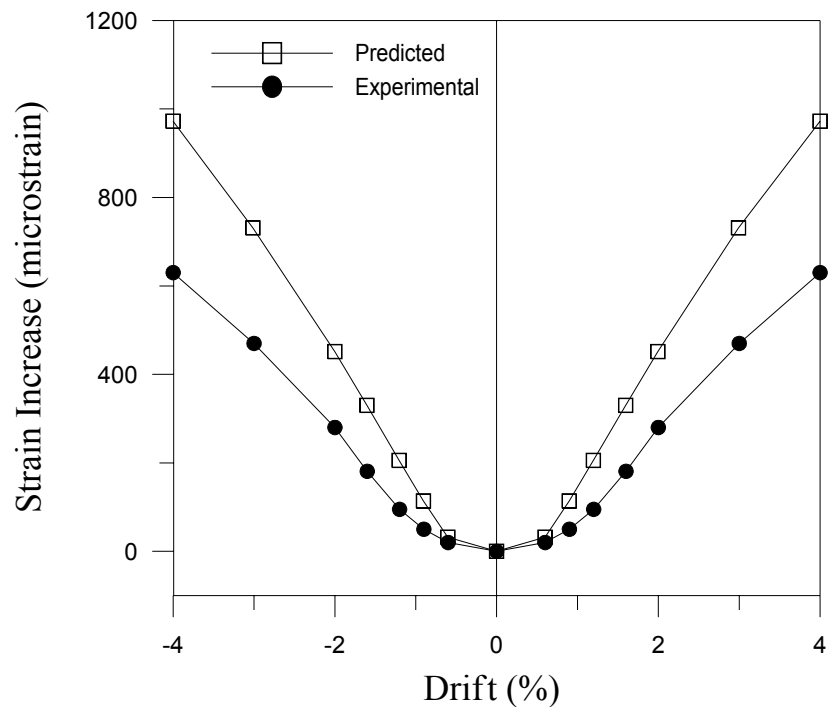Figure 4.65 JH2 – Test 1 Curvature along column height

Figure 4.66 JH2 – Test 1 Predicted and experimental tendon strain increase

Steel Jacket Strain

Hoop strains in the steel jacket at the north and south generators are shown in Figures 4.67 and 4.68, respectively. Note that the strain gage mounted near the top of the jacket at the north generator did not function during the test. The hoop strain at the jacket toe was approximately equal to the yield strain for a drift of 2.0%. At 3.0% drift, the hoop strain near the base was several times yield, while at 4.0% drift the jacket was strained to approximately 10 times the yield strain of the material. The large jacket hoop strains near the base are due to the large concrete compression strains and associated dilation of the concrete at the compression toe of the column. Yielding occurred as high as mid-height of the segment at 4.0% drift.

Figures 4.69 and 4.70 illustrate hoop strain profiles for the east and west generators. At the west generator, the gage mounted at mid-height of the jacket did not function during testing and was not used to construct the strain profiles. The maximum hoop strain occurred near the base for the east generator and was approximately 1800 $\mu\varepsilon$. The strains increase down the jacket height due to the confining effect of the jacket on the core concrete at the compression generators. At the west generator, the maximum hoop strain was observed at the gage located 140 mm above the bottom of the jacket and was approximately 2600 $\mu\varepsilon$.

The vertical strain profiles for the north and south sides of the jacket are displayed in Figures 4.71 and 4.72, respectively. The vertical strains are relatively small except for drifts of 3.0% and 4.0%. Strain profiles are shown for all three cycles at the 4.0% drift level. The vertical strains at mid-height of the north side of the jacket continued to increase significantly for each cycle at 4.0%. The high strains mark the beginning local buckling of the jacket: during the second test of specimen JH2 (results given later in this chapter), a significant bulge in the jacket at mid-height of the column was observed at a drift of 3.0%. Large vertical compressive strains also occurred at the south generator near the base of the jacket.

Transverse Spiral Strain

The hoop strain profiles for the transverse spiral are shown in Figures 4.73 – 4.76. The strains at the north and south generators increase down the height of the column since the tendency for concrete dilation increases down the column height with increasing moment. The maximum strain occurred at the south generator near the base of the second column segment at 4.0% drift and was 950 $\mu\varepsilon$. The observed strains were well below the material yield strain of 2200 $\mu\varepsilon$. Shear induced strains in the spiral reinforcement measured at the east and west generators were small for all drifts.
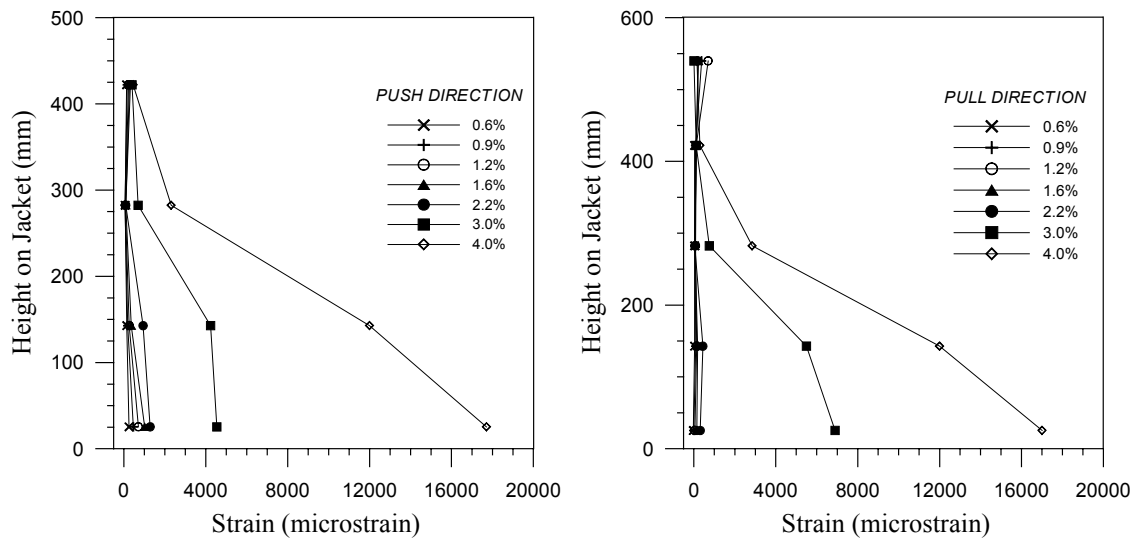
Figure 4.67 JH2 – Test 1 Jacket hoop strain at north generator
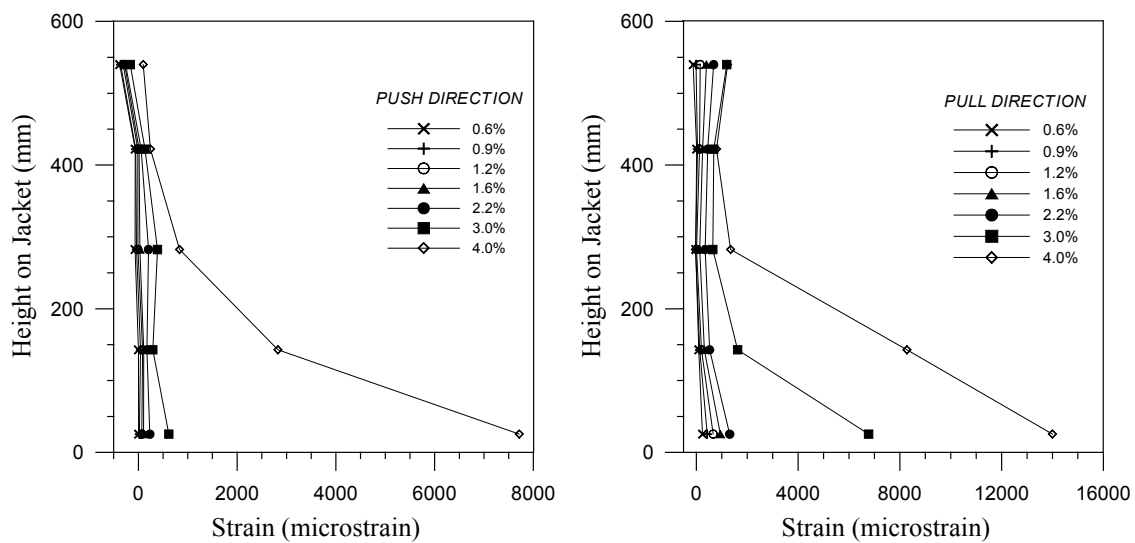
Figure 4.68 JH2 – Test 1 Jacket hoop strain at south generator
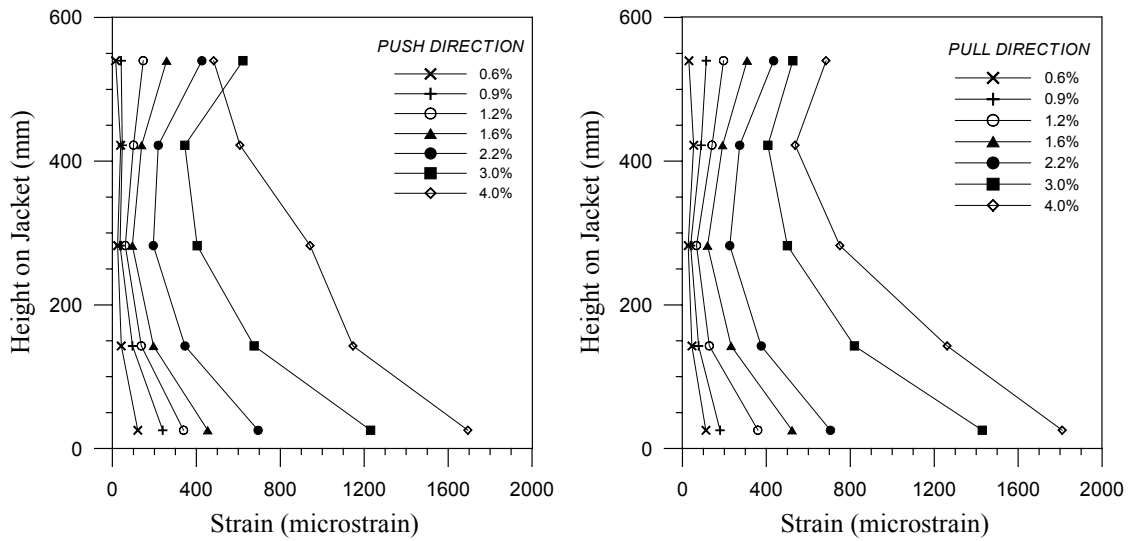
Figure 4.69 JH2 – Test 1 Jacket hoop strain at east generator
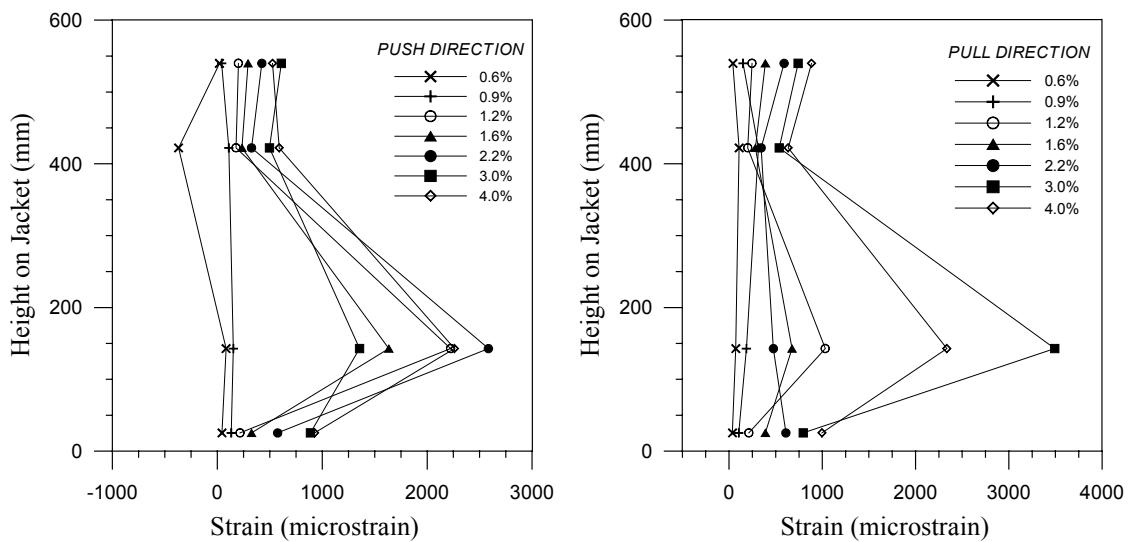
Figure 4.70 JH2 – Test 1 Jacket hoop strain at west generator
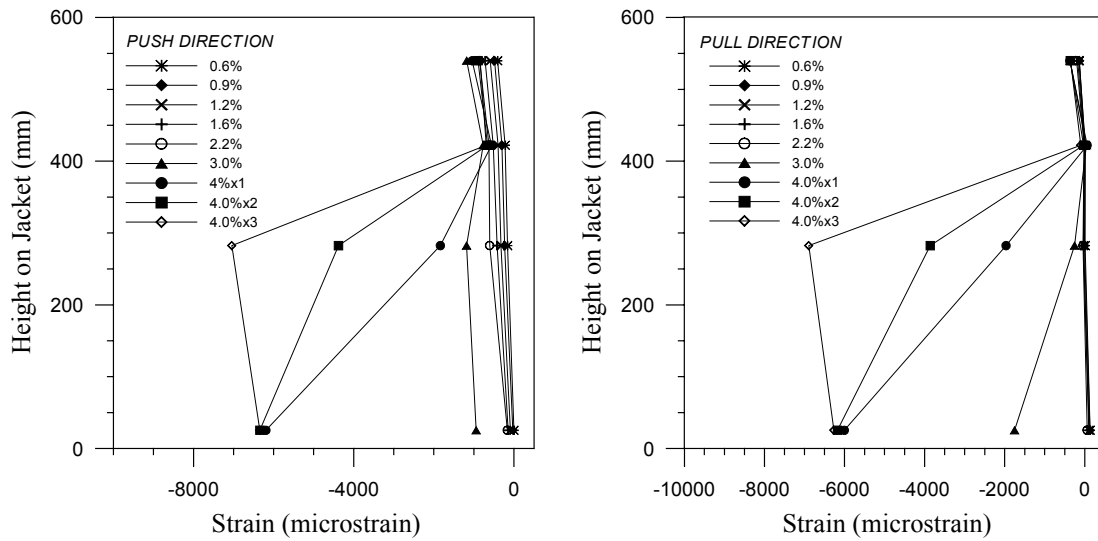
Figure 4.71 JH2 – Test 1 Jacket vertical strain at north generator
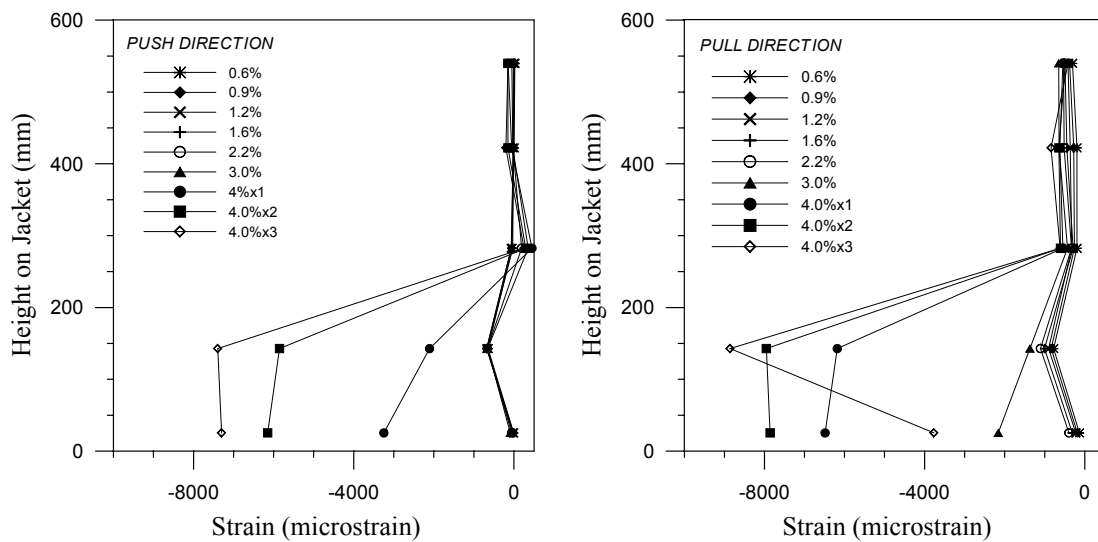
Figure 4.72 JH2 – Test 1 Jacket vertical strain at south generator
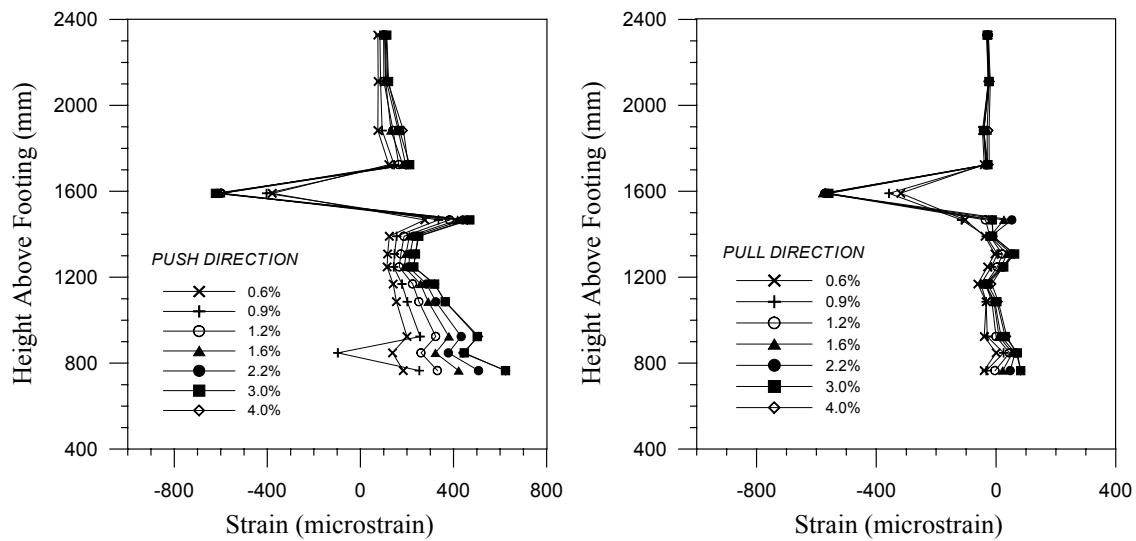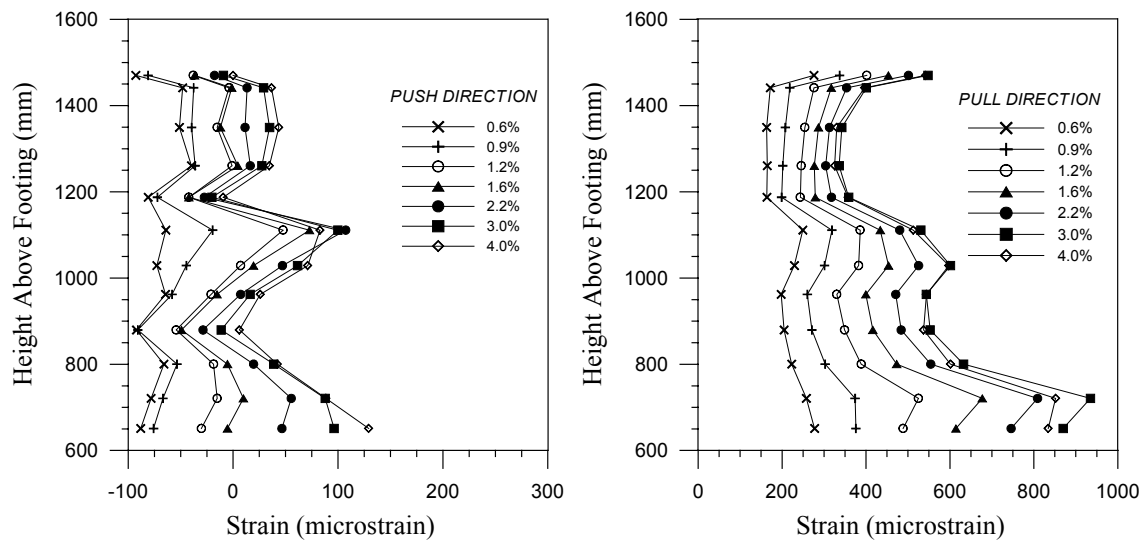
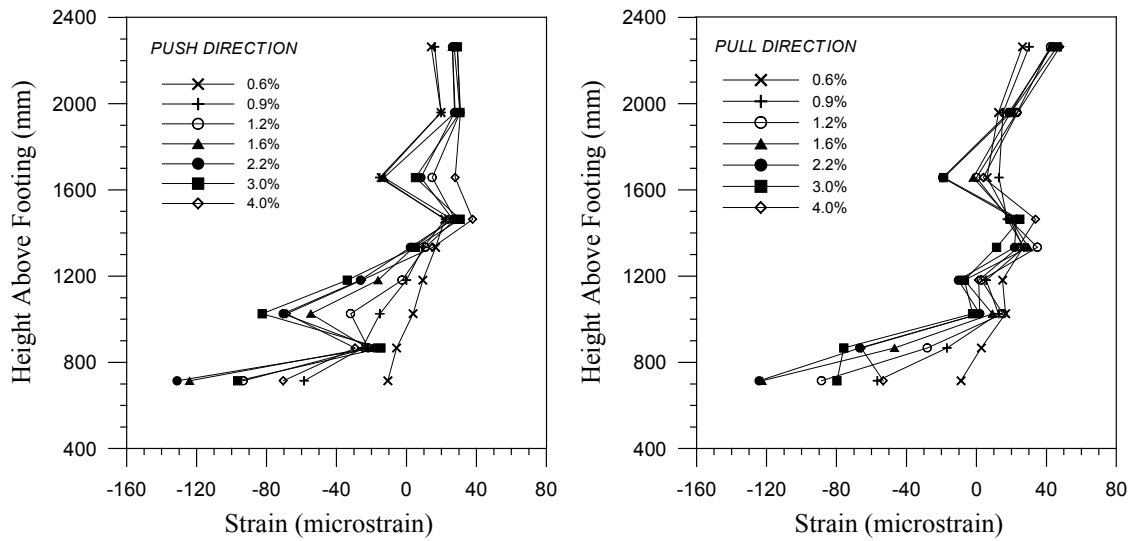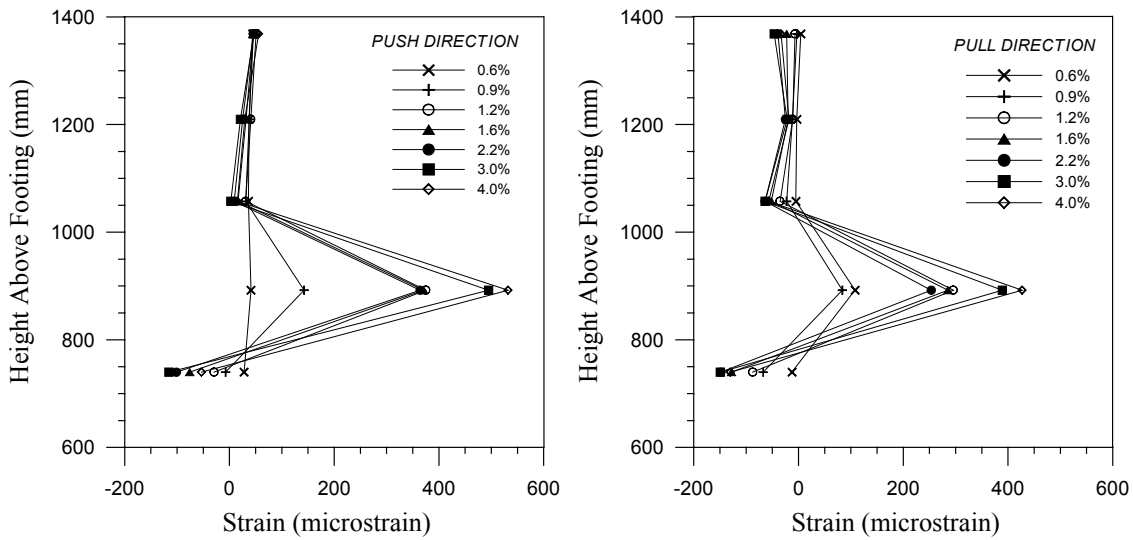Figure 4.73 JH2 – Test 1 Spiral strain at north generator

Figure 4.74 JH2 – Test 1 Spiral strain at south generator

Figure 4.75 JH2 – Test 1 Spiral strain at east generator

Figure 4.76 JH2 – Test 1 Spiral strain at west generator

4.8 Experimental Results – Specimen JH2-T2

4.8.1 Observations under Repeated Cyclic Loading

A description of the behavior of specimen JH2 during the second test is given along with some supporting photographic illustrations. The planned loading sequence called for one cycle each to be performed in force control at one-half, one, and one-and-a-half times the theoretical force to cause decompression at the critical section (P_1). After switching to displacement control, three cycles were to then be performed at twice the decompression force. The displacement predicted for the next target level of **2 x P_1** was reached before the force of **1.5 x P_1.** Thus, the test was switched to displacement control of the actuator after the first cycle at the given displacement.

±0.5 P_1 (P_{max}= 37.5 kN and P_{min}= -38.3 kN)
No cracking was observed.

±P_1 (P_{max}= 75.4 kN and P_{min}= -76.1 kN)
Flexural cracking was observed at the base of the column, where the depth to the neutral axis from the extreme compression fiber was around 450 mm.

3 cycles at 0.45% (P_{max}= 101.6 kN and P_{min}= -93.7 kN)
The neutral axis depth at the base of the column was approximately 400 mm from the compression edge. The width of the base crack was around 1 mm.

3 cycles at 0.6% drift (P_{max}= 122.5 kN and P_{min}= -111.4 kN)
The neutral axis depth decreased to 360 mm. No new cracks were noted.

3 cycles at 0.9% drift (P_{max}= 154.2 kN and P_{min}= -137.6 kN)
The crack at the base of the column extended to approximately mid-depth of the section and the width increased to 2 mm. Cracking in the second column segment at locations of

113

previous cracks (from the first test) was observed. The cracks were visible at the gaps between the fiberglass bands.

3 cycles at 1.2% drift (P_{max}= 173.3 kN and P_{min}= -154.9 kN)

Continued flexural cracking in the second column segment was observed. Some new cracks were observed at the gaps between the fiberglass bands.

3 cycles at 1.6% drift (P_{max}= 188.2 kN and P_{min}= -172.7 kN)

The distance to the neutral axis from the compression edge at the column base was around 250 mm. The width of the base crack increased to 4 mm. Minor extension of existing cracks was observed.

3 cycles at 2.2% drift (P_{max}= 195.4 kN and P_{min}= -189.0 kN)

The neutral axis depth decreased to approximately 225 mm and the base crack width, as measured at the extreme tension fiber, increased to 6 mm. Cracking was observed at several of the crack locations from the first test.

3 cycles at 3.0% drift (P_{max}= 189.8 kN and P_{min}= -190.8 kN)

The base crack widened to around 11 mm and the neutral axis depth decreased to just under 200 mm. A significant "bulge" in the steel jacket was observed at the north side of the column at a height of about 300 mm above the footing. It appeared as if the jacket had buckled outward from the core concrete. The buckled area was approximately 125 mm in height. The epoxy at the compression toe below the jacket appeared to be in good condition with no deformation or crushing observed.

3 cycles at 4.0% drift (P_{max}= 177.4 kN and P_{min}= -185.4 kN)

The bulge at the north generator was more significant for the first push loading. The bottom of the jacket was also noticeably "belled" due to the large hoop straining caused by dilation of the core concrete at the compression toe. Lift-off of the column base from the footing at the extreme tension edge was about 19 mm at this drift level. The gap

between the bottom of the jacket and top of the footing decreased slightly to around 22mm due to jacket slippage and rotation of the segment (the gap prior to testing was 28 mm).

3 cycles at 5.0% drift (P_{max}= 164.5 kN and P_{min}= -174.1 kN)

The crack at the footing level increased to 25 mm, as measured at the extreme tension edge. Horizontal translation of the column base with respect to the footing in the amount of 5 – 6 mm was noted at this drift. The translation was towards the north, or in the direction of the column shear for the push direction. The gap width between the jacket toe and footing decreased to approximately 18 mm

Test End

A photo of steel jacket at the north generator taken after testing is shown in Figure 4.77. A bulge at mid-height of the jacket is visible. The lower half of the jacket is noticeably 'belled' due to the severe hoop straining at the critical section. The residual drift of the column at the end of the test was on the order of 0.7%. Part of this was due to the translation of the column base with respect to the footing noted above. As was the case for the first test, significant damage was observed below the jacket due to the high longitudinal compressive strains at the compression toe of the column. No damage was observed in the column segments above the steel jacket other than the minor flexural cracks detailed above. No inclination of cracks was observed, and all cracks – except for the crack at the base of the column – closed completely once the lateral force was removed from the column. A residual crack at the column base existed at each loading generator due to the deformed epoxy and crushed concrete. As noted, significant deformation of the steel jacket was observed for cycles at high drift levels. The prestressing steel did not fracture during testing.

Figure 4.77 JH2 – Test 2 Bulge in steel jacket at north generator after testing

4.8.2 Force – Displacement Response

The second test lateral force-displacement response of specimen JH2 is shown in Figure 4.78. Stable hysteretic response was observed during the test, up to the maximum imposed drift of 5.0%. Approximately equal strengths were achieved for the two loading directions. Significant non-linear response initiated at around 170 kN. This force level corresponds to approximately 2.4 x P_1. The maximum column strengths were 195.4 kN and −190.8 kN for the push and pull directions, respectively. The maximum strength for the push direction occurred at a drift of 2.2%, while that for the pull direction was observed at 3.0% drift. At a drift of 5.0%, the column strength had decreased to 16% and 8 % of the maximum achieved strength for the push and pull directions, respectively.
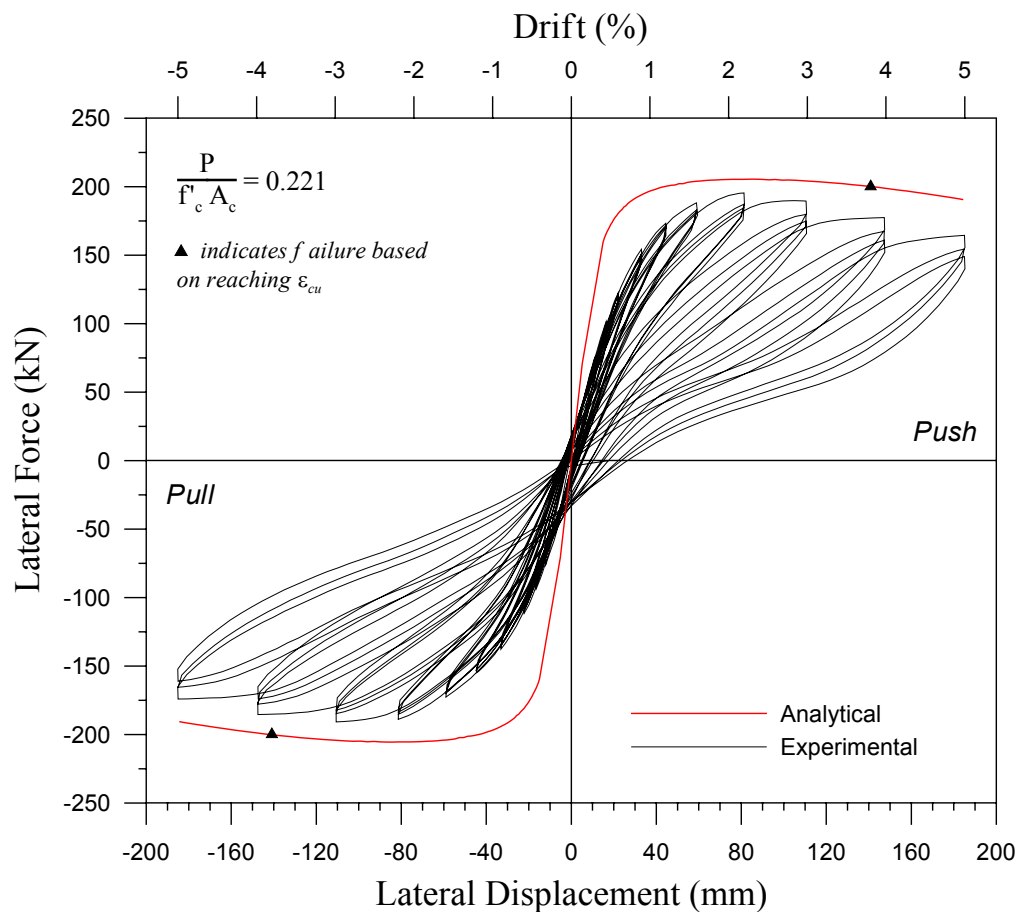
Figure 4.78 JH2 – Test 2 Force-displacement response

The predicted force-displacement response envelope based on the analytical model is shown in Figure 4.78 along with the experimental hysteresis curve. Both the initial stiffness and column strength are over-predicted. The error in the analytical curve is approximately 6% at 2.2% drift, and increases to 16% and the maximum imposed drift of 5.0%. This may be because the column was subjected to relatively high drifts during the first test, with the effect of causing significant damage to the core concrete within the steel jacket. Since the concrete was encased by the jacket and thus concealed, it was not possible to determine the extent of the damage or repair it prior to the second test. The repair measures taken may not have been sufficient to restore the structural integrity of the column. In addition, the possible over-estimation of concrete strength and ductility by the Mander model for the high strength concrete may contribute to the error. Considering the above, the difference between the observed and predicted column strength is reasonable. The predicted failure of the test unit is also shown on the analytical curve. As was noted for unit JH1, the value of ultimate concrete strain given by Eq. 2.29 is typically conservative by 50%. It is thus expected that the unit posses significant displacement capacity after the predicted failure point.

The initial loading stiffness of the specimen for both the first and second test is shown as a function of the imposed drift level in Figure 4.79. It can be seen that the stiffness was restored to 65% of the original value observed for test 1 after repairing the damage above and below the jacket and restressing to the higher force level. The degree of stiffness degradation from one drift level to the next for the second test was similar to that observed for the first. At the maximum drift of 5.0%, the loading stiffness was only 10% of the original stiffness observed at the decompression force during the first test. Considering the hysteretic response in Figure 4.78, it is seen that the initial loading stiffness of the column for high drift levels was equal to the effective column stiffness, K_{eff}, at maximum drift. Thus, the response was no longer bilinear elastic, but rather linear with stiffness equal to the effective stiffness.

Figure 4.80 shows the equivalent hysteretic damping calculated for both the first and second tests. As was observed for the first test, the damping increased with increasing drift. On average, the hysteretic damping was higher for the first test than the second was. The slight difference may be due to the extra energy dissipated during the first test by crushing of the concrete below the jacket toe and the spalling of the cover concrete at the base of the second column segment. The difference between the tests is rather small however, and an average of the two curves could be taken to represent the damping versus drift relationship.

4.8.3   Test Data

Column Curvature

The curvature distribution along the height of the column for the second test of specimen JH2 is shown in Figure 4.81. The curvatures shown are higher than those observed for the first test because of the higher total vertical force acting at the critical section. The largest curvatures occurred at the base of the column and at the interface between the jacketed segment and second column segment. The measured curvatures within the height of the jacket were small, as were those observed above the bottom of the second column segment. The maximum curvature at the column base was observed at a drift of 5.0% and was $2.7x10^{-4}$ mm^{-1} for the push direction and $2.5x10^{-4}$ mm^{-1} for the pull direction of loading. The associated concrete longitudinal compression strain is:

$$\varepsilon_c = \frac{12.4 \text{ mm}}{173 \text{ mm}} - (60 \text{ mm})(2.7x10^{-4} \text{ mm}^{-1}) = 0.057$$

The values used in the above calculation were observed for the push direction of loading. A calculation for the pull direction of loading gave an extreme concrete strain at of 0.049. The predicted strain from the moment-curvature analysis is 0.03, somewhat lower than the experimental values given above.
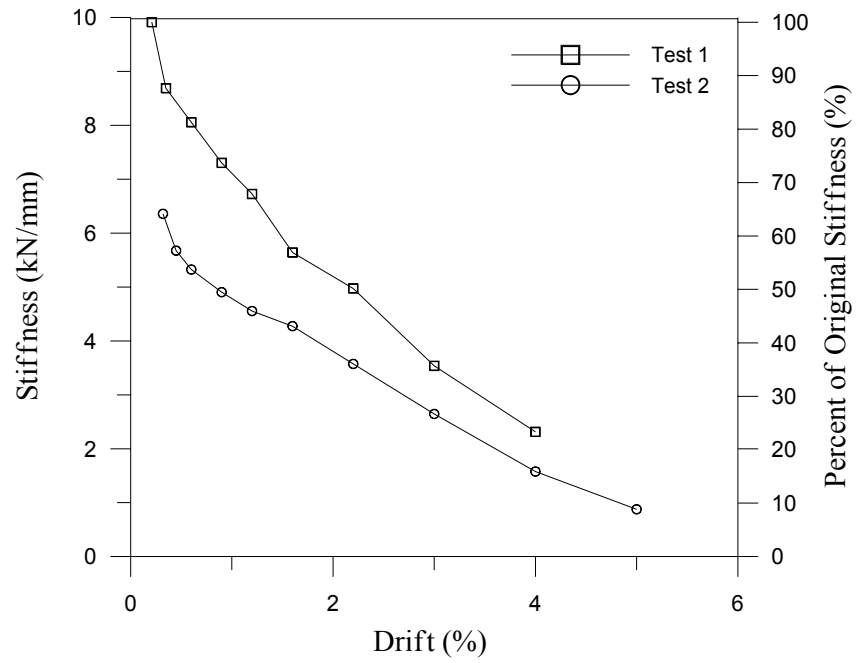
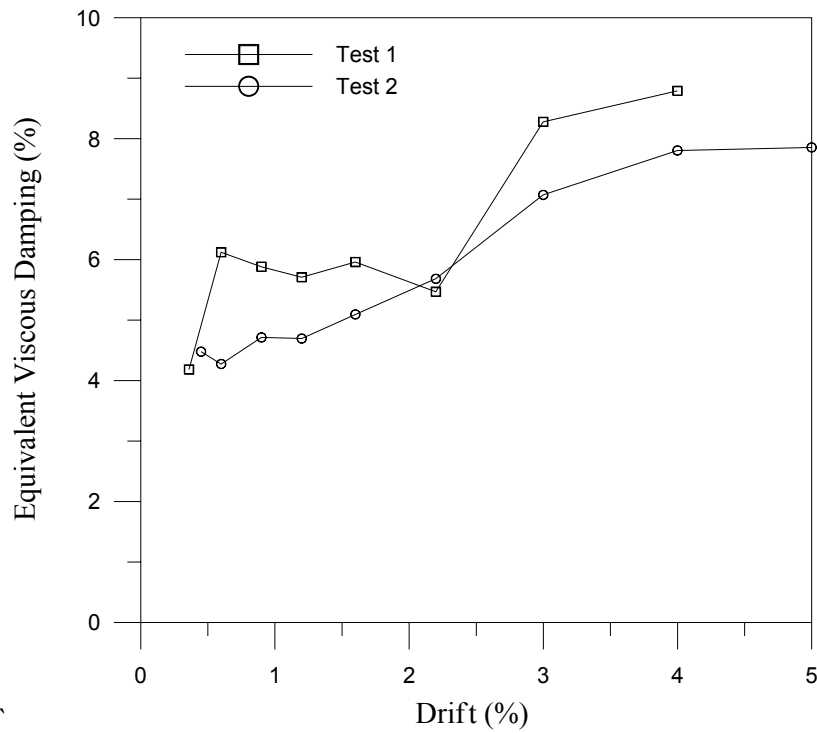Figure 4.79 JH2 – Test 2 Initial loading stiffness versus drift

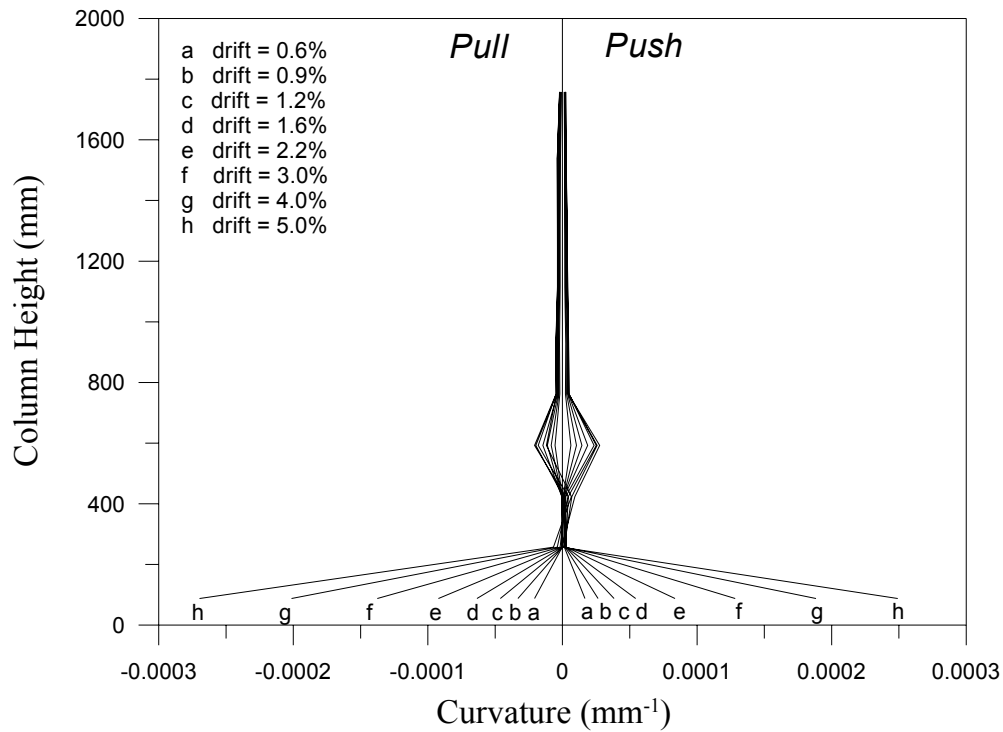Figure 4.80 JH2 – Test 2 Equivalent viscous damping

120

Figure 4.81 JH2 – Test 2 Curvature along column height

Prestressing Steel Strain

The predicted prestressing steel strain increase is shown in Figure 4.82 along with the experimental results. As can be seen, the strain increase was over-predicted by a substantial amount. This implies that the neutral axis depth from the compression edge was under-predicted. This is explained by the same reasoning given in Section 4.5.3 for specimen JH1. In addition, if the core concrete within the steel jacket was damaged significantly during the first test, the epoxy grouting of the base crack probably did not restore the concrete to its original undamaged condition. If the strength and integrity of the core concrete was not good for the second test, the analytical model cannot be expected to predict with much accuracy the increase of tendon strain.

Steel Jacket Strain

Hoop strains at the north and south generator are shown in Figures 4.83 and 4.84, respectively. Hoop straining at the jacket toe was extreme due to the dilation of the

121

concrete at the compression toe caused by high longitudinal compression strains. At the north generator, the maximum strains occurred at approximately mid-height of the jacket. However, the readings from the gage at mid-height are believed to be inaccurate due to gage instability. It can be seen that the gage mounted near the bottom of the jacket at the south generator showed little variation in strain and indicated strains lower those at the north generator. Strains at the east and west generators are shown in Figures 4.85 and 4.86, respectively. The maximum hoop strains occurred at the jacket toe for both the east and west sides. The reason for the compressive strains indicated at jacket mid-height at the east generator is not known. The strains near the bottom of the jacket are significantly higher at the west generator, with a maximum strain of approximately 16,000 $\mu\varepsilon$. It is difficult to explain the complex patterns of strain shown for the north, south, east and west locations. When gages on opposite sides of the jacket show significantly different readings, it is difficult to know which gage better represents the actual physical behavior. From the strain profiles shown, it can be said however that very high strains were induced in the jacket at high drifts.

The vertical strain distributions along the height of the jacket at the north and south sides of the column are shown in Figures 4.87 and 4.88. At the north generator, high compression strains occurred at mid-height of the jacket. This location coincides with the area where outward buckling of the jacket was observed. High compression strains can also be seen at mid-height at the south generator. The vertical strains caused by bending of the segment increase significantly at higher drifts since transfer of stresses from the core concrete to the jacket is enhanced by concrete dilation at the compression toe.

Transverse Spiral Strains

Strain profiles for the spiral reinforcement are displayed in Figures 4.89 – 4.92. The strains at the north, south, east and west generators are small in general. A trend of increasing strain down the height of the column can be seen for the north and south sides. This is due to the increasing effect of the confinement action of the spiral on the core concrete down the column height. The maximum hoop strains occurred near the base of

the second column segment and were on the order of 300 – 500 με. Shear strains at the east and west sides of the column were negligible.

Fiberglass Jacket Strain

Fiberglass jacket hoop strain profiles are shown in Figures 4.93 and 4.94 for the north and south sides of the column, respectively. At the north generator, the strains are higher for the push direction while at the south generator, they are higher for the pull direction. At the north side, the maximum hoop strain occurred just above the top of the steel jacket and was approximately 850 με. The maximum strain for the south generator was approximately 550με. Hoop strains in the fiberglass jacket indicate that the jacket was "activated" by dilation of concrete in segment two and that it was providing confinement to the concrete.
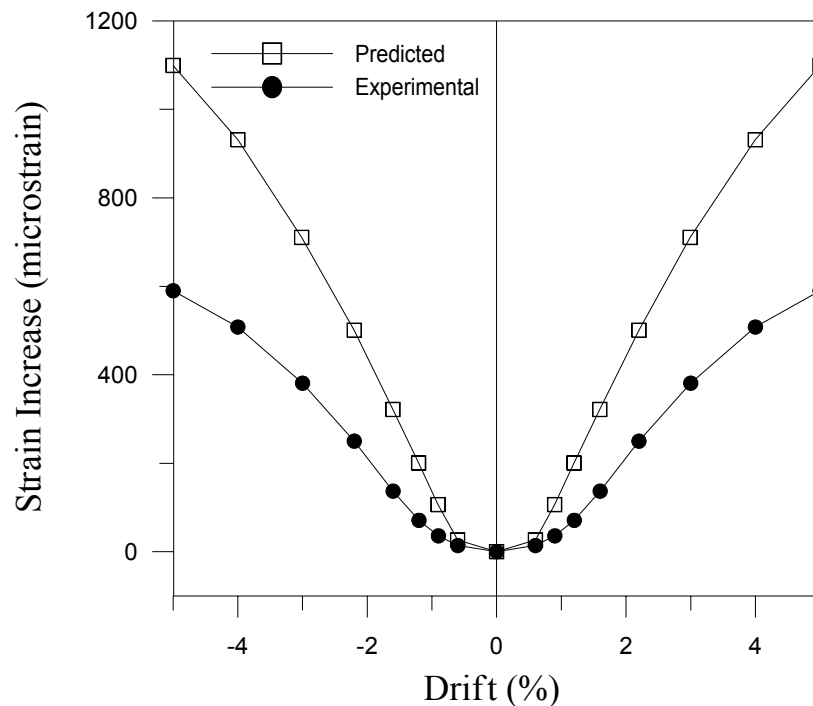
Figure 4.82 JH2 – Test 2 Predicted and experimental tendon strain increase
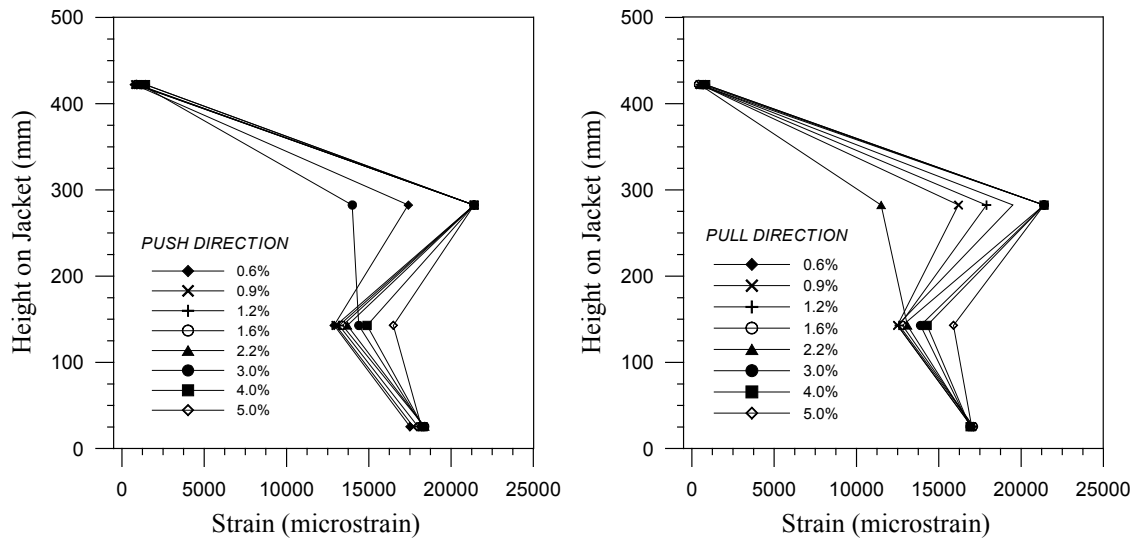
Figure 4.83 JH2 – Test 2 Jacket hoop strain at north generator
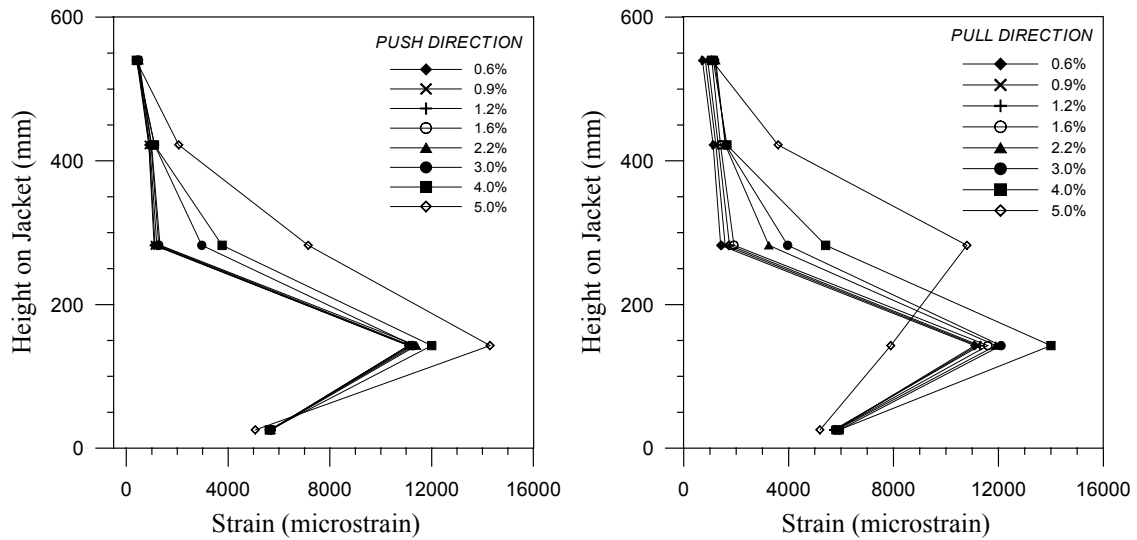
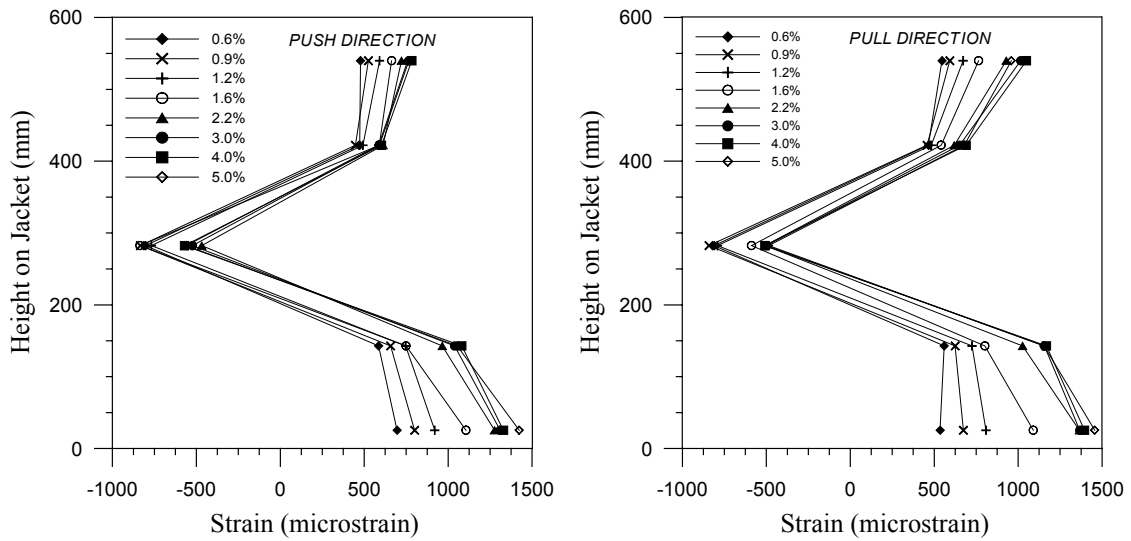Figure 4.84 JH2 – Test 2 Jacket spiral strain at south generator

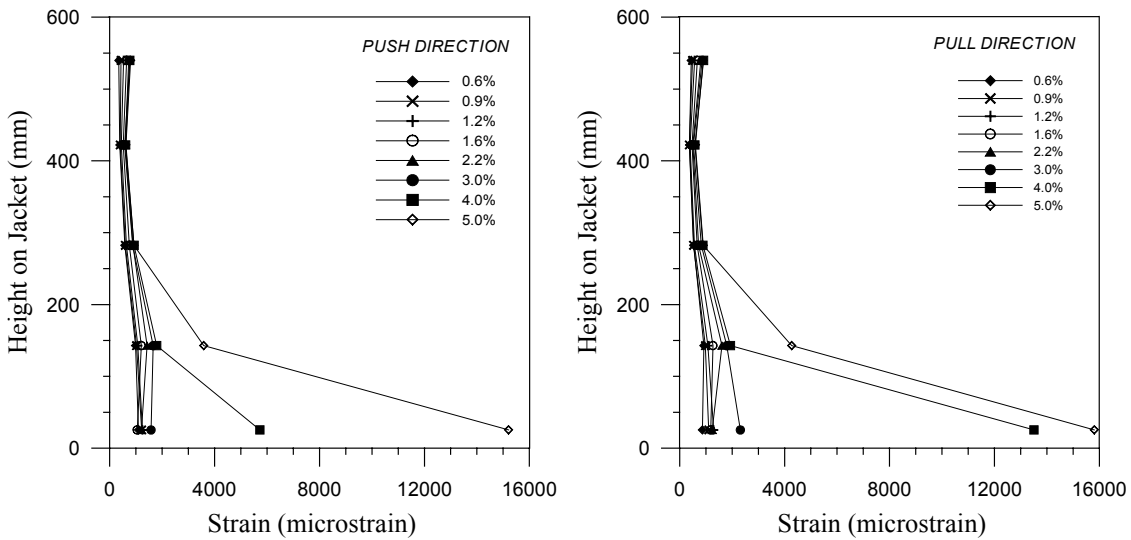Figure 4.85 JH2 – Test 2 Jacket hoop strain at east generator

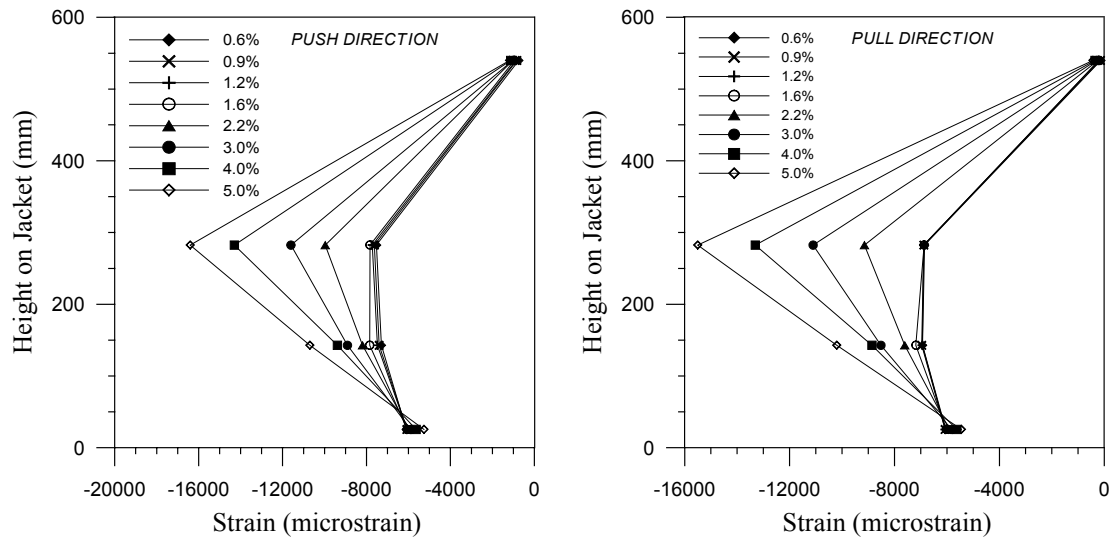Figure 4.86 JH2 – Test 2 Jacket hoop strain at west generator

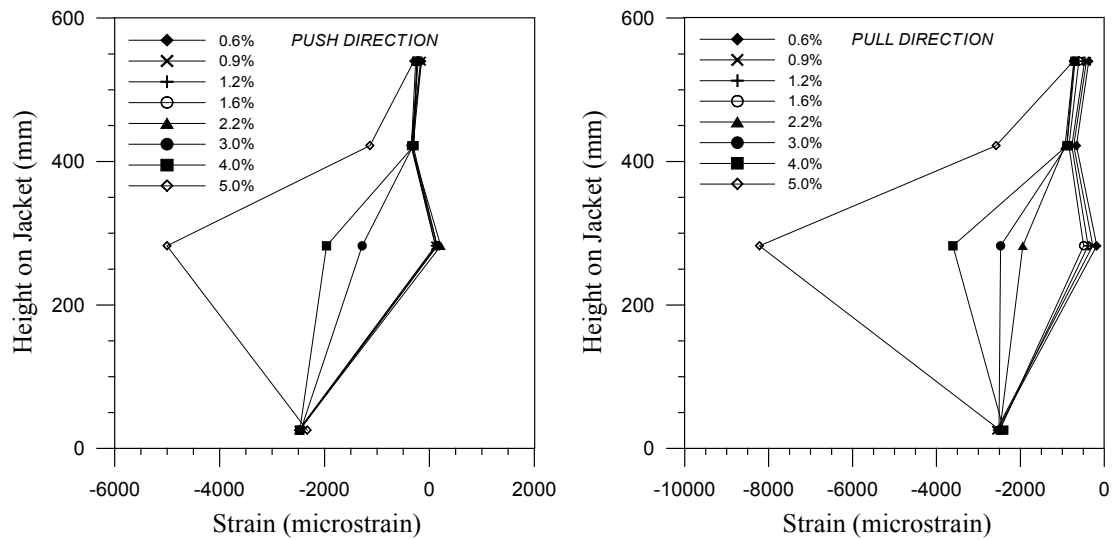Figure 4.87 JH2 – Test 2 Jacket vertical strain at north generator

Figure 4.88 JH2 – Test 2 Jacket vertical strain at south generator
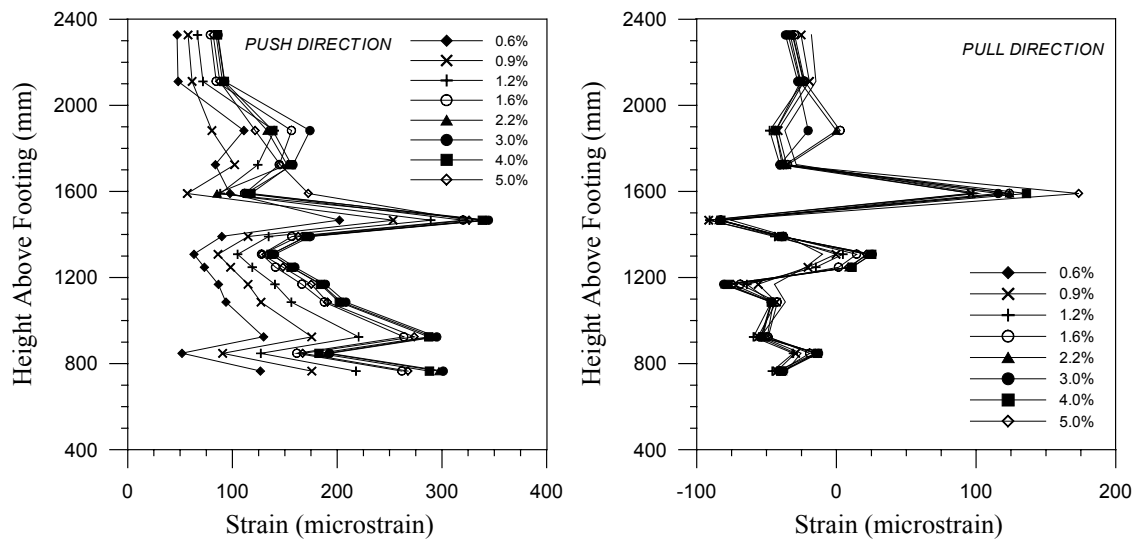
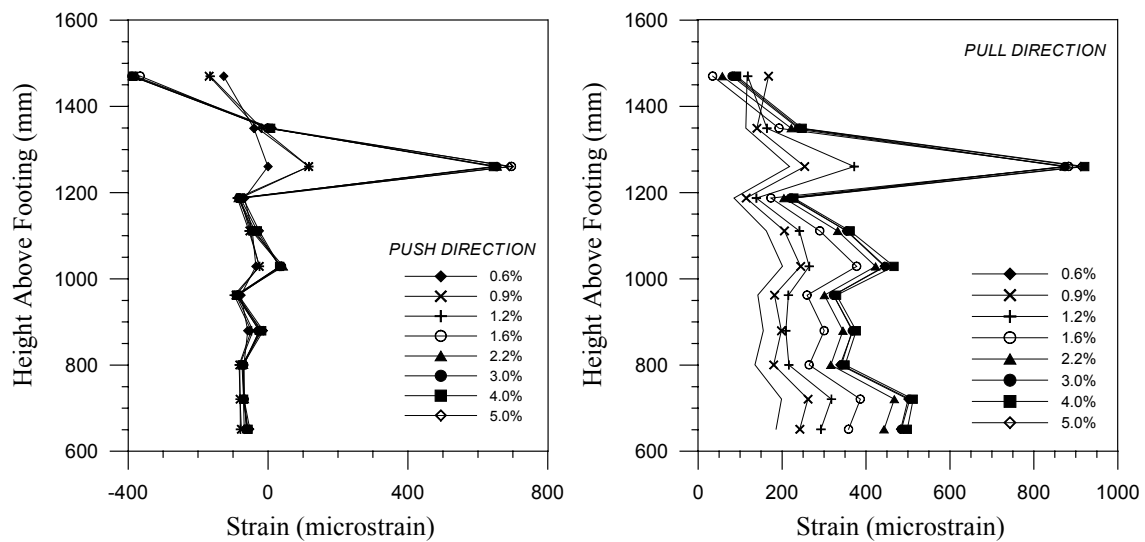Figure 4.89 JH2 – Test 2 Spiral strain at north generator

Figure 4.90 JH2 – Test 2 Spiral strain at south generator
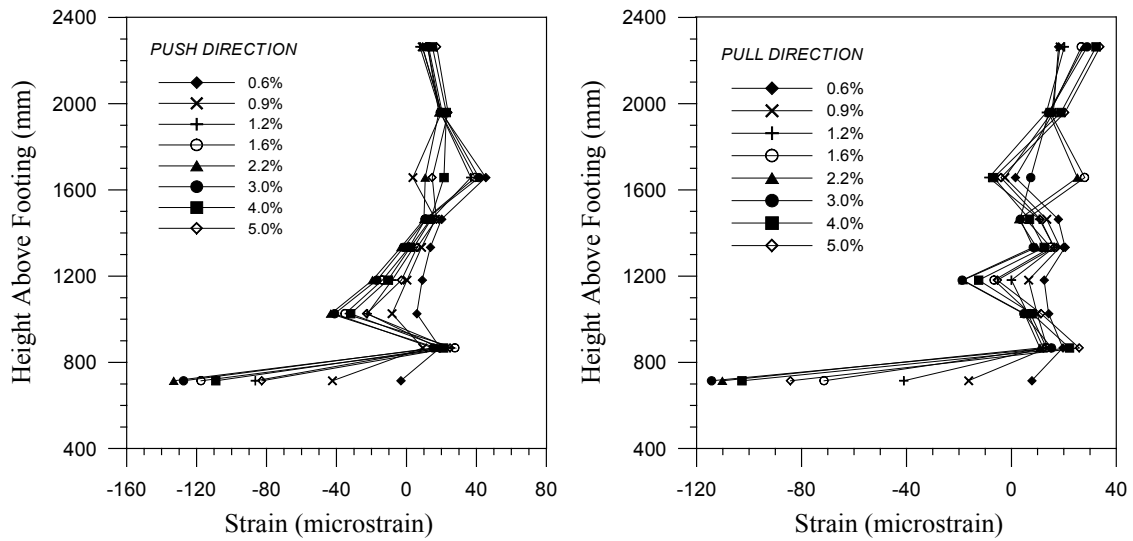
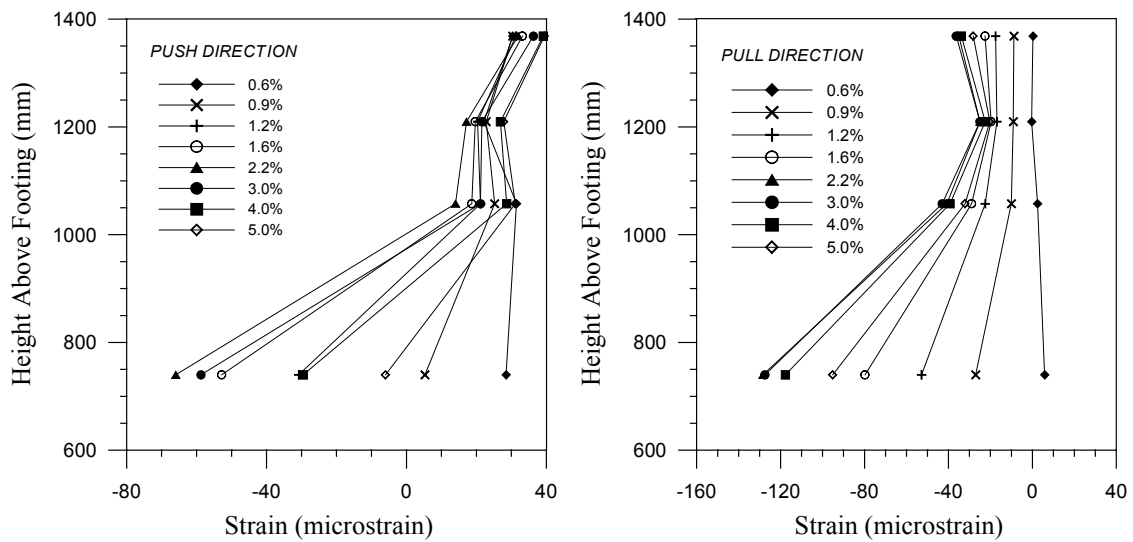Figure 4.91 JH2 – Test 2 Spiral strain at east generator

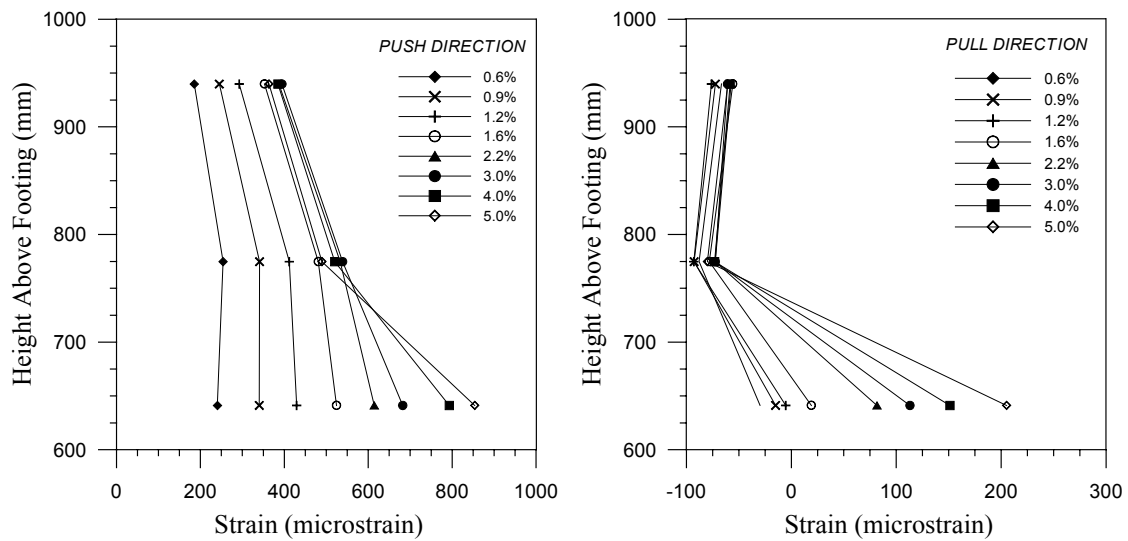Figure 4.92 JH2 – Test 2 Spiral strain at west generator

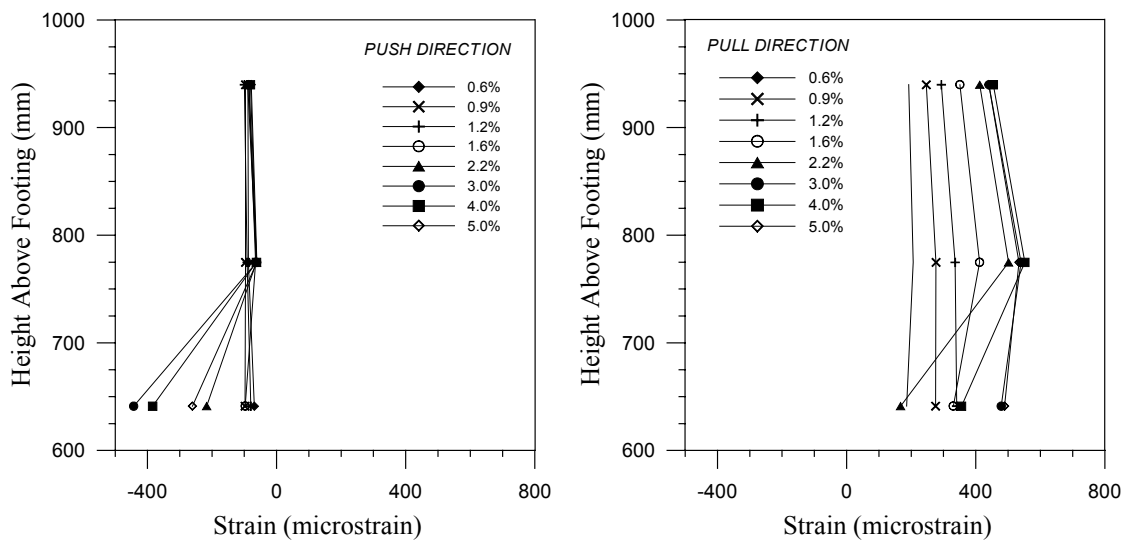Figure 4.93 JH2 – Test 2 Fiberglass jacket hoop strain at north generator

Figure 4.94 JH2 – Test 2 Fiberglass jacket strain at south generator

4.9   Discussion of Results

The seismic design and experimental testing of two high aspect ratio precast segmental bridge columns were presented in this chapter. The prestressing steel was unbonded to the concrete along the full height of the column. Each unit was tested once, with a given total prestress force in the tendon. After the first test, both test units were repaired by epoxy grouting the base crack, reinstating spalled cover concrete, and by wrapping the region above the steel jacket in a fiberglass jacket. The units were then restressed to a higher tendon force level and tested a second time. Column JH1 used a jacket thickness approximately twice that used in specimen JH2. A comparison of the performance for the first and second test of each unit is given in this section. A comparison between the performance of the units is also given.

The force-displacement response for the first and second test of unit JH1 are shown in Figure 4.95. While the total prestress force for the second test was approximately 22% higher than that for the first test, the maximum observed strength was only about 14% higher than the strength for the first test. It should be noted that despite the higher prestress force, the axial load ratio was actually lower for the second test since the concrete continued to gain strength during the time between the first and second tests. The experimental response for the two tests of unit JH2 are shown in Figure 4.96. The prestress force for the second test was about 21% higher than that for the first test, but the maximum observed second test strength was actually 5% less than that for the first. It is believed that the damage to the core concrete within the steel jacket was significant for the first test and thus adversely affected the second test performance of JH2. Confinement of the core concrete by the steel jacket near the column base may have been compromised for the second test due to the large inelastic hoop straining of the jacket observed for the first test.
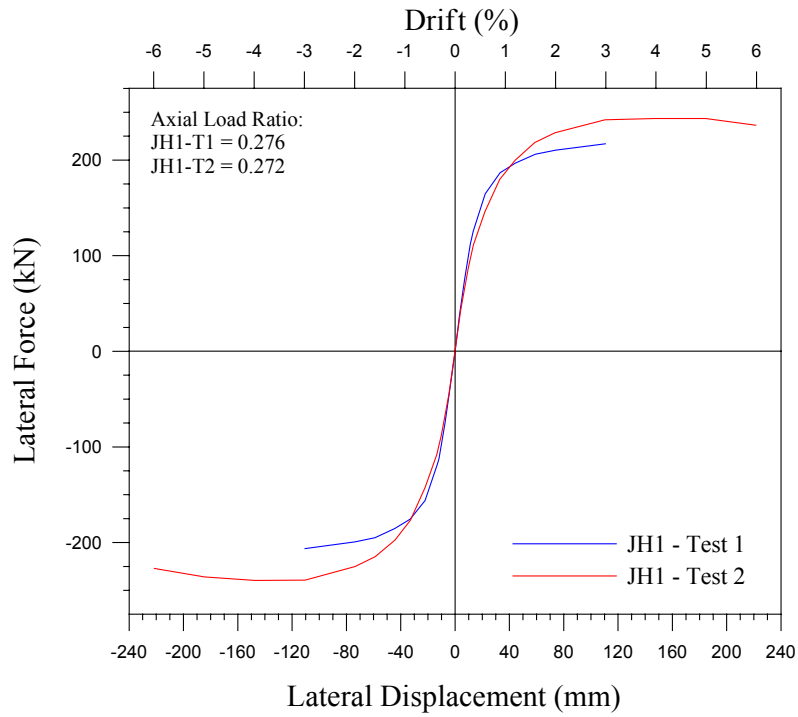
Figure 4.95 JH1 - Test 1 and 2 force-displacement response comparison
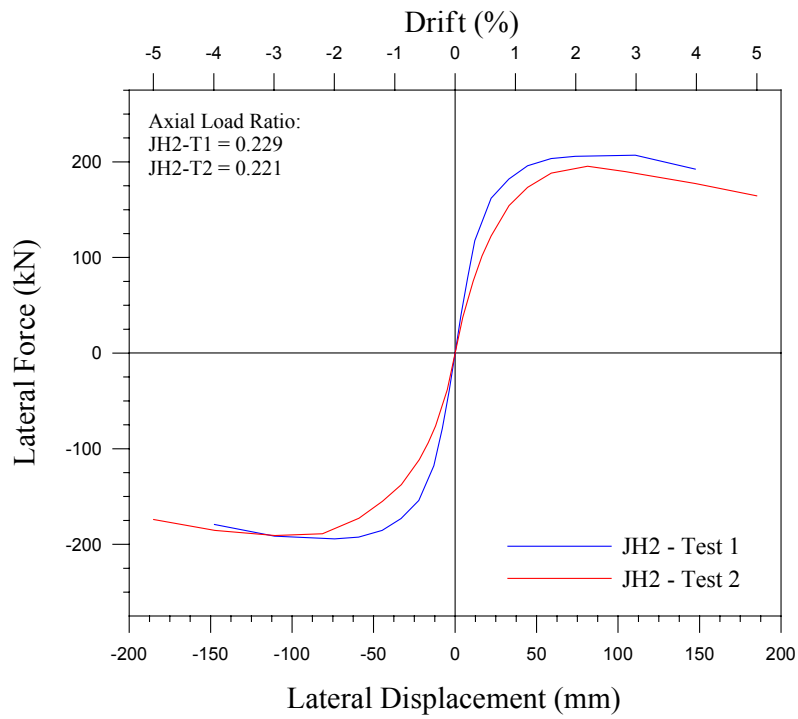

Figure 4.96 JH2 Test 1 and 2 force-displacement response comparison

A comparison between the performance of JH1 and JH2 for the first and second tests is given in Figures 4.97 and 4.98, respectively. It can be seen that for the first test, the force-displacement response of each unit is similar. The column strengths matched almost exactly up to approximately 2% drift. At 3.0% drift, the strength of JH1 was only slightly higher than that of JH2. This indicates that for moderate drift levels, variations in the prestress force and jacket thickness do not appreciably affect the strength and ductility of the column. It can be seen however that the strength of unit JH2 began to degrade after the 3.0% drift level. The strength of unit JH1 on the other hand was still increasing at 3.0% drift. For the higher axial load level of the second test, degradation of column strength for JH2 initiated at approximately 2.2% drift, while little drop in capacity was observed for specimen JH1 at the maximum imposed drift of 6.0%. Thus, it may be concluded that the level of confinement provided by the thinner jacket will result in good performance up to drifts of around 3% for axial load ratios around 0.2-0.25. For higher axial load ratios and drift levels, the higher level of confinement provided by the thicker jacket is more appropriate.

In general, the analytical model presented herein correlated reasonably well with the experimentally observed behavior of the columns for each test. In some cases, the predicted strength was higher than the actual column strength. The reasons for discrepancies between analytical and experimental response were explained previously, but are given here again. First, the value for the initial prestress force in each column prior to each test was determined by analyzing data recorded the post-tensioning operation. The prestress force values are however only "best estimates", and there does exist a degree of uncertainty regarding the true or exact prestress force induced in each column for each test. It is believed that errors in the prestress force for a given column and test were at a maximum, 15%. Since additional axial load was applied to model column dead load, the error in the total vertical force acting at the critical section is less than 15%. The small differences in strength could thus be due to small errors in the total vertical force acting on the section.

132

Another source of error in the analytical response could be the use of the Mander Model for confined concrete. As was detailed in Chapter 2, the model may overestimate both the confined concrete strength and ductility of high strength concrete. If this is the case, then predicted column strengths would tend to be higher than actual and the predicted post-elastic stiffness might exhibit a more gradual decrease in strength at high drift levels.

Comment is due regarding the spalling of cover concrete observed at the base of the second column segment during the first test of each specimen. Design of the columns was based on the premise of limiting the damage level to a low amount at design drift levels. Spalling of concrete in the non-jacketed segments was to be avoided. The unexpected spalling observed during testing may be due to the use of the Mander model for confined concrete in the sectional analysis of the non-jacketed segment. Since the model may over-predict concrete strength and ductility for high strength concrete, the calculated moment at first crushing could have been over-estimated. To obtain a better estimate of the section moment capacity at incipient spalling, a stress-strain model developed for high strength concrete should be used in the moment-curvature analysis. Alternatively, the Mander model could be used, but with extra conservatism.

It can be said that the both test units performed well overall. For unit JH1, capacity degradation under increasing cyclic displacements was minimal for both tests, while unit JH2 exhibited some strength degradation at drifts of 4.0% and 5.0% during the second test. Residual drift of the columns was low: for JH1, the residual drift at the end of the second test was approximately 0.2% while that for JH2 was 0.7%. Overall, damage to the columns was low after testing. The spalling of cover concrete above the jacketed segment could have been avoided by extending the steel jacket further up the column height. Test unit JH2 incurred more damage than JH1 due to the thinner jacket and hence lower confinement at the column base. The degree of concrete degradation at the compression toe and the strain levels in the steel jacket were higher for unit JH2.
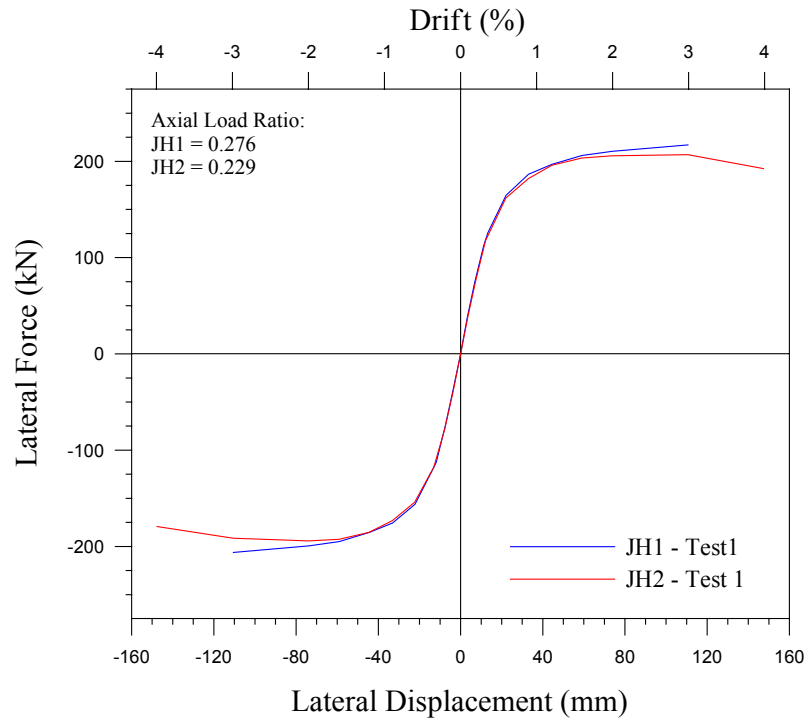
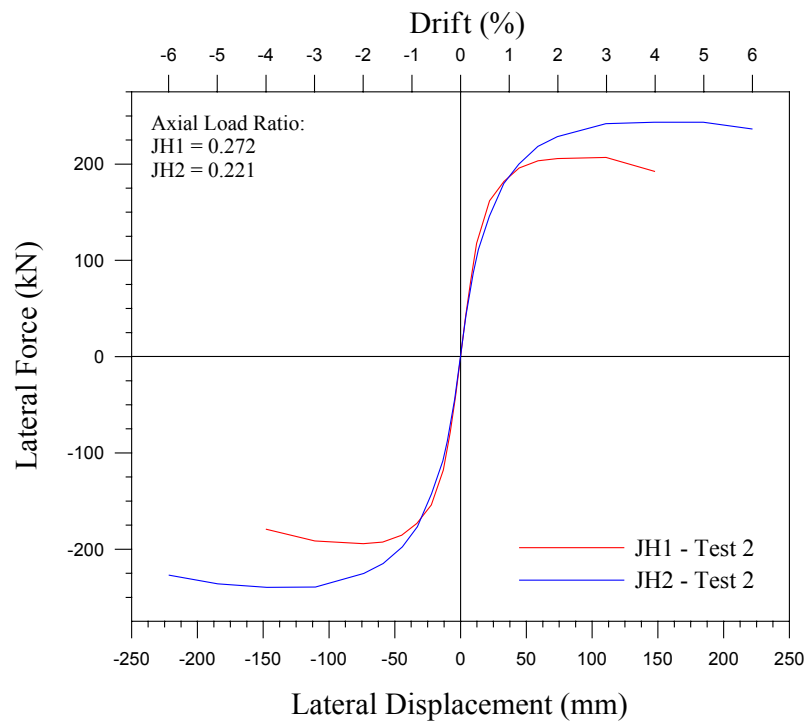Figure 4.97 JH1 and JH2 Test 1 force-displacement response comparison

Figure 4.98 JH1 and JH2 Test 2 force-displacement response comparison

CHAPTER 5 LOW ASPECT RATIO COLUMNS

5.1   Design of Columns

Specimens JH3 and JH4 were one-half the height of JH1 and JH2 and had an aspect ratio **H/D** of three. Each specimen was built using segmental construction and consisted of a precast footing and load stub and two precast 610 mm diameter cylindrical column segments. The overall geometry and reinforcement details of each specimen are shown in Figure 5.1. Selection of the jacket height, jacket material thickness, and initial prestress force was based on studies mentioned previously and on the observed performance of the higher aspect ratio columns tested earlier in the research program and reported in Chapter 4.

The main longitudinal reinforcement in each column consisted of a single unbonded tendon comprised of (27) 12.7 mm diameter ASTM A779 Grade 270 low-relaxation steel prestressing strands with a total cross-sectional area of 2665 mm^2. The upper column segment also contained eight Grade 60 #4 longitudinal bars spaced evenly around the perimeter of the section, with a cover of 25.4 mm. The lower segment of each column was encased in an ASTM A569, A36 steel shell with a wall thickness of 2.8 mm and 6.0 mm for test units JH3 and JH4 respectively. The steel jacket did not extend the full height of the lower segment, but rather terminated approximately 21 mm above the bottom surface.   The upper column segment in both specimens was reinforced transversely with Grade 60 #3 (10mm) bar spiral spaced at 150 mm with a cover of approximately 12 mm. A target initial stress in the tendon of 40% and 60% of the ultimate stress was chosen for the first and second test of each specimen, respectively.

5.2   Construction Procedure

Existing precast footings and load stubs from the first phase of the experimental testing program were used in the construction of test specimens JH3 and JH4. The tendon and anchor head from previous tests were removed from each footing by sliding both out an

access hole located at the underside of the footing. The new tendon and anchor head were installed by the reverse process. This process is depicted in Figure 5.2. The access hole on the underside of each footing was filled with Hydrostone so that the tendon and anchor assembly would not move once the footings were placed in the upright position. After each footing was positioned, Hydrostone was placed under it to provide a level, uniform bearing surface.

The upper and lower column segments were precast individually. The reinforcing cages for the upper segments were tied and positioned on the casting beds along with the steel jackets for the lower segments. Lengths of sonotube were used as the formwork for the upper column segments while the steel jackets served as the forms for the lower segments. Ducts for the prestressing steel were provided at the center of the section of each segment using PVC pipe with inside and outside diameters of 127 mm and 140 mm respectively. The indexing mechanism used to align column segments during the assembly process, described in Section 4.1 for the construction of units JH1 and JH2, was also used for JH3 and JH4.

After the concrete had cured sufficiently, the mating surfaces of the components were cleaned with a wire-brush to remove any loose cement and to roughen the surface. The surfaces were washed with water to remove any remaining cement particles and then were allowed to dry completely. After the components were moved into the laboratory, each specimen was assembled by lowering the steel jacketed segment down over the tendon and onto the footing top. The segment was bonded to the footing using Sikadur-31. The upper column segment and the load stub were placed in the same manner. During assembly, vertical plumb of the specimen was monitored and ensured by placing aluminum shims of different thickness in between the top surface of one component and the bottom of the next before epoxy was applied at the joint. Figures 5.3 - 5.6 depict the construction sequence. After assembly of the specimens was completed, each was painted white in order to accentuate any cracks that formed during testing.

After the first test on each specimen, the damaged region at the column base below the jacket toe was repaired. Loose concrete was removed from the gap between the bottom of the jacket and footing and the area scrubbed with a wire brush. The region was rinsed with water to remove any remaining concrete and was then allowed to dry completely. The residual crack was then grouted using Sikadur 35, as described for the high aspect ratio columns reported on in Chapter 4.

(27) 12.7 mm diameter Grade 270 low-relaxation prestressing strands

610mm

Section A-A

610mm

Section B-B

#4 longitudinal bar

A36 steel jacket; 6 mm and 2.8 mm thickness for JH1 and JH2

#3 spiral @ 150 mm

A36 steel jacket

140 mm diam. PVC tendon duct

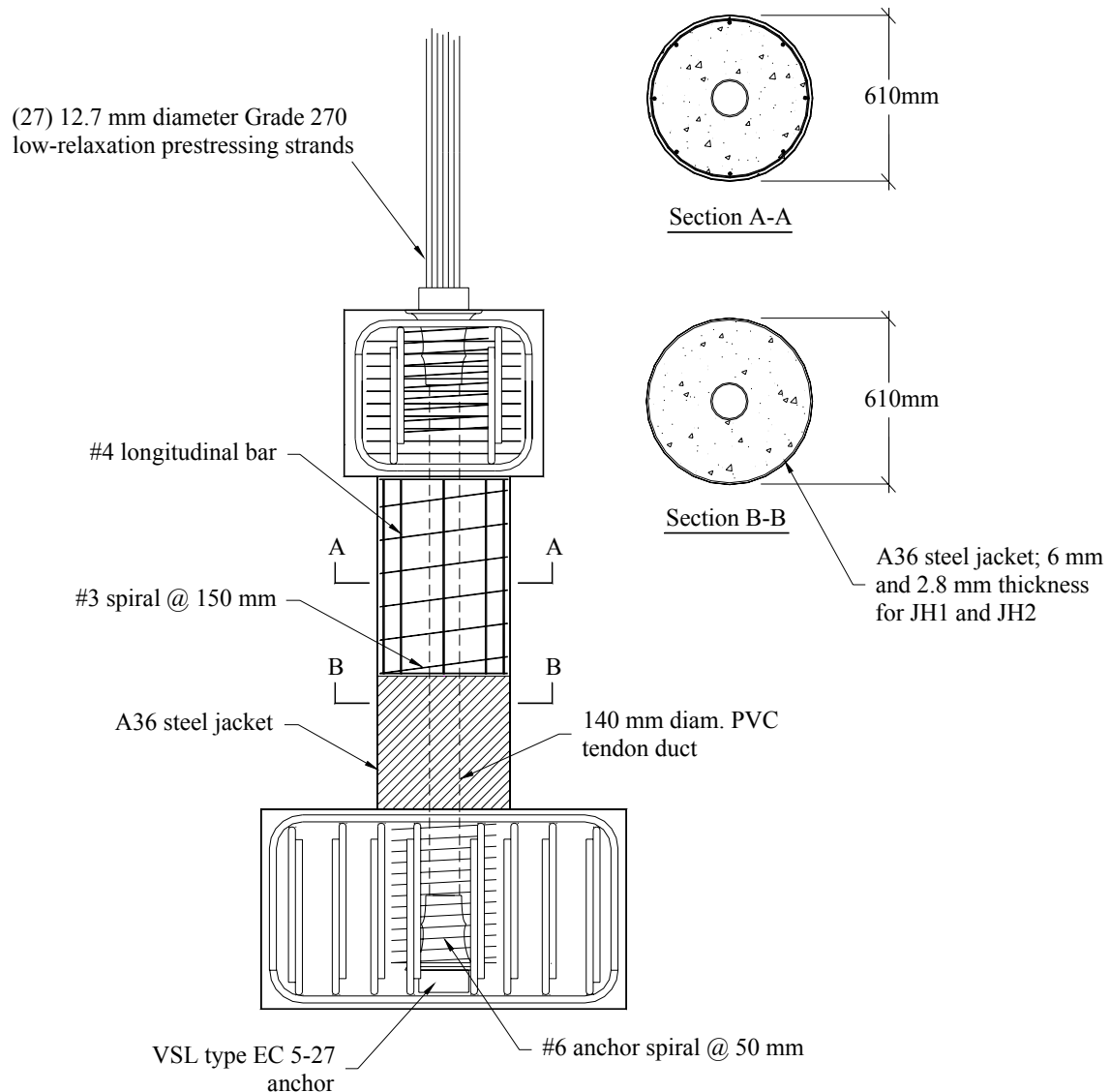VSL type EC 5-27 anchor

#6 anchor spiral @ 50 mm

Figure 5.1 Test unit JH3 and JH4 reinforcement details

Figure 5.2 Threading tendon through base (rotated 90 degrees)

Figure 5.3 Footing after installation of tendon

Figure 5.4 Installation of lower column segment

Figure 5.5 Installation of column load stub

Figure 5.6 Completed column

5.3   Materials Testing

Material properties of concrete and steel used in the construction of specimens JH3 and JH4 were determined through testing at UCSD's Charles Lee Powell Structural Research Laboratories.   The compression strength of concrete was measured at 7 days, 21 days, and 28 days and on the day of each test. The results are listed in Table 5.1. The values in the table are an average strength based on three tests on unconfined concrete cylinders (152.4 mm diameter x 304.8 mm height) that were cast during the pour.

Table 5.1 Concrete compressive strengths for specimens JH3 and JH4 ($f_c^{'}$, MPa)

Specimen	7-Day	21-Day	28-Day	Day of Test 1	Day of Test 2
JH3	37.1 ± 1	45.2 ± 1.1	48.5 ± 1.1	57.3 ± 1.6	57.1 ± 0.8
JH4	37.1 ± 1	45.2 ± 1.1	48.5 ± 1.1	58.1 ± 1.1	57.8 ± 1.7

Tensile tests were conducted on the steel reinforcement used in the upper column segment and on the plate material used for steel jackets. Three coupons 305 mm in length were tested in a SATEC 490 kN capacity uniaxial testing machine for each of the reinforcing bar sizes. A complete stress-strain relationship up to the ultimate stress was obtained for each coupon. A well-defined yield plateau was observed for the tests on both the #3 and #4 bars. Values for the yield strength and ultimate strength are listed in Table 4.2. 'Dog-bone' shaped coupons were manufactured for tensile tests on the steel jacket material. The dimensions, tolerances and manufacturing procedure of the coupons conformed to ASTM standards. Three coupons each were tested for the two material thickness, with a complete stress-strain relationship up to the ultimate stress obtained for each coupon.   Since a well-defined yield point was not observed in tests on either material thickness, the yield strength was taken as the stress at 0.2% offset strain, consistent with ASTM standards. The yield and ultimate strengths are listed in Table 5.2.

Table 5.2 JH3 and JH4 Yield and ultimate strengths of reinforcing steel

Description	Size	Yield Strength (MPa)	Ultimate Strength (MPa)
Longitudinal bars	#4 (12.7mm)		57.1 ± 0.8
Spiral	#3 (9.5mm)	441 ± 3.7	710 ± 3.7
Thin coupons	2.8 mm thick	290	364
Thick coupons	6.0 mm thick	317	463

The adhesive used to bond the precast components together was Sikadur 31 – High Mod Gel. It is a two component solvent-free, moisture insensitive, high modulus, high strength epoxy adhesive. The expected properties of this material at the age of 14 days were compressive strength of 82.7 MPa, tensile strength of 24.8 MPa, and shear strength of 23.4 MPa.

5.4   Column Prestressing

5.4.1   First Stressing

The specimens were post-tensioned using a hydraulic stressing ram at a concrete age of 77 days. Strain gages mounted on the tendon strands, transverse spiral and steel jacket were connected to the data acquisition system and an initial set of readings was taken prior to the post-tensioning operation. Strain on the concrete surface was measured at six points around the circumference of the column using a demountable mechanical strain-measuring device (demec device). An initial set of readings was taken for the demec points prior to stressing.

During stressing, load levels in the tendon were calculated using both an analog and a digital pressure transducer connected to the ram hydraulics and a calibration chart. Also, ten electrical resistance strain gages mounted on the tendon strands and connected to a data acquisition system with real-time digital display were used to monitor strains in the prestressing steel.

Because of the short tendon length, significant strain losses due to mechanical seating of the strand wedges in the anchor head were expected. Thus, to achieve the design initial prestress of 1984 kN (= 0.4 x 1861.6 Mpa x 2665 mm^2 x10^{-3}), a total force of 3055 kN was applied to each specimen. This was based on an assumed wedge seating of 6.4 mm. In light of the relative uncertainty in actual seating losses and because each column was to be tested within a few days of stressing, no account was taken for time dependent effects.

Figure 5.7 shows the measured strains in the tendon strands during stressing of specimens JH3 and JH4. For specimen JH3, the readings from six strain gages (four of the ten gages read a constant -21x10^3 $\mu\varepsilon$ indicating a bad connection, and were not used) were averaged and indicated a prestressing force of 1957 kN immediately after stressing. As seen in Figure 5.7 (b), data from nine strain gages was obtained for specimen JH4.

143

However, data from only eight of the gages was used to calculate the average prestressing force since it was felt that the low strains recorded by one gage were an anomaly and did not represent the true average strain in the tendon strands. A force of 2039 kN after stressing was calculated for specimen JH4.

Readings from the demec points gave a concrete strain of 257 $\mu\varepsilon$ and 245 $\mu\varepsilon$ for specimens JH3 and JH4 respectively. Using an elastic modulus based on the compressive cylinder strength of the concrete and the above strain values, the prestressing force after stressing was calculated to be 2260 kN and 2150 kN for specimens JH3 and JH4 respectively.

Based on the above, a force of 2100 kN was taken as the average prestressing force in each column tendon immediately after the post-tensioning operation. Continuous readings were taken for the demec points in the time between the post-tensioning operation and first test of each specimen. Using these readings and also the initial strain readings in the tendon strands on the day of testing, a prestress loss corresponding to 80$\mu\varepsilon$ was calculated for specimen JH3. For JH4, an average prestress loss of 47 $\mu\varepsilon$ was calculated from the demec and prestressing strand readings. Using the observed strain losses and an elastic modulus of 196.5 Gpa for the prestressing steel, the day of test total prestress force for specimen JH3 was taken as 2060 kN, while that for JH4 was taken as 2077 kN. These tendon force levels correspond to approximately 42% of the ultimate strength of the tendon.

5.4.2 Second Stressing

The specimens were post-tensioned a second time approximately three weeks after the first stressing, and subsequent to stage 1 testing. A prestress level of 60% of the ultimate strength of the tendon was desired for the second test of each specimen. Due to the short tendon length and wedge seating however, it was not possible to achieve the required prestress force without exceeding the prestressing steel limit of proportionality, $\mathbf{f_{lp}}$. Using

a conservative estimate for the steel yield level, a maximum prestressing force of 3600 kN was applied to each column.

Tendon strains during the second post-tensioning of both specimens are shown in Figure 5.8. For specimen JH3, an average strain of 5188 $\mu\varepsilon$ corresponding to a force of 2717 kN, was calculated from six strain gages. Of the ten strain gages mounted on the tendon in specimen JH4, eight gave unstable readings during stressing or did not function at all and were not used. An average of the readings from the remaining two gages indicated an average tendon strain of 5096 $\mu\varepsilon$, corresponding to a force of 2669 kN.

The concrete surface strain increase measured using the demec points was 110 $\mu\varepsilon$ and 106 $\mu\varepsilon$ for specimens JH3 and JH4, respectively. Using an elastic modulus based on the compressive cylinder strength of the concrete, the above strain values correspond to an increase of the tendon force of 972 kN for specimen JH3 and 933 kN for JH4. To evaluate the predicted concrete strain increase, consideration of the tendon force prior to the start of the second post-tensioning must be given. Readings from the tendon strain gages after the first test of each specimen indicated a decrease in the total prestress force of 169 kN and 116 kN for specimens JH3 and JH4 respectively. Thus the force level in each tendon prior to the second stressing was 2060 kN – 169 kN = 1891 kN for JH3, and 2077 kN – 116 kN = 1961 kN for JH4. Using an assumed mechanical seating of strand wedges of 6.4 mm and the unbonded tendon length of 3137 mm, a strain loss due to wedge seating of 2024 $\mu\varepsilon$ was calculated. The theoretical prestress force immediately after stressing was thus 3600 kN – 1060 kN = 2540 kN. The predicted increase in prestress force was thus 2540 kN – 1891 kN = 650 kN for specimen JH3 and 2540 kN – 1961 kN = 580 kN for JH4. The corresponding predicted concrete strain increase was 73.5 $\mu\varepsilon$ and 65.6 $\mu\varepsilon$ for specimens JH3 and JH4 respectively.

It is believed that the discrepancy between the observed and theoretical concrete strain increase was caused by a lower value for the prestress loss due to wedge seating than assumed. The induced prestress after losses was thus higher than predicted. The final

estimate of the total tendon prestress force immediately after stressing was based on the strain gage readings from the tendon strands. The observed prestress loss in between the time of the second stressing and second test of each specimen was less than one percent of the total prestress force. Thus the day of test prestress force for specimen JH3 was taken as 2717 kN, while that for JH4 was 2669 kN.
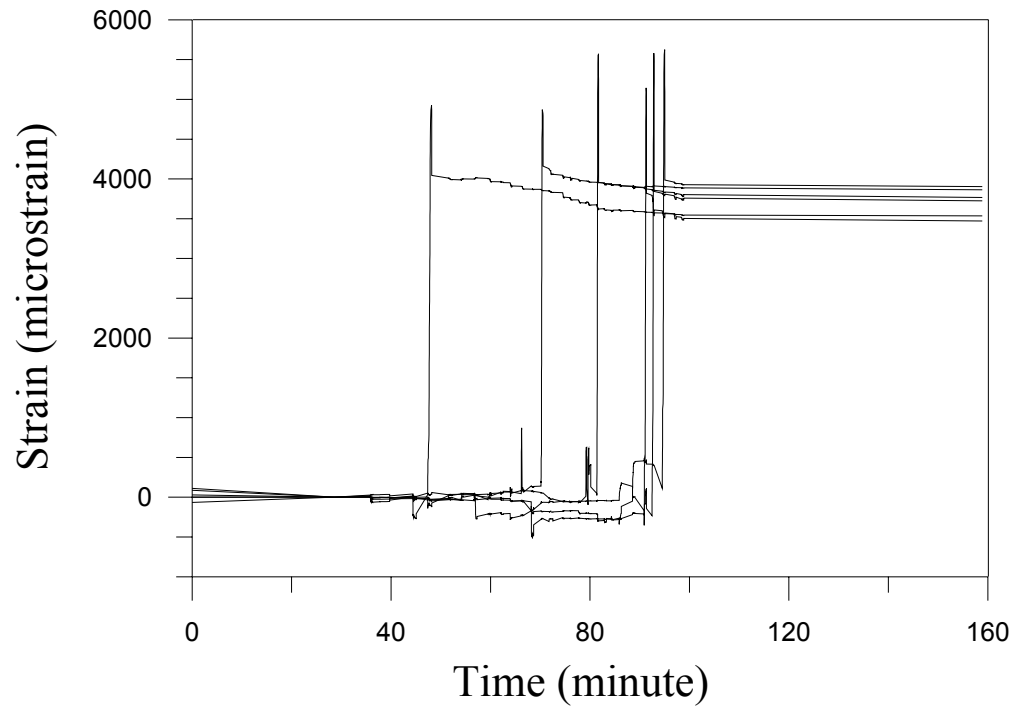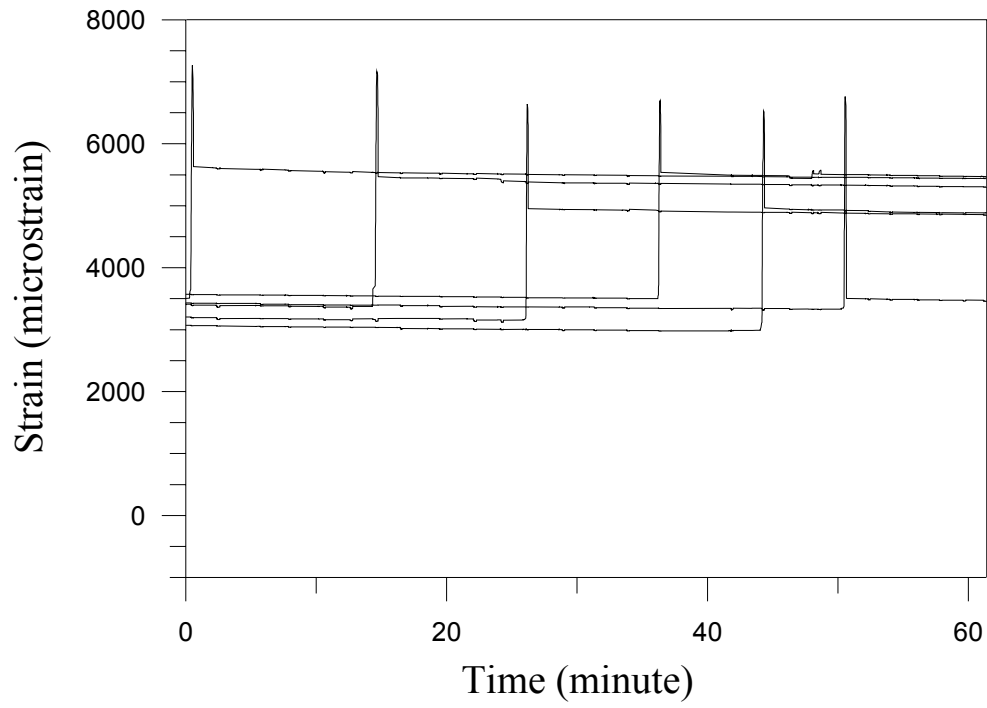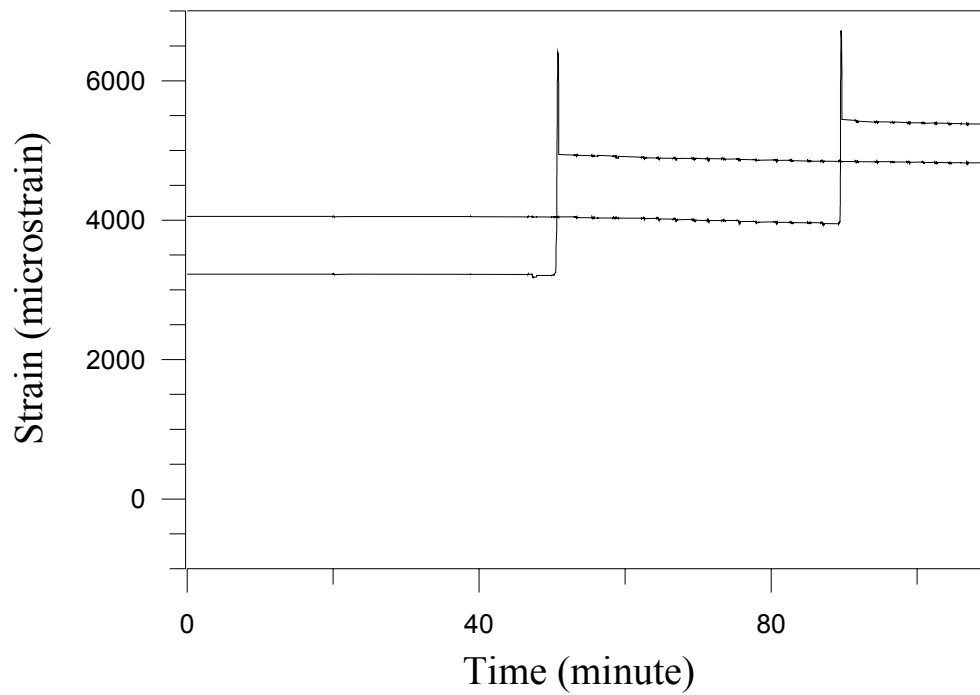
(a) Specimen JH3
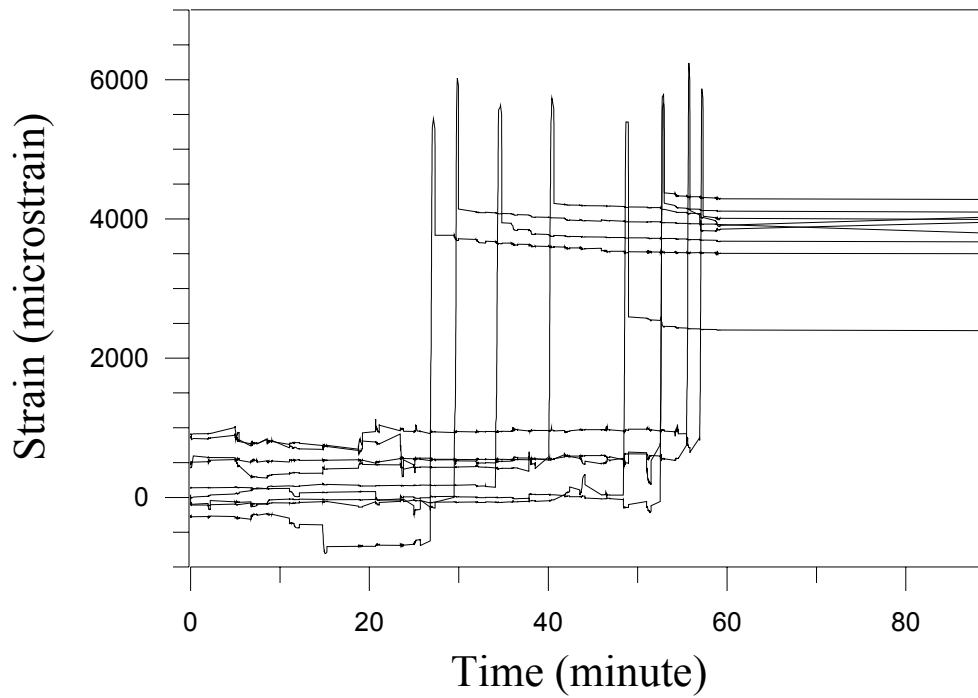
(b) Specimen JH4

Figure 5.7 Tendon strains for first prestressing of specimens JH3 and JH4

147

(a) Specimen JH3

(b) Specimen JH4

Figure 5.8 Tendon strains during the second prestressing of specimens JH3 and JH4

148

5.5   Experimental Results – Specimen JH3-T1

5.5.1   Observations under Repeated Cyclic Loading

The test was conducted in force control for the initial elastic stages. One cycle each was performed at one-half, one, and one-and-a-half times the theoretical force to cause decompression at the extreme tension fiber of the critical section (P_1). The test was then switched to displacement control and three cycles each, were performed at increasing drift levels up to the maximum imposed drift of 4.0%. A summary of the observed behavior is given below. The push direction of loading is represented by a plus sign (+), while the pull direction is signified by a minus sign (-). Several photographs taken during the various stages of testing are shown.

±0.5 Pd (Pmax= +61.7 kN and Pmin= -59.4 kN)

No cracking was observed for either direction of loading.

±P_d (P_{max}= +122.6 kN and P_{min} = -122.3 kN)

No cracking was observed for either direction of loading.

±1.5 P_d (P_{max}= 183.8 kN and P_{min}= -184.5 kN)

The formation of a crack at the joint between the upper and lower column segments was observed for both the push and pull loading directions. However, the gap may have been due to slippage of the steel shell with respect to the concrete core of the segment, and may not have represented actual cracking of the section at that level. A hairline crack at the extreme concrete fiber, below the steel jacket at the level of the footing, was observed for pull direction of loading. The crack was approximately one inch in length as measured along the circumference of the section.

3 cycles at 0.2% drift (P_{max}= +220.4 kN and P_{min}= -226.5 kN)

More noticeable cracking at the footing level was observed for the first push and pull cycle. The crack extended approximately 75 mm into the section depth from the extreme tension fiber.

3 cycles at 0.6% drift (P_{max}= +334.1 kN and P_{min}= -342.8 kN)

Cracks in the upper column segment at heights of 175 mm and 225 mm above the top of the steel jacket were observed for the push and pull directions respectively. The neutral axis depth at the column base was approximately 225–250 mm from the extreme compression fiber at this drift level. The crack width at the column base was 1.0 – 1.5 mm.

3 cycles at 1.2% drift (P_{max}= +377.5 kN and P_{min}= -389.7 kN)

The neutral axis at the column base was observed to be approximately 175 mm from the extreme compression fiber for both directions of loading. The width of the crack at the footing level, as measured at the extreme tension fiber, increased to 4–5 mm. The beginning of concrete crushing below the jacket was observed during the first cycle. Concrete continued to spall during the third cycle at this drift. New cracks in the upper column segment at heights of 300mm and 375 mm above the jacket were observed during the first cycle for the push and pull directions, respectively.

3 cycles at 1.6% drift (P_{max}= +382.3 kN and P_{min}= -397.4 kN)

An increased amount of spalling below the steel jacket at the column base was noted for cycles at this drift. The zone of crushing extended around the circumference to a depth, as measured along the section dimension, of approximately 50 – 63mm. The neutral axis depth at the base decreased to about 138 – 150 mm while the crack width increased to 6 mm at the extreme tension fiber. Several new flexural cracks in the upper column segment, as well as extension of existing cracks, were noted for this drift. Figure 5.9 shows the test unit during cycles at this drift. Note the relative lack of significant damage along the height of the column.

3 cycles at 2.2% drift (P_{max}= +393.0 kN and P_{min}= -412.6 kN)

The degree of spalling below the jacket was increased at this drift in both the level of penetration into the section and the distance along the circumference from the extreme compression fiber. The neutral axis depth at the base remained around 140 mm, while the crack at the base widened to about 8–9 mm. Figure 5.10 gives a close-up view of the column base. The significant crack opening and minor concrete crushing are visible in the photo.

3 cycles at 3.0% drift (P_{max}= +399.0 kN and P_{min}= -418.7 kN)

The zone of crushing progressed around the circumference of the column to 75-100 mm in depth, as measured along the section dimension. The neutral axis decreased to 125–138 mm, while the base crack width increased to about 12 mm. The degree of concrete crushing at the column compression toe is shown in Figure 5.11. The damage at this drift was minimal.

3 cycles at 4.0% drift (P_{max}= +391.0 kN and P_{min}= -417.9 kN)

The neutral axis depth was estimated to be around 125-150 mm from the extreme compression fiber and the crack opening at the base of the column around 16–17 mm. Figure 5.12 shows a close-up photograph of the base crack. The extent of spalling along the circumference of the section below the jacket increased to approximately 150mm in depth as measured along the section dimension. The gap between the bottom of the steel jacket and top of the footing at the compression toe was reduced significantly – to about 9 mm. The as built gap width before the start of the test was approximately 21 mm. Figure 5.13 shows the extent of damage below the jacket as well as the lift-off of the bottom of the lower column segment from the footing at the extreme tension fiber. An overall view of the column at the 4.0% drift level is shown in Figure 5.14. In the photo, the column seems to be rotated in an almost rigid fashion about its base. This was indeed the case, and the overall column behavior after the initial elastic stage may be described as rigid-body rotation about the compression toe.

Test End

Overall, damage to the column was minimal at the end of the test, consisting of only the spalled region of concrete below the jacket. Due to the crushed concrete in that region, a residual crack existed on either side of the section. The damage at the base was however, essentially cosmetic, and could be expected to be repaired relatively easily. No damage to the footing at the interface with the column base was observed. The width of cracks observed in the upper column segment remained small throughout the test – on the order of 0.5 mm or less – and closed completely once the lateral force was removed. No inclination of the cracks was observed. Fracture of strands did not occur during the test. As expected, the residual drift of the system at the end of the test was small, and was equal to just under 0.1%.
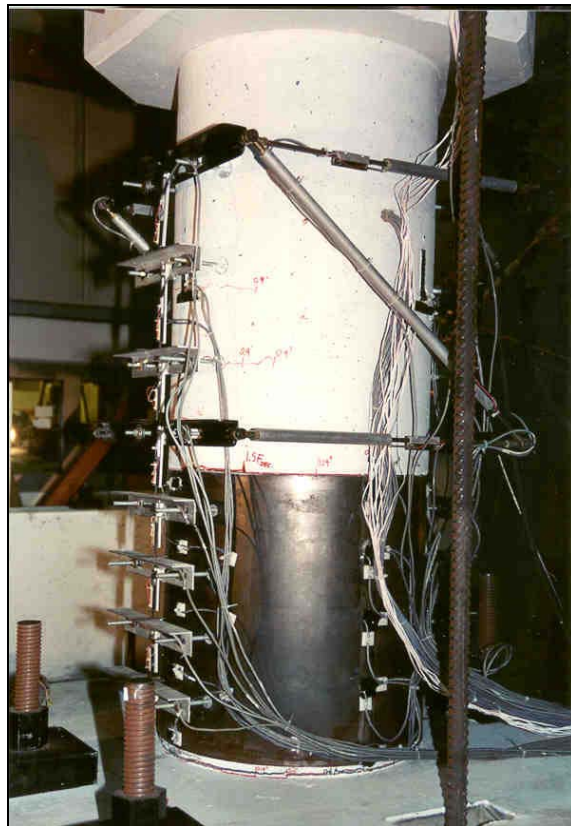
Figure 5.9 JH3 – Test 1 Column at −1.6% total drift

Figure 5.10 JH3 – Test 1 Damaged region below jacket at 2.2% drift

Figure 5.11 JH3 – Test 1 Close-up of damage at compression toe of column at 3.0% drift

Figure 5.12 JH3 – Test 1 Base crack opening at 4.0% total drift
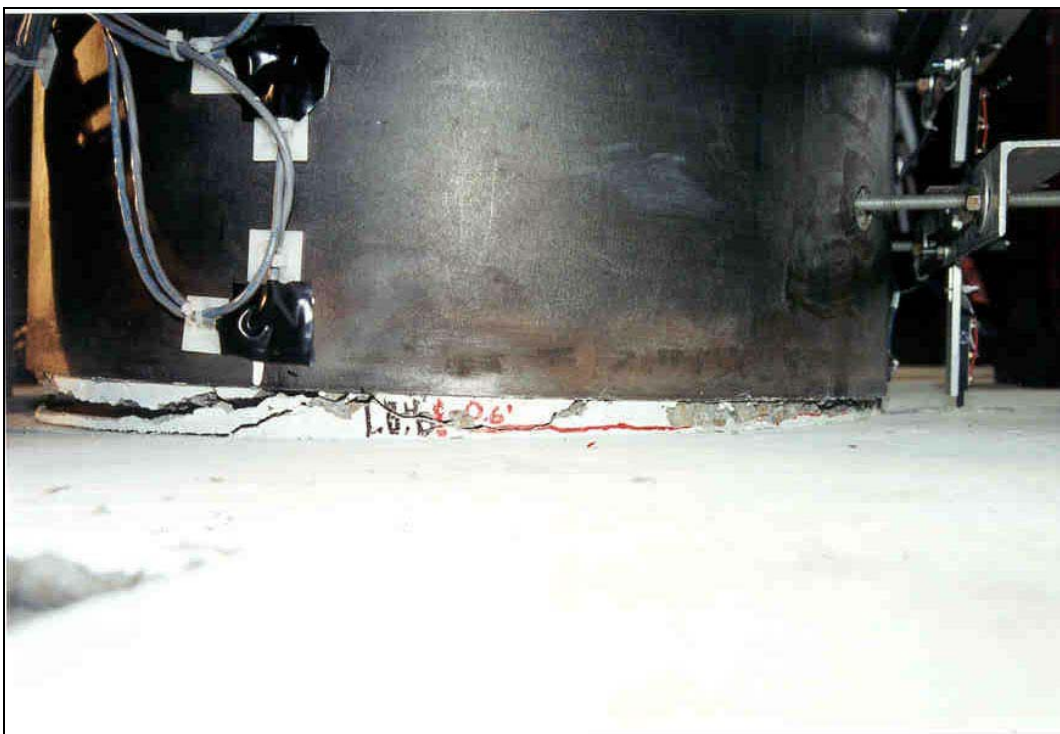
Figure 5.13 JH3 – Test 1 Base crack and crushed region below jacket at 4.0% drift

154
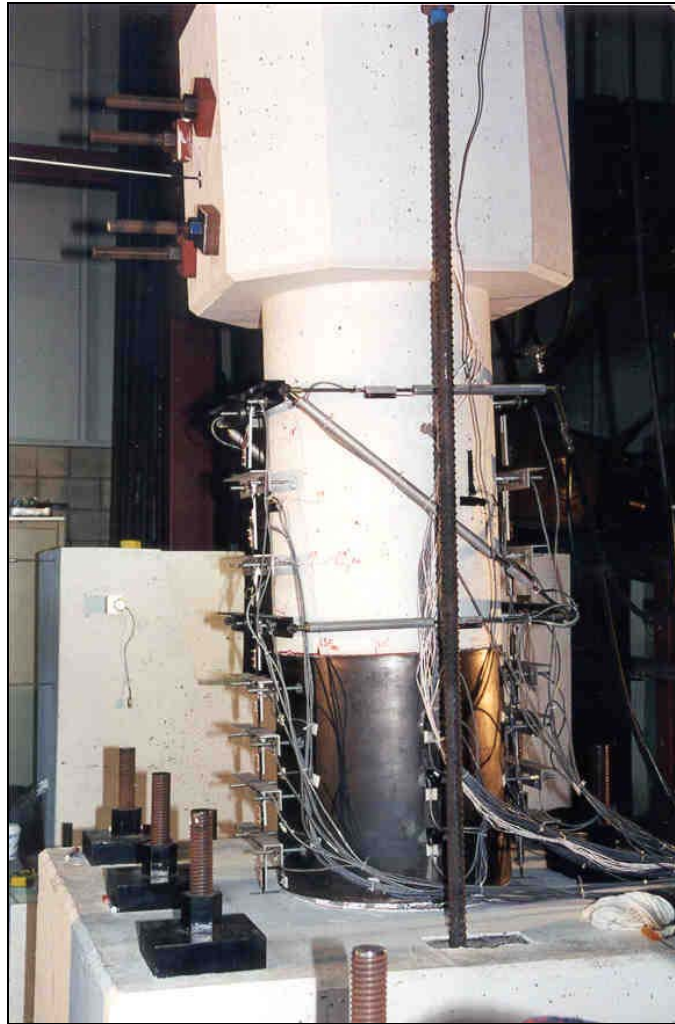
Figure 5.14 JH3 – Test 1 Column during third push cycle at 4.0% drift

5.5.2 Force – Displacement Response

The measured force–displacement response of specimen JH3-T1 is shown in Figure 5.15. As can be seen, the specimen exhibited stable hysteretic response in both directions of loading up to the maximum imposed drift of 4.0%. The force-displacement loops are essentially symmetric, with only slightly higher strengths achieved in the pull direction of loading. The loops are pinched near the origin due to the clamping force provided by the prestress. The onset of significant non-linearity in the response occurred at a force of around 245-265 kN, or approximately twice the theoretical force to cause decompression at the critical section. The peak strengths for both directions of loading occurred during the first cycle at 3.0% and were 400 kN and -419 kN for the push and pull directions, respectively. No significant strength degradation was observed during the test, with capacities at the 4.0% drift level only slightly lower than those observed at 3.0% drift (a 5% drop in strength by the third cycle at 4.0%).
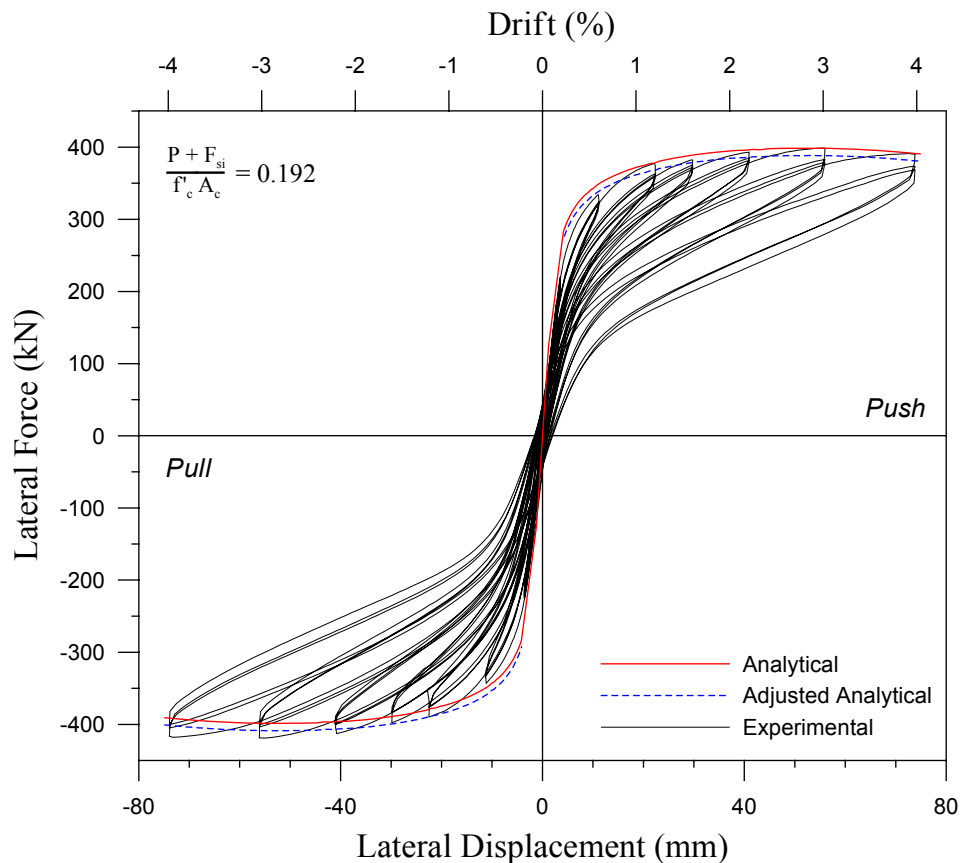
Figure 5.15 JH3 – Test 1 Force-displacement response

The analytical force-displacement response envelope is shown along with the experimental response in Figure 5.15. The difference in strength between the pull push loading directions is attributed to accidental eccentricity of the axial load as described previously in Chapter 4 for test unit JH1. With this taken into account, the adjusted analytical response was calculated and the result is indicated in the figure by the blue dashed line. The observed initial stiffness for the specimen is slightly lower than the predicted initial stiffness. After the initial elastic stages, the response is well predicted with the theoretical peak strengths within approximately 5% of the experimental.

The initial loading stiffness of the specimen did not deteriorate drastically until high drift levels. The decrease in initial column stiffness is depicted in Figure 5.16. The reduction in stiffness with increasing drift is similar to that observed for tests on the high aspect ratio columns JH1 and JH2. At a drift of 2.2%, the stiffness had decreased by approximately half, while at the maximum imposed drift of 4.0%, it had dropped to just over 30% of its original value. The decrease in stiffness is due to concrete softening and reduction of the effective section moment of inertia at the column base where concrete is crushed at the compression toe of the column.

The equivalent viscous damping is shown in Figure 5.17 as a function of imposed drift. The damping did not increase appreciably with increases in drift. The average damping for all drifts is approximately 5%.
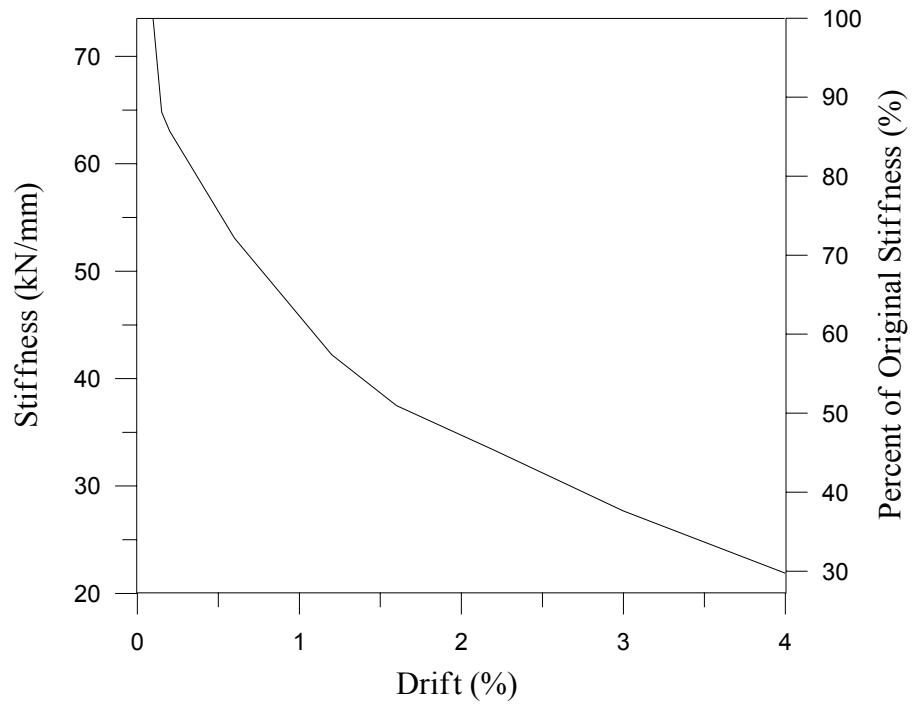
Figure 5.16 JH3 –Test 1 Initial loading stiffness versus drift
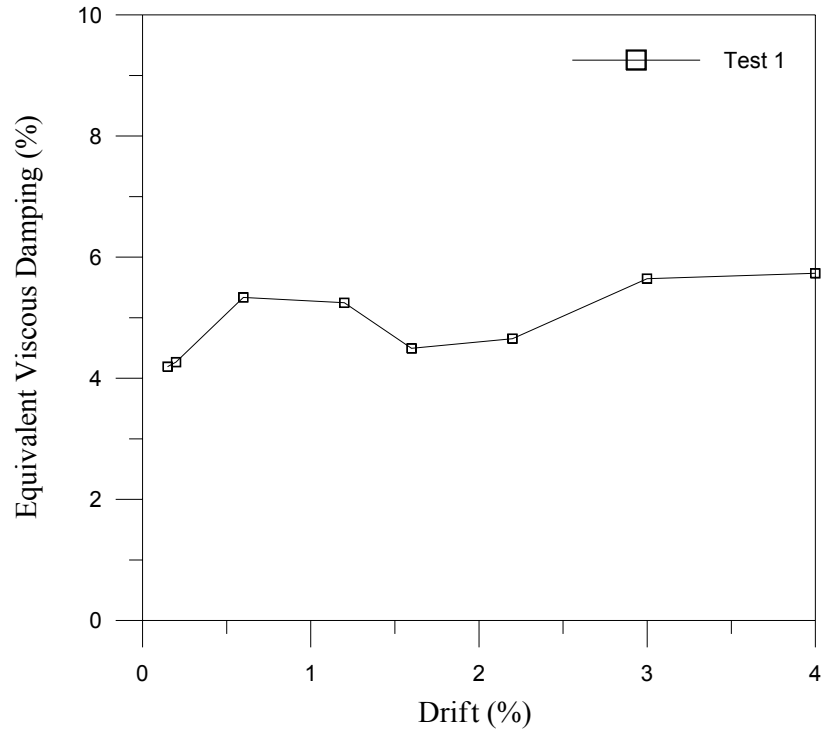

Figure 5.17 JH3 – Test 1 Equivalent viscous damping versus drift

5.5.3   Test Control Data

A large array of instrumentation was used to monitor various quantities of interest during the test. This included linear potentiometers to measure displacements and curvature, and strain gages mounted on reinforcing steel. The data recorded during testing is presented in a reduced form as strain and curvature profile plots using values recorded at peak displacements during the first cycle of loading.

Column Curvature

Curvature along the column height is shown in Figure 5.18. The curvature values were calculated as previously described. It can be seen that from the early stages of testing on, much of the column rotation was concentrated at the base where the large crack formed below the bottom of the steel jacket at the level of the footing. This is evidenced by the large spike in curvature near the bottom of the column in the curvature plot. It is believed that the curvatures shown at the column base are higher than the actual values since the assumption that plane sections remain plane may not be valid, and since the calculation of curvature uses the linear potentiometer readings from both sides of the section. A calculation of curvature based on the potentiometer reading on only the compression generator side and on the neutral axis depth is more appropriate. Calculations were performed using estimates for the neutral axis depth recorded during testing and this approach. The curvatures obtained using the "correct" method were on average, 20% lower than those calculated using potentiometer readings from both sides of the column section.

An estimate of the concrete strain in the region at the column base may be obtained by averaging the curvatures for the push and pull directions for a given level of drift and then multiplying by the observed neutral axis depth. The procedure is not exact but should yield a number representative of the magnitude of compression strain at the column base. An estimate of the compression strain at the 4.0% drift level is given by:

$$\varepsilon_c = 0.8 \; \phi_{ave} \, c \; = \; 0.8 \, (0.00028 \text{ mm}^{-1}) \, 135 \text{ mm} \; = \; 0.03$$

where ϕ_{ave} is the average of curvatures calculated for the push and pull direction at 4.0% drift, **c** is the estimated neutral axis distance from the compression edge at the base of the column and the 0.8 is to account for the curvature being overestimated as described above.
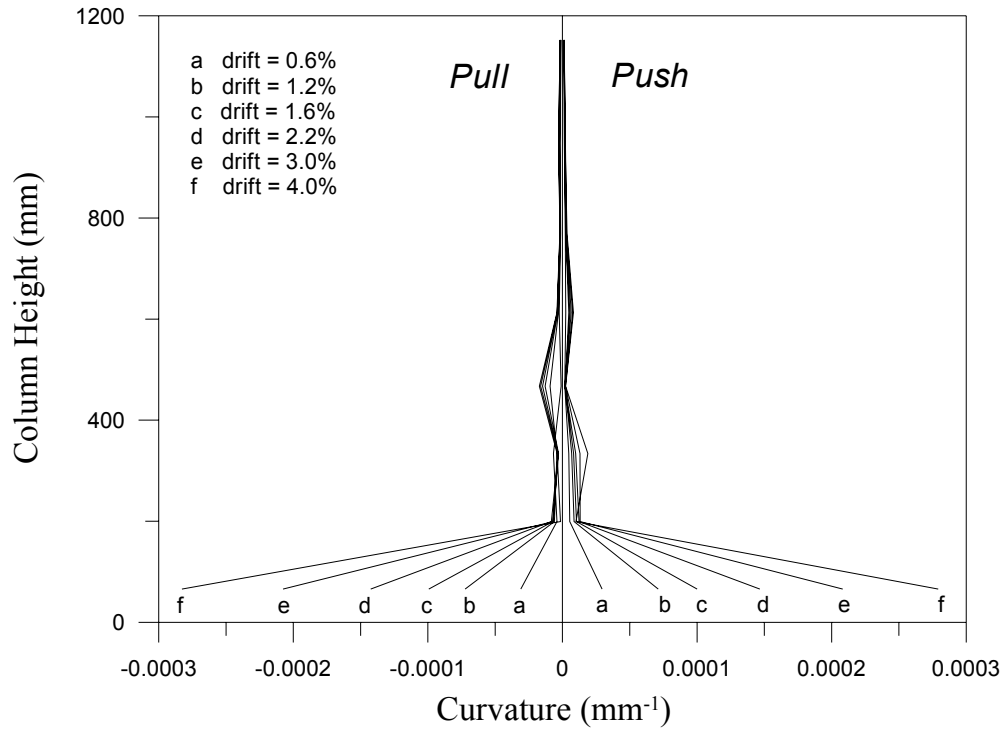

Figure 5.18 JH3 –Test 1 Curvature along column height

Prestressing Steel Strain

A comparison between the predicted and experimental increase in tendon strain due to opening of the crack at the column base is shown in Figure 5.19. The experimental curve was constructed as described in Section 4.5.3. As can be seen, excellent agreement was achieved between the experimental and analytical prediction. The good correlation of strain increase might be due to the relatively high number of strain gages used on the tendon. In other words, the larger the number of gages used to monitor a given quantity, the more confidence one can have in the validity of the data (barring any systematic errors).

160

Steel Jacket Strains

Five pairs of orthogonal strain gages were mounted on the east and west (shear) generators of the steel jacket oriented in the vertical and horizontal directions. At the north and south generators, five horizontal gages were mounted to monitor hoop strains in the jacket. Figures 5.20 and 5.21 show the hoop strains developed during testing on the north and south generators, respectively. Note that the strain profiles are viewed from left to right for increasing force/displacement levels, starting with 0.5 *x* P_1 and ending with the maximum drift of 4%. At the compression generators, circumferential tension is induced in the jacket by the dilation of compressed concrete in that region. As seen in the figure, particularly high hoop strains were developed at the jacket toe where the longitudinal compression strain in the concrete was highest. Significant increases in hoop strains at the jacket toe from one drift level to the next occurred at 2.2%, 3% and 4% drift. At a drift of 4.0%, the hoop strain near the bottom of the jacket was well beyond yield and was on the order of 5000 $\mu\varepsilon$.

Figures 5.22 and 5.23 show the hoop strain profiles for the east and west generators. Jacket strains at the shear (east/west) generators are due to the shear force acting on the column and to some degree, the confining action of the jacket on the compressed concrete. As seen in the figure, the hoop strains increased down the height of the jacket and were smaller in magnitude than those observed at the north and south locations. The maximum observed strain was approximately 800 $\mu\varepsilon$. Thus, shear-induced strains were much lower than confinement strains.

Vertical strains at the east and west generators are displayed in Figures 5.24 and 5.25, respectively. Vertical strains at the east side are small along most of the jacket height except near the toe of the jacket where substantial tension strains existed. These strains are likely a result of the bending action acting on the segment. At the west generator, significant compressive strains developed at both the top and bottom of the jacket. It is not clear why the strains were compressive in nature. The maximum absolute magnitude of the vertical strains at both east and west generators was approximately 800 $\mu\varepsilon$.

Transverse Spiral Strains

Figures 5.26 through 5.29 show strain profiles for the upper column segment spiral reinforcement. The confining action of the spiral reinforcement at the north and south generators is illustrated in Figures 5.26 and 5.27, where the hoop strains are seen to be increasing down the height of the segment. The maximum observed strain occurred at the base of the segment at 4.0% drift and was approximately 800 $\mu\varepsilon$. The strain in the transverse reinforcement at the east and west generators is shown in Figures 5.28 and 5.29. The strains are relatively low since the column shear force is carried by the horizontal component of the diagonal compression strut and since the concrete dilation is less at the sides of the column than at the compression generators.
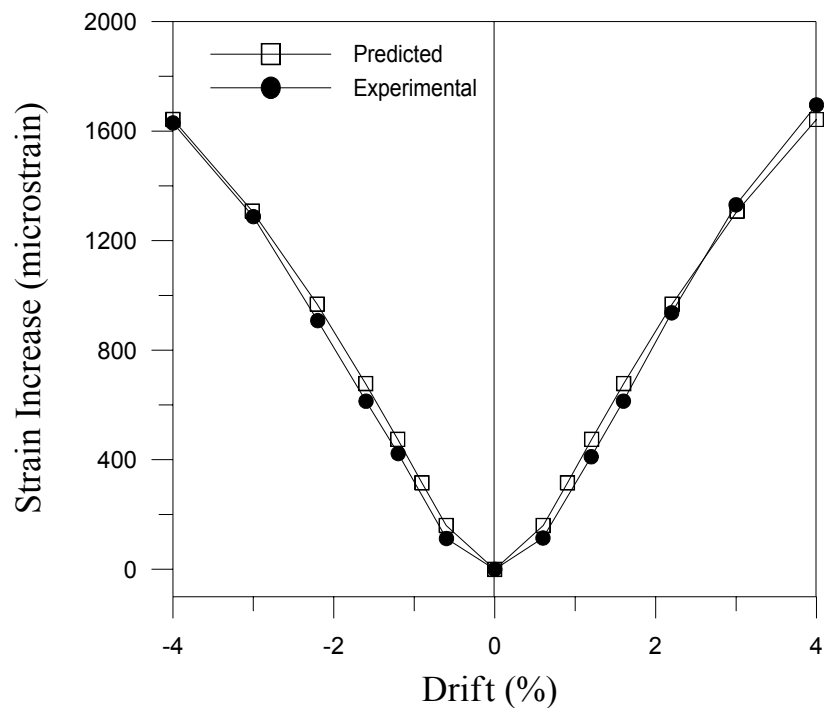
Figure 5.19 JH3 – Test1 Predicted and Experimental Tendon Strain Increase
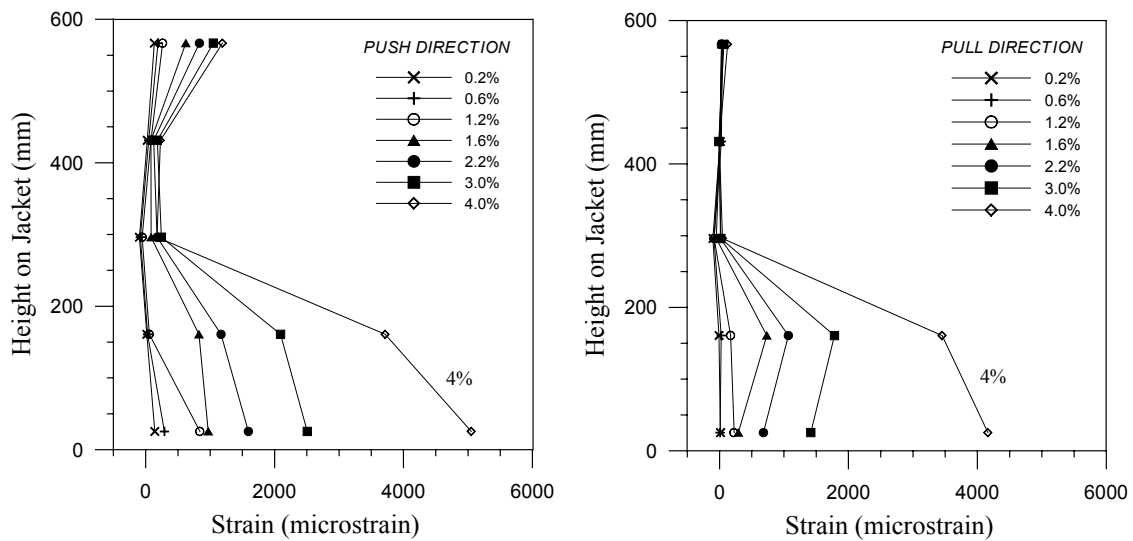
Figure 5.20 JH3 – Test 1 Jacket hoop strain at north generator
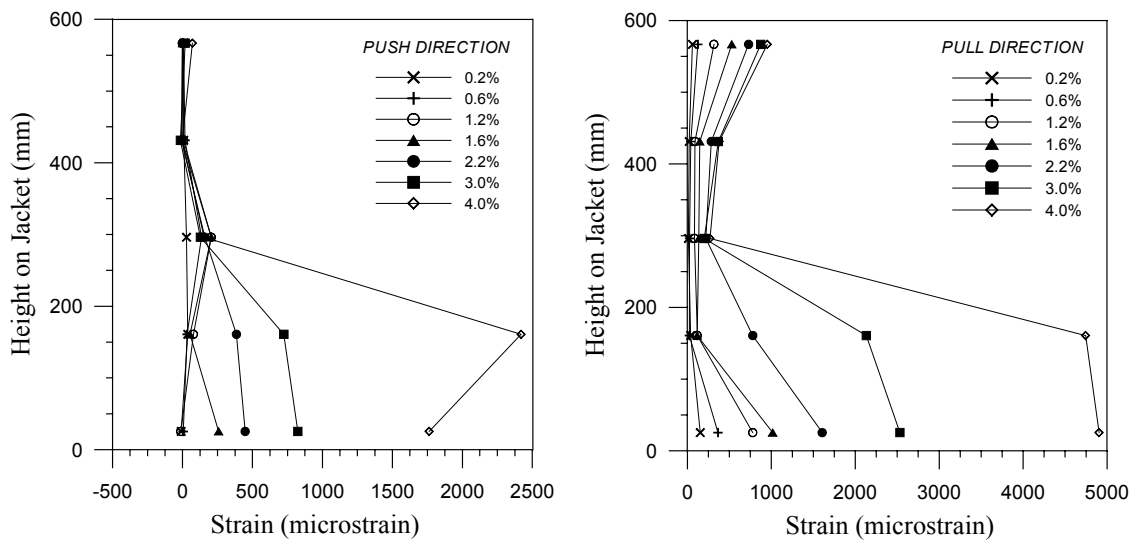
Figure 5.21 JH3 – Test 1 Jacket hoop strain at south generator
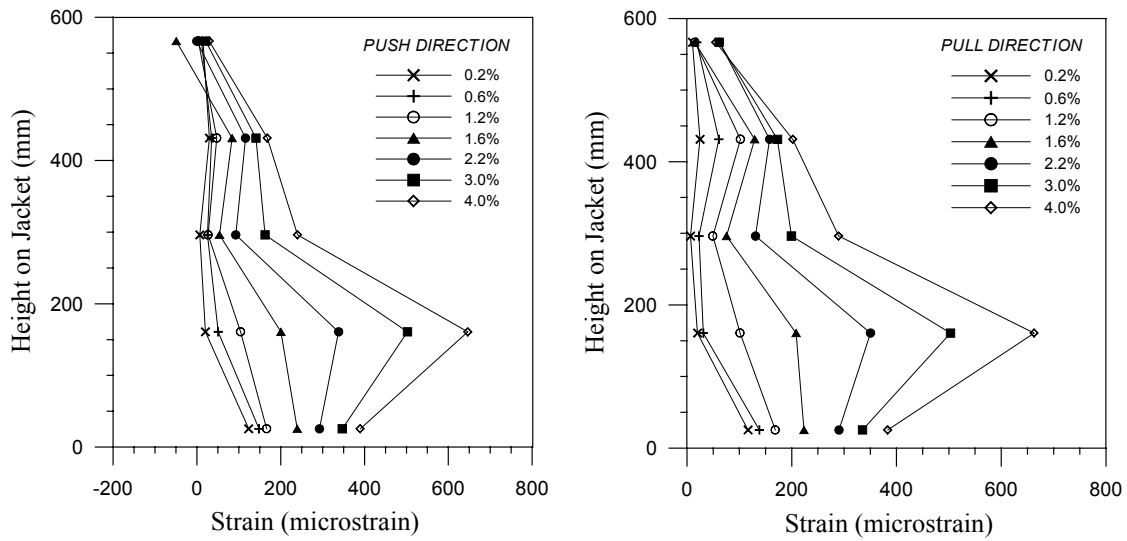
Figure 5.22 JH3 − Test 1 Jacket hoop strain at east generator
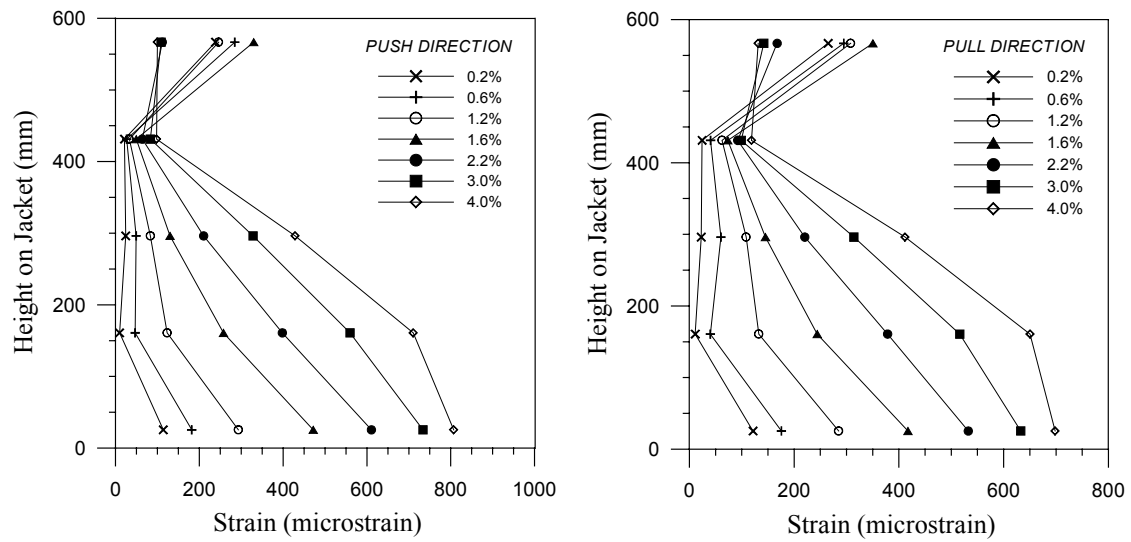
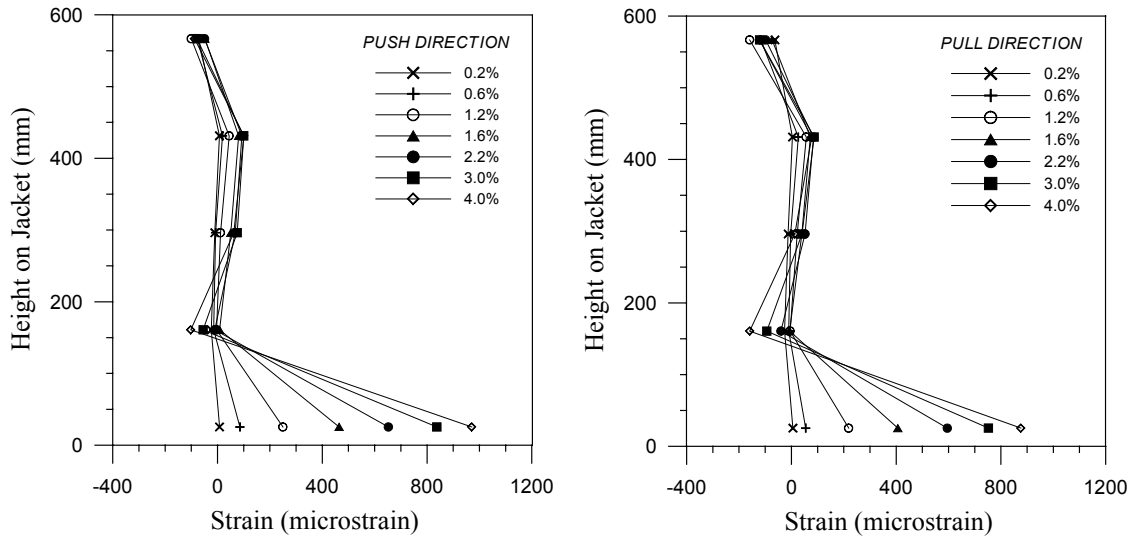Figure 5.23 JH3 − Test 1 Jacket hoop strain at west generator

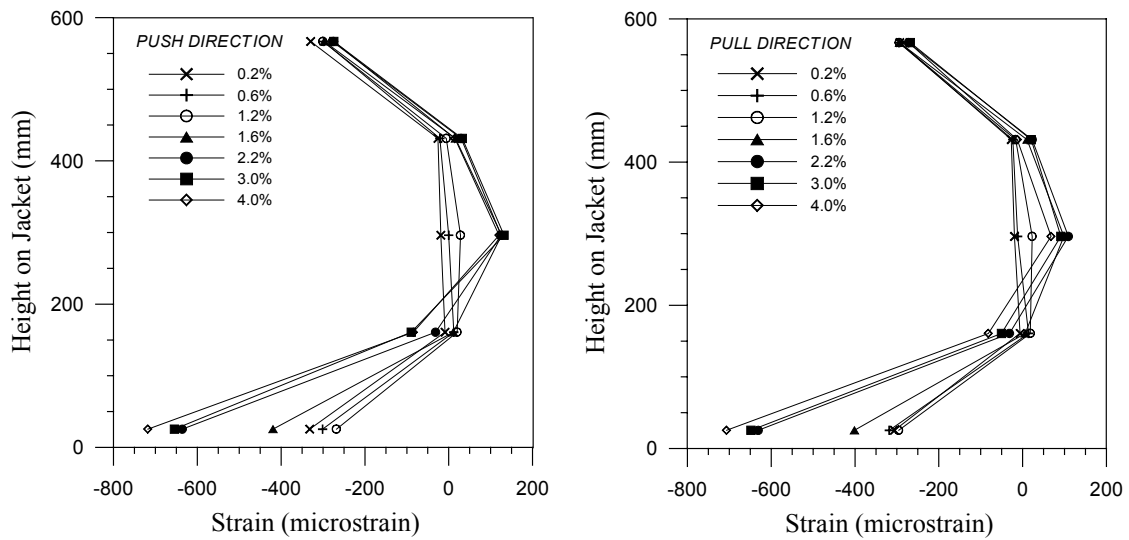Figure 5.24 JH3 – Test 1 Jacket vertical strain at east generator

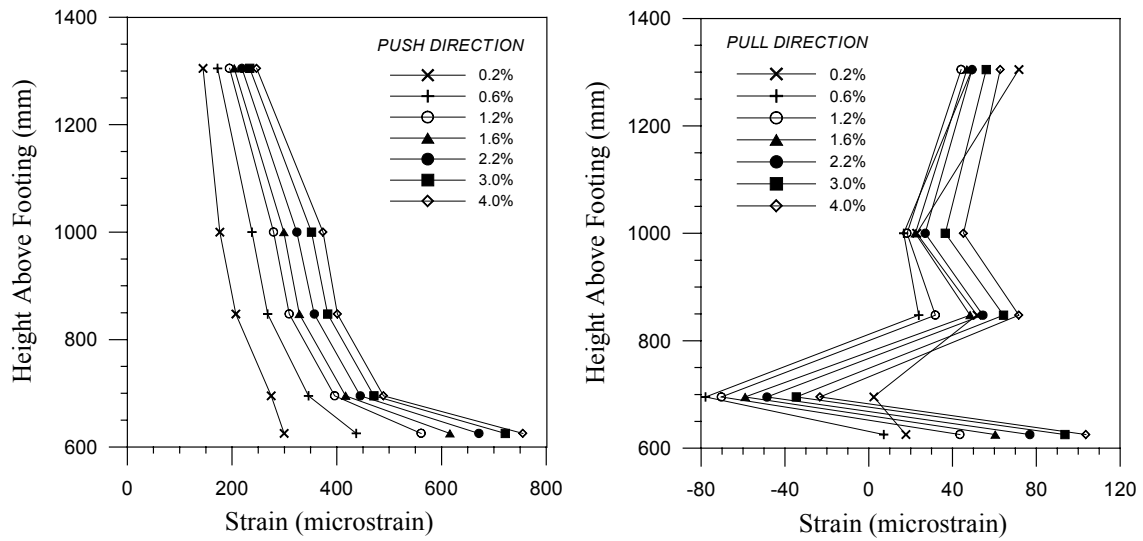Figure 5.25 JH3 – Test 1 Jacket vertical strains at west generator
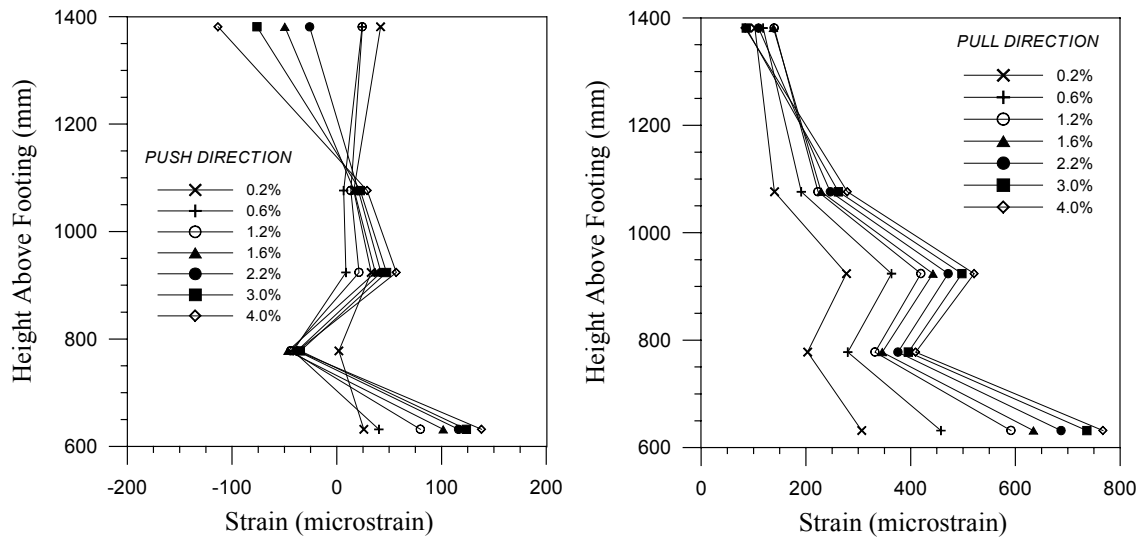
Figure 5.26 JH3 – Test 1 Spiral strains at north generator

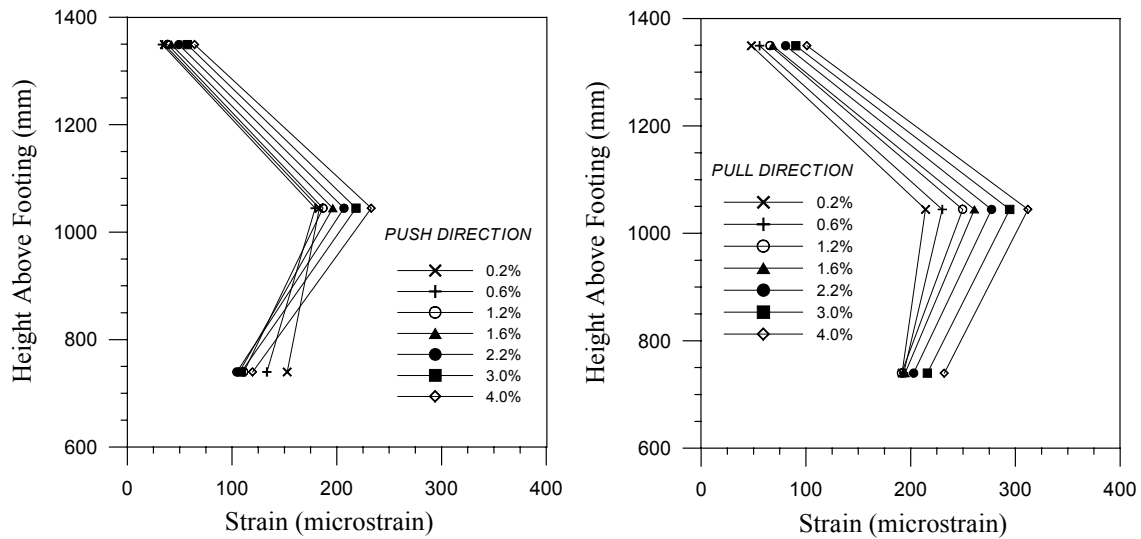Figure 5.27 JH3 – Test 1 Spiral strains at south generator

166

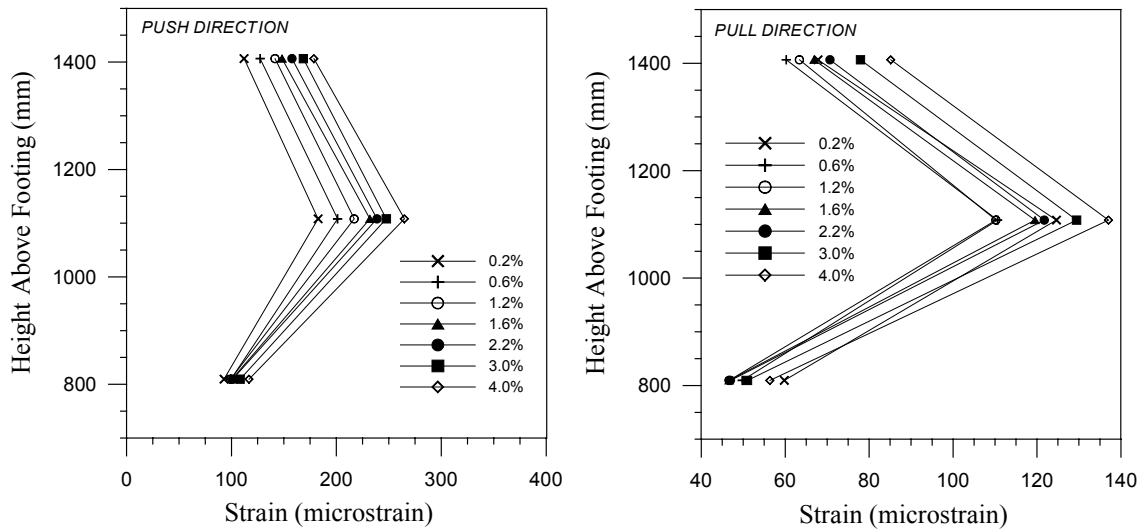Figure 5.28 JH3 − Test 1 Spiral strains at east generator

Figure 5.29 JH3 − Test 1 Spiral strains at west generator

167

5.6   Experimental Results – Specimen JH3-T2

5.6.1   Observations under Repeated Cyclic Loading

The planned loading sequence described in Section 3.5 was altered for the same reasons and in the same manner as explained for the second tests of units JH1 and JH2. A summary of the observed behavior is given below. The push direction of loading is represented by a plus sign (+), while the pull direction is signified by a minus sign (-).

$\pm 0.5\ P_d$ (P_{max}= +81.3 kN and P_{min}= -81.4 kN)

No cracking was observed for either direction of loading.

$\pm P_d$ (P_{max}= +161.5 kN and P_{min} = -162.6 kN)

Cracking at the column case below the steel jacket was observed for both the push and pull loading directions. The crack extended to a depth of approximately 50-75 mm into the section from the extreme tension fiber for the push direction, but only a few millimeters into the section for the pull direction.

$\pm 1.5\ P_d$ (P_{max}= 242.7 kN and P_{min}= -242.2 kN)

The crack at the column base extended significantly during the first cycle at this force level – to a depth of around 175-200 mm from the extreme tension fiber. Cracking was not observed in the upper (non-jacketed) segment.

3 cycles at 0.6% drift (P_{max}= +287.1 kN and P_{min}= -318.5 kN)

Flexural cracks in the upper column segment were noted during cycles at this drift and occurred at locations of previous cracks from the first test.   A single crack at approximately 175 mm above the jacket was noted for the push direction and two cracks, one at 125 mm and the other at 275 mm above the jacket, were observed for the pull direction. The depth of the neutral axis at the column base was on the order of 275 mm from the tension edge.

3 cycles at 0.9% drift (P_{max}= +331.7 kN and P_{min}= -363.2 kN)

The neutral axis depth at the column base was estimated to be about one-half the total section depth at this drift level. The width of the crack at the footing level, as measured at the extreme tension fiber, was approximately 2 mm. Minor extensions of cracks in the upper column segment were observed.

3 cycles at 1.2% drift (P_{max}= +359.1 kN and P_{min}= -396.3 kN)

The neutral axis at the column base was observed to be approximately 200-225 mm from the compression edge for both directions of loading. The width of the crack at the footing level, as measured at the extreme tension fiber, increased to 3–4 mm. Two new cracks in the upper column segment at heights of 38 mm and 460 mm above the jacket were observed during the first and third pull, respectively. Similar to the first test however, the crack widths in the upper column segment remained small throughout the test, while the crack at the column base continued to widen as the drift level increased.

It was at this drift level that spalling below the jacket at the extreme compression fiber was observed during the first test of specimen JH3. For this the second test however, the compression toe below the jacket at the column base had been repaired by epoxy injection of the residual crack and the extreme compression fiber consisted of epoxy rather than concrete. Thus, it was not possible to discern the state of the concrete within the region of the repair.

3 cycles at 1.6% drift (P_{max}= +389.4 kN and P_{min}= -425.1 kN)

The neutral axis depth at the column base was approximately 175-200 mm from the extreme compression edge. The base crack width was observed to be 4-5 mm. No further cracking was noticed in the upper column segment.

3 cycles at 2.2% drift (P_{max}= +419.7 kN and P_{min}= -456.4 kN)

New cracks in the upper column segment at heights of 450 mm and 600 mm above the top of the jacket were noted during the first push and pull, respectively. At the base of

the column, the crack opening at the extreme tension fiber increased to 9 mm and the neutral axis decreased to around 170 mm. Degradation of the concrete below the jacket near mid-depth of the column cross-section (east shear generator) was noted during the third cycle.

3 cycles at 3.0% drift (P_{max}= +432.1 kN and P_{min}= -463.1 kN)

The neutral axis depth appeared to be unchanged at the column base for this level of drift. It was difficult to determine with certainty the exact value however, as the base crack became inclined near the neutral axis and propagated into the core region within the jacket. The lift-off of the column base at the tension side was increased to approximately 12 mm at this drift. Continued degradation of concrete below the jacket at the east shear generator was noted during the third cycle. In addition, small particles of concrete fell onto the top of the footing from up inside the jacket on the tension side. At the compression toe, a significant reduction in the gap width between the bottom of the jacket and the top of the footing was noted (gap reduced to about 12 mm compared to the pretest, as-built value of 21 mm).

3 cycles at 4.0% drift (P_{max}= +416.5 kN and P_{min}= -452.4 kN)

The neutral axis depth was estimated to be, with some uncertainty, around 150-175mm. The gap between the toe of the jacket and the footing top decreased slightly to 11 mm. The liftoff of the column base was approximately 17-19 mm. Slippage of the jacket with respect to the concrete core in the amount of 5 mm was observed at this drift level. This was noticed at the bottom curvature rod locations where a hole through the jacket to the core had been provided. An increased level of damage to the concrete below the jacket at the east side of the column was noted.

3 cycles at 5.0% drift (P_{max}= +399.7 kN and P_{min}= -433.1 kN)

The depth of the neutral axis from the compression edge was noted to have increased to around 175-190 mm. The gap between the footing top and the bottom of the jacket

decreased to 9.5 mm, and the crack opening at the extreme tension fiber increased to approximately 22 mm.

3 cycles at 6.0% drift (P_{max}= +376.3 kN and P_{min}= -408.7 kN)

The toe of the jacket on the compression side was noted to be nearly in contact with the footing surface, with a measured gap width of only 6-7 mm. The crack at the column base increased in width to around 25 mm. Figure 5.30 shows a view of the east generator below the steel jacket, where significant crushing of concrete occurred. An overall view of the column at 6.0% drift is shown in Figure 5.31.

Test End

Damage to the column was minimal at the end of the test, consisting of only the region below the jacket where epoxy and concrete were crushed. Due to the crushed epoxy in that region, a significant residual crack existed on either side of the section. No damage to the footing at the interface with the column base was observed. The width of cracks observed in the upper column segment remained small throughout the test – on the order of 0.5 mm or less – and closed completely once the lateral force was removed. No inclination of the cracks was observed in the upper column segment. Fracture of strands did not occur during the test. The residual drift of the system at the end of the test was 0.2%.

Figure 5.30 JH3 –Test 2 View of east generator below jacket at 6.0% drift

Figure 5.31 JH3 –Test 2 Overall view of column at 6.0% drift

5.6.2   Force – Displacement Response

The experimental force–displacement response for the second test of specimen JH3 is shown in Figure 5.32.   The specimen exhibited stable hysteretic response in both directions of loading up to the maximum imposed drift of 6.0%. The force-displacement loops are essentially symmetric, with slightly higher strengths achieved in the pull direction of loading. The onset of significant non-linearity in the response occurred at a force on the order of 300kN, which corresponds to twice the theoretical decompression force (2 x P_1). The peak strengths for both directions of loading occurred during the first cycle at 3.0% drift and were 432 kN and -463 kN for the push and pull directions, respectively. Column strength began to degrade after the 3.0% level of drift, and had decreased by 12% from the peak observed strength at a drift of 6%.
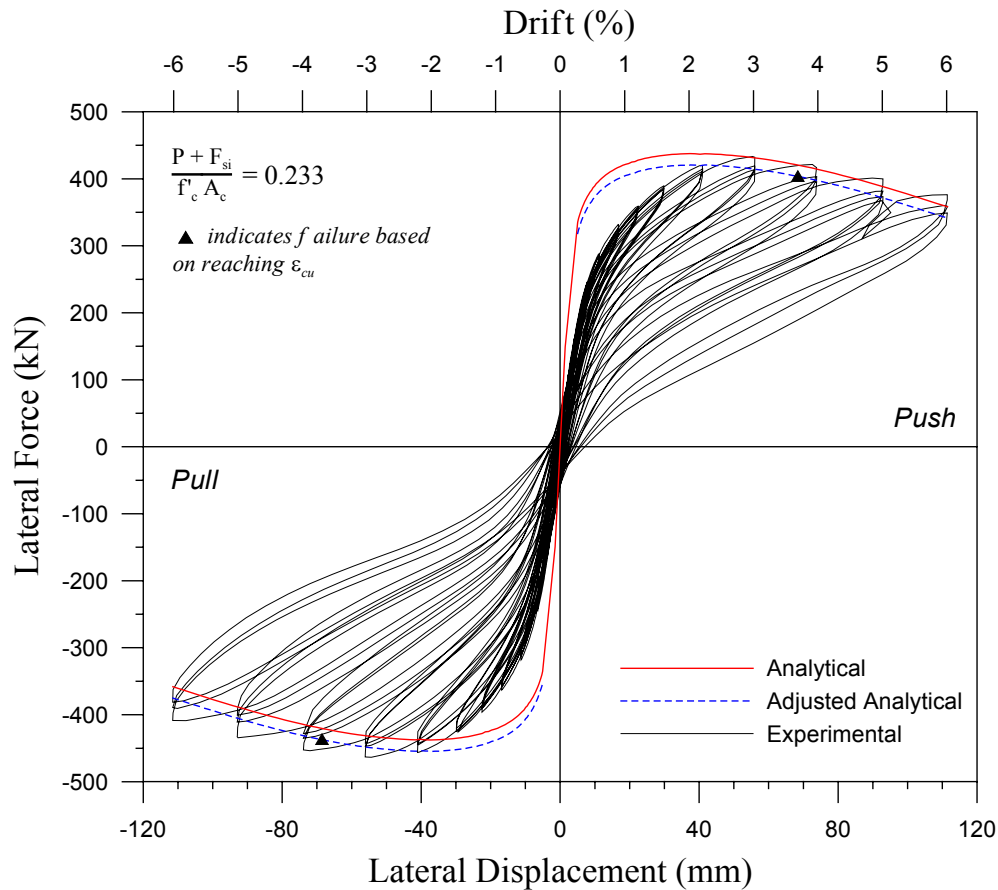
Figure 5.32 JH3 – Test 2 Force-displacement response

The initial stiffness of the specimen and peak strengths at early drift levels are not well predicted. This is expected for the same reason detailed in Section 4.6.2. The slightly higher strengths observed in the pull direction of loading could be due to eccentricity of the axial load transfer beam as explained for other tests earlier in the report. The adjusted analytical response is given by the blue dashed line in Figure 5.32. At drift levels equal to and greater than 2.2%, the analytical force-displacement envelope gives a reasonable estimate the experimental. The second slope behavior is modeled well, with the analytical curve following the decrease in strength at drifts greater than 3.0%. Predicted peak strengths are within 5% of the experimentally observed strengths for drifts up to around 4.5%, after which point the error increases to approximately 8.5%.

The initial loading stiffness of the specimen, as measured at the theoretical decompression force, is plotted as a function of drift in Figure 5.33. The stiffness observed during the first test of specimen JH3 is also shown. It can be seen that the epoxy grouting of the base crack restored the column stiffness to approximately 50% of that observed at the beginning of the first test. Other than at the early stages of the testing, the second test stiffness is very similar to that observed for the first test. The loading stiffness decreased to only 10% of original column stiffness at the maximum imposed drift of 6.0%. During cycles at drifts of 5% and 6%, the initial loading stiffness was essentially equal to the effective column stiffness, K_{eff}.

The hysteretic damping was low for the second test of JH3. Figure 5.34 shows the calculated equivalent viscous damping for both tests of the specimen. The trend of increasing damping with drift is evident. At low drifts, the second test damping is lower than that of the first. The damping level at moderate drifts is similar for both tests. At drifts of 5% and 6%, the equivalent damping was on the order of 7%.
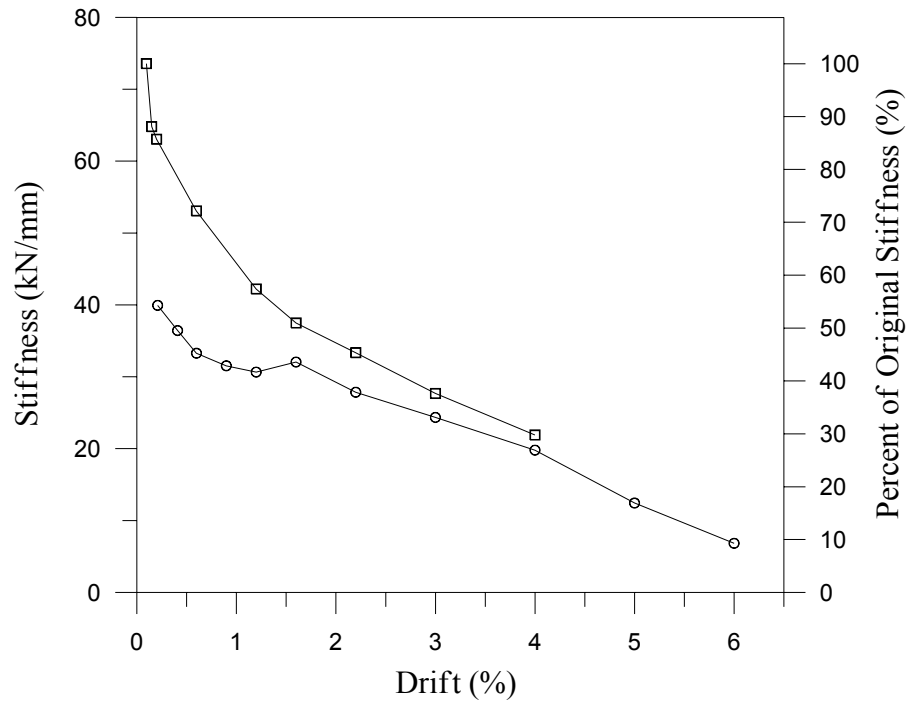
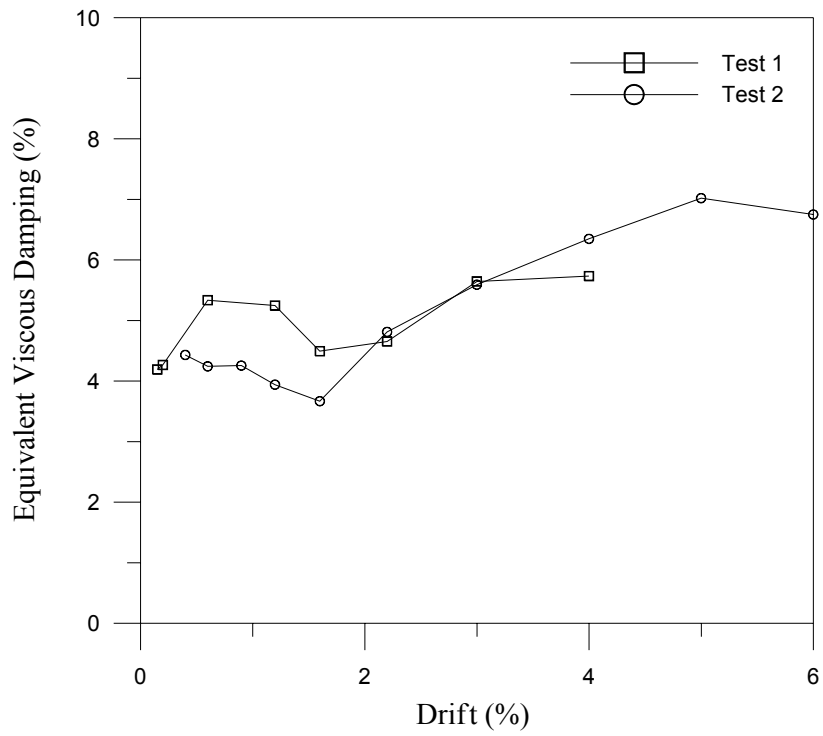Figure 5.33 JH3 − Test 2 Initial loading stiffness versus drift

Figure 5.34 JH3 −Test 2 Equivalent viscous damping versus drift

5.6.3 Test Data

The data recorded during the second test of specimen JH3 is presented in a reduced form as strain and curvature profile plots using values recorded at peak displacements during the first cycle of loading.

Column Curvature

Curvature along the height of the column is shown in Figure 5.35. Note that curvatures for the 6% drift level are not shown since the linear potentiometers at the column base did not have sufficient compression or extension travel. As was observed in the first test of specimen JH3, from the early stages of testing on, the majority of the column rotation is concentrated at the level of the footing. Curvatures at the column base at a drift of 4.0% are slightly higher than those observed at the 4.0% drift level during the first test. A curvature of 0.00036 mm^{-1} was observed at 5.0% drift. It is again noted that the curvatures shown are believed to be higher than the actual curvatures due to the phenomenon described previously.
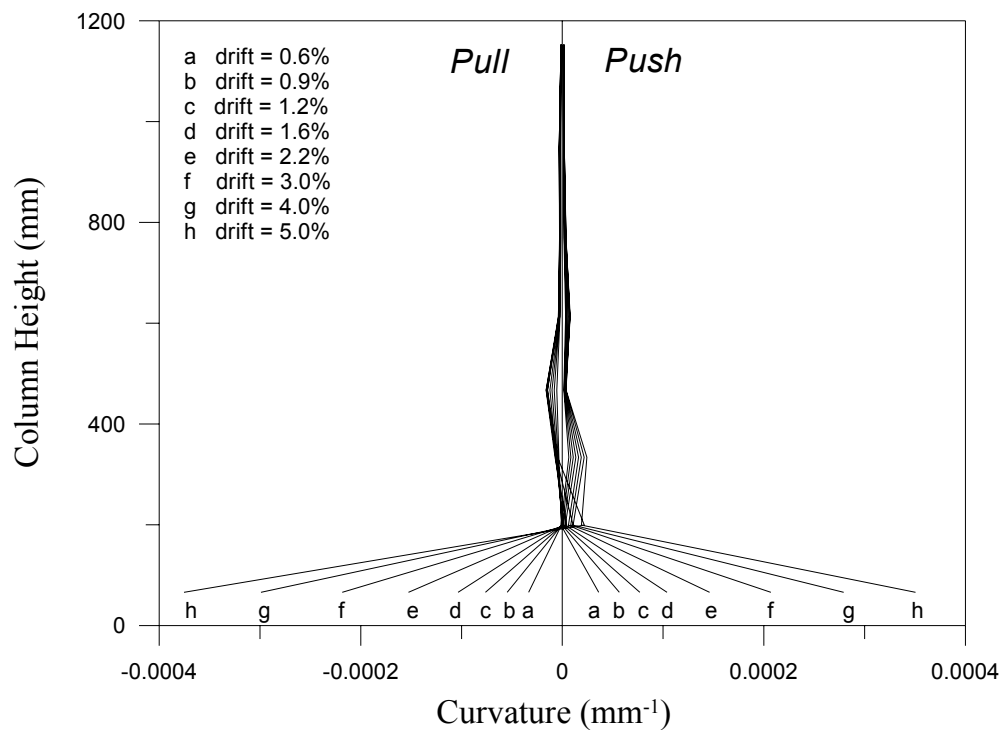
Figure 5.35 JH3 – Test 2 Curvature along column height

Prestressing Steel Strains

The analytical and experimental increase in tendon strain due to the opening of the crack at the column base is shown in Figure 5.36. The analytical slightly over-predicts the increase of strain in the tendon for low and moderate drifts. The opposite is observed at higher drifts where the actual strain increase is higher than the predicted. The observed increase in strain for the push direction of loading at drifts of 5.0% and 6.0% is higher than that observed for the pull loading direction. Following the analytical model, this implies a smaller neutral axis depth for the push direction than the pull at those drifts. It is not clear why a difference in neutral axis depth would exist for the two directions of loading. Overall, the analytical model provides a reasonable estimate of the tendon strain increase.

Steel Jacket Strains

Hoop strains in the steel jacket at the north and south generators are illustrated in Figures 5.37 and 5.38, respectively. The strain profiles in each figure are for increasing drifts from left to right and are shown for drift levels of 0.6% to the maximum imposed drift of 6.0%. For the low-level cycles (on the far left in each figure), hoop strains on the order of 5000 $\mu\varepsilon$ were observed. These are residual strains from the first test of the specimen. At drifts of 3.0% and 4.0%, the observed strains are significantly higher than those observed for the same drift during the first test. This is likely due to the higher axial load ratio for the second test. Since higher concrete compression strains at the base would generally be expected because of the increased axial load level, the tendency for dilation of concrete at the compression toe would be increased. This in turn would lead to increased hoop straining of the jacket as it acts to confine the expanding concrete. Significant yielding of the jacket occurred as high as mid-height on the jacket. Hoop strains near the base of the jacket for the maximum drift of 6.0% were approximately 12 times the yield strain of the material.

Hoop strains in the jacket at the east and west generators are displayed in Figures 5.39 and 5.40, respectively. It is believed that the compressive strains indicated near the

jacket toe for the east generator are likely due to a faulty gage and do not represent actual jacket strains. In general, the hoop strains increase down the height of the jacket for both the east and west sides (except as already noted) and are of much smaller magnitude than those observed at the north and south faces. The higher strains near the bottom are a result of the confining action of the jacket on the highly compressed concrete at the column compression toe.

Figures 5.41 and 5.42 show the vertical strains in the jacket for the east and west generators, respectively. Minimal vertical strains were observed along most of the jacket height, except near the bottom where significant tension strains were present. It is believed that the strains are due to bending action acting on the segment. At the east side, strains on the order of the material yield strain were observed at 6.0% drift, while maximum strains several times yield were observed at the west side.

Transverse Spiral Strains

Strains in the transverse spiral in the upper column segment are shown in Figures 5.43 through 5.46. Hoop strains at the north and south generators, for the push and pull directions respectively, increase down the height of the segment because of higher concrete dilation near the bottom. Maximum strains near the bottom of the segment at 6.0% drift are similar to those observed for the first test at 4.0% drift. The maximum hoop strains are just over one-half the yield strain for both the north and south generators. Hoop strains at the east and west generators are smaller than those observed at the north and south faces of the column. The maximum hoop strain for both the east and west generators occurred at mid-height of the segment at a drift of 6.0% and were on the order of 300-350 $\mu\varepsilon$.
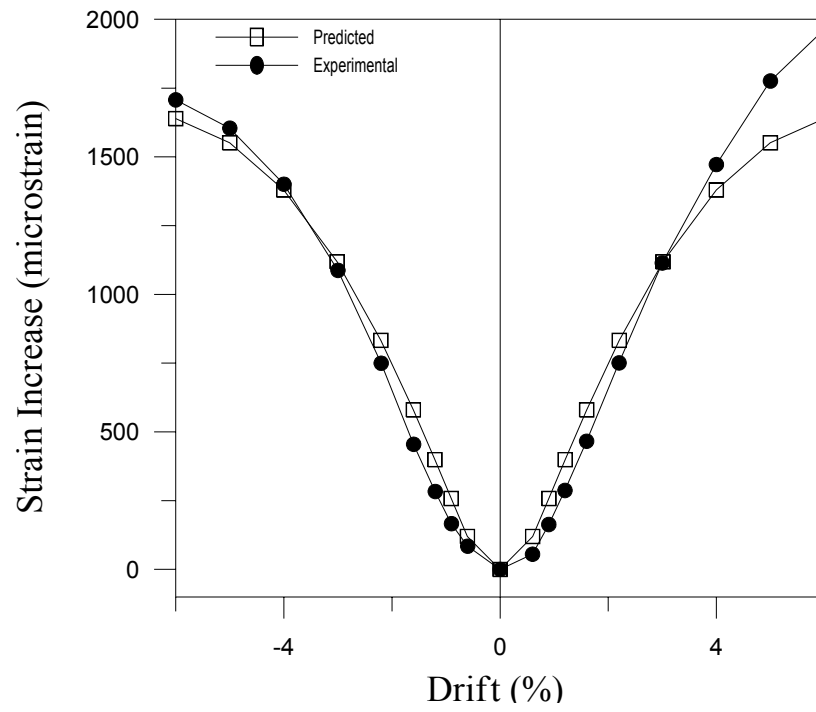
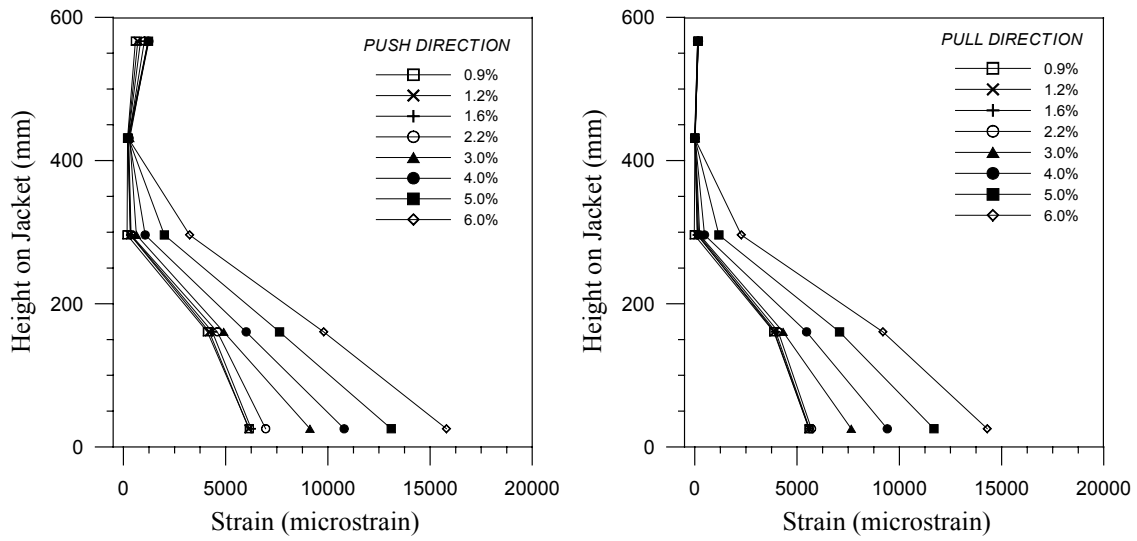Figure 5.36 JH3 – Test 2 Predicted and experimental tendon strain increase

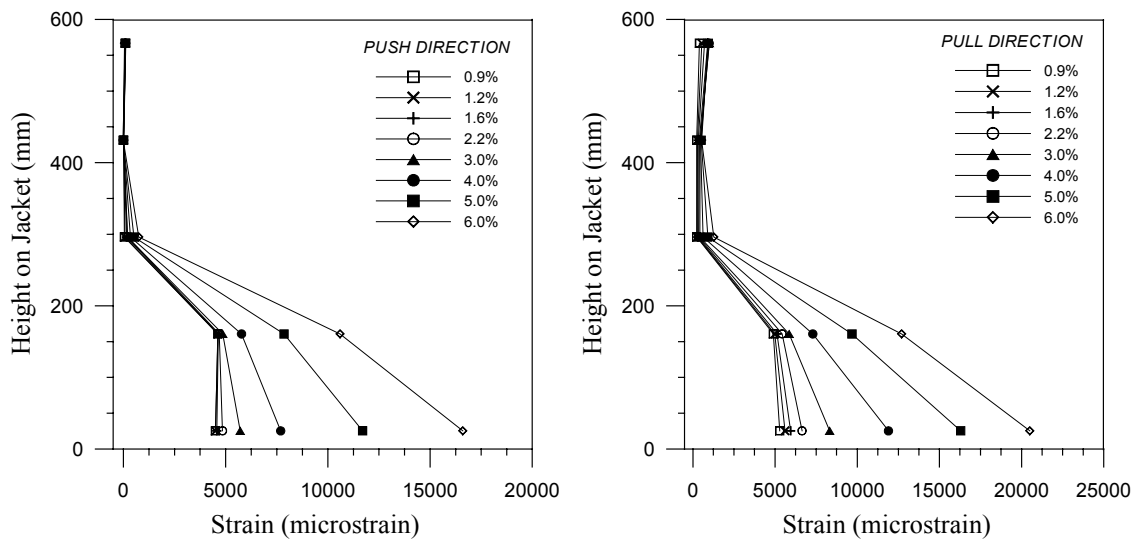Figure 5.37 JH3 – Test 2 Jacket hoop strain at north generator

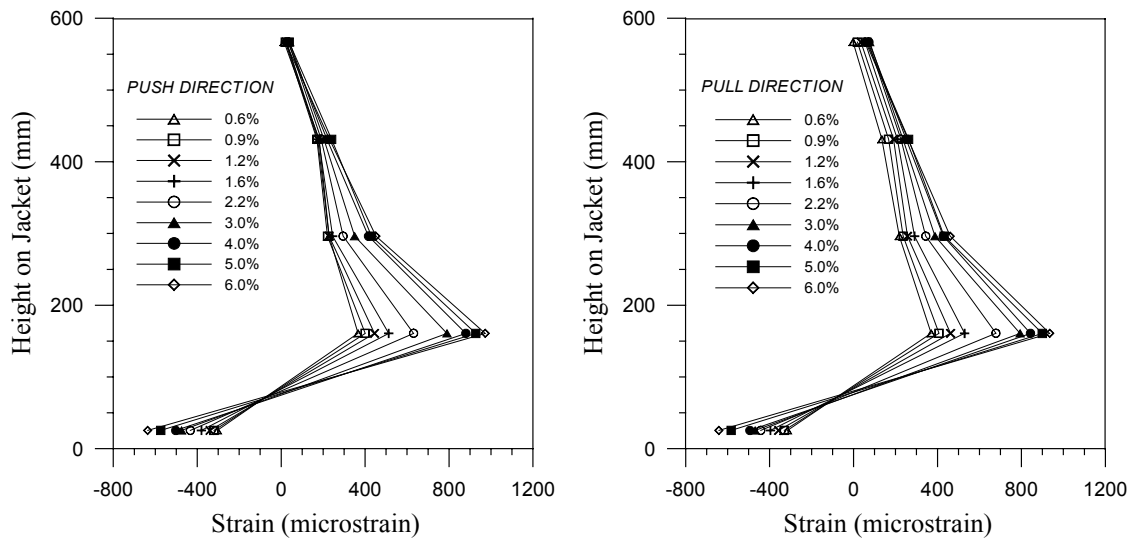Figure 5.38 JH3 – Test 2 Jacket hoop strain at south generator

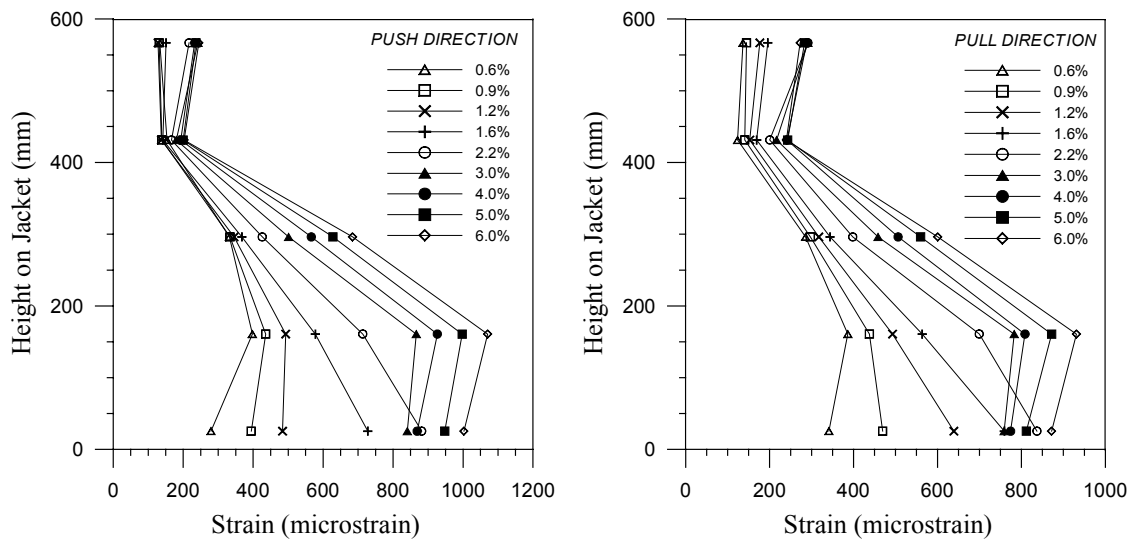Figure 5.39 JH3 Test 2 Jacket hoop strain at east generator

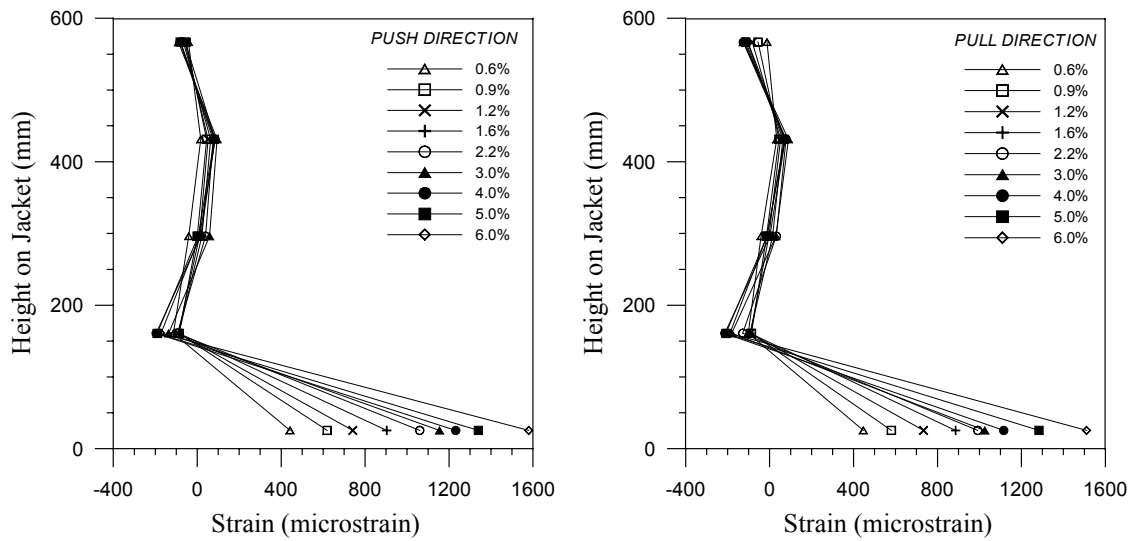Figure 5.40 JH3 –Test 2 Jacket strain at west generator

181

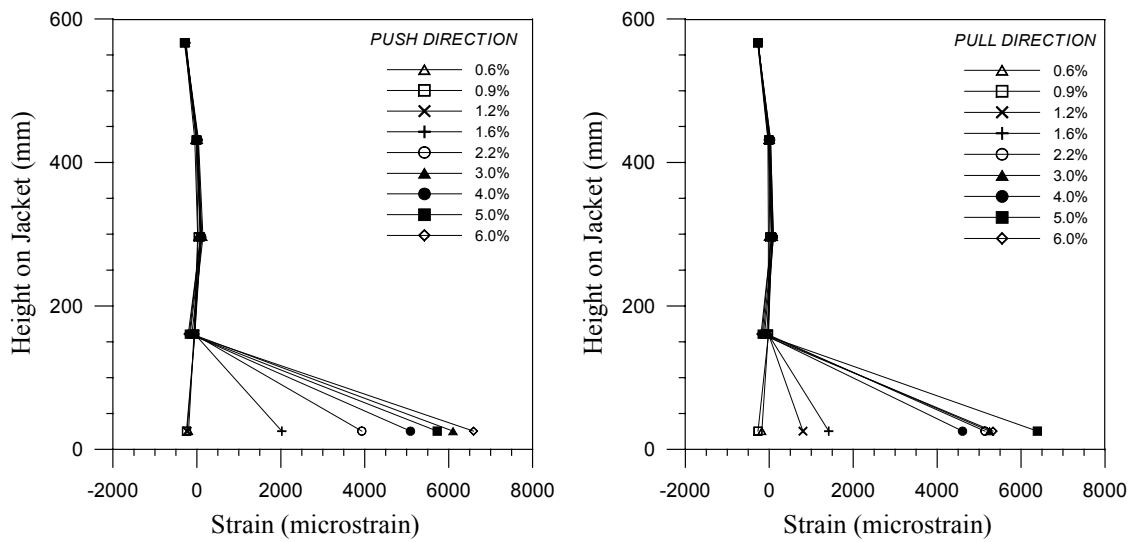Figure 5.41 JH3 – Test 2 Jacket vertical strain at east generator

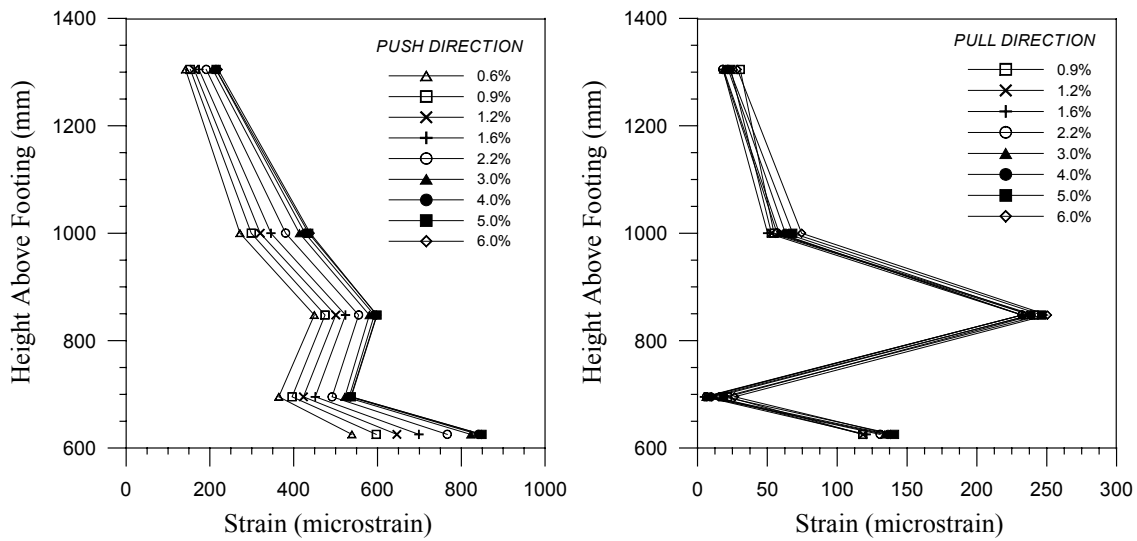Figure 5.42 JH3 – Test 2 Jacket vertical strain at west generator

Figure 5.43 JH3 – Test 2 Spiral strains at north generator
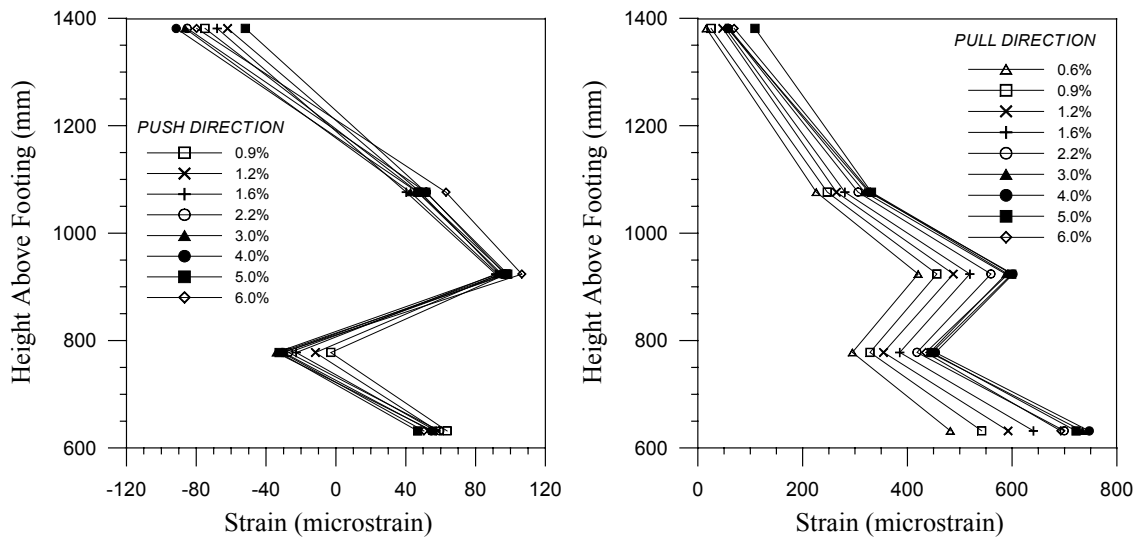

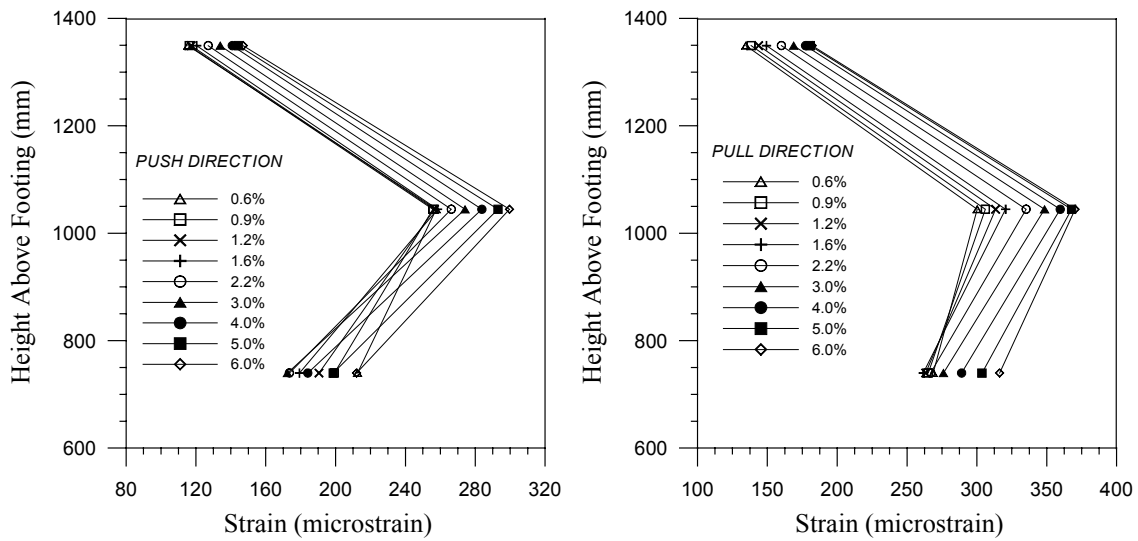Figure 5.44 JH3 – Test 2 Spiral strains at south generator

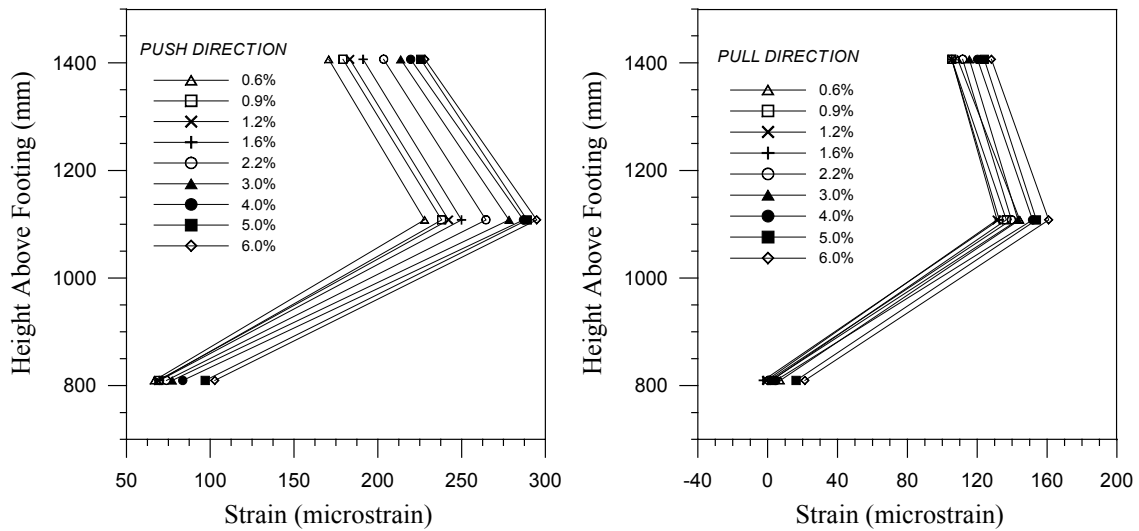Figure 5.45 JH3 – Test 2 Spiral strains at east generator

Figure 5.46 JH3 – Test 2 Spiral strains at west generator

184

5.7 Experimental Results - Specimen JH4-T1

5.7.1 Observations under Repeated Cyclic Loading

±0.5 P$_1$ (P$_{max}$= +62.1 kN and P$_{min}$= -61.7 kN)

No cracking was observed for either direction of loading.

±P$_1$ (P$_{max}$= +124.4 kN and P$_{min}$= -124.8 kN)

A hairline crack was observed adjacent to the top of the jacket for the pull direction of loading. It was felt however that this was not an actual crack in the concrete section at that level, but rather a gap between the jacket top and the bottom of the upper column segment due to slippage of the jacket with respect to the lower segment concrete core.

±1.5 P$_1$ (P$_{max}$= +187.2 kN and P$_{min}$= -186.6 kN)

A faint, hairline crack at the interface between the footing and column base was noted for both directions of loading.

3 cycles at 0.2% drift (P$_{max}$= +226.2 kN and P$_{min}$= -226.5 kN)

More significant cracking at the base of the column was observed for either loading direction, with the crack extending to a depth of 100 mm from the extreme tension fiber.

3 cycles at 0.6% drift (P$_{max}$= +335.8 kN and P$_{min}$= -331.0 kN)

Flexural cracking in the upper column segment was noted at a height of 175-200 mm above the top of the jacket during the first push and pull loading. An additional crack approximately 225 mm above the jacket was noted during the third cycle pull. The crack at the base of the column extended significantly at this drift, with the neutral axis depth estimated to be 275 mm from the compression edge. The crack width at the base at the extreme tension fiber was 2 mm. Possible incipient spalling at the compression toe of the column below the jacket was noted.

3 cycles at 0.9% drift (P_{max}= +364.0 kN and P_{min}= -358.1 kN)

The neutral axis depth at the column base was estimated to be about 215 mm from the compression edge and the crack width at the base approximately 3 mm. New cracks at 325 mm above the top of the jacket for the push direction, and 600 mm above the jacket for the pull, were observed during the first cycle. Minor spalling of concrete at the column compression toe was noted during the first cycle. The spalling in that region was increased for the third cycle of loading.

3 cycles at 1.2% drift (P_{max}= +380.2 kN and P_{min}= -377.3 kN)

The neutral axis at the column base was observed to be approximately 170 mm from the extreme compression fiber for both directions of loading. The width of the crack at the footing level as measured at the extreme tension fiber, increased to 4–5 mm. Extension of cracks in the upper column segment was noted during the first loading cycle. The degree of concrete crushing below the jacket at the compression toe was increased over that observed at 0.9% drift.

3 cycles at 1.6% drift (P_{max}= +392.4 kN and P_{min}= -392.6 kN)

Spalling at the base progressed around the circumference to a distance, as measured along the section depth from the compression edge, of about 60-75 mm. The neutral axis at the column base decreased to about 160 mm at this drift, and the crack width at the base was approximately 6-7 mm. The crack opening at the footing level during the third pull, as well as the spalled region below the jacket from the push direction of loading, are shown in Figure 5.47.

3 cycles at 2.2% drift (P_{max}= +404.8 kN and P_{min}= -416.5 kN)

Minor extension of cracks in the upper column segment occurred. The neutral axis at the base decreased slightly to around 150 mm and the base crack widened to 8-9 mm.

3 cycles at 3.0% drift (P_{max}= +415.1 kN and P_{min}= -428.9 kN)

Spalling below the toe of the jacket increased a little during cycles at this drift, progressing around the circumference to a depth, as measured along the section dimension from the compression edge, of 75-100 mm. The neutral axis depth decreased slightly and the lift-off of the base of the column from the footing at the tension side increased to around 12-13 mm.

3 cycles at 4.0% drift (P_{max}= +419.7 kN and P_{min}= -438.7 kN)

The neutral axis depth appeared to be unchanged at this drift. A base crack opening of 15-16 mm was observed at the tension edge. The gap between the toe of the jacket and the top of the footing was reduced from the as-built value of 22 mm, to approximately 11 mm. Spalling along the circumference of the base of the column progressed to a depth from the compression edge of about 125 mm. Figure 5.48 shows the damaged region below the jacket at the compression toe for the third push at 4.0% drift. Slippage of the jacket with respect to the core is visible in the photo: the bottom curvature rod, originally at the center of the hole in the jacket, is nearly touching the top of the hole. The downward slippage of the jacket was estimated to be on the order of 5 mm. A photo of the column for the third pull to 4.0% drift is shown in Figure 5.49. The large crack opening at the column base is visible, and the column appears to be rotated rigidly about its compression toe.

Test End

Damage to the column was minimal at the end of the test, consisting of only the spalled region of concrete below the jacket. A close-up photo of the damaged region below the jacket is shown in Figure 5.50. The residual crack caused by the crushing of concrete in that region is visible. No damage to the footing at the interface with the column base was observed. Other than the flexural cracks detailed above, no damage occurred in the upper, non-jacketed column segment. No inclination of the flexural cracks was observed, and all cracks closed completely once the lateral force was removed. Fracture of strands did not occur during the test. The observed column residual drift was 0.05%.

Figure 5.47 JH4 – Test 1 Crack at column base at 1.6% drift

Figure 5.48 JH4 – Test 1 Crack at column base and damaged region at 4.0% drift

Figure 5.49 JH4 – Test 1 Overall view of specimen at 4.0% drift

Figure 5.50 JH4 – Test 1 Close-up of damaged region below jacket at test end

189

5.7.2 Force – Displacement Response

The lateral force–displacement response for the first test of unit JH4 is displayed in Figure 5.51. The force–displacement loops are symmetric and approximately equal strengths were obtained for both directions of loading. As noted for specimen JH3 and as characteristic of the unbonded design in general, the hysteresis loops are pinched near the origin. The beginning of significant non-linear response occurred at about 300 kN, or approximately 2.4 times the theoretical decompression force, P_1. Peak strengths of 420 kN and –439 kN were achieved at the maximum imposed drift of 4.0% for the push and pull directions of loading respectively.
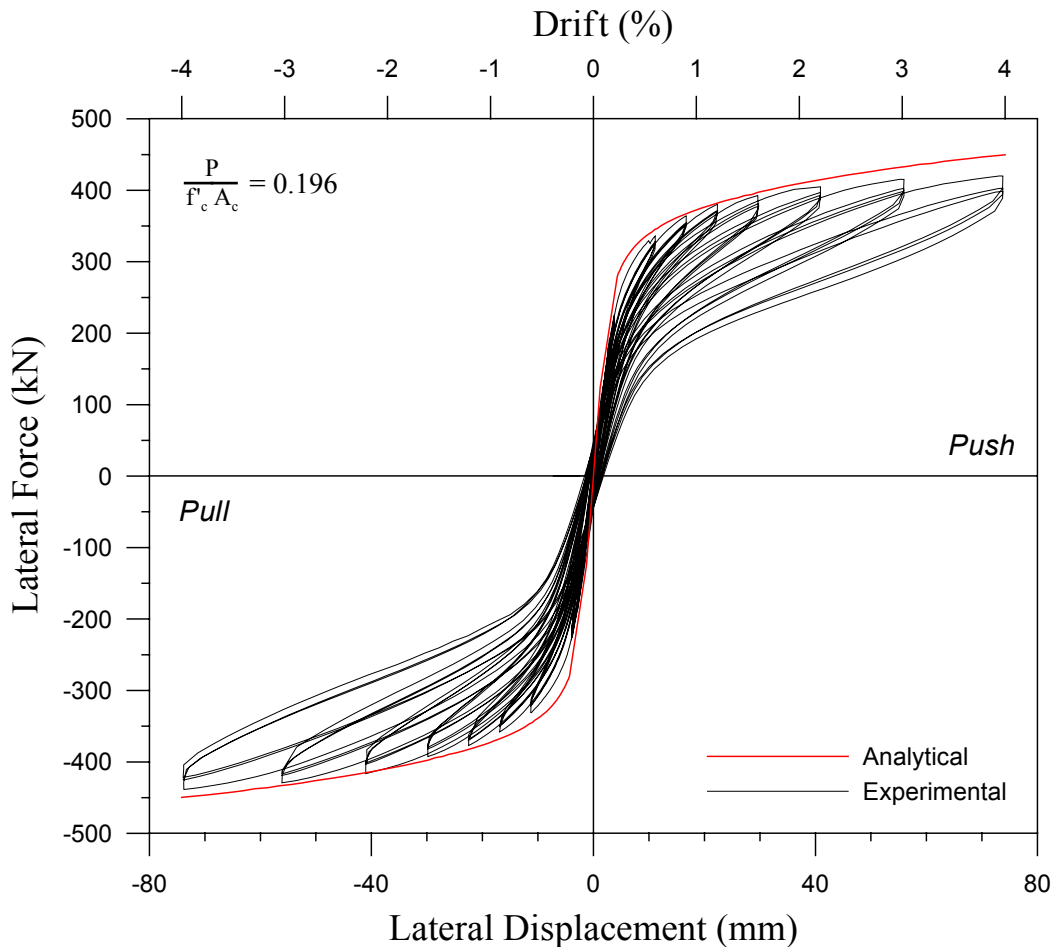

Figure 5.51 JH4 – Test 1 Force-displacement response

The analytical force-displacement response envelope is shown along with the experimental response in Figure 5.51. The analytical initial elastic stiffness matches well the experimental. For drift levels around 0.5%, the analytical column strength is slightly higher than the observed. At moderate to high drift levels, the column strength is well predicted by the analytical model, with a maximum error of 7% at 4% drift. Acceptable agreement is achieved in general for the entire column response.

The decrease of the initial loading stiffness of the column as a function of imposed drift level is shown in Figure 5.52. At moderate drift levels, the stiffness had decreased by approximately 50%, while at the maximum imposed drift of 4.0% the initial loading stiffness was 35% of the original. The decrease in stiffness with increasing drift observed for unit JH4 is almost identical to that for JH3.
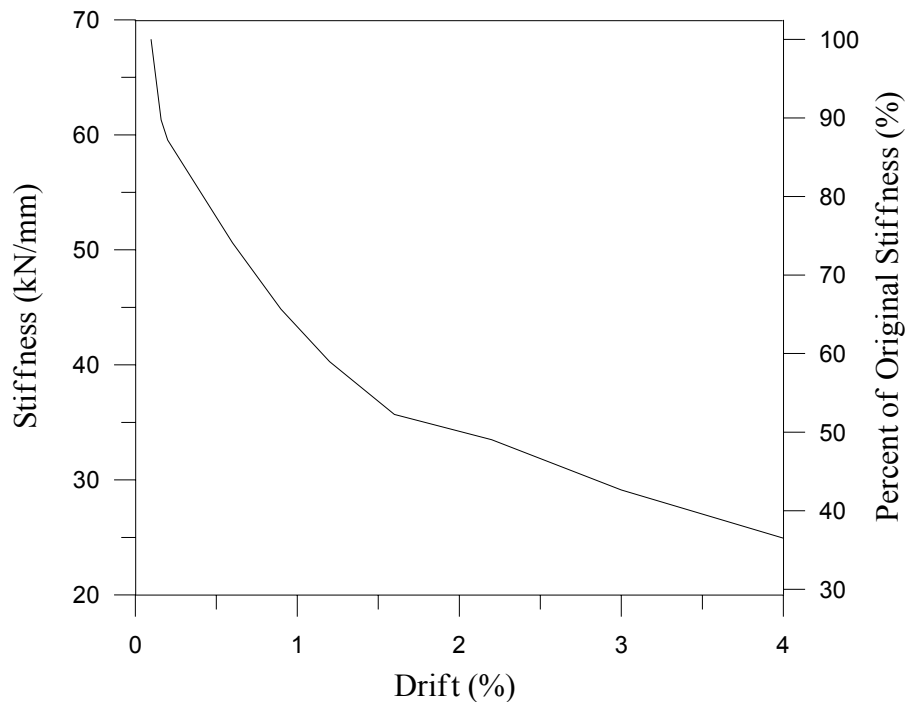

Figure 5.52 JH4 – Test 1 Initial loading stiffness versus drift

The hysteretic energy dissipation of the specimen, indicated by the area within the force-displacement loops, was low for all drift levels. The calculated damping coefficient is shown as a function of drift in Figure 5.53. It can be seen that the damping was essentially constant throughout the test, averaging approximately 5%.
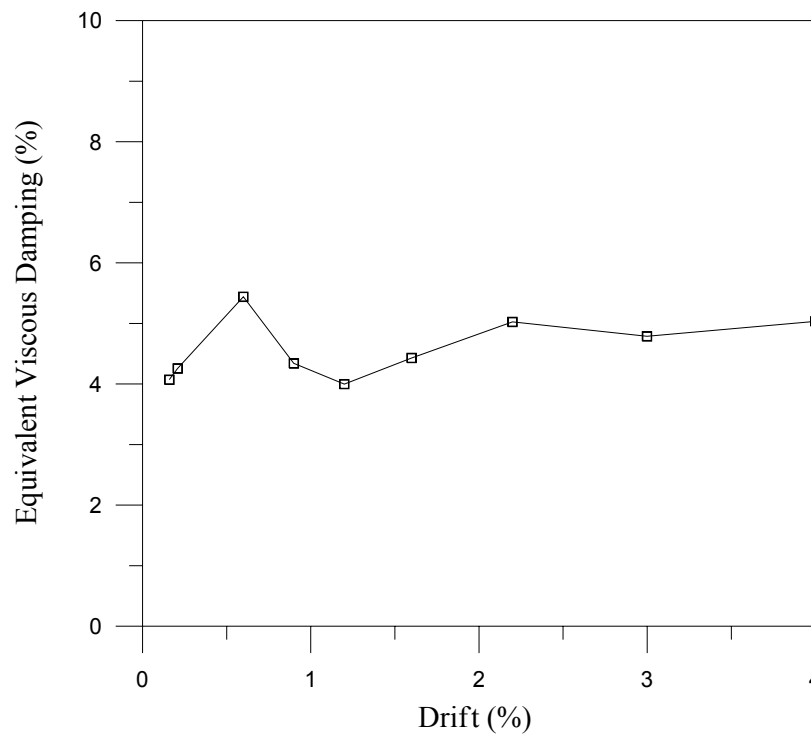

Figure 5.53 JH4 – Test 1 Equivalent viscous damping versus drift

5.7.3 Test Data

Profiles of strains measured in the steel jacket, transverse spiral, prestressing steel, and of curvature along the column height are shown plotted as a function of drift in this section. Again, the plots were constructed using data recorded at peak displacement during the first cycle of loading and include data for cycles between 0.2% and 4.0% drift.

Column Curvature

Curvature along the column height is shown in Figure 5.54. Similar to that observed for tests on specimen JH3, the column rotation was concentrated at the base of the column as evidenced by the high curvatures there. Curvatures shown at approximately 460 mm above the footing are significantly higher for the push direction than the pull direction of loading. This discrepancy was caused by slippage of the north linear potentiometer at that level during early stages of testing. The curvatures at 330 mm above the footing are noticeably higher for the pull direction of loading. This was also caused by slippage of the curvature measuring instrumentation at that level. As was explained for specimen JH3, it is believed that the curvatures shown at the base are higher than actual due to the discontinuity of the section there. Thus, the curvature profiles as shown give more of a qualitative than quantitative measure of column curvature. When profiles for the first test of JH3 and JH4 are compared, it can be seen that almost identical curvatures were measured at the column base. Since the curvatures and observed neutral axis depths for the two tests are similar, concrete compressive strains at the base of JH4 should be of the same magnitude as that calculated for specimen JH3. The predicted longitudinal compressive strain at the extreme fiber of the critical section was 0.019. This value is lower than the experimental value of 0.030 calculated for the first test of specimen JH3 in Section 5.5.3, but is reasonable in light of uncertainties regarding the estimated neutral axis and the calculated curvature from the experimental data.

Prestressing Steel Strain

Figure 5.55 shows the analytical and experimental tendon strain increase. It can be seen that the predicted curve overestimates the incremental tendon strain increase, with errors greater than 20% except at drifts of 3.0% and 4.0%. It is found that the error does not significantly affect the predicted response of the column since the prestress force increase associated with the strain increase is but a small fraction of the total vertical load acting on the column. As illustrated previously, the analytical model adequately predicted the force-displacement response of the column despite the tendon strain increase error. It is envisioned that for typical axial load and initial prestress force levels, the theoretical

response should be relatively insensitive to even considerable errors in the predicted prestress force increase. Over prediction of the strain increase implies that the neutral axis depth is underestimated by the analytical model (see Eq. 2.16).
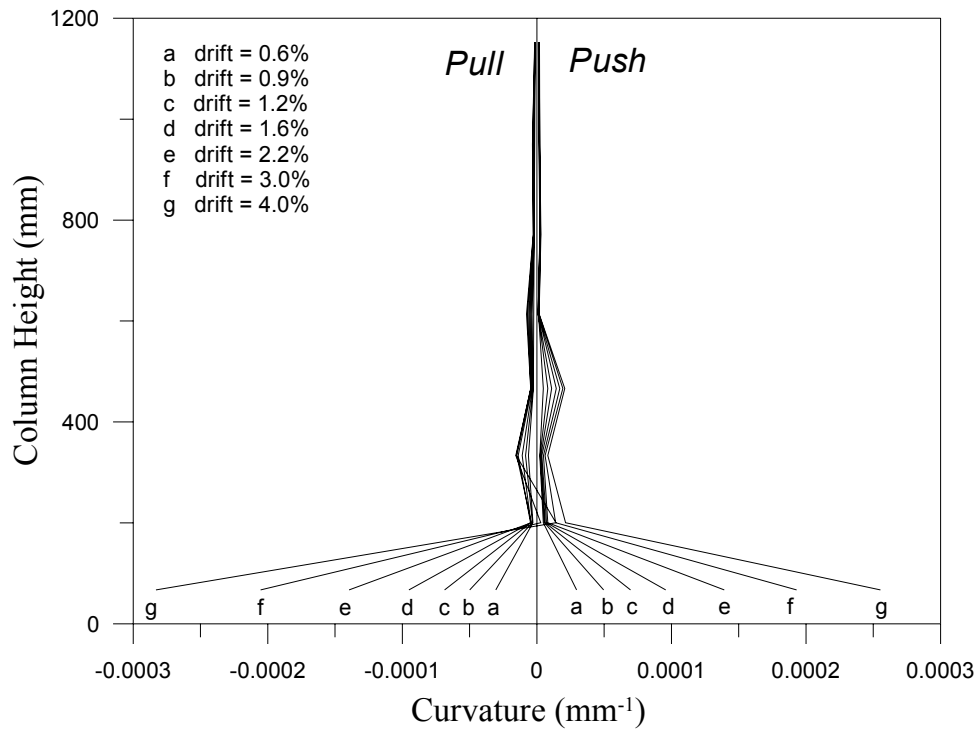

Figure 5.54 JH4 – Test 1 Curvature along column height

Steel Jacket Strain

Hoop strains in the steel jacket at the north and south generators are shown in Figures 5.56 and 5.57, respectively. The strain gage mounted at the top of the jacket at the north side did not function properly and was not used in the strain profile. The strain profiles are similar to those observed for specimen JH3, with increasing hoop strain down the height of the jacket. Higher strains near the toe of the jacket are expected since the larger concrete longitudinal compressive strains at the column compression toe cause greater dilation of concrete. Significant increases in strain from one drift level to the next were observed, starting at 1.6% drift. The maximum observed strains at the base of the jacket were on the order of several times the yield strain. Hoop strains at a height of 175 mm on

the jacket were significantly higher for the push direction of loading than the pull. Upon inspection of the data, it was found that the north gage at that location read around 2000 $\mu\varepsilon$ prior to the start of the test. Similar readings for the north and south gages are obtained if the north gage is biased by the above amount.

The jacket hoop strains measured at the east and west generators are shown in Figures 5.58 and 5.59, respectively. In general, the strains increase down the height of the jacket, due to the confining effect of the jacket near the base. The maximum strains are below the yield strain of the material and are slightly higher than those observed for the thinner jacket of specimen JH3. The vertical strains at the east and west sides of the jacket are shown in Figures 5.60 and 5.61. High compressive strains, well above the material yield, for the east gage at 175 mm above the bottom of the jacket are believed to be spurious and not representative of the actual jacket strain.

Transverse Spiral Strains

Strain profiles for the transverse reinforcement in the upper column segment for the north, south, east and west generators are shown in Figures 5.62, 5.63, 5.64, and 5.65, respectively. The hoop strains increase down the height of the segment at the north generator for the push direction and at the south generator for the pull direction. Maximum strains for the north and south sides occur near the bottom of the segment at a drift of 4.0% and are on the order of 800-900 $\mu\varepsilon$. The maximum strains are well below the material yield strain of approximately 2200 $\mu\varepsilon$. Strains at the north generator for the pull, and south generator for the push, are low since the concrete is not dilated on the tension side of the section. Hoop strains at the east and west sides of the column are minimal because the column shear is carried by the horizontal component of the diagonal compression strut formed between the column top and column compression toe.
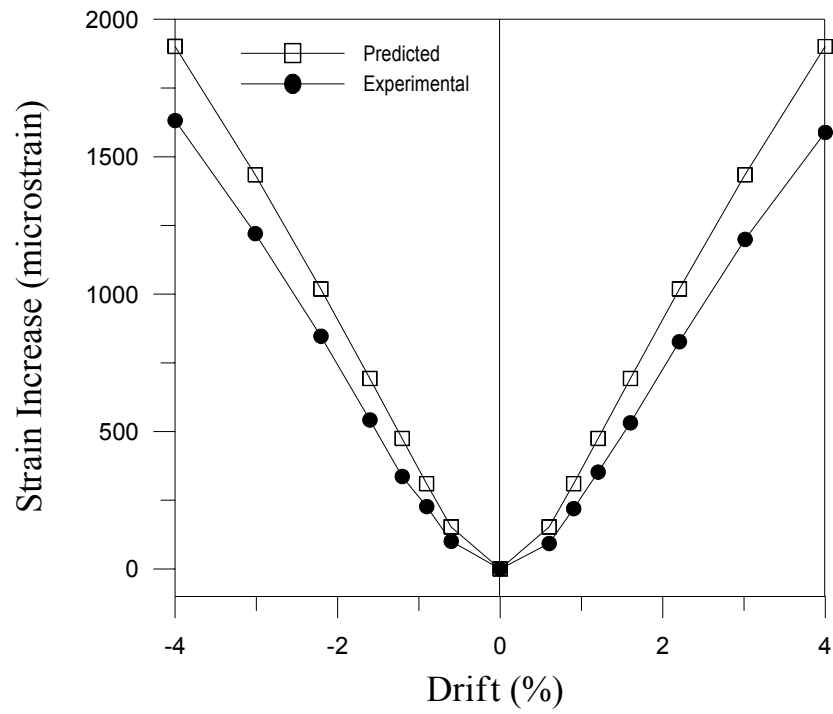
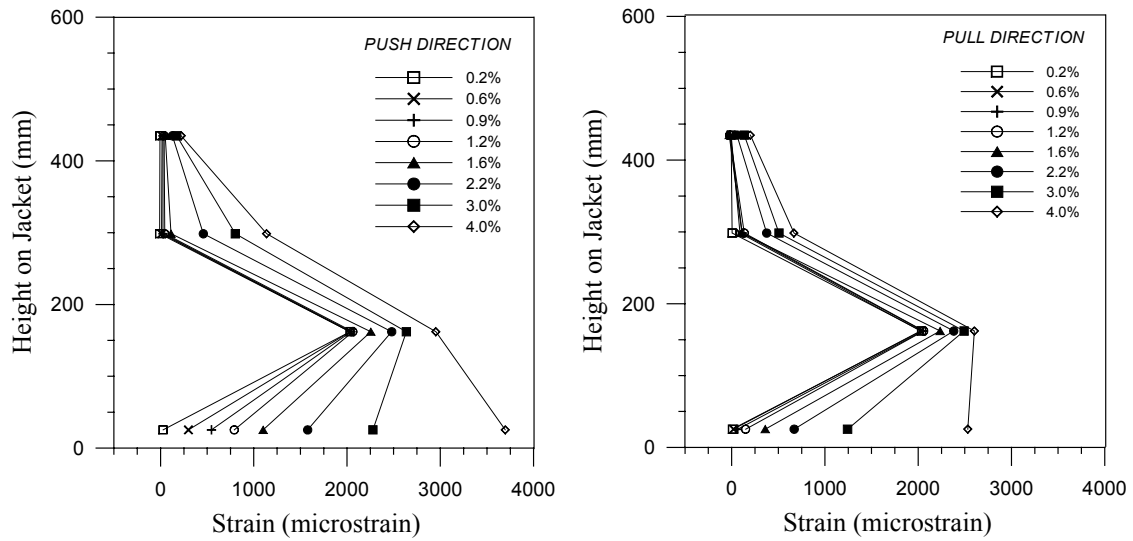Figure 5.55 JH4 – Test 1 Predicted and experimental tendon strain increase

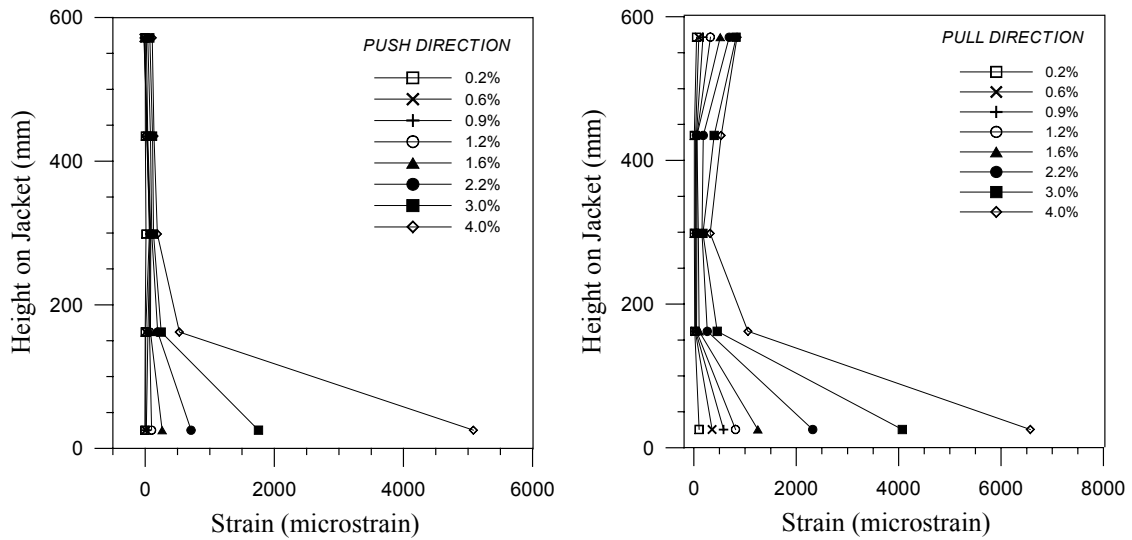Figure 5.56 JH4 – Test 1 Jacket hoop strain at north generator

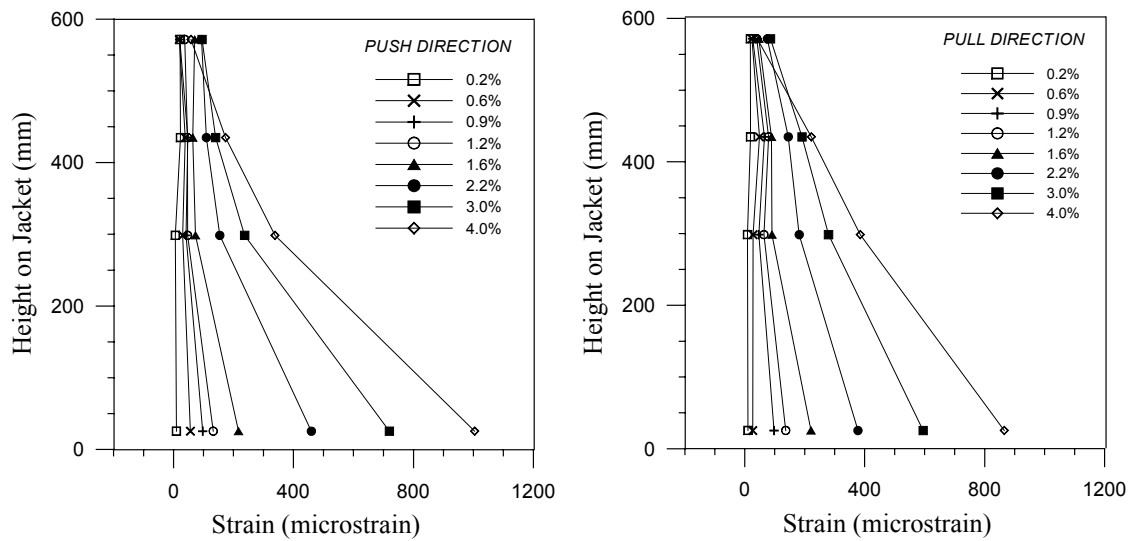Figure 5.57 JH4 – Test 1 Jacket hoop strains at south generator

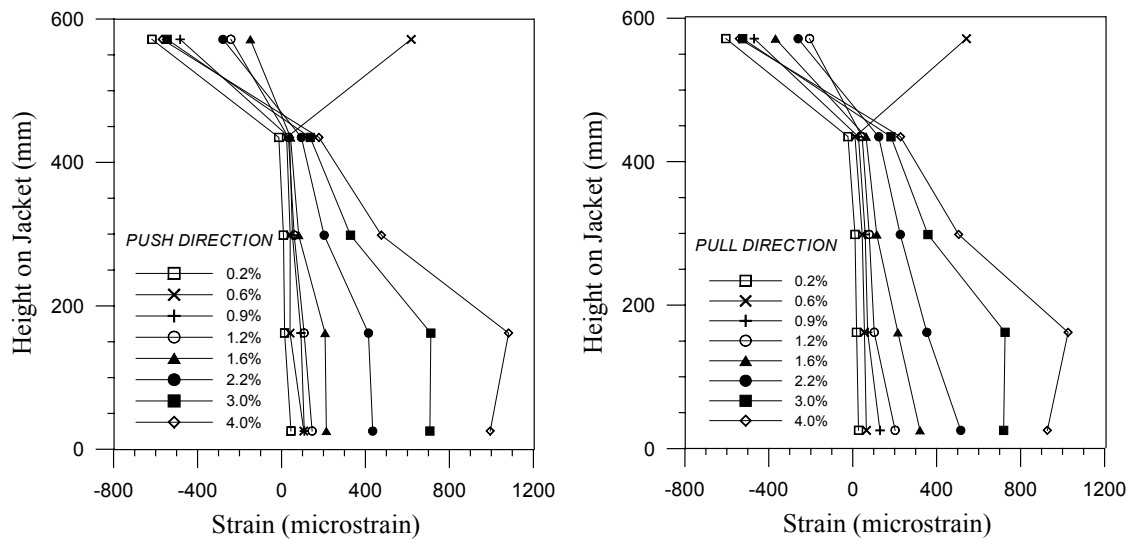Figure 5.58 JH4 – Test 1 Jacket hoop strains at east generator

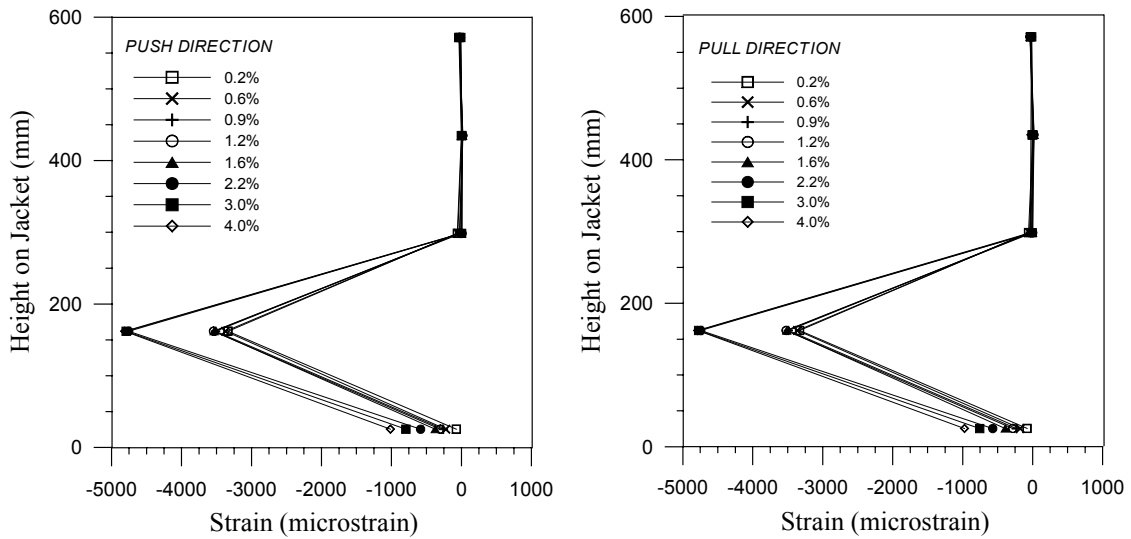Figure 5.59 JH4 – Test 1 Jacket hoop strains at west generator

Figure 5.60 JH4 – Test 1 Jacket vertical strains at east generator
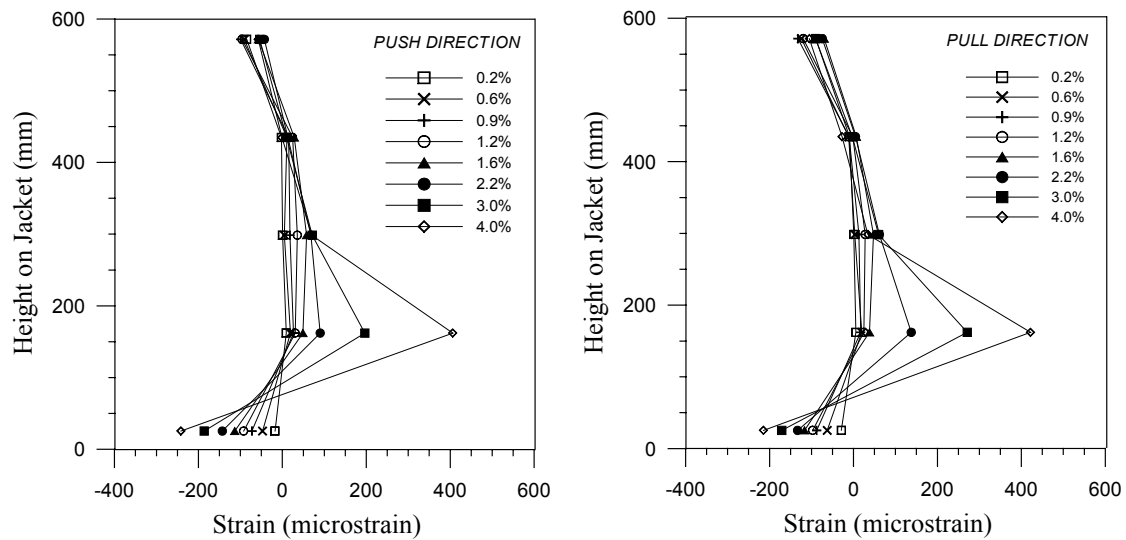

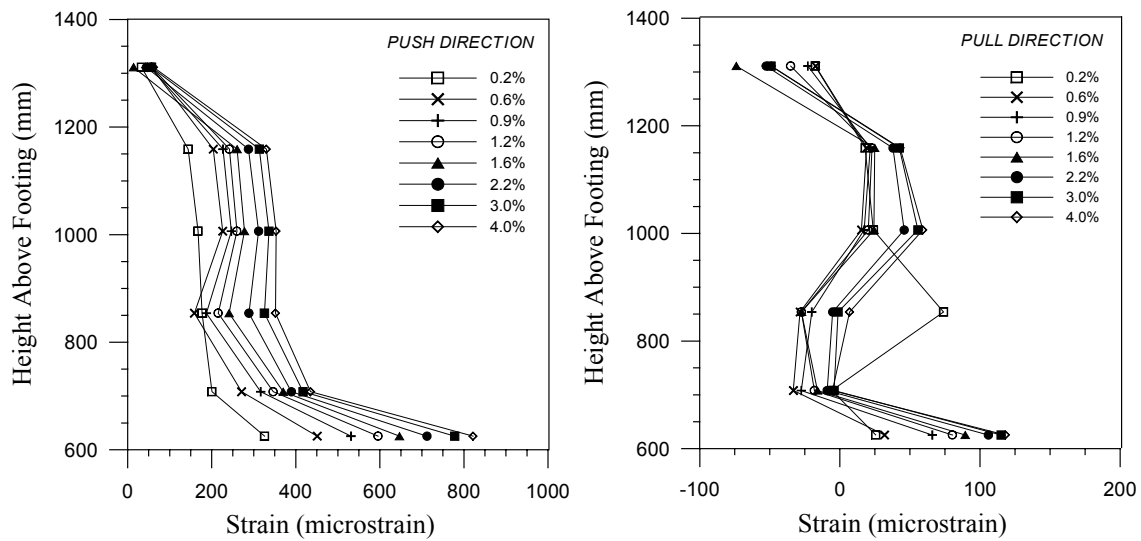Figure 5.61 JH4 – Test 1 Jacket vertical strains at west generator

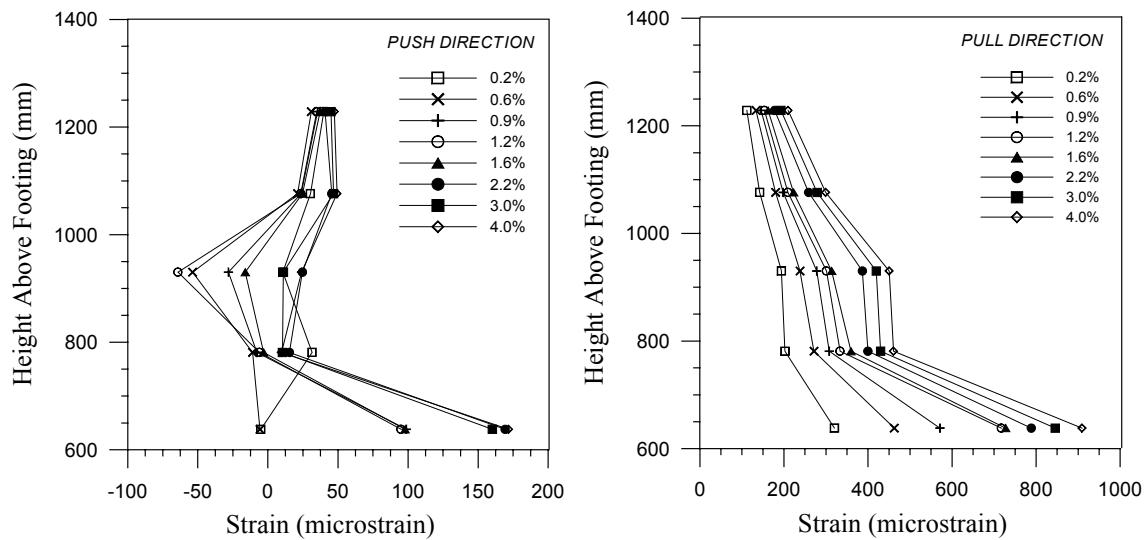Figure 5.62 JH4 – Test 1 Spiral strains at north generator

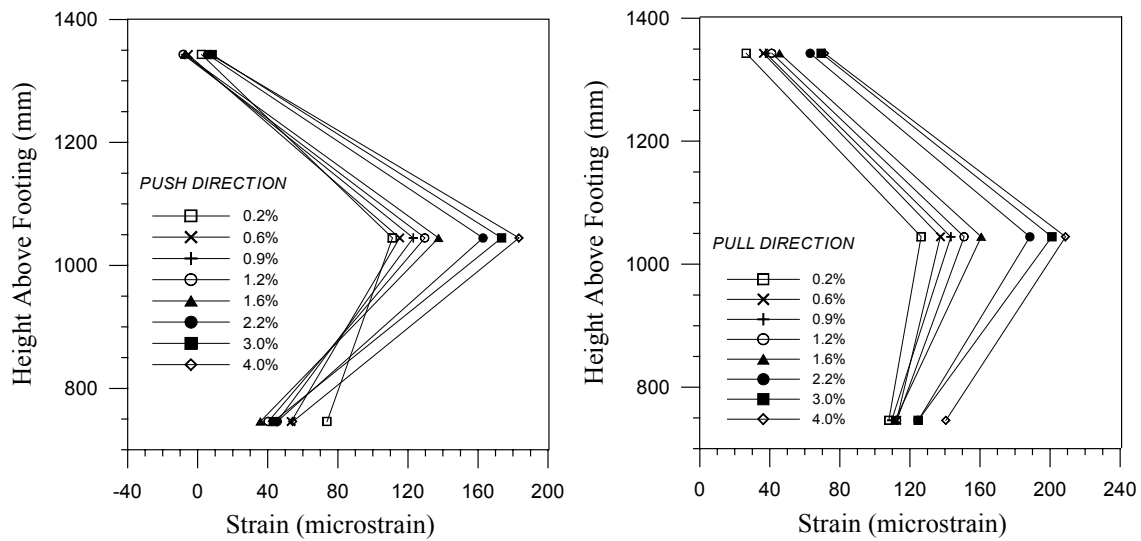Figure 5.63 JH4 – Test 1 Spiral strains at south generator

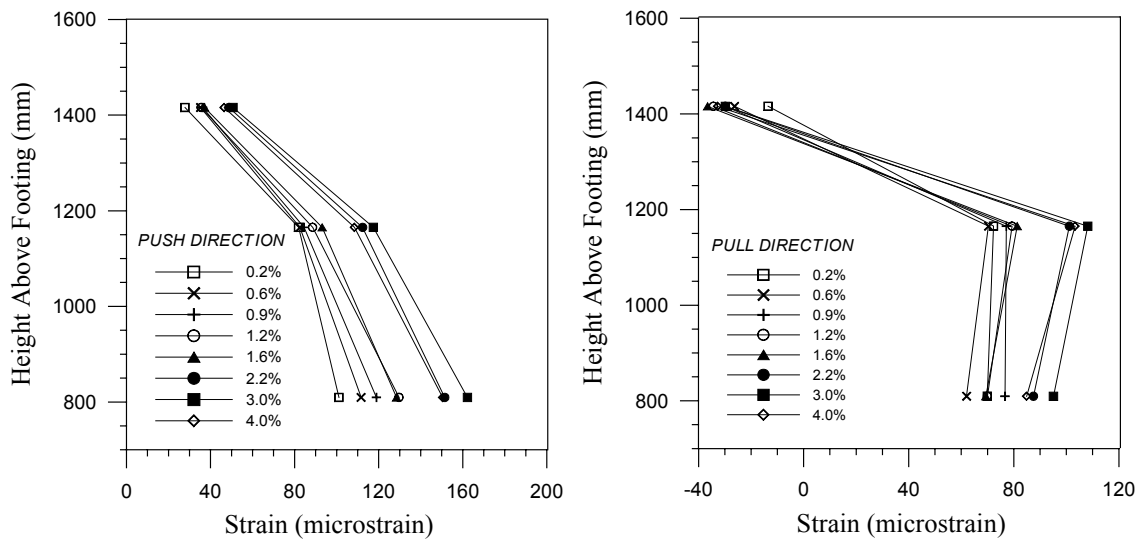Figure 5.64 JH4 – Test 1 Spiral strains at east generator

Figure 5.65 JH4 – Test 1 Spiral strains at west generator

5.8 Experimental Results – Specimen JH4-T2

5.8.1 Observations under Repeated Cyclic Loading

The planned loading sequence after epoxy grouting the base crack and re-stressing to the higher force level called for one cycle each to be performed in force control at one-half, one, and one-and-a-half times the theoretical force to cause decompression of the extreme tension fiber at the critical section (P_1). After switching to displacement control, three cycles were to then be performed at twice the decompression force. The displacements observed during the first cycle at **1.5 x P_1** however, were larger than those predicted for the next target level of **2 x P_1**. It was thus decided to switch to displacement control after the first cycle at **1.5 x P_1** and then perform two more cycles at that level.

A problem with the actuator control system was noticed at **-1.5 x P_1**, and the test was paused. A faulty connection between the controller and the actuator was discovered and fixed. Upon reloading during the second cycle, it was immediately noticed on the x-y chart recorder that the column stiffness had increased significantly. This was not expected and thus the test was paused a second time to recheck the controls system. It was determined that prior to fixing the bad connection, the force readings indicated for the actuator were lower than actual. Thus, two more cycles were performed at a drift equal to that observed for the first cycle. Forces indicated below for cycles at **0.5 x P_1**, and **P_1** are likely lower than the actual force applied to the specimen

±0.5 P_1 (P_{max}= +72.8 kN and P_{min}= -73.5 kN)
No cracking was observed for either direction of loading.

±P_1 (P_{max}= +145.0 kN and P_{min} = -145.5 kN)
Cracking at the base of the column was noted for both the push and pull directions. The crack extended approximately 125 mm into the section from the extreme tension fiber.

3 cycles at 0.34% drift (P_{max}= 258.4 kN and P_{min}= -260.4 kN)

The base crack extended to about 225 mm from the tension edge for cycles at this drift

3 cycles at 0.6% drift (P_{max}= +328.8 kN and P_{min}= -339.2 kN)

The crack at the base of the column extended to mid-depth of the section. In the upper column segment, flexural cracking 225 mm above the jacket at locations of previous cracks (from the first test) was observed during both the first push and pull loading.

3 cycles at 0.9% drift (P_{max}= +377.3 kN and P_{min}= -384.0 kN)

Minor extension of cracks in the upper segment was observed, while the base crack extended to a distance of 230 mm from the compression edge. The crack opening at the column base at the tension edge was 2-3 mm.

It was at this drift level that spalling below the jacket at the compression toe was observed during the first test of specimen JH4. For this the second test however, the compression toe below the jacket at the column base had been repaired by epoxy injection of the residual crack and the extreme compression fiber consisted of epoxy rather than concrete. Thus, it was not possible to discern the state of the concrete within the region of the repair.

3 cycles at 1.2% drift (P_{max}= +410.1 kN and P_{min}= -413.4 kN)

Spalling of concrete below the jacket at approximately 150 mm from the compression edge was observed at this drift. Note that the location where the crushing was observed coincided with the point where the epoxy repair ended and "good" (or undamaged concrete from the first test) concrete began. The depth to the neutral axis from the extreme compression fiber was on the order of 210 mm. The crack width at the base was noted to be 4-5 mm.

3 cycles at 1.6% drift (P_{max}= +437.2 kN and P_{min}= -439.5 kN)

The neutral axis depth continued to decrease; measuring approximately 185 mm. Lift-off of the column base at the tension edge was 6 mm.

3 cycles at 2.2% drift (P_{max}= +459.9 kN and P_{min}= -465.3 kN)

The neutral axis and crack width at the column base were approximately 160 mm (from the compression edge) and 9 mm respectively. Crushing of the epoxy at the column compression toe was noted.

3 cycles at 3.0% drift (Pmax= +471.5 kN and Pmin= -484.0 kN)

A reduction in the depth of the neutral axis to 125-150 mm was noted. The base crack width was approximately 12-13 mm. Slippage of the jacket with respect to the core concrete was noticed at the bottom south curvature rod location where the jacket was observed to be bearing on the top of the rod.

3 cycles at 4.0% drift (P_{max}= +479.1 kN and P_{min}= -492.4 kN)

The lift-off of the bottom of the column from the footing top at the tension edge was around 17 mm. The depth to the neutral axis remained unchanged. At the compression toe, the gap between the jacket and the footing was reduced to 9 mm for the push direction and to about 12 mm for the pull direction.

3 cycles at 5.0% drift (P_{max}= +475.5 kN and P_{min}= -493.3 kN)

The neutral axis depth again appeared unchanged while the crack at the base widened to about 21 mm. A slight decrease in the gap width between the jacket toe and the top of the footing at the compression side was observed for both directions of loading.

3 cycles at 6.0% drift (P_{max}= +467.1 kN and P_{min}= -490.6 kN)

The crack opening at the column base increased to approximately 25 mm at the extreme tension fiber. The jacket was observed to be nearly touching the top of the footing at the column compression toe, with the gap there reduced to around 5 mm. The wide crack

opening at the footing level associated with the rotation of the column about its compression toe is visible as well.

Test End

As was the case for the first test of specimen JH4, the damage to the column was concentrated at the column base below the jacket where high longitudinal compression strains that developed caused concrete crushing. No spalling was observed in the upper, non-jacketed column segment. Cracks in the upper column segment showed no inclination and closed completely after testing was complete. No damage to the footing at the interface with the column base was observed. Fracture of the prestressing steel did not occur. The residual drift of the system was 0.1%.

5.8.2　Force – Displacement Response

The lateral force–displacement response for the second test of specimen JH4 is displayed in Figure 5.66. The force-displacement loops are symmetric and approximately equal strengths were obtained for both directions of loading. The beginning of significant non-linear response occurred at about 325 kN, a force level corresponding to 2.2 times the theoretical force to cause decompression at the column base. The peak column strength for the push direction of loading was 480 kN and occurred at a drift of 4.0%. For the pull loading direction, a maximum strength of 490 kN was achieved at a drift level of 5.0%. Little strength degradation occurred during cycles at higher drift levels, with a drop in strength of only 0.5% and 2.5% observed at the maximum imposed drift of 6.0% for the push and pull directions, respectively.
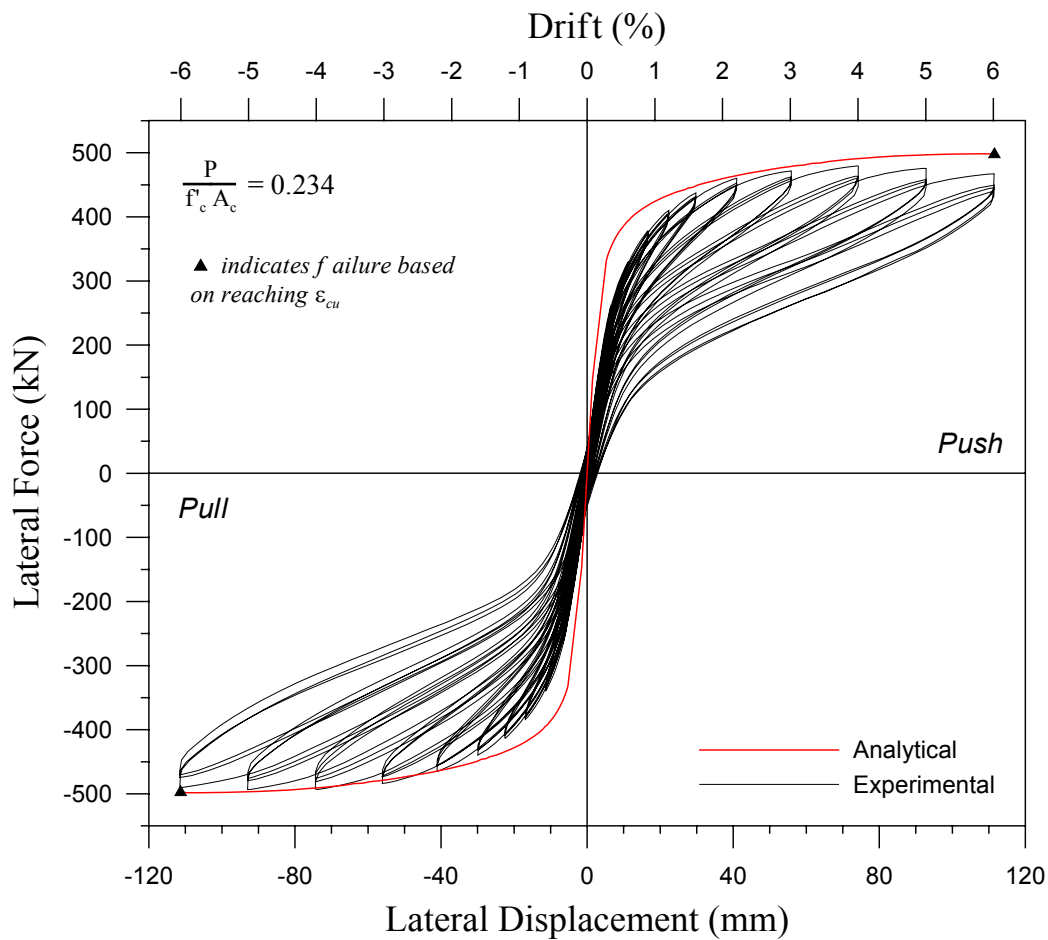

Figure 5.66 JH4 – Test 2 Experimental force-displacement response

The analytical force-displacement response envelope is shown along with the experimental in Figure 5.66. Similar to what was observed for the second tests of other units, the initial stiffness of the specimen is not well predicted. This is again attributed to the fact the column had already been tested, and the repair measures did not restore the column to a damage free state. The match between the predicted and experimental strength at moderate drifts is good, with predicted strengths within about 3% of the observed. At higher drifts, the predicted response deviates more significantly for the push loading direction with column strength overestimated by 7% at the maximum imposed drift of 6.0%. The slight difference in strength between the two directions of loading did not appear to be caused by eccentricity of the applied axial load, as was the case for other tests. In general, the analytical and experimental curves correlate well.

The initial loading stiffness of the specimen for both the first and second test is shown in Figure 5.67 as a function of imposed drift. The epoxy grouting of the base crack after the first test restored the stiffness of the column to approximately 70% of that observed for the first test. At drifts of 1.6% and 2.2%, the stiffness was identical to that observed during the first test, while at higher drifts, the initial stiffness for the second test was actually higher than the first. Deterioration of the column stiffness at high drifts was not as significant as that observed for the second test of specimen JH3. At the maximum imposed drift of 6.0%, the stiffness of specimen JH3 had decreased to less than 10% of its original value, while that for JH4 had decreased to 40% of the original stiffness. This is likely due to the higher level of confinement at the column base provided by the thicker jacket of specimen JH4.

The hysteretic energy dissipation of the specimen was low for all levels of drift. The equivalent viscous damping ratios calculated for each drift level are shown in Figure 5.68. It can be seen that the hysteretic damping was approximately constant, increasing only slightly from around 4% for low drifts, to 5% for the higher drift levels. The damping ratios calculated for the first test of specimen JH4 are also shown in the figure. The system damping was approximately the same for both tests.
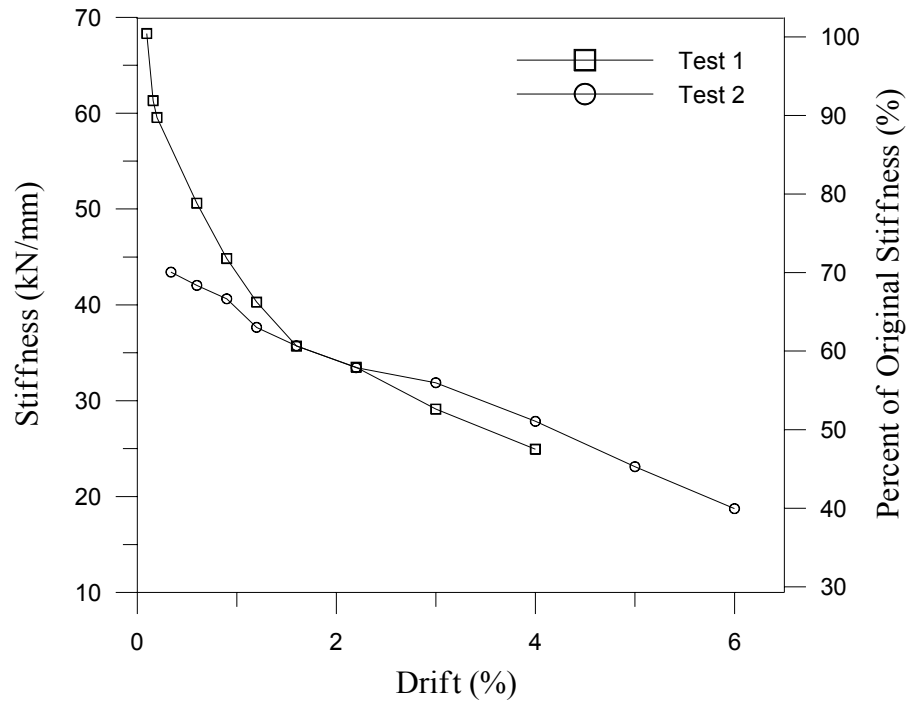
Figure 5.67 JH4 − Test 2 Initial loading stiffness versus drift
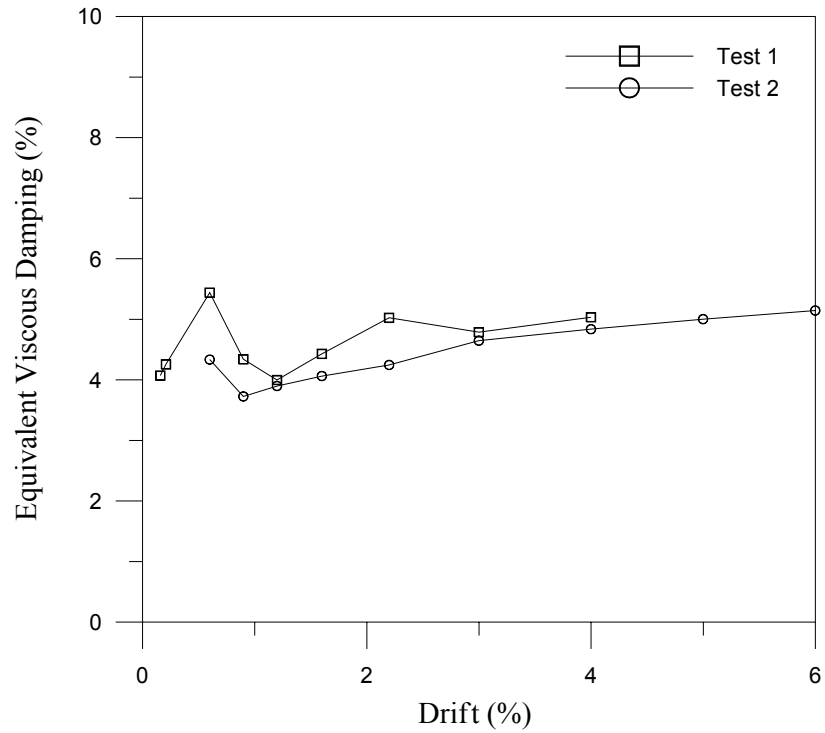

Figure 5.68 JH4 − Test 2 Equivalent viscous damping versus drift

5.8.3   Test Data

Strain and curvature profile plots are presented in this section. The profiles shown are for drifts between 0.34% and 6.0% unless noted otherwise.

Column Curvature

Curvature along the height of the column is shown in Figure 5.69. Curvatures at 6.0% drift are not shown since the linear potentiometers did not possess enough displacement capacity in either compression or tension. The curvature is noted to be high at the bottom of the column where the wide crack formed as the column displaced laterally.   The observed curvatures are nearly identical to those observed during the first test. It is again mentioned that the actual curvatures at the base are likely lower than the calculated, as explained previously.   An approximate value for the concrete strain at the compression edge is calculated as:

$$\varepsilon_c = 0.8 \; \phi_{ave} \, c \; = 0.8 \, (0.00034 \; mm^{-1}) \; 135 \; mm \; = 0.038$$

where ϕ_{ave} is the average of curvatures calculated for the push and pull direction at 5.0% drift, c is the observed neutral axis distance from the compression edge at the base of the column and the 0.8 is to account for the curvature being overestimated as described previously. The predicted extreme fiber concrete compression strain at 5.0% drift was 0.026.

Prestressing Steel Strain

The predicted incremental tendon strain for the second test is shown along with the experimental in Figure 5.70. In general, analytical prediction overestimated the tendon strain increase. Despite the observed error, the model gives an acceptable approximation to the actual behavior since as stated previously, the predicted column force-displacement response should be fairly insensitive to errors in the predicted prestress force. Again, the over prediction of strain increase implies an under prediction of neutral axis depth.
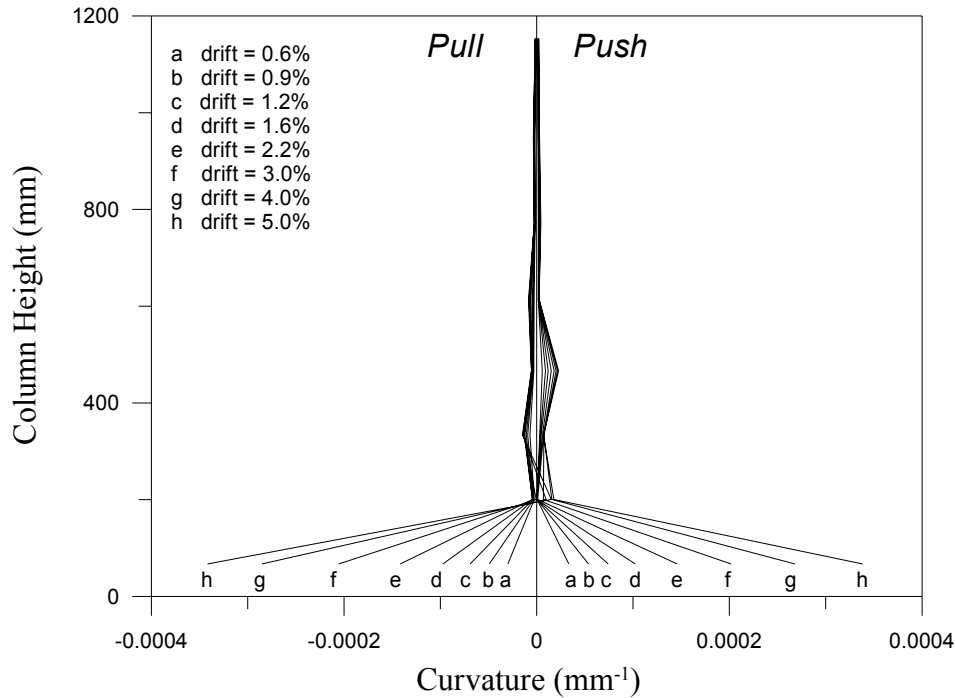
209

Figure 5.69 JH4 – Test 2 Curvature along column height

Steel Jacket Strain

Hoop strains in the steel jacket at the north, south, east and west generators are shown in Figures 5.71, 5.72, 5.73, and 5.74, respectively. The hoop strains are seen to be increasing down the height of the jacket. The high hoop strains near the toe of the jacket at the north and south generators are caused by dilation of the concrete core due to localized high compressive strains in the concrete. The maximum strains at the base were observed at a drift of 6.0% and were approximately 9000 $\mu\varepsilon$ and 15,000 $\mu\varepsilon$ at the north and south sides of the jacket. These levels of strain are significantly higher than the material yield strain of around 1500 $\mu\varepsilon$, and slightly lower than those observed during the second test of specimen JH3. Strains at the east and west generators are higher near the base due to the influence of the confining action of the jacket on the compressed concrete at the north/south generators. The strains are on the order of the material yield strain and are similar in magnitude to those observed for the second test of specimen JH3. The vertical strains in the jacket at the east and west sides of the column are shown in Figures

5.75 and 5.76, respectively. The strains are in general, compressive in nature and higher near the base. Considerably higher strains at the jacket toe are noted for the east generator.

Transverse Spiral Strains

Figures 5.77 through 5.80 illustrate the hoop strains in the spiral reinforcement of the upper column segment. The highest strains are at the base of the segment and are not much higher than those observed for the first test and are well below the yield strain. Thus, the spiral was not fully activated by dilation of the concrete at the compressive faces of the segment. The strains at the east and west faces of the segment are low, indicating that the column shear was carried primarily by the horizontal component of the diagonal concrete compression strut.
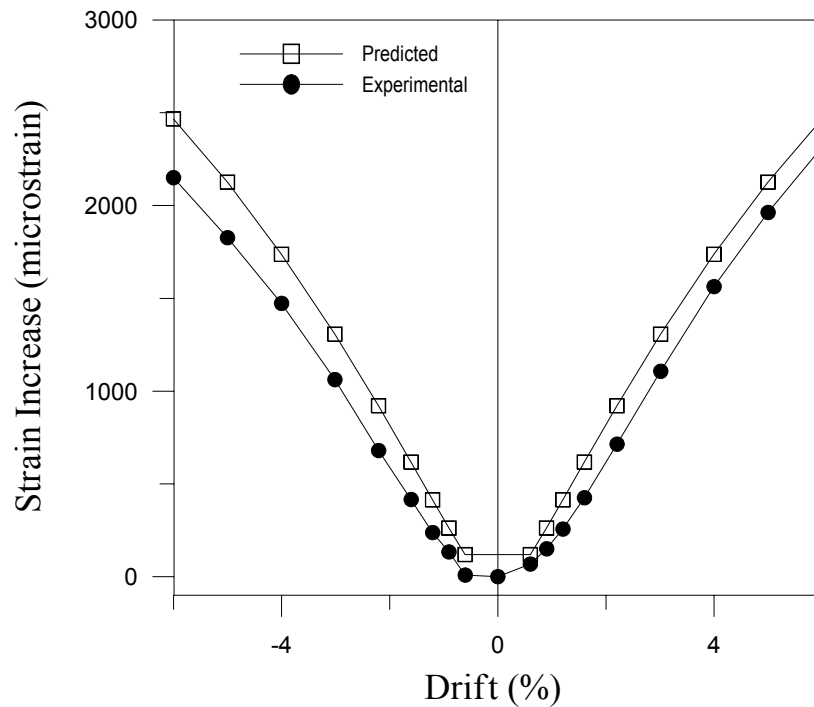

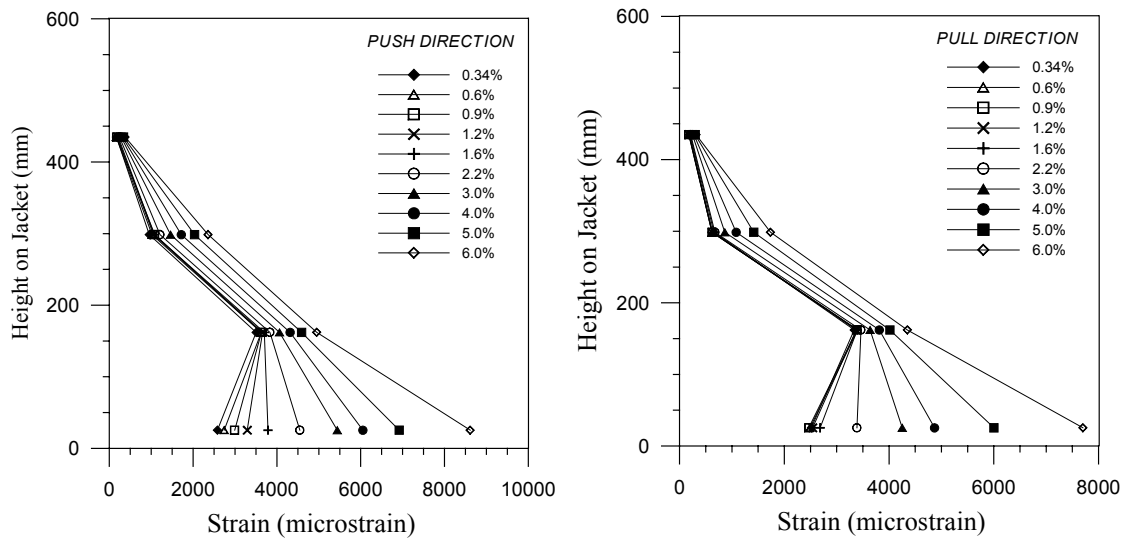Figure 5.70 JH4 – Test 2 Predicted and experimental tendon strain increase

Figure 5.71 JH4 – Test 2 Jacket hoop strain at north generator

Figure 5.72 JH4 – Test 2 Jacket hoop strain at south generator
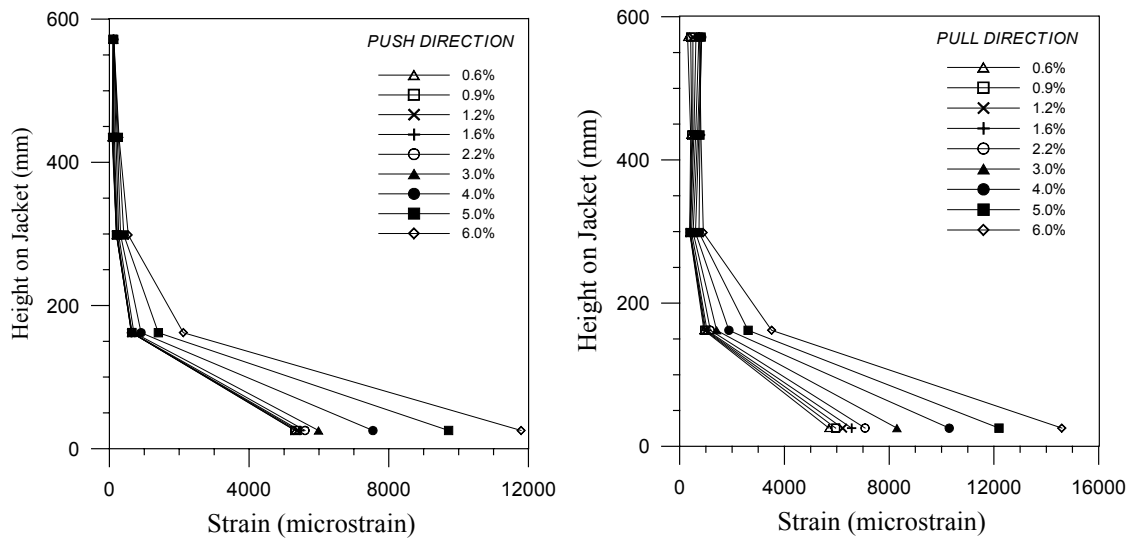
Figure 5.73 JH4 – Test 2 Jacket hoop strain at east generator

Figure 5.74 JH4 – Test 2 Jacket hoop strain at west generator
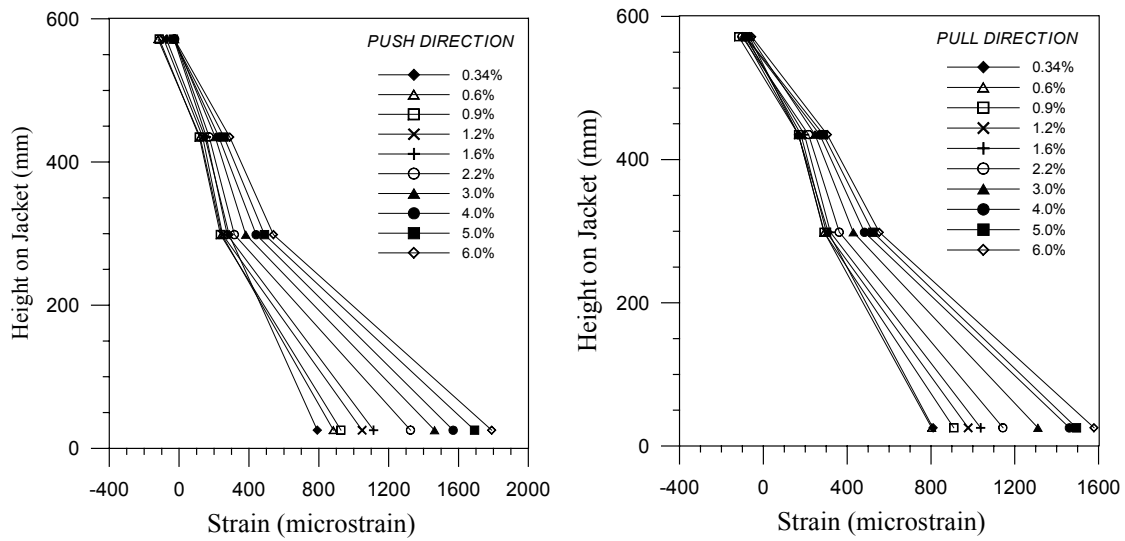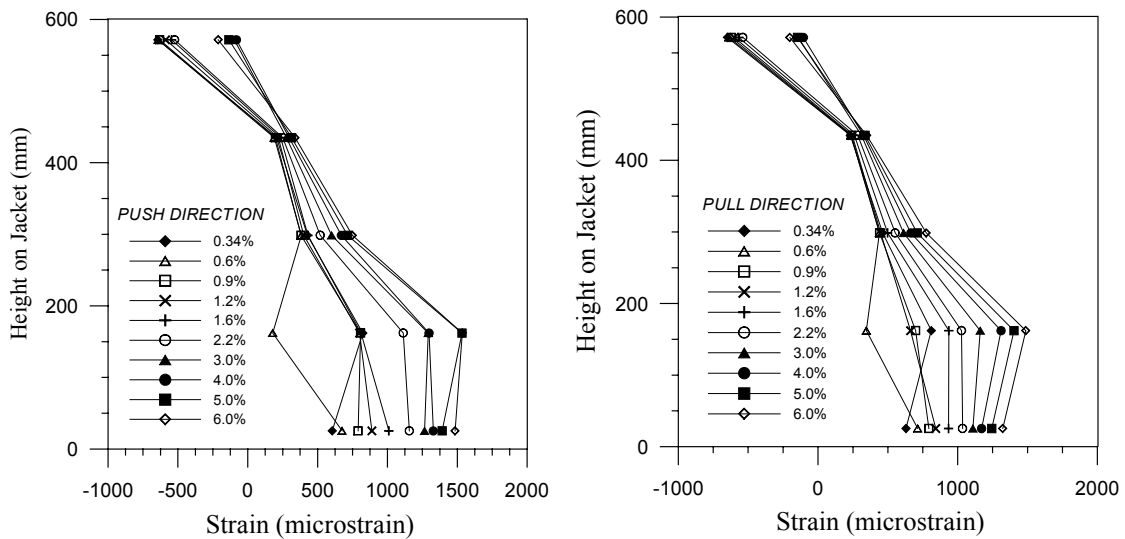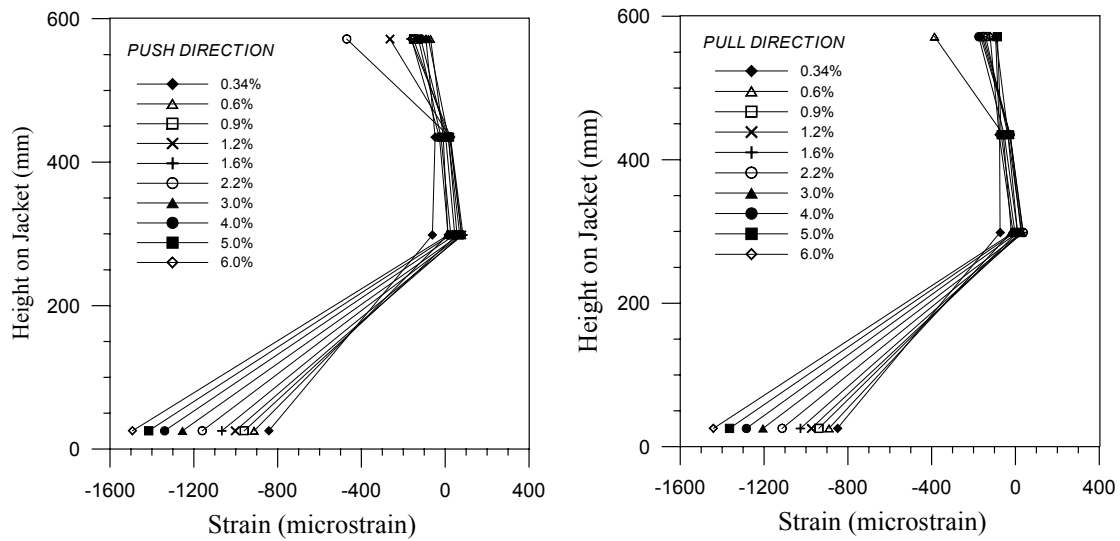
Figure 5.75 JH4 – Test 2 Jacket vertical strain at east generator
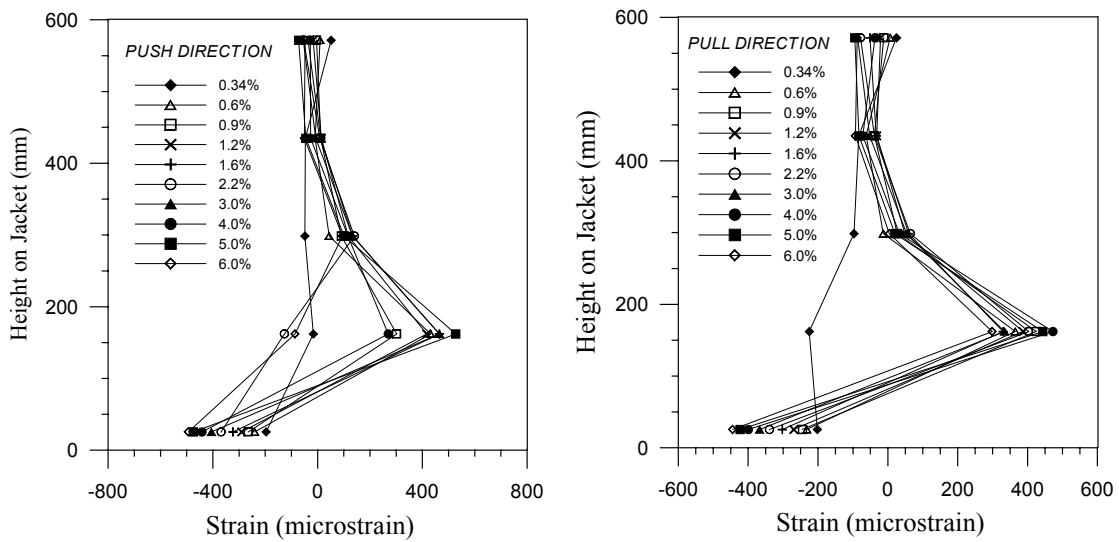

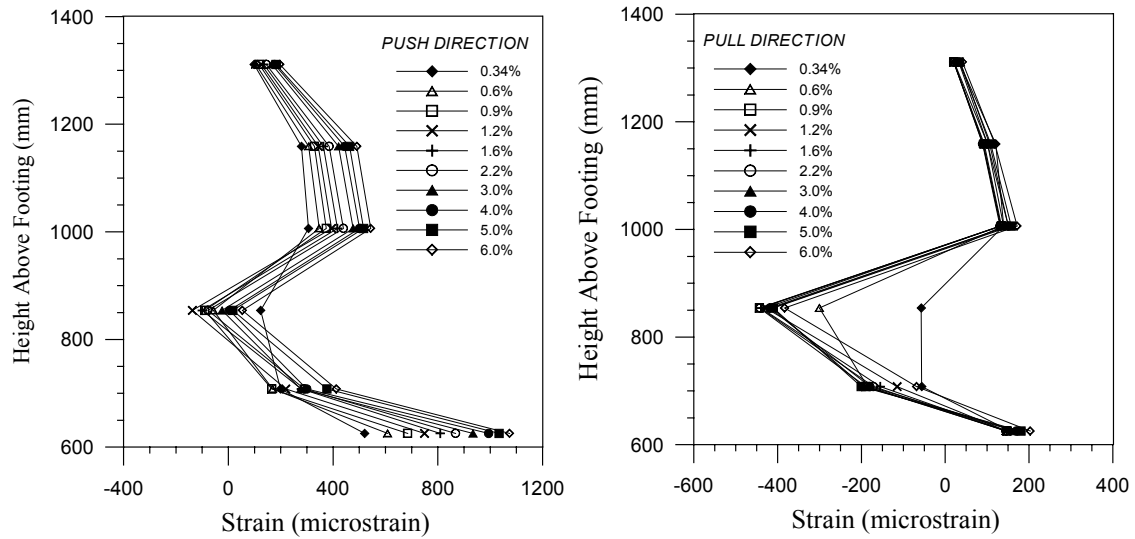Figure 5.76 JH4 – Test 2 Jacket vertical strain at west generator

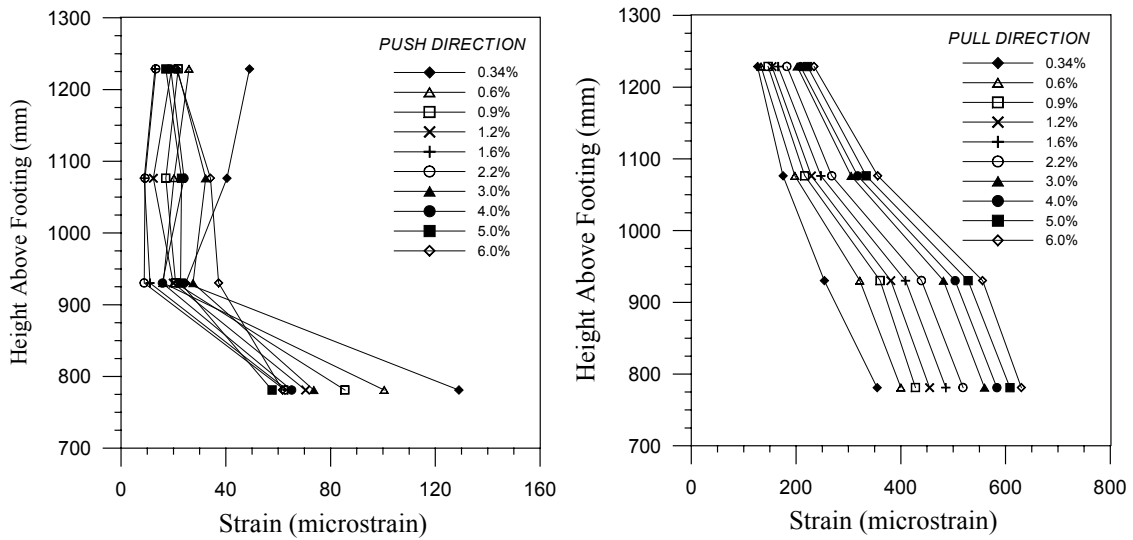Figure 5.77 JH4 – Test 2 Spiral strains at north generator

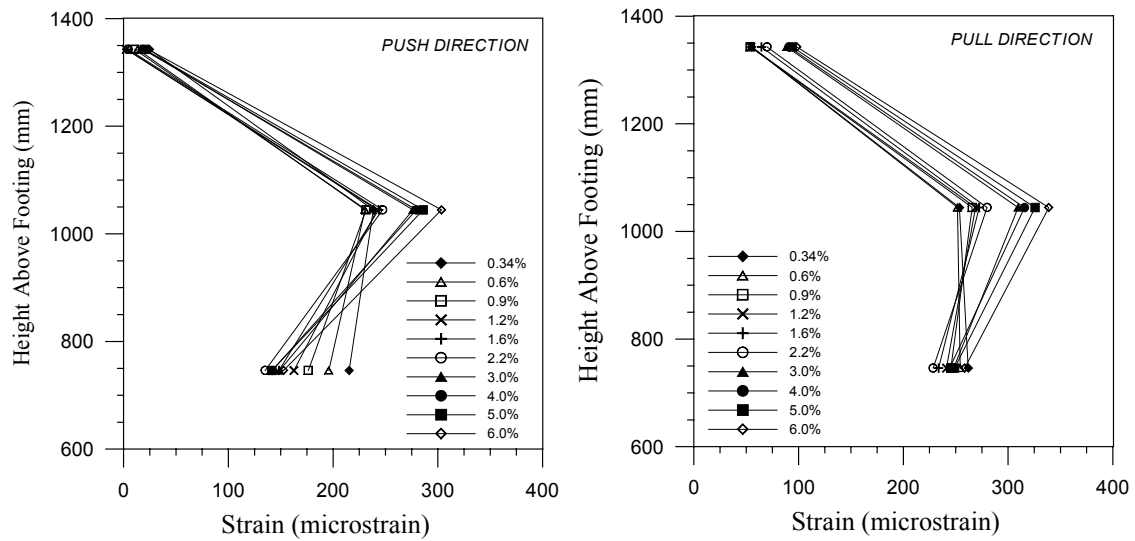Figure 5.78 JH4 – Test 2 Spiral strains at south generator

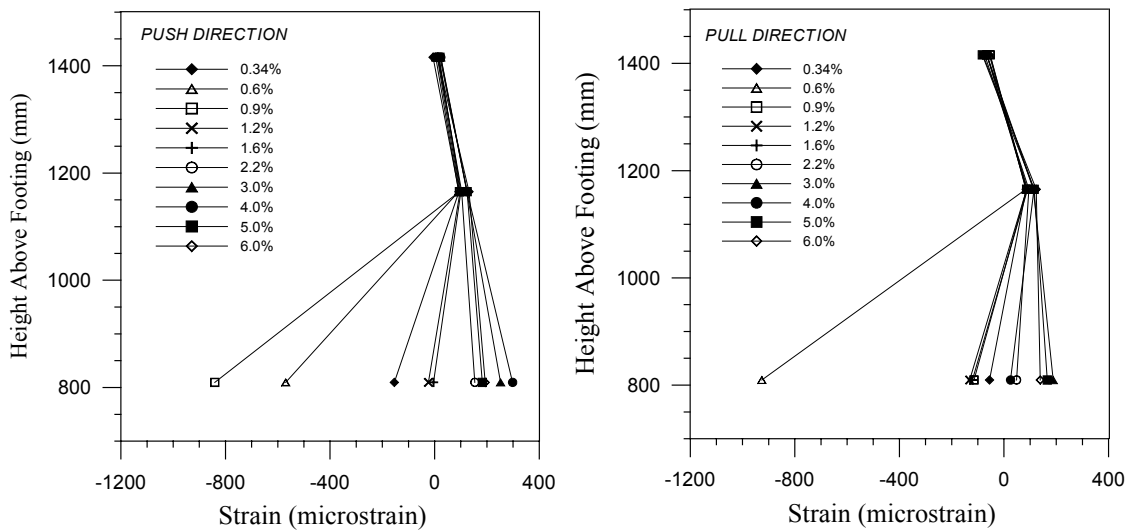Figure 5.79 JH4 – Test 2 Spiral strains at east generator

Figure 5.80 JH4 – Test 2 Spiral strains at west generator

5.9 Discussion of Results

The seismic design and experimental testing of two low aspect ratio precast segmental bridge columns were presented in this chapter.   Each test unit was reinforced longitudinally with an unbonded prestressing tendon and was tested a first time under a given level of total prestress force. After the first test, both units were repaired by epoxy grouting the base crack and then restressed to a higher tendon force level. Unit JH4 used a jacket thickness approximately twice that used in JH3.   A comparison of the performance of the specimens is given in this section.

Figure 5.81 shows the force-displacement response envelopes for the two tests of test unit JH3. It can be seen the maximum observed strength for the second test was only 10% higher than the maximum strength of first test. The prestress force was however 32 % higher for the second test. The drop in strength from 3.0% drift to 4.0% drift was more significant for the second test because of the higher axial load level. The experimental force-displacement response curves for the first and second test of unit JH4 are shown in Figure 5.82. An increase in the maximum strength over that observed for the first test of approximately 13% was observed for the second test. Similar to JH3, the second test total prestress force for JH4 was 32% higher than the first test.

The force-displacement response of the first test of unit JH3 is compared with that for JH4 in Figure 5.83. The responses of the columns are very similar and only at high drifts, where the strength of JH4 is slightly higher than JH3, do the envelopes deviate appreciably. The strength of JH3 peaked at about 3.0% drift while for specimen JH4, the maximum strength was attained at the maximum imposed drift of 4.0%. Figure 5.84 gives a comparison of the second test force-displacement envelopes for JH3 and JH4. Despite having an approximately equal total prestress force, the maximum strength achieved for specimen JH4 was approximately 8% higher than that for JH3. Similar to the first test, the strength of specimen JH3 reached a maximum at 3.0% drift while the maximum strength for JH4 occurred at 4.0% drift. The above may be attributed to the higher confinement level provided at the critical section by the thicker jacket of unit JH4.

The increased confinement would provide for greater confined concrete strengths, thus increasing the column strength, and enable higher compression strains to be sustained without significant concrete strength deterioration. Similar to that concluded in Section 4.9 for the high aspect ratio columns, the thinner jacket used in JH3 may be sufficient for drifts on the order of 3.0%. For higher drifts, a confinement level equal to that provided by the thicker jacket of JH4 may ensure good performance.

Comments regarding the force-displacement response predictions for low aspect ratio test units JH3 and JH4 are similar to those presented in Section 4.9 for the high aspect ratio test units JH1 and JH2. The agreement between the analytical and experimental force-displacement response curves was in general, good. Slight differences between the curves might be due to errors in the initial prestress force value used in the moment-curvature analysis for each unit and test.

Both columns performed well overall. Both exhibited stable response up to the maximum imposed drift of 4.0% for the first tests. Specimen JH4 performed better than JH3 for the second test due to the higher level of confinement at the critical section. No spalling of concrete was observed in the non-jacketed upper column segment of either specimen. Shear induced strains in the transverse spiral reinforcement were low for all tests, and no inclinations of the flexural cracks were observed. Thus, the column shear strength was provided by the horizontal component of the diagonal compression strut of the column. Damage to both columns was minimal, even after imposed drifts of 5.0% and 6.0%. As was observed for tests on the high aspect ratio columns, the measured residual column drift was low, and equal to less than 0.2% for all four tests.
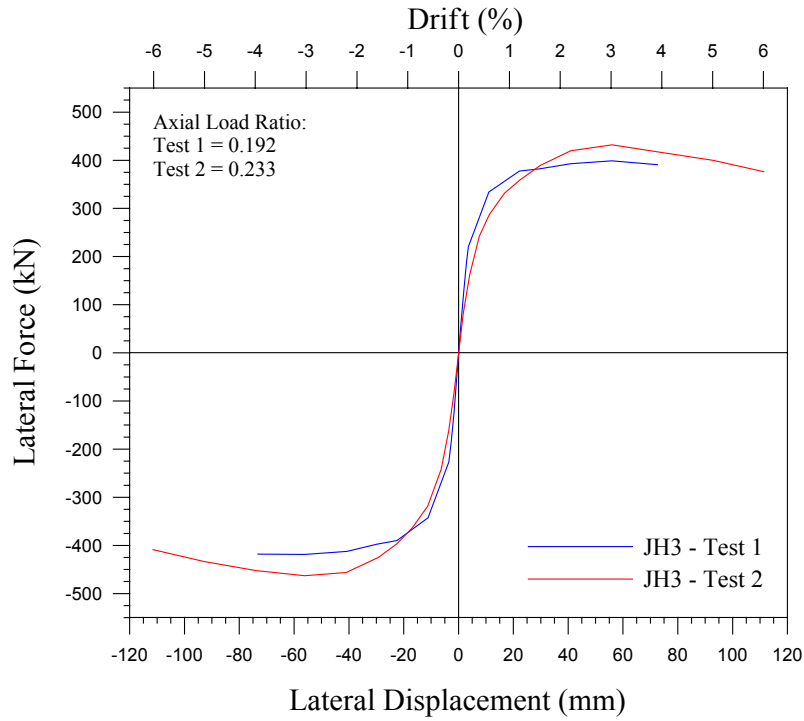
Figure 5.81 JH3 Test 1 and 2 force-displacement response comparison
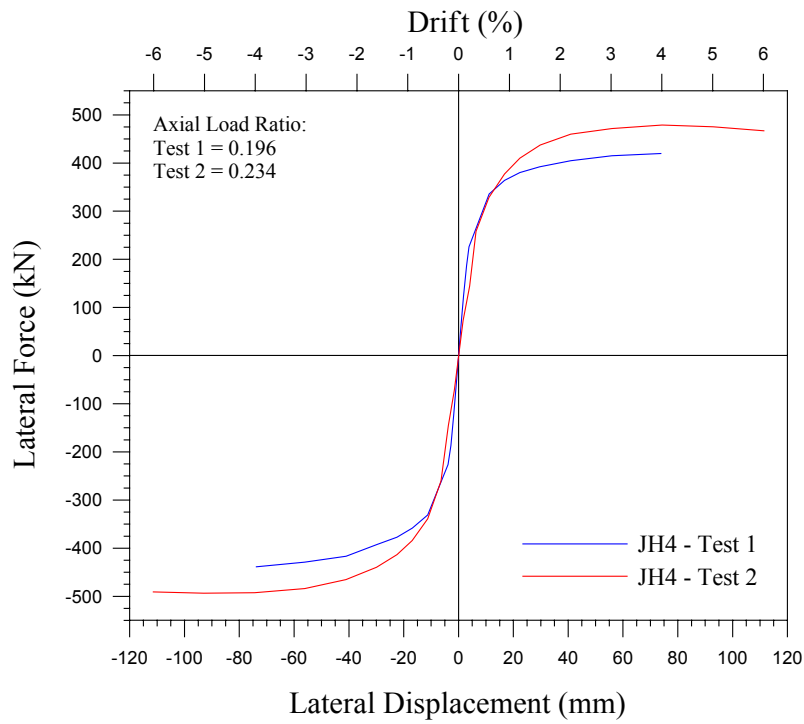

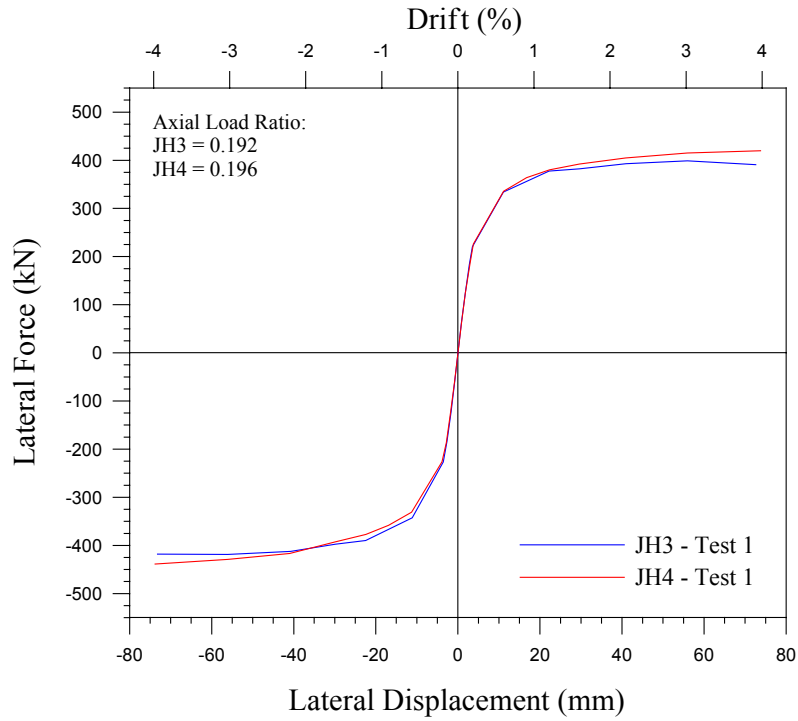Figure 5.82 JH4 Test 1 and 2 force-displacement response comparison

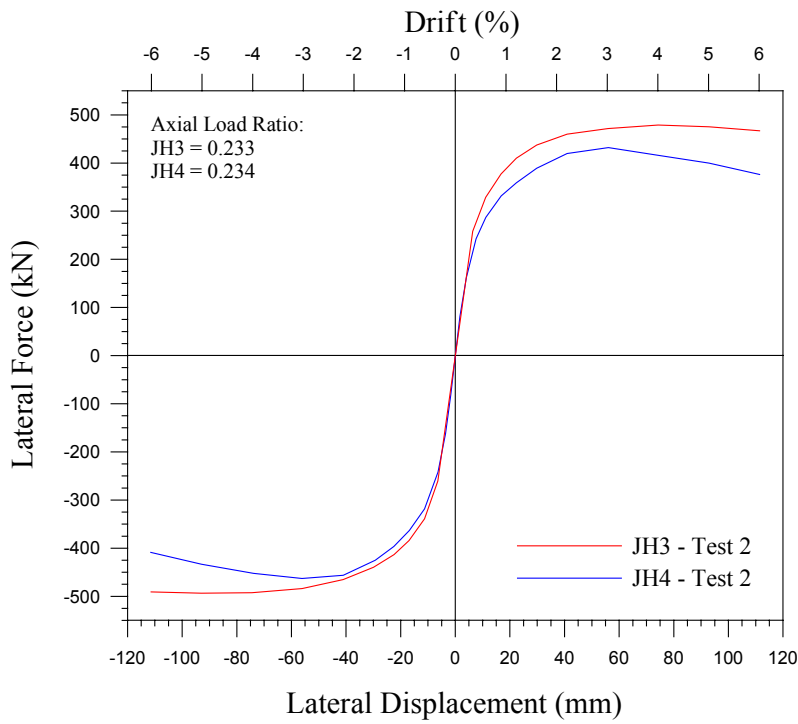Figure 5.83 JH3 and JH4 Test 1 force-displacement response comparison

Figure 5.84 JH3 and JH4 Test 2 force-displacement response comparison

CHAPTER 6 CONCLUSIONS AND DESIGN RECOMMENDATIONS

6.1   Overview

This research involved the analytical and experimental investigation of the performance of unbonded post-tensioned precast concrete segmental bridge columns under lateral earthquake loading. Four large-scale columns were constructed in a laboratory setting and tested under increasing cyclic fully reversed loads/displacements simulating seismic input. The columns were constructed by stacking precast segments on top of each other and then post-tensioning the assembly with vertical prestressing steel located at the center of the column cross-section. The bottom segment in each column was encased in a steel jacket while the segments above were reinforced with conventional spiral reinforcement. The column tendons were unbonded for all tests. In the first phase of the research, two high aspect ratio columns with identical prestressing steel reinforcement but different jacket thickness were tested. Specimens with similar details but of a lower aspect ratio were tested in the second phase of the project. Each specimen was tested twice, the first time with a low-moderate initial prestress force and a second time with a higher tendon prestress level.

6.2   Summary of Test Results and Conclusions

With the exception of specimen JH1, each of the test units achieved a drift of 4.0% during the first test with little or no degradation of strength. For JH1, significant spalling of cover concrete above the steel jacket initiated at 3.0% drift, and the test was therefore stopped at that level. All test units behaved in a ductile manner, exhibiting nonlinear response while having negligible residual displacement after the tests. Measured residual column drifts were on the order of 0.10%, except for unit JH2 that had 0.3% residual drift at test end. The low residual drift resulted from the high total vertical force on the column (prestress force plus applied dead load), which provided a large recentering or restoring force. Since the tendons were unbonded, inelastic straining of the tendon did

not occur and the original prestress force was maintained. The observed damage during the first tests of JH1 and JH2 was greater than anticipated. In addition to the expected concrete crushing below the jacket toe, unexpected spalling of cover concrete occurred in the non-jacketed segments directly above the steel jackets to a height of 300mm above the top of the jacket. The steel jackets should thus have extended higher up on the columns. The damage to units JH3 and JH4 was low for the first test. Only minor crushing of concrete at the gap between the top of the footing and bottom of the jacket occurred. No spalling was observed in the upper non-jacketed column segments of those columns. All cracks observed during testing remained horizontal (i.e., no inclined flexure-shear cracks were observed), indicating that the full column shear was carried by the horizontal component of the diagonal compression strut.

The hysteretic energy dissipation of the test units was relatively low, but did increase slightly with increasing drift. For the early stages of testing the equivalent viscous damping was, on average, approximately 5%. For units JH1 and JH2, the damping did increase markedly at a drift of 3.0% because of the energy dissipated by the spalling of concrete in the non-jacketed segments. In general, units JH2 and JH3 with the thinner jackets showed a greater increase in damping with higher drifts than did the test units with the thick jackets. This was likely due to the lower confinement level provided by the thinner jackets and thus higher degree of crushing at the column base.

Columns JH1 and JH4 with the thicker jackets performed better than JH2 and JH3 for the second test. At the maximum imposed drifts of 5.0% and 6.0% for units JH2 and JH3 respectively, the strengths had dropped on average by 12% from the maximum observed strengths. A decrease in capacity of only 3% on average was observed for units JH1 and JH4 at the maximum imposed drift of 6.0%. In addition, the column strengths were substantially higher than those were for JH2 and JH3. The above is because the thicker jackets provided approximately double the level of confinement at the critical section than did the thinner jackets of JH2 and JH3. The substantially higher confinement level enabled the core concrete to sustain higher longitudinal compression strains without

deterioration of the integrity of the core concrete. The average residual drift observed for the columns at the end of the second test was 0.15%, except for JH2, which had 0.7% residual column drift. Damage for the second tests consisted of only the crushing of concrete below the bottom of the jacket and significant yielding of the steel jacket in hoop tension.

Failure was predicted for each of the second tests based on reaching the ultimate concrete compression strain. For units JH1 and JH4 with the thicker jackets, failure was predicted for approximately the 6.0% drift level, while for units JH2 and JH3 with the thinner jackets failure was predicted at drifts significantly less than the maximum imposed drift. This was not expected since the procedure used to calculate the ultimate concrete compression strain is typically conservative by 50%. It is noted that concrete compression strains obtained using the analytical model may not be representative of actual strain levels at the critical section. Specifically, it was seen that the analytical model tended to underestimate the concrete strain at the column base at high drift levels.

The hysteretic energy dissipation for the second tests was again, observed to be low. For units JH1 and JH4 with the thicker jackets, the calculated equivalent damping was approximately 5% - 6% on average. For the specimens with thinner jackets, an average damping level of 6%-7% was observed. The difference between damping levels is minor, and in light of the many uncertainties and approximations that exist in earthquake engineering design, it is hard to argue against assuming a damping level of 5% equivalent viscous damping for all drifts levels and design conditions.

It was found that the gap provided between the jacket toe and footing allowed sufficient clearance for the longitudinal slippage of the jacket with respect the concrete core and lowering of the jacket due to column rotation without the jacket bearing on the footing. However, at drifts on the order of 5% or 6%, the bottom of the jacket was nearly in contact with the footing. Relative shear slip between the segments was not a problem during testing. Since no shear keys were provided at the interface between segments, the

column shear was transferred entirely by friction. It is felt that for most designs, this will generally be the case since the total vertical force on the column is substantial. However, for very squat columns or for columns with a low total vertical force, the need for shear keys should be investigated. In addition, significant vertical downward accelerations during an earthquake could cause a reduction in the effective vertical compression force thus reducing the shear friction capacity at segment interfaces. It is unlikely however, that vertical accelerations of the magnitude required to significantly reduce the precompression on the section would occur in conjunction with significant horizontal accelerations.

The analytical model presented in Chapter 2 adequately predicted the response of the test units. In general, the theoretical force-displacement response calculated for each unit gave a reasonable estimate of the actual column behavior. Small differences in strength in the two loading directions for some of the tests were likely due to accidental eccentricity of the externally applied axial load. Discrepancies between the analytical and experimental response are attributed to small errors in the calculated initial prestress force.

Based on the analytical and experimental results, the followings conclusions are drawn. Concrete bridge columns built using segmental construction, and reinforced longitudinally with unbonded prestressing steel can safely and effectively resist lateral earthquake forces. The columns are capable of undergoing large nonlinear displacements without experiencing significant or sudden loss of strength. Residual displacements after the seismic event should be minimal, and the damage incurred low. Only minor repair work would be required after the earthquake, thus reducing costs and limiting the amount of disruption of normal use of the bridge structure.

6.3   Recommendations for Seismic Design of Precast Segmental Columns

Preliminary recommendations for the seismic design of precast concrete segmental columns based on tests documented in this report are given. Full design

recommendations based the experimental results and on a current analytical research study are to be published in a companion report.

6.3.1 General Design Issues

The design of precast columns for seismic forces should be based on capacity design principles. Displacements of the precast system are assumed due to rigid body rotation of the column about the base and conservative transverse reinforcement details near the base should be adopted. Other regions of the column and other structural components that are to remain essentially elastic should be designed for the expected moment capacity of the column critical section achieved at the design drift level.

6.3.2 Longitudinal Reinforcement Details

Selection of the prestressing steel area and initial stress can be guided by a trial and error approach using the analytical force-displacement response model presented in Chapter 2 of this report. The response curves shown in Figure 6.1 are given as an example of a parametric study used to guide the design of the precast column test units for this experimental research program. The curves shown in the figure were created by keeping the prestressing steel area constant while increasing the initial prestress stress (and hence increasing the initial axial load ratio), and are for a transverse reinforcement volumetric ratio, ρ_j, of 4.0%. The initial axial load ratio, equal to the axial dead load plus the initial prestress force, is listed for each curve. The axial load ratio at the maximum displacement is shown in parentheses next to the initial value. It can be seen that using a very low axial load ratio results in a response with a steep, positive second slope stiffness while using an extremely high initial axial load ratio results in less overall ductility and a negative post-elastic stiffness. Clearly, the response obtained using a high initial axial load ratio in not desirable due to the above mentioned behavior. Using a low initial axial load ratio may not be desirable either since relatively low column strengths would be achieved with reasonable column diameters. It is noted that the second slope stiffness

and system ductility will also depend on the transverse reinforcement ratio provided near the column base.

It would seem that the ideal option for design would be to strike a balance between strength and ductility. The curve given for an initial axial load ratio of 0.20 exhibits a positive second slope stiffness and significant displacement ductility. Both the initial axial load ratio and axial load ratio at the maximum displacement for the 0.20 curve are similar to those observed during the tests documented in this report. Thus, damage levels consistent with those observed during testing should result with an axial load ratio of this magnitude. Based on the above, considerations for the level of prestress given below seem reasonable.

- The initial prestressing steel stress should be such that an initial axial load ratio of approximately 0.20 is achieved.

- The maximum axial load ratio during the seismic event should be less than or equal to approximately 0.30.

These values should be used only as a guide, and should not be taken as absolute minimums/maximums. It is up to the designer to consider the influence of the above variables on column response and make their appropriate selection so that the desired performance is achieved.
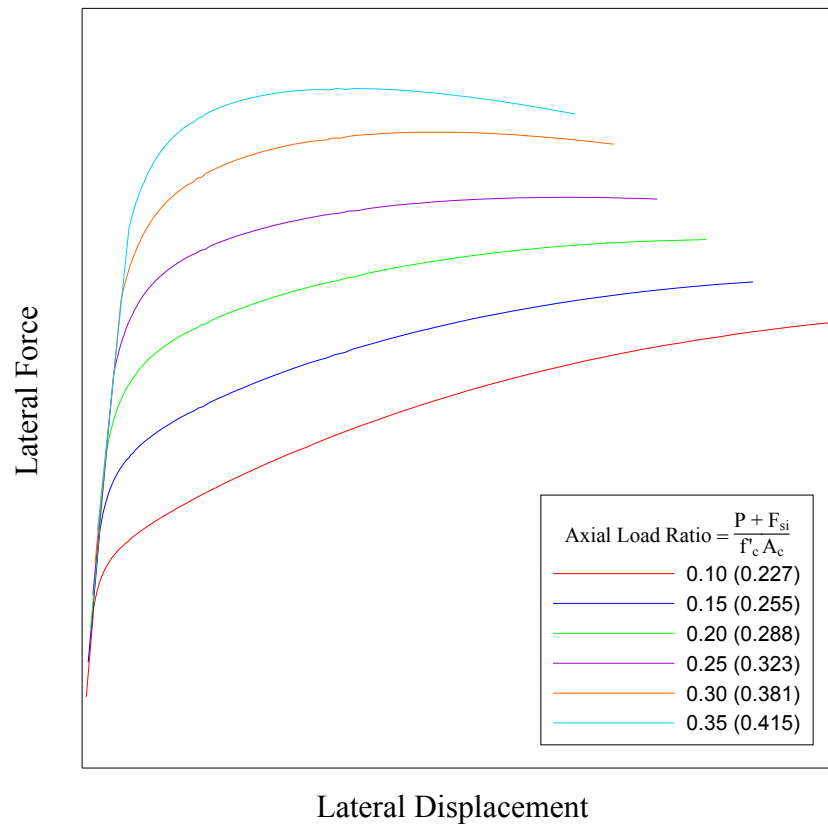
Figure 6.1 Influence of initial axial load ratio on column response

6.3.3 Transverse Reinforcement Details

The detailing adopted for transverse reinforcement is critical to the seismic performance of the precast system. High longitudinal concrete compression strains are expected at the base, and thus significant confinement levels are required to prevent early degradation of concrete strength and ensure a high ultimate concrete compression strain, ε_{cu}. The level of confinement to be provided by the steel jacket at the plastic end region will depend on the design drift and the axial load ratio. The selection of jacket thickness will also depend on the performance level objective. A jacket with a volumetric ratio of 2.0% might provide for sufficient column ductility, but could result in extensive permanent hoop strains after the seismic event. If the performance level objective calls for "minimal repair required", then the volumetric ratio of the jacket should be relatively high.

227

The ultimate displacement capacity of the precast system may be conservatively estimated using the ultimate concrete strain given by Eq 2.29 repeated below.

$$\varepsilon_{cu} = 0.004 + \frac{1.4\rho_j f_{yj} \varepsilon_{sm}}{f'_{cc}} \tag{2.29}$$

The ultimate displacement calculated using the above ultimate strain would likely be very conservative. However, until more research is conducted on the behavior of the precast system under seismic loading, it is felt this conservatism is appropriate. For the axial load ratios suggested above, a minimum volumetric steel ratio of 2.0% is reasonable for drifts up to 3.0%. For higher drifts and/or axial load ratios, an increased volumetric ratio on the order of 4.0% is suggested. Calculation of the full force-displacement response behavior should be performed to evaluate column performance for a given steel jacket volumetric ratio.

The height of the steel jacket should also be conservatively chosen if spalling of concrete above the jacket is to be avoided. A moment-curvature analysis of the non-jacketed segment directly above the jacketed segment can be used to determine the required height to avoid spalling. First, the maximum expected column moment to be developed at the critical section during seismic response should be determined. The maximum axial force – equal to the axial dead load plus the initial prestress force plus the incremental prestress force – should be calculated as well. A moment curvature analysis is then run for the non-jacketed segment, with the axial load equal to the value determined above. From the analysis, the moment when the concrete strain is equal to $\varepsilon_c = 0.004$ is found. The ratio of this moment to that at the critical section gives the height of the column that does not require a jacket to prevent cover concrete spalling. The jacket height determined in this manner should be increased by a safety factor to account for the possibility of maximum column strength being higher than predicted. In addition, the confined concrete stress-strain model used in the moment-curvature analysis should be representative of the

concrete used. That is, a model appropriate for high strength concrete should be used if high strength concrete is in the design.

As an alternative to the above, selection of the jacket height can be guided by the recommendations below. The values for the extent of jacketing given below are similar to those suggested in Ref. 5, and are appropriate based on the experimentally observed performance of the test units.

- For axial load ratios (maximum axial load ratio during the seismic event) of 0.30 or less, the jacketed region is equal to (1) the section dimension in the direction considered, or (2) the region over which the moment exceeds 75% of the maximum moment.

- For axial load ratios great than 0.30, the above values should be increased by 50%.

It is stressed that the axial load ratio referred to above is that at the maximum displacement response since the total axial load acting on the column increases from its initial value as the prestressing steel is stretched.

REFERENCES

1. ATC, *Improved Seismic Design Criteria for California Bridges,* Report ATC-32, Applied Technology Council, Palo Alto, Calif., August, 1983

2. Hose, Y.D., Seible, F. and Preistley, M. J. N., *Strategic Relocation of Plastic Hinges in Bridge Columns*, Structural Systems Research Project, Report No. SSRP 97/05, University of California at San Diego, La Jolla, California, September 1997.

3. Kowalsky, M. J., Priestley, M. J., "Improved Analytical Model for Shear Strength of Circular Reinforced Concrete Columns in Seismic Zones", *ACI Structural Journal*, American Concrete Institute, Vol. 97, No. 3, May-June 2000

4. Mander, J. B., Priestley, M.J.N., and Park, R., "Theoretical Stress-Strain Model For Confined Concrete", *Journal of the Structural Division, ASCE*, Vol. 114, No. 8, August 1988, pp. 1804-1826

5. Priestley, M.J.N., Seible, F., Calvi, G.M., *Seismic Design and Retrofit of Bridges*, John Wiley & Sons, New York, 1996.

6. CALTRANS SESIMIC DESIGN CRITERIA, California Department of Transportation, Sacramento, CA., 1999